Etude multi-échelles et multiphysiques des mécanismes de fissuration dans les matériaux à base de fibres naturelles

Victoria Krasnoshlyk

Communauté
UNIVERSITÉ Grenoble Alpes

THÈSE

Pour obtenir le grade de

DOCTEUR DE LA COMMUNAUTÉ UNIVERSITÉ GRENOBLE ALPES

Spécialité : **Matériaux, Mécanique, Génie Civil, Électrochimie**

Arrêté ministériel : 25 mai 2016

Présentée par

Victoria KRASNOSHLYK

Thèse dirigée par **Sabine ROLLAND DU ROSCOAT** et codirigée par **Pierre DUMONT** et **Per ISAKSSON**

préparée au sein du **Laboratoire Sols, Solides, Structures, Risques 3SR** et **Laboratoire Génie des Procédés Papetiers LGP2**

dans **l'École Doctorale Ingénierie – Matériaux, Mécanique, Environnement, Énergétique, Procédés, Production**

Étude multi-échelles et multiphysiques des mécanismes de fissuration dans les matériaux à base de fibres naturelles

Thèse soutenue publiquement le 29 juin 2017,

devant le jury composé de :

M^me^ Evelyne MAURET
Professeur, Université Grenoble Alpes (Présidente)

M. Pascal CASARI
Professeur, Université de Nantes (Rapporteur)

M. Moussa GOMINA
Chargé de recherche, CNRS, ENSI Caen (Rapporteur)

M^me^ Sabine ROLLAND DU ROSCOAT
Maître de Conférences, Université Grenoble Alpes (Directeur de thèse)

M. Pierre DUMONT
Professeur, Institut National des Sciences Appliquées de Lyon (Co-Directeur de thèse)

M. Per ISAKSSON
Professeur, Université d'Uppsala (Co-Directeur de thèse)

M^me^ Karine CHARLET
Maître de Conférences, SIGMA Clermont (Examinateur)

M. Samir ALLAOUI
Maître de Conférences, Université d'Orléans (Examinateur)

Acknowledgement

I would like to thank my supervisors: Sabine Rolland du Roscoat, Pierre Dumont and Per Isaksson for their guidance, encouragement and expertise that contributed to the quality of this work. Thank you for making it such a rewarding experience from which I have grown as a scientist, researcher and, of cause, as a person. BIG thanks for supporting me all the way until the end!

Also I would like to thank the members of the jury including Evelyne Mauret, Pascal Casari, Moussa Gomina, Karine Charlet, Samir Allaoui, for the evaluation of my work, for your feedback, interesting discussion and questions.

I would like to express my gratitude to both laboratories 3SR and LGP2 for providing all the necessary facilities for this research. I would like to thank the laboratory collaborators and colleagues for administrative and technical support including Carole Reverdit, Aurélie Linares, Sheherazade Mezenner, Mireille Desousa-Pfister, Jérôme Branon-Maillet, and Rémi Cailletaud. Many thanks go to Maxime Terrien, Pascal Charrier, Stéphane Dufreney, Mikaël Party, Denis Curtil for providing technical assistance for the experiments. During the PhD work I have had the opportunity to carry out experiments at synchrotron facilities, i.e. ESRF (France) and SLS (Switzerland). Big thanks to the scientific group and PhD students who helped me with the long and complicated experiments. You rock!

It was a great pleasure to work in the CoMHet team, gathering of amazing scientists and researchers. I would like to thank everybody in this team for welcoming me to the group, for your support, collaboration, and for sharing good moments together.

Special thanks for the help and the scientific discussions go to Edward Andò, Raphaël Passas, Jean-Francis Bloch, as well as to the PhD students: Thanos Papazoglou, Jeanne Doreau Malioche, Thibaud Cochereau and Abdelali Dadda (for your positive vibes as well!). I would like to acknowledge my former colleagues who have a special place in my heart: Tanguy, Dimitri, Stiven, Benj, Ghonwa, Stéphane, Timos, Audrey, Sylvie, Maxime. Good memories about the lab life and outside of it! Thanks to my office mates: Gus, Flo-flo, Mohamed, Franck for being so kind, helpful and funny.

I would like to thank my friends from all over the globe, especially from Sweden, Russia and France. I'm grateful for the good time shared with Elsa, Maxime, Bart, Lucas, Ying, Yutta, Boris, Dima, Lena, Dilyara, Xavier, "les super-colocs", "les

strasbourgeois", Rita, Katya, Julian, Sacha, and Dasha. Thank you so much for your support, positive altitude and encouragement, especially during the tough moments.

Thank you for everything, dear Louis, Elisabeth, Bernard, Clemy and Franky! It is a blessing to have such amazing and caring people in life who I can call my family. Always positive, joyful and nice time with you, guys! And of cause, infinite thanks to my beloved Russian family for their unconditional love and support: благодарю вас, родители и сестричка, за любовь, поддержку и заботу, которую дарили мне в течении всего времени моей диссертации. Я очень вас люблю! Thank you, everybody, whom I have ever met on this way and who has influenced my life even a tiny bit! Thanks to salsa, yoga and reggae music for keeping the mood up all the way through.

Abstract

This study deals with the experimental multiscale characterization of fracture mechanisms in low density papers, i.e., sparse fibrous networks, which exhibit a very specific behaviour in regards to crack propagation such as, for instance, a low sensitivity to defects unless these defects reach a critical length. Several various original experiments were performed to investigate these mechanisms. First, a series of macroscopic single edge-notched fracture tests were performed to investigate the structural changes and deformation mechanisms of tested fibrous networks under various relative humidity conditions. Fracture localization in these papers was shown to be related to local variations in mass distribution, i.e., the flocs and the so-called antiflocs, these terms being used to designate mesoscale structures of local high mass distribution and low mass distribution in the fibre networks, respectively. Then, a gradient-enhanced theoretical model was used in order to quantitatively capture these subscale length-effects. In addition, *in situ* micromechanical tests coupled with advanced imaging techniques (optical microscopy and more particularly X-ray microtomography) were used to investigate the structural changes and deformation mechanisms at the meso- and microscales of tested fibrous networks under various relative humidity conditions. These experiments enlightened the structural modification of paper during crack initiation and propagation. The analysis of these 3D images enlightens the scenario of crack initiation, propagation and, finally, breakage of paper samples, as well as the associated deformation mechanisms at both mesoscale and microscale. For instance, these experiments enabled mesoscale structural variations such as localized variations of thickness variations or porosity, size of the fracture process zone in front of the crack tip to be characterized, as well as the deformation mechanisms of fibres and bonds in the zone of deformation localization and crack path.

Résumé

Cette thèse porte sur la caractérisation expérimentale multiéchelle des mécanismes de fissuration dans les papiers faible grammage, c'est-à-dire des milieux fibreux très poreux qui présentent un comportement très particulier lors de la propagation de fissures en leur sein. Par exemple, par la présence d'hétérogénéités structurales dans ces matériaux affectent très peu la localisation et la propagation de défauts tels que des entailles à moins que ces défauts atteignent une taille critique. Plusieurs analyses expérimentales ont été menées afin d'étudier ces phénomènes. Une série de tests de fissuration sur des éprouvettes entaillées a été réalisé dans différentes conditions d'humidité relative. La localisation du trajet suivi par les fissures dans ces milieux a ainsi pu être reliée à la présence de flocs, c'est-à-dire d'agrégats fibreux qui sont des zones de grammage supérieur au grammage moyen du papier. Ensuite, une théorie basée sur une approche non-locale a été utilisée pour quantifier les effets liés à une longueur critique propre au matériau sur les phénomènes de localisation de fissures, longueur critique d'un défaut pour qu'une fissure localise et se propage au travers du matériau depuis son voisinage. Cette longueur critique a été reliée à la distribution de la taille des flocs présents dans les papiers de faible grammage. Enfin, des essais de fissuration sous imagerie (en lumière visible et principalement en tomographie à rayons X) ont été réalisés. L'analyse des images ainsi obtenues a permis de décrire les mécanismes se produisant aux échelles mésoscopiques et microscopiques dans la zone d'élaboration en front de fissure, encore appelée Fracture Process Zone, et le long de la fissure. La taille de la zone d'élaboration, les mécanismes de déformation des fibres et de rupture des contacts en front de fissure ainsi que les variations locales de porosité et d'épaisseur le long de la fissure ont ainsi pu être mis en évidence.

Table of contents

List of figures

List of tables

General introduction

A variety of different fibrous materials made up of synthetic and/or natural fibres are present in everyday life materials. For example, composite parts dedicated to automotive or electrical applications are made up of 2D random glass fibre mats impregnated by a polymeric resin. Composite parts dedicated to the aerospatial applications are made up of a woven carbon fibre network impregnated by a carbon resin. Another example concerns the printing and packaging industry where paper and paper boards, made up of natural cellulosic fibres, are involved. Despite the variety of manufacturing processes of such materials and wide range of application, all of them can be considered as being formed by a network of fibres interconnected via contacts or bonds.

In the case of materials made up of natural cellulosic fibres such as papers and paperboards, the fibres are chemically linked to each other to form a complex network. The fibres' structural characteristics (length and diameter) are affected by the relative humidity of the surrounded area. During papermaking process, a planar fibrous network of paper is formed. Depending on the papermaking conditions, the fibres can also be more or less orientated along the machine direction. The paper fibre networks also exhibit mesoscale heterogeneities that are referred to flocs that correspond to areas where fibres aggregate more than in average during the papermaking process.

During their time life, paper materials undergo severe exploitation leading, for example, to desired or not paper failure. For example, failures of the paper web at the paper manufacture can be due to defects in the paper's constituents, holes or variation in web tension at the production process. Such problems need to be avoided to increase the reliability of the production and of the products. Some papers material, e.g. corrugated boards, tissue papers are often subjected to cut-outs or perforation in order to facilitate the converting or end-use operation. For example, through the perforation, one can easier separate postage stamp or a piece of tissue from the rest (Figure 0-1 c and d). However, cut-outs and perforation operations create stress concentrations at the tips of prefabricated notches or holes. Thus, undesirable crack propagation may be triggered by those operations as it is shown in example for a corrugated board in Figure 0-1b.

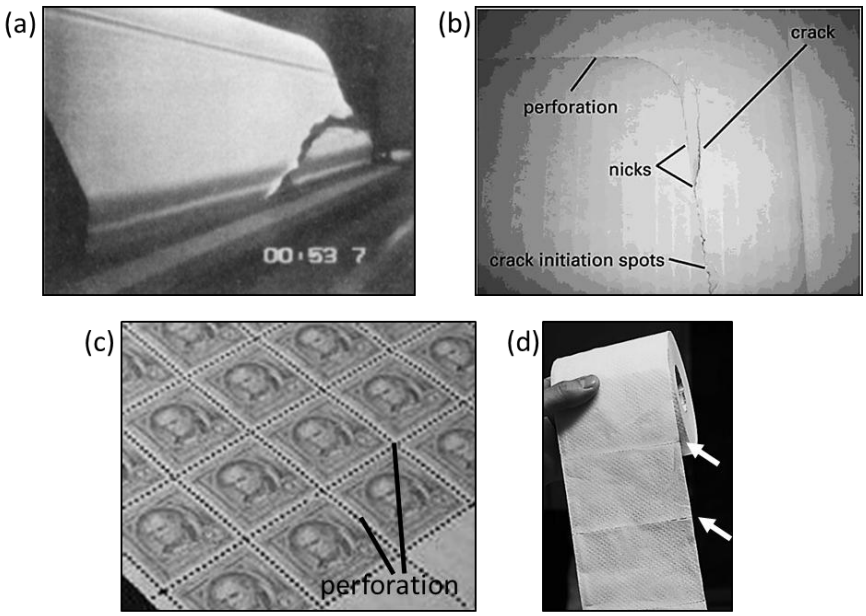

Figure 0-1 : (a) Failure of the paper during production (Östlund and Märkelä, 2012); (b) Crack occurred due to perforation operation of a corrugated board (Östlund and Märkelä, 2012); (c) Rows of perforations in a sheet of postage stamps (https://en.wikipedia.org/); (d) Tissue paper with the lines of perforations indicated with the arrows.

The crack propagation phenomena in natural cellulosic fibre material depend on the geometrical and mechanical properties of the constituents (individual mechanical properties of fibres and inter-fibre bonds), and of the architecture of the fibrous network (porosity, spatial distribution of mass), these properties being moisture dependent. For instance, papers of high density exhibit straight propagation in front of a notch tip, whereas papers of low density present a diffuse behavior which is significantly affected by the mass distribution. Fibres and inter-fibre bonds induce long range mechanical interactions within the paper network. Moreover, due to the mass variation of the network, papers exhibit heterogeneous strain and stress fields under the loading.

The mechanical models based on classical continuum theories fail to predict crack initiation, especially for sparse networks, when structural defects are of the same order of magnitude as any characteristic length of the material, for example, pores because of length-scale effects. A nonlocal (or gradient) model can be employed providing a framework that enables microstructural effects to be taken into account by including an internal length parameter in the constitutive equations. However, the link between the structural characteristics of the fibre network and the internal length parameter still remains unclear. These uncertainties emphasize a need to bridge the scales: micro fractures have to be coupled to the global macroscopic scale. Moreover, despite the large number of studies on moisture effects on paper's mechanical properties, the effect of moisture variations on paper's fracture phenomenon has been overlooked.

All these effects must be taken into account to complete the mechanical approaches for the prediction of crack growth in paper materials. Therefore, the general aim of this study is to investigate the fundamental mechanisms leading to crack growth in paper, especially in low–density papers. Recent advances in experimental mechanics allow such a study from the fibre scale up to the fibre network scale to be carried out. The X-ray microtomography that allows the inner structure of the materials to be captured has been intensively used to characterise the paper structure as well as the fibres and inter-fibre bonds/contacts. Employing this technique will help to describe the micromechanisms that occur during fracture and deduce the important governing structural parameters.

To summarize, the **motivation of this PhD work** is to perform:

- An enhanced multiscale description of crack propagation mechanisms in papers;
- A study of the effect of the paper structural parameters on crack propagation;
- And of the effect of relative humidity/moisture content on crack propagation;
- An improvement of the models for crack propagation in papers by including the structural parameters, using more particularly non-local continuum models for the description of the onset of crack propagation.

The methodological aim of the PhD work is to develop original tools to study the aforementioned mechanisms by performing:

- Series of macroscopic mechanical tests to investigate the structural changes and deformation mechanisms at macroscale of tested fibrous networks under various relative humidity conditions.
- And more originally, *in situ* micromechanical tests coupled with advanced imaging techniques (optical microscopy and more particularly X-ray microtomography) to investigate the structural changes and deformation mechanisms at the meso- and microscales of tested fibrous networks under various relative humidity conditions.

Following the objectives this thesis is organised as following:

- **Chapter 1** is a "State of the art" that briefly introduces paper with a focus on its constituents, its processing methods, and its structural and mechanical properties. A synthesis of the current work on fracture mechanisms is presented as well as the recent progress on paper microstructural characterisation by X-ray microtomography.
- **Chapter 2** "Materials and methods" summarises the developed experimental methodology. The chapter presents the studied samples and details the developed set-ups to investigate the fracture behaviour of paper

under various relative humidity conditions at several length scales: macro, meso and micro. An accurate description of the image processing tools developed to characterize the structural and mechanical evolution of the paper while loading is proposed.

- **Chapter 3** "Influence of mass distribution in cellulosic fibre materials on the fracture behaviour at different moisture conditions" carries out the experimental and analytical studies of the fracture processes in two different moisture-sensitive paper materials such as a low- and a high-density papers at macro- and mesoscales. The difference in fracture localization in those papers was studied in regard to local mass distribution in paper. A gradient-enhanced theoretical model was used in order to quantitatively capture subscale length-effects.
- **Chapter 4** "3D visualisation and quantification of the fracture mechanisms in sparse fibrous networks assessed with multiscale X-ray microtomography" presents the experimental study where the fracture mechanisms were observed at meso- and microscales in the ambient conditions using the interrupted and the real-time *in situ* X-ray imaging during the tensile tests at ambient conditions.
- **Chapter 5** "3D X-ray real-time and *in situ* characterisation of fracture phenomena of sparse fibre network under different humidity conditions" presents the investigation of the influence of moisture on the fracture mechanisms at meso- and microscales.

Conclusions and perspectives end this manuscript.

Chapter 1. State of the art

Content

1.1 Introduction

This chapter presents the literature overview. We structured this chapter as follows:

- Section 1.2 introduces paper materials, raw materials, pulp and papermaking main operations;
- Section 1.3 focuses on the mechanical and hygro-mechanical behaviour of paper;
- Section 1.4 presents the fundamentals of fracture mechanics and their application on the fibrous materials and paper;
- Section 1.5 describes X-ray tomography as a 3D technique used to investigate the hygro-mechanical behaviour of the paper.

1.2 Paper materials

1.2.1 Introduction

Paper is a porous material that consists of natural cellulosic fibres. Moreover, mineral fillers can be introduced in the structure in order to improve, for example, brightness and surface properties of paper.

Figure 1-1 illustrates the wide range of paper used in everyday life, chosen for their differences in end-use properties.

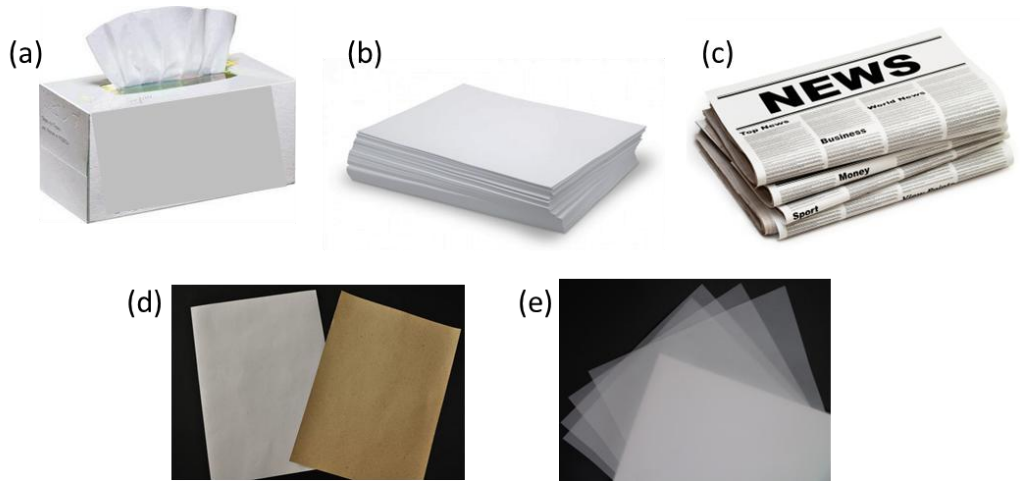

Figure 1-1 : Examples of paper materials ordered by their density: (a) tissue paper; (b) office paper; (c) newspaper; (d) liner; (e) tracing paper.

a) ***Tissue paper***, such as paper towels, napkins, or toilet paper: Their main features are the fibre ability to absorb the liquids, the strength of the structure, and the softness (Huang, 2010; Monica Ek et al., 2009b; Ramasubramanian, 2001; Hollmark et al., 1978; Raunio and Ritala, 2013).

b) ***Office paper*** is used in copy machines and printers: the main feature of such paper concerns their surface aspect such as brightness and roughness, their

optical properties such as opacity, their mechanical properties for converting operation such as strength and resistance to fracture and their transfer properties such as electrical conductivity, ink absorptivity or wettability (Ström, 2009).

c) ***Newspapers:*** one of the main requirements is its suitability for printing text and pictures, opacity, durability and strength to endure web manufacturing, usage and folding (Boadway et al., 1963; Moffat et al., 1973; Gregersen et al., 2000; Ström, 2009).

d) ***Liner or linerboard*** is usually used for the production of *corrugated board* that is a sandwich construction of several liner layers, the liner strength as well as its resistance to fracture are the crucial parameter (Westerlind et al., 1991; Södemark and Tryding, 2009).

e) ***Tracing paper*** is used to copy the drawings from one paper to the other one, this kind of paper has to have low opacity and low roughness to satisfy the main function of this kind of paper. When used for printing application, it should have the same mechanical and transfer properties as copy papers.

Despite their difference in structural, physical and mechanical properties, all these papers have in common to be constituted of natural cellulose fibre networks, produced on paper machines that present similar processing of operations. The choice of raw materials (Section 1.2.2) and the manufacture operations (Section 1.2.3) affect the papers' structure and their physical properties such as strength, opacity, brightness, hygroexpansion, and liquid permeability. The papers' constituents and the pulp preparation are presented in section 1.2.2, the paper papermaking process is briefly summarised in Section 1.2.3. The main characteristics of the resulting fibrous structure are described in Section 1.2.4.

1.2.2 Main constituents of paper and pulp production

The main constituent of the paper materials are cellulosic fibres. The fibres properties affect the formation and the consolidation of paper structure in the papermaking process. They are also responsible for the hygroscopic properties of paper. The fibres will be briefly described and the processes of pulp preparation that highly affects the structure and mechanical properties of paper will be discussed below.

1.2.2.1 Morphology of the wood fibres

Wood fibres are the main raw material source for the paper production. Depending on the wood species, growth site, and pulp and papermaking treatment the fibre properties differ remarkably. The wood species introduced into the pulp can either come from the softwood trees such as spruce, pine or larch, or from the hardwoods such as birch, aspen or eucalyptus. The softwood's fibres are about 2.8 – 7.2 mm long and 30 – 50 µm wide whereas the hardwood's fibres are in general 0.8 -

1.3 mm long and 14 – 28 µm wide (Retulainen et al., 1998; Gustafsson and Niskanen, 2012). The composition of wood fibres at the different scales is shown in Figure 1-2.

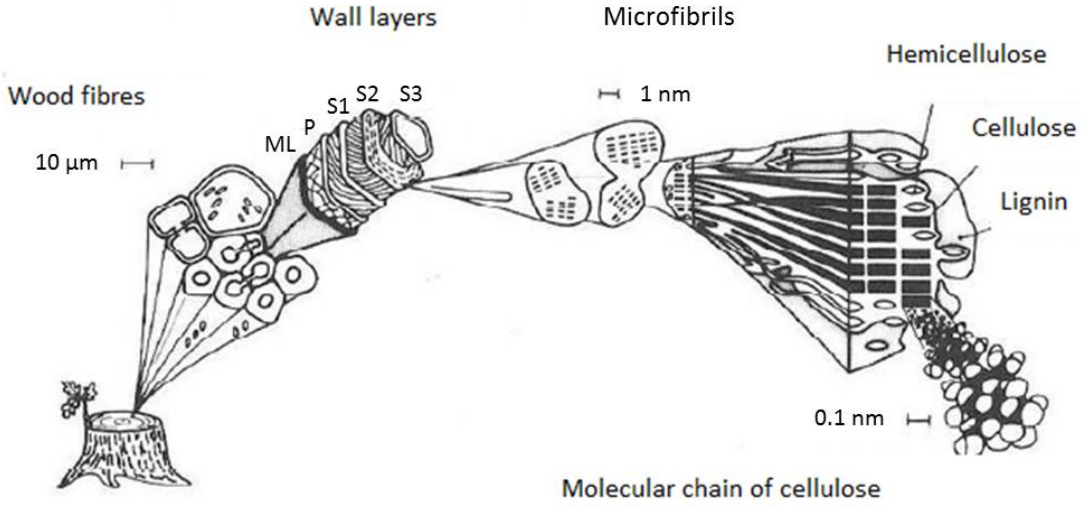

Figure 1-2 : Scheme of a wood fibre exhibiting its different scales (Viguié, 2010).

A wood fibre consists of several cell wall layers that have an helical internal structure as it is shown in Figure 1-3a. In the centre along the fibre length, a fibre has a hollow area, called *lumen,* which may collapse during papermaking process. The cell wall layers are:

- The Primary wall (P) (thickness: 200 to 300 nm).
- The Secondary wall (S1, S2 and S3) (2 – 3 µm). S2, usually the thickest wall, is the most dominative in the mechanical properties of fibre.
- The Middle lamella (ML), mainly consisting of the lignin, glues the fibres to each other.

The layers of the fibres in the secondary wall consist of the microfibrils, small bundles of primarily cellulose molecules, which wind around the cell. The microfibrils present a constant orientation fibril angle, unique for each layer (Figure 1-3b). This angle, called microfibril angle (MFA), refers to the angle between the long axis of the fibre and the cellulose microfibrils (Barnett and Bonham, 2004). The angle controls the capacity of the wall to be deformed. The amorphous matrix of hemicellulose and the lignin surrounding the stiff fibrils is ductile. This all makes each fibre distinctive. The links between the different constituents of the layers gives the cohesive properties of the fibre as well as their rigidity.

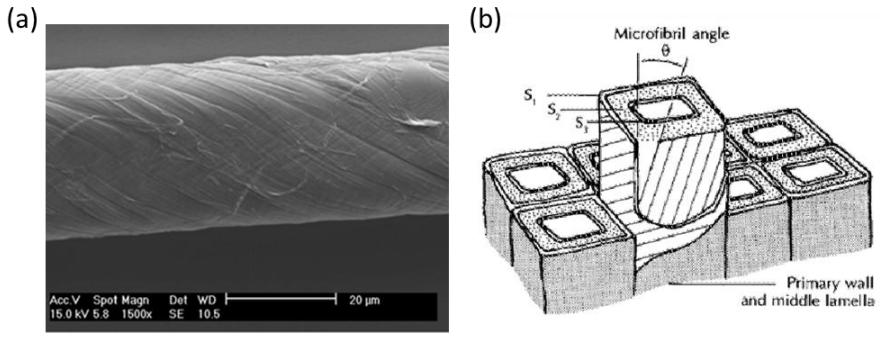

Figure 1-3 : (a) Helical structure of a Norway spruce fibre in the green state is captured in Scanning-electron micrographs. The microfibrils of cellulose are wound around the longitudinal axis of the fibre. From (Joffre et al., 2016) (b) Representation of microfibril angle in the layer S2 in relation to the vertical axis of wood fibre. From (Walker and Butterfield, 1996).

Cellulose is the most important constituent of the cell walls and is responsible for the load-bearing capacity of the fibre. Table 1-1 summarises the thickness of each layer of a softwood summerwood fibre and its relative composition by mass of cellulose, hemicellulose and lignin, the dominant orientation of the microfibrils for each layer.

Table 1-1 : Characteristics of the cell wall in wood (Berg and Gradin, 1999). Parameters and components of each layer of the cell wall such as ML – middle lamella, P – primary wall, and secondary wall divided into S1, S2, S3.

Layer	*MFA* [°]	Thickness [µm]	Cellulose [%]	Hemicellulose [%]	Lignin [%]
ML	None	0.50	8	36	56
P	None	0.10	15	32	53
S1	70	0.30	28	31	41
S2	15	4.00	50	31	19
S3	70	0.04	48	36	16

1.2.2.2 Pulp preparation

The aim of the pulping process is to extract fibres from the wood bulk. The wood is usually cut into wood chips that are disintegrated into fibres either mechanically or chemically. In general, Norway spruce, aspen, and radiata pine are suitable for both chemical and mechanical pulping process, whereas Scots pine, eucalyptus, and birch are more used in chemical pulping. The two main ways of pulping are described in details below:

Mechanical pulping

This pulping is performed by grinding wood or wood chips that releases the fibres: rotating steel plates shear the wood chips. The applied steam softens the lignin that holds fibres together as well as the cellulose of the fibre cell wall, reducing the fibre damage. Depending on the specific manufacturing process, different types of mechanical pulp can be distinguished: thermomechanical pulp (TMP), chemi-

thermomechanical pulp (CTMP), and groundwood (GW) (Gustafsson and Niskanen, 2012).

Mechanical pulp consists of a mixture of fibres, fibre fragments and fines (fragments from fibre walls) (Figure 1-4a) which have been produced during the processing that causes a wide distribution of size fractions and mechanical properties. In mechanical pulp, the undamaged long fibres, that have a high bending stiffness, get generally attached to each other through the large amount of fines and fibre fragments.

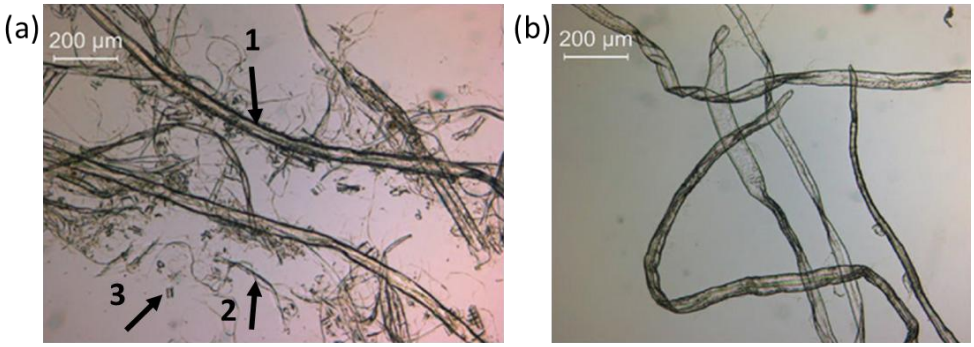

Figure 1-4 : Pulp fibres: (a) thermomechanical pulp TMP: fibres (1), fibre fragments (2), and fines (3) obtained from spruce wood; (b) chemical mildly refined made of pine wood. Modified from (Gustafsson and Niskanen, 2012).

Chemical pulping

The main principle of the chemical pulping is to remove most of the lignin and thereby release the fibres. Thus, the wood chips are cooked with chemicals such as sodium hydroxide, and sodium sulphide in order to dissolve lignin. The kraft process obtained with sodium sulphide is the dominant chemical pulping method that does not affect the fibre length. Usually the yield (dry mass retaining in the fibres) of the chemical pulping is a little more than 50 % whereas for the mechanical pulp it is about 90 %.

Once the fibres are separated from each other, the obtained pulp may further undergo the following operations:

Bleaching

Bleaching is a chemical process performed on different wood pulp to decrease the colour of the pulp. Bleached pulp gives to the papers a better contrast between the paper and the print, therefore, improves the print quality. Moreover, bleaching improves the cleanliness of the paper and ability of paper to resist to ageing (Brännvall, 2009). Mechanical pulp, a lignin-rich pulp, has often undergone bleaching using chemicals such as dithionite and hydrogen peroxide (Brännvall, 2009). The chemical pulp is generally bleached due delignification in the pulping process.

Deinking

Deinking is the industrial process of removing printing ink from the fibres of recycled paper by mechanical or chemical means.

Refining or beating

Beating is one of the key operations in papermaking affecting the fibre structure (Ebeling, 1980; Page, 1989). Beating refers to the mechanical treatment of the pulp resulting in fibre flexibility, increase of inter-fibre bonding in the final sheet (Retulainen et al., 1998; Vainio and Paulapuro, 2007). After beating, the cell wall microstructure of fibres and fibre dimensions are changed (Emerton et al., 1961). Chemical pulp is generally subjected to beating where the structure of the fibre wall (*internal fibrillation*) and surface (*external fibrillation*) become loosen. The internal fibrillation causes increases of the swelling degree, flexibility and conformability of the wet fibre wall whereas the external fibrillation is responsible for bonding strength. Fibrils caused by external fibrillation are spread out from the fibre surfaces.

To obtain the desired end-use properties of the paper, the fibres and their treatment to form the paper sheet must be carefully selected. For example, in the case of paper material presented in Figure 1-1, the following fibres and pulp characteristics are generally used:

a) Tissue paper: the chemical pulp or either deinked pulp.
b) Copy paper: besides a mixture of short (from hardwood) and long fibres (from softwood), office paper contains a big amount of fillers (mainly precipitated calcium carbonate) introduced to improve the optical properties, i.e. brightness.
c) Newspaper: deinked pulp or/and mechanical pulp are preferred.
d) Kraftliner is manufactured from the virgin pulp, whereas a testliner is made of the recycled linerboard.
e) Usually tracing paper is produced from sulphite pulp by highly refining the fibres.

1.2.3 Paper manufacture

After the fibres were liberated from wood, they have to be assembled to create a paper network. The paper making process using, for example Fourdrinier paper machine, is schematically presented in Figure 1-5.

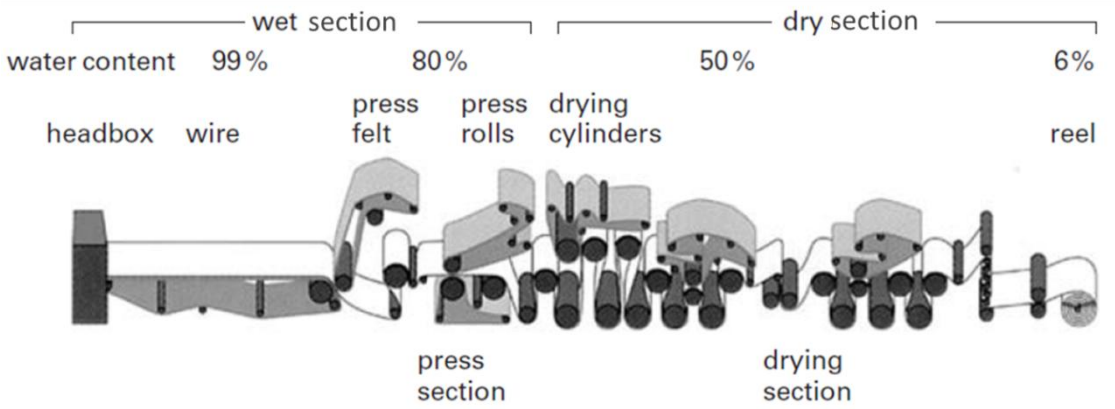

Figure 1-5 : Scheme of the paper production: Fourdrinier paper machine with a straight outline from beginning to end. Modified from (Brännvall, 2009).

Typically, the paper machines are several hundred meters long where the wet section and dry section can be distinguished. The paper machines are organised as following:

- The *Headbox*, a pressurised flow box, spreads out the furnish, mixture of cellulose fibres and water (0.1 - 1.0 % dry solids content), to form the paper web (Brännvall, 2009; Monica Ek et al., 2009a). The solid content of the furnish is low in order to achieve uniformity of the paper web (Gustafsson and Niskanen, 2012). Apart from fibres, mineral fillers (up to 40 % of mass), i.e. particles, may be added to the pulp. Mineral fillers, e.g. calcium carbonate (natural ground and precipitated), clay, talcum, and titanium dioxide, varying their shapes and sizes 0.3 – 20 µm, improve paper optical properties, the surface properties or the printability, although they may decrease the mechanical properties of paper.
- Then the paper web is transported with a woven wire, endless moving belt, allowing the water to be drained and retaining the fibres (Rolland du Roscoat, 2007; Brännvall, 2009). The water is removed through the wire by foils and vacuum boxes. On the leaving the *forming section*, the sheet has around 80% of water content (Sampson, 2006).
- In the *press section,* the paper web transferred onto a felt, i.e. high specification textile with nonwoven surface, is passed between steel pressing rolls. Together the forming and pressing sections form the "wet" section of paper machine (Figure 1-5). On the leaving the press section, the web has been densified and fibres are in contact with each other (Sampson, 2006). At this stage, tension forces hold the planar fibre network together giving it viscoelastic character (Alava and Niskanen, 2006). After this procedure, the sheet contains still about 60 % of water.
- Then the paper is dried by the cylinders that are steam-heated. The paper sheet is held against the cylinder using a woven textile (Sampson, 2006). In the *drying section* the amount of water in paper web drops from 60 to 10 %.

The paper properties depend on the amount of decreased water content and the shrinkage of paper. During this process the fibres connect to each other creating fibre bonding: the water menisci between fibres decrease pulling fibres together so that hydrogen bonds can form between them (Alava and Niskanen, 2006). Paper gains its strength during drying process. The largest part of the produced paper is dried on a multi-cylinder paper dryer (M. Ek et al., 2009): the surfaces of the web are alternating between contact with a hot cast iron cylinder and transport in hot humid air between the cylinders. The temperature varies from 60 °C up to 110 °C between the sets of cylinders. The process is repeated until the moisture content has been reduced to a desire level. The other example of drying system used for tissue papers is through-air-drying (TAD). In the TAD-dryer the web is dried on a porous TAD-cylinder by sucking hot air (150 - 250 °C) through the web which eventually does not densify the web as much as the other methods.

- The *Calendering* and/or the *coating* of the paper are optional operations which both aim at improving the surface properties of paper by, mainly making it smoother (Monica Ek et al., 2009b; Kajanto et al., 1998). The roughness of paper is reduced proportionally more than thickness due to higher compressibility of the surface layers (Kajanto et al., 1998).

The running direction of the web is referred to the machine direction (MD), cross-machine direction (CD) is perpendicular to MD and the thickness direction is ZD (Figure 1-6). Since MD and CD have much higher dimension than the thickness of paper at the macroscale, paper is often considered as a two-dimensional material (Monica Ek et al., 2009a; Gustafsson and Niskanen, 2012).

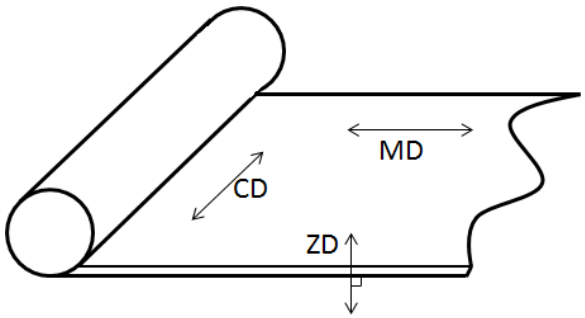

Figure 1-6 : Definition of the three directions in paper.

1.2.4 Paper structure

The section starts with the description of the macroscopic structural characteristics of the papers such as grammage, thickness, and density. These properties are important in many end-use paper materials as well as they describe indirectly the three-dimensional paper structure (Kajanto et al., 1998).

At the smaller scale, paper structure presents distribution of its components, e.g. fibre, fillers. Fibres being principal structural elements of paper affect the properties

of paper as well the bonding between them (Retulainen et al., 1998). However, the physical properties of paper is dictated by network of the fibres, for example, mechanical paper properties depends on the direction of the web, thus, on the main fibre orientation in the network.

1.2.4.1 Macroscopic structural properties

Grammage

The grammage (g) or basis weight is a fundamental property of the paper materials defined as the mass per unit area, [g/m^2]. Traditional method of measuring paper grammage is gravimetrical by dividing the weight of a region by its in-plane area. The distribution of grammage or local mass variation is referred to the formation of paper detailed in Section 1.2.4.2.

Thickness and its measurements

Thickness *(t)*, [µm] of paper is generally defined as the perpendicular distance between two surface planes of a paper sheet (Scott et al., 1995). Accurate measurement of the thickness is essential since it is used to compute one of the other fundamental structural characteristics of paper such as density. The true thickness of paper is tricky to measure due to the paper roughness and local mass variation in thickness direction affected by papermaking process. Therefore, measurement of the thickness has to be considered in the details.

Apparent thickness (t_{app}). Following ISO 534: 2011(F), the thickness of paper sheet can be measured using an apparatus with two plane parallel circular plates (16 mm in diameter) placed in contact with the sample surfaces (Figure 1-7a). This kind of measurement is called the apparent thickness where pressure of 0,1 MPa is used. One plate is fixed and the other is movable in a direction perpendicular to the plane of the fixed face. The thickness measured as a distance between the two plates can be apparently overrated due to the paper surface unevenness.

Bulking thickness (t_b) is thickness of a single sheet of paper, calculated from the thickness of several superimposed sheets in a pack. One can measure bulking thickness using the same apparatus (Figure 1-7a). Since surfaces of the adjacent layers adjust to each other at the macroscopic scale, piling thickness is lower than t_{app}. Although the surface unevenness effect cannot be totally eliminated (Fellers, 2009).

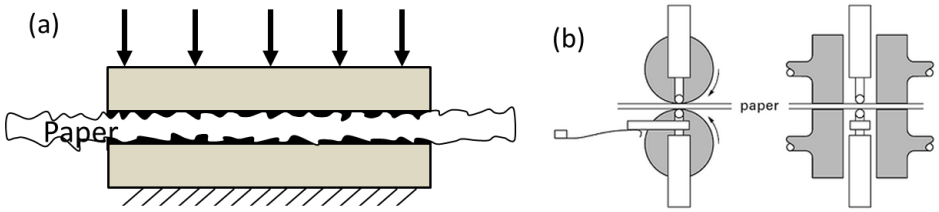

Figure 1-7 : (a) Scheme of apparent thickness measurement according to SCAN-P 7; (b) Scheme of structural thickness measurement according to SCAN P-88:01 (Fellers, 2009).

Effective thickness (Kajanto et al., 1998) **or structural thickness** (Fellers, 2009) (t_{eff}). Measurement of the effective thickness is one of the most difficult among the contact methods. There are two methods used to perform the measurement of t_{eff}.

According to SCAN P-88:01, the thickness of paper is the mean value of the distance between two opposite measuring points. The paper sheets, one by one, are fed through a nip between the spherical probes at a constant speed as it is shown in Figure 1-7b. The obtained thickness profile shows how the paper thickness changes along line across a paper sheet. In comparison, in this case $t_{app} \sim$ max of t_{eff}.

For the other method one needs: soft rubber platens, surface profilometry, or mercury displacement (see more in (Kimura et al., 1979; Kajanto et al., 1998). In this case, empirically the relationship between t_{eff} and t_{app} or t_b was found: t_{app} is 10 – 20% higher than t_{eff} influenced by the grade of paper.

The effective thickness method gives the values closer to the "true" thickness than the apparent method, however it is a contact method meaning that some pressure is applied to the surface of the paper. For the office papers those methods may work with a significantly high accuracy due to the relative uniformity of the surface and thickness of paper. On the other hand, tissue and towel papers, for example creped or embossed during manufacturing process (Huang, 2010), represent high compressibility and web discontinuity (Figure 1-8); therefore it becomes difficult to measure their thickness properly. Also it does not provide the information on the localized point wise thickness variation within the fibrous web (Feng, 2012).

Figure 1-8 : Cross section of a low grammage paper (23 g m^{-2}) presented in the X-ray binarised image (fibres in white). Significant local thickness variation can be observed.

Over the past few years, high resolution non-contact thickness methods were developed to measure thickness of paper materials including:

Twin laser profilometer (TLP) (Sung et al., 2005; Keller et al., 2012; Huang, 2010; Izumi and Yoshida, 2001) where two auto-focusing opposing laser sensors were placed

above and below paper samples. Thickness measurement was based on the values from both lasers although for embossed and cockled papers (with surface roughness 10^{-2} mm and cockle (1 mm)) lasers were incapable to measure significant out-of-plane deformations.

X-ray scanning of paper materials allowing 3D structural measurement is used, among others, to measure the thickness variation too (Huang, 2010; Holmstad, 2004). For the details, please, proceed to the Chapter 1.5.

The existing online thickness measuring techniques were successfully implemented at the industry based on contact as well as non-contact approach (Graeffe and Nuyan, 2005; Nuyan et al., 2006).

Density

The density (ρ), [kg/m^3] is one of the most important macroscopic characteristics of paper structure because it can be used to estimate many other properties of paper such as tensile strength, elastic modulus and light scattering coefficient (Kajanto et al., 1998). The density is calculated as:

$$\rho = {}^{g}/_{t} \tag{1-1}$$

where t is the thickness defined according to the chosen method and g is the paper grammage.

Table 1-2 presents the grammage, the apparent thickness and the density of the types of paper shown in Figure 1-1.

Table 1-2 : Examples of paper materials and their structural properties.

Property	Tissue	Office	News	Liner	Tracing
Grammage, [g/m^2]	23	80	45	140	47
Apparent thickness, [µm]	113	111	61	158	44
Apparent density, [kg/m^3]	204	721	738	886	1068

Porosity

One of the structural characteristics of paper is its porosity Φ [-]. Porosity is the ratio of pore volume to total volume of material. If there are no fillers in the paper structure, the porosity is calculated as:

$$\Phi = 1 - {}^{\rho}/_{\rho_{fibre}} \tag{1-2}$$

where ρ_{fibre} – fibre density [kg/m^3] is assumed to be 1550 kg/m^3 that equals to density of the fibre wall.

1.2.4.2 Structural characteristics

Fibre network

Paper can be considered as a composite material with a non-woven structure. During drying process at the papermaking the fibres link to each other without any adhesive material. Chemical inter-fibre bonds (Section 1.2.4.3) hold the fibre network and are the building units of paper structure.

The denser paper the more contacts per fibre (Retulainen et al., 1998). Examples of two papers of different density are shown on Figure 1-9, tissue paper (a) has a sparser network compare to the liner (b) with larger pores and less bonds per fibre. The network of tissue paper (Figure 1-9a) represents local variabilities including a local mass variation in the structure that is generally caused by manufacturing process. The local mass variation, called formation, is not visible in the volume of the denser network shown in Figure 1-9b but can still exist in such dense network as in example from (Hagman and Nygårds, 2017). Therefore, the mass distribution of paper has been subjected to a thorough analysis among the researchers.

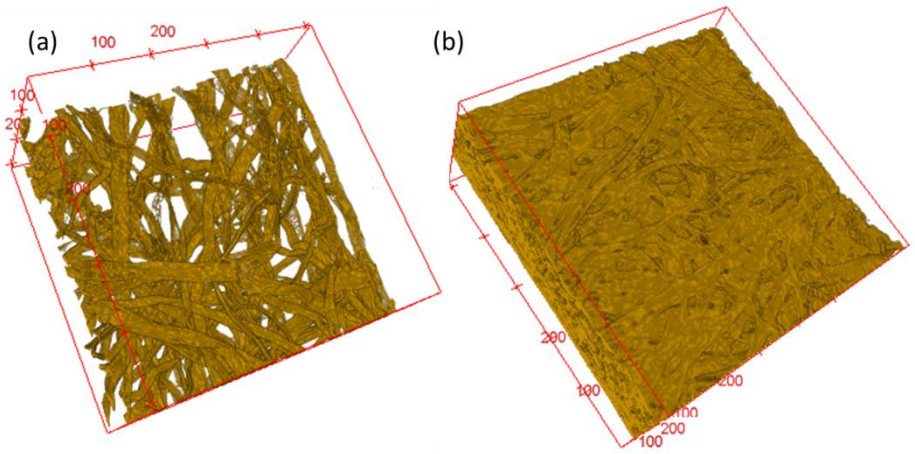

Figure 1-9 : X-ray image of paper networks: (a) low density paper (tissue paper) with a grammage of 23 g/m^2. The X-ray volume is 700 x 700 x 450 µm^3. (b) High density paper (liner) of 140 g/m^2. The X-ray volume is 700 x 700 x 350 µm^3.

Local variability of the paper structure

Flocculation of the network is caused by a consequent fibre interaction in the suspension during motion (Sampson, 2001). In paper materials the fibres, the fibre fragments, the fillers, and the chemical additives may not be equally spread in the sheet (Niskanen et al., 1998). One can simply view variability in the structure with a naked eye placing a paper material against the light (Niskanen et al., 1998; Sampson, 2001): depending on the local areal density, i.e. local grammage, the regions in paper may have different opacities. For the low density papers variance of the local density is greater than for the papers of higher density (Dodson et al., 2001). The origin of variability observed in the paper structure is caused by nonuniformity of basis weight, the spatial variation of fibre orientation, the bonding degree of fibres, drying shrinkage and furnish (Niskanen et al., 1998).

Heterogeneous in-plane mass distribution is named *formation* (Gustafsson and Niskanen, 2012) (Figure 1-10). Its quality is influenced by pulp properties (fibre length and coarseness) (Corte and Kallmes, 1962; Dodson, 1996), ratio of wire and jet speeds, and waiting time at the forming operations (Cresson and Luner, 1990; Farnood, 1995; Lindström, 2008; Hämäläinen, 2008; Isokangas and Leiviskä, 2011). The papers that consist of shorter fibres have generally a higher degree of uniformity (Sara, 1978). By increasing the turbulence in the headbox and on the wire (see Section 1.2.3) we reduce the flocculation of fibres. *Flocs* are the mesoscale regions of higher density than the average of the paper sheet (Deng and Dodson, 1994; Farnood, 1995; Sampson, 2001; Isokangas and Leiviskä, 2011).

Characterisation of formation in paper network

Most of the indirect techniques measuring local grammage distribution are based on the attenuation of electromagnetic or nuclear particle beam in paper (Farnood, 1995). Visible light transmission is one of them that is commonly used at the industry (Kallmes and Ayer, 1987). The lower paper grammage is, the more density variation you can see in the structure. The light goes almost unscattered through a sheet of unbeaten light-weighted uncalendered paper (Komppa, 1988). Therefore, the relationship between local light transmission and local grammage is approximately linear for the low density paper (Bernie and Douglas, 1996). For the other grades of paper whose density is higher, the light transmission technique is not suitable for the analysis of mass distribution (Sampson, 2001). The other indirect techniques such as beta-ray absorption and X-ray radiographies can be used for measuring mass distribution in a paper sheet (Farnood, 1995; Komppa, 1988; Feng, 2012; Cresson et al., 1990; Cresson and Luner, 1990). Beta-ray absorption technique consists in irradiating a paper sample by beta-ray beam and in recording the transmitted-through-paper beam, whose attenuation being proportional to the amount of fibres located in a position and, thus, to the local basis weight. Beta-rays are not scattered compare to the light since the wavelength of beta radiation is large (Komppa, 1988; Ramasubramanian, 2001). The measured values are easily calibrated to basis weight values (Niskanen et al., 1998). However, this method is quite time-consuming and rather suitable for the sheets of mean grammage less than 150 g m^{-2}. The X-ray radiography does not have limit related to the grammage of a studied paper, moreover, the spatial resolution is improved (Sampson, 2001).

Two maps of the local grammage of the paper samples formed with the same global average grammage (60 g m^{-2}) but with different degrees of uniformity are presented in Figure 1-10. The two samples are made from the same type of fibres (softwood fibres) but the manufacturing conditions differ, which altered the paper structure: in Figure 1-10b one can observe the “clumpy” texture comparing to the image in Figure 1-10a where the sample has more uniform structure.

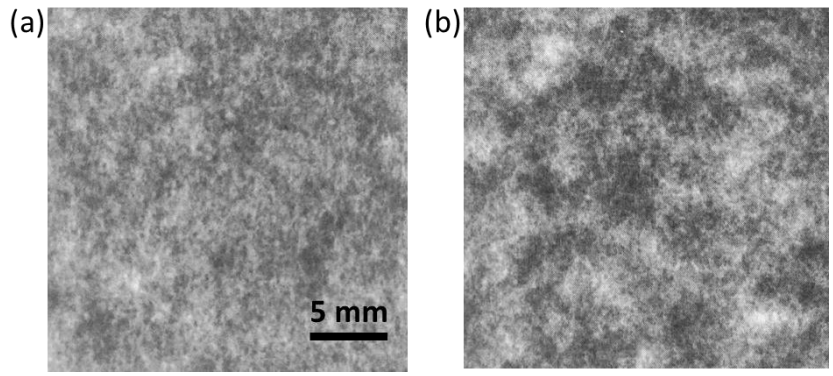

Figure 1-10 : Maps of local grammage for two paper samples with bad formation (a) and good formation (b) obtained by radiography. The dark areas correspond to high local average grammage, and thus high local coverage. Modified after (Sampson, 2008).

Several quantitative descriptors of the nonuniformity in the fibrous structure are reported in the literature. The structure of paper was characterised by dividing a texture map into the adjacent square zones of side 1 mm and computing the local average grammage within each area such that the coefficient of variation of local grammage could be calculated (Sampson, 2001):

$$CV_x(\tilde{g}) = {}^{\sigma_x(\tilde{g})}/_{\bar{g}} \qquad (1\text{-}3)$$

where $\sigma_x(\tilde{g})$ is the standard deviation of local grammage at zone size x and $\bar{g}$ is the mean sheet grammage.

The coefficient of variation of the paper formation is classically used to give an estimate of overall variation in grammage. However, using this method, is not possible to distinguish between structures with different textures due to the limited scale of inspections such as the size of the square zone (Cresson and Luner, 1990). The other existing parameter is a specific perimeter (SP) of all objects in 2D image of the network after applying a threshold at the median grammage (Jordan, 1986; Trepanier et al., 1998). SP is defined as a ratio of the summary of floc perimeters to the total scanned paper area (Figure 1-11). The higher SP is, the better the paper formation and vice versa because the uniform paper sheet contains a big number of the small flocs with large total perimeter, whereas a poorly formed sheet has fewer larger flocs with a small total perimeter (Laleg and Nguyen, 1995). The SP was found to be independent of changes in the paper opacity measured by transmitted light but dependent on the change in sheet density (Laleg and Nguyen, 1995).

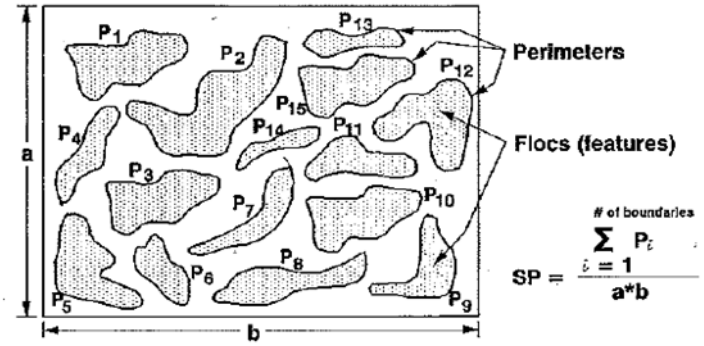

Figure 1-11 : 2D contour lines showing the definition of specific perimeter (Laleg and Nguyen, 1995).

Wavelet transform was applied to the characterisation of formation that provides profiles of local variability (Keller et al., 1999; Sung et al., 2007). (Sung et al., 2007) characterised formation anisotropy such as floc orientation in MD and CD direction including the orientation distribution and the major oriented angle of the flocs.

Fibre orientation

Fibre orientation is affected by the forming process: oriented flows and jet-to-wire speed dictates the fibre orientation distribution (Niskanen et al., 1998). A smooth spreading of the furnish is usually achieved with a small speed difference between the wire and the headbox's furnish jet resulting in alignment of fibres in more parallel way to the machine direction MD. Fibre orientation in the plane of the sheet can vary through the thickness of the sheet (Enomae et al., 2008). Moreover, in the thickness direction fibres may be slightly tilted, less than 5 degrees (Niskanen et al., 1998). Therefore, paper can be considered as a layered structure, each layer having its own orientation.

1.2.4.3 Microstructural characteristics

Inter-fibre bonds

The mechanisms of fibre bonding were subjected to an extensive study throughout the years (Luner et al., 1961; Ebeling, 1976; Salminen et al., 1996; Lindström et al., 2005; Vainio and Paulapuro, 2007; Schmied et al., 2013; Hirn and Schennach, 2015). We describe briefly the inter-fibre bond nature, its formation between the fibres and the structural characterisation using different methods.

Nature and formation of inter-fibre bonds

During the whole papermaking process the inter-fibre bonds in paper develop gradually as solid content increases. At first, the fibres are held closely together by the effect of surface tension forces called the Campbell effect (Campbell, 1959) once water is removed. Among the several mechanisms of the inter-fibre bonding formation, the hydrogen bonds considered to be the main source for bonding (Retulainen et al., 1998; Perkins, 2002; Guerrero Serrato, 2008). The hydrogen bonds

linking the fibres' surfaces together are special chemical bonding having a linear chain such as O - H · · · O where "-" is a covalent bond and " · · · " is the hydrogen bond. The bonding energy of a hydrogen bond is between 8 – 32 kJ/mol depending on the surrounding molecular structure (Retulainen et al., 1998). Gradual transition from the Campbell effect to the hydrogen bonding formation starts at approximately 50% of the solid content. However, the dominant mechanism of fibre bonding has been questioned in the very recent research (Schmied et al., 2013; Hirn and Schennach, 2015). Using a quantitative analysis consisting in measuring the bonding energy of the existing bonding mechanisms, Van der Waals forces were considered to be the main contributors to the inter-fibre bonding (Hirn and Schennach, 2015). Although it was stated that the bonding energy does not directly relate to bonding strength, thus force-distance relationship for each mechanism should be taken into account.

Pulping process – refining (Section 1.2.2.2) and added mineral fillers and chemicals modify the bonding process between fibres in paper (Vainio and Paulapuro, 2007). For example, unbeaten fibres provide a weak bonding for the paper (Figure 1-12a) when the beaten fibres create a network with strong bonds (Figure 1-12b). External fibrillation and fines in the intersurface facilitate the inter-fibre bonds formation linking two fibre surfaces closer to each other (Retulainen et al., 1998). Beating increases the specific surface area of the fibres, the number of inter-fibre bonds and their thickness due to the enlarged number of fines and released fibrils on the fibre surfaces.

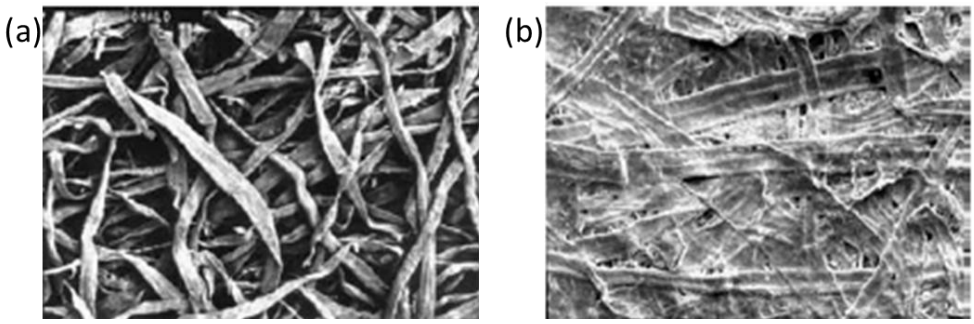

Figure 1-12 : Image of dried pulp samples representing: (a) unbeaten and (b) highly beaten pulp. The conformability of the fibres highly increases with beating, resulting in a much better bonded network (Monica Ek et al., 2009b).

Structural characterisation of inter-fibre bonds / contacts

Among several characteristic parameters of the inter-fibre bond, the bonding fibre area is a very significant in terms of impact on the mechanical properties of paper (Retulainen et al., 1998). Traditionally, the inter-fibre bonding areas are quantified by the Relative Bonded Area (RBA) that is the ratio of bonded area to the total surface area of each fibre. There were several methods for measuring RBA mentioned such as polarization microscopy methods (Page, 1960) and light microscopy (Kappel et al., 2009) using microtome serial sectioning and image analysis. The latter author concludes that the measured bonded area was on average 60 % lower than the

geometrically calculated bonded area (only dependent on fibre width and crossing angle) due to incomplete bonding of overlapping fibre regions. (Marulier et al., 2015) using X-ray microtomography showed that the mean bonding degree ratio, i.e. relation of actual bonding area to the fibre width, was low and ranged between 30 and 40 % for the studied specimens. The incomplete bonding occurred mostly at the edges of the contacts. The holes in the bond played a minor role in this difference which is independent of the fibre morphology (Kappel et al., 2009). Working with the image analysis tools, one should be careful because fibres in contact area not necessarily chemically bonded and the contact are may, hence, be larger than the bonded area (Malmberg et al., 2011; Wernersson, 2014). The term inter-fibre contact is used to describe contact between fibres studied using digital images.

Another way of bonding description is to study its statistic geometry: spatial density of inter-fibre contacts, degree of contacts between fibres, the free fibre segment length (Corte and Kallmes, 1962; Sampson, 2004; Batchelor et al., 2006; Marulier et al., 2015).

1.2.5 Conclusion

In this part, the main constituents of paper sample and the process that assemble them to form paper are briefly recalled. This summary is completed by a description of the structural parameters of paper sample and of their measurements. This section highlights that paper is a complex fibrous and porous material that:

- Exhibits a multiscale microstructure (Figure 1-13);
- Exhibits structural heterogeneities;
- Has a layered structure;
- Has orthotropic structure.

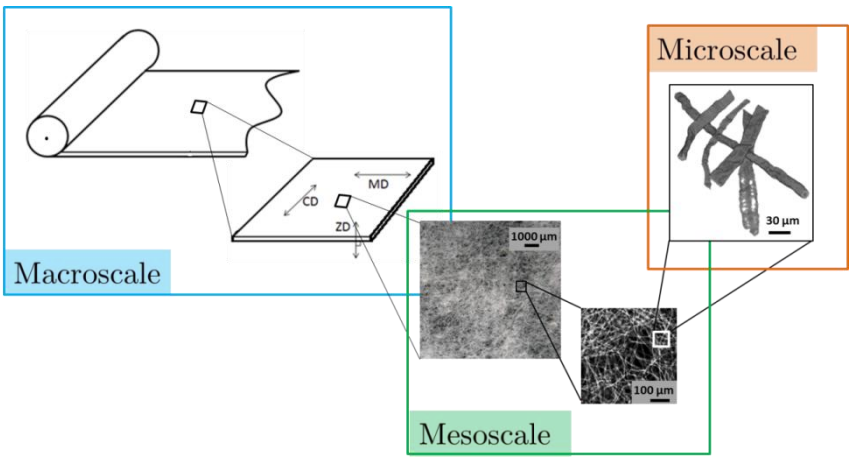

Figure 1-13 : A hierarchy of scales in paper: macro, meso and microscales. From left to right : roll of paper on a paper machine (~10 m wide); paper sheet (scale of centimetres); fibre network with the local non-uniformities (scale of mm); zoomed fibre network (scale of µm); fibre and inter-fibre bonds (scale of µm and nm).

1.3 Mechanical and hygro-mechanical properties of paper

1.3.1 Introduction

This section starts with the description of the in-plane mechanical behaviour of various paper grades and the nature of the mechanical properties of paper (section 1.3.3). Thereafter, we will discuss influence of the paper structure as well as fibres and inter-fibre bonds on the mechanical respond of paper (section 1.3.4). Mechanical properties of the individual fibres, inter-fibre bonds and micromechanical phenomena occurred in paper materials are summarised in section 1.3.4.3. Finally, the influence of humidity on the mechanical properties of paper will be presented.

1.3.2 Generalities

Figure 1-14 shows examples of load - elongation / force – displacement curves for different paper specimens subjected to a tensile load in various in-plane directions. In mechanics, it is common to calculate stress σ of a material [MPa], which is defined as the load F [N], divided by the cross section area A [mm^2], where A is calculated as the width w [mm] of the sample multiplied by its thickness t [mm]. The strain ε [-] is calculated as the elongation or displacement divided by the sample length defined by the distance between holding clamps h [mm]. As it was discussed in section 1.2.4.1, the measurement of the thickness is not straightforward for paper materials, thus, instead of σ, (F/w) is generally used representing the directly measured quantity of the force over the specimen width.

For paper materials in tensile loading, the force – displacement curve initiates with a linear region smoothly transitioning to the non-linear region (Figure 1-14).

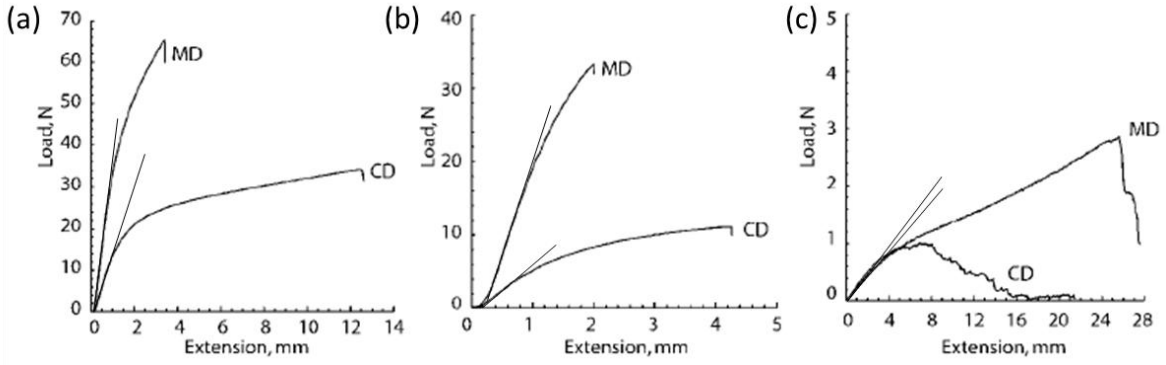

Figure 1-14 : Load-extension curves obtained during uniaxial tensile test for different paper materials: (a) office paper; (b) newsprint; (c) low density paper such as tissue paper. Tensile tests were performed using samples of 15 mm width and 180 mm length that were cut in MD and CD directions. Straight lines help reader to observe the linear regions. Modified from (Sampson, 2009).

Young's modulus

From the linear, i.e. elastic, region of the stress-strain curve, Young's modulus or elastic modulus E [MPa] can be evaluated according to the Hooke's law as following:

$$E = \sigma/\varepsilon_{el}, \quad (1\text{-}4)$$

where ε_{el} is the elastic strain [-]. It measures the force that is needed for a small elongation of the specimen (Niskanen and Kärenlampi, 1998). In the case of paper, the elastic modulus controls the bending stiffness and the structural rigidity of paper and board sheets. The paper materials have generally Young's modulus in MD (E_{MD}) that is 2-4 times larger than in CD (E_{CD}) (Gustafsson and Niskanen, 2012). In Table 1-3, orders of magnitude of E are presented for the type of papers discussed in section 1.2.1.

Table 1-3 : Examples of paper materials and their Young's moduli.

Property	Office	News	Liner
E_{MD}, [MPa]	6540	4560	6470
E_{CD}, [MPa]	3130	870	3240

Poisson's ratio

Under uniaxial loading of the paper specimen deformation occurs generally in three directions: the network deforms in the direction of loading as well as in the directions perpendicular to it. This phenomenon is characterised by the Poisson's ratio ν, that is defined as the negative ratio of transverse / lateral strain to axial strain. Poisson's ratios are usually evaluated in the three main directions, for example, in case of the load applied in MD:

$$\nu_{CD,MD} = -\varepsilon_{CD}/\varepsilon_{MD};\ \nu_{ZD,MD} = -\varepsilon_{ZD}/\varepsilon_{MD} \quad (1\text{-}5)$$

Handsheets produced in a laboratory are isotropic papers and have in-plane value $\nu_{CD,MD} = 0.3$ whereas the industrial papers which are rarely isotropic exhibit in-plane Poisson's ratio varying from 0.1 to 0.5 depending on the anisotropy.

1.3.3 Tensile behaviour of paper materials

The characterisation of the mechanical behaviour of papers is discussed for uniaxial in-plane loading, i.e. the case where the stress and strain are measured in the same in-plane direction.

1.3.3.1 In-plane anisotropic mechanical response

Figure 1-14 illustrates the mechanical behaviour for papers in both in-plane directions MD and CD. One can observe mechanical anisotropy: the slope of the linear part is steeper in MD direction than in CD. The mechanical anisotropy is attributed, first, to the fibre orientation caused by the manufacturing process, and second, to the restraint applied in the MD during drying operation at the manufacture, such that the sheet being unstrained and therefore prone to shrinkage in the CD (Niskanen and Kärenlampi, 1998; Sampson, 2009). The ratio between both moduli is often used as an indicator of anisotropy.

For the majority of papers, the sheet fails at a higher load in MD than in CD. Moreover, the failure strain is greater in the CD than in the MD, however, it is not

the case for the tissue paper (Figure 1-14c) whose mechanical behaviour was affected by the creping of this paper during the drying process (Raunio and Ritala, 2012).

1.3.3.2 Influence of sample size on the mechanical response

Figure 1-15a shows two load – elongation curves for paperboard (120 g m^{-2}) samples of two different width and height (w/h) ratios. The curve denoted $h = 5$ mm presents a stable decrease of the load, i.e. stable fracture, whereas the curve denoted $h = 100$ mm presents an immediate decrease of the load, i.e. immediate fracture, as it was also observed for the papers in Figure 1-14a and b (Tryding, 1996).

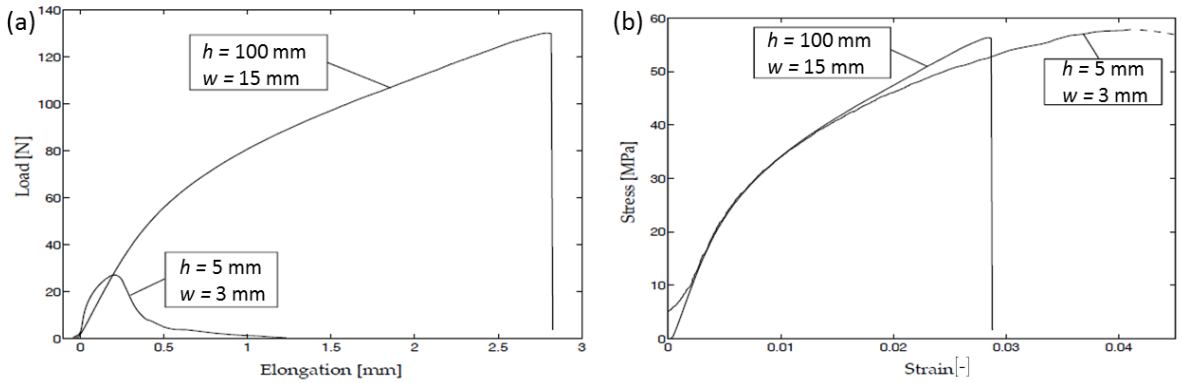

Figure 1-15 : Influence of the sample size on load-elongation (a) and stress-strain (b) curves obtained during the uniaxial tensile test in the MD for the same paperboard (120 g m^{-2}). Modified from (Tryding, 1996).

The load – elongation curves transformed into the strain-stress curves are presented in Figure 1-15b. One can notice that the two stress – strain curves are very similar. However, several variations are observed: first, in the beginning at very small strain the mechanical behaviour of the sample with $h = 5$ mm is affected by the test equipment and is not typical for the performance of the paper (Tryding, 1996); second, the diversity between the graphs starts from $\varepsilon = 1.5$ % caused by different w/h ratio. Figure 1-16 presents the strain at the failure ε_f in function of w/h ratio. When w/h ratio tends to zero, the failure strain equals to the uniaxial failure strain due to zero transverse stress. When w/h increases, the failure strain approaches a failure strain restrained by the zero transverse strain (Tryding, 1996).

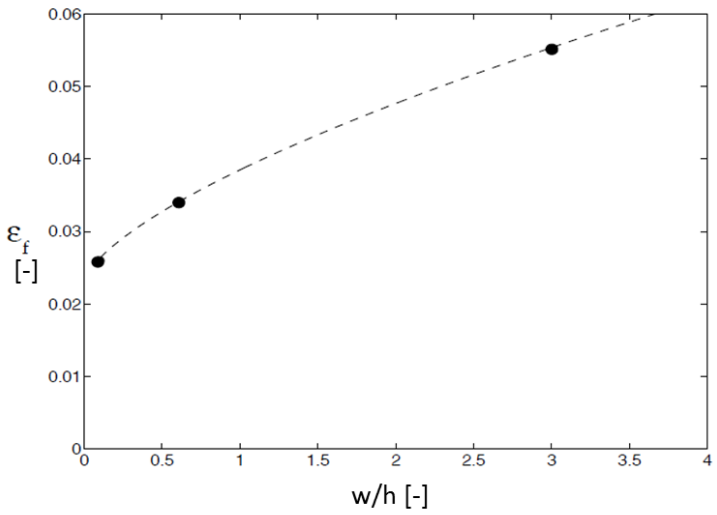

Figure 1-16 : ε_f vs w/h curve for paperboard of 120 g m^{-2}. Modified from (Tryding, 1996).

1.3.3.3 Viscoelastic-plastic behaviour of paper

A typical cyclic stress – strain curve for paper materials is shown in Figure 1-17a. The elastic modulus is almost invariant during straining. Part of the strain is irreversible which is the cause of the nonlinearity of the mechanical curve shown, for example, in Figure 1-15. It suggests that the microscopic fibre network structure undergoes permanent plastic deformations that do not weaken elastic stiffness of the fibres (section 1.3.4.3).

The effect of strain rate on the in-plane tensile behaviour of paper is shown in Figure 1-17b. One can observe the linear slope of the curve (elastic modulus) and the strength of the paper increase with the strain rate growth. It is not shown in the particular example but often the increase in strain rate leads to a reduction in the failure strain of paper since the material is considered to become more brittle at high strain rates (Gustafsson and Niskanen, 2012; Niskanen and Kärenlampi, 1998). The mechanical respond of paper materials changes with the time. Using relaxation (constant strain) or creep (constant stress) tests the viscous nature of paper can be observed (Fellers, 2009; Hämäläinen et al., 2014). Therefore, paper is considered as material with viscoelastic, plastic properties (Seth and Page, 1983; Alava and Niskanen, 2006).

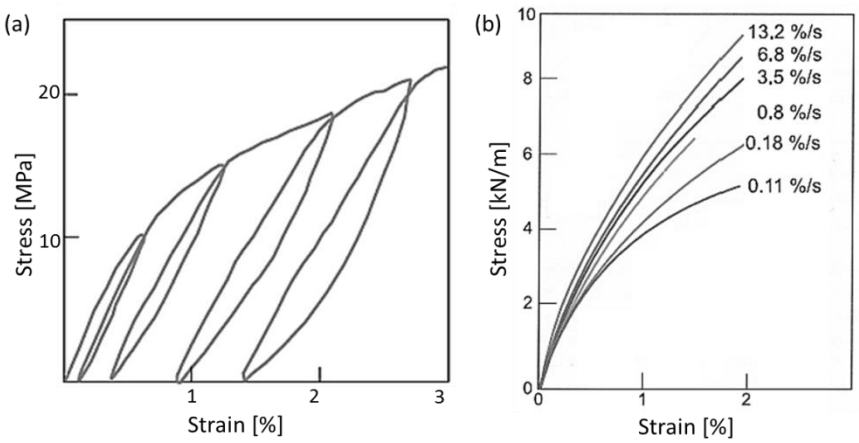

Figure 1-17 : (a) Cyclic stress-strain curve of paperboard (120 g m^{-2}) in CD; (b) Stress-strain curves at different strain rates for a wrapping paper (80 g m^{-2}). The stress values are multiplied by the thickness of paper (Gustafsson and Niskanen, 2012).

1.3.4 Influence of paper structure and of the constituents on its mechanical behaviour

The mechanical properties of paper depend on the cellulosic fibres' properties and the network the fibres assembled into. One can distinguish several factors such as density, properties of individual fibre and inter-fibre bonds and the sheet heterogeneities (formation).

- **Density of paper**

The specimen of a higher density paper, for example, shown in Figure 1-14a and b breaks at higher load rather than the one of a lower density (Figure 1-14c). In Figure 1-14a and b one can observe that the load decreases to zero immediately after the maximum tensile load for the office grades of paper and the newsprint, respectively, whereas for the bathroom tissue (Figure 1-14c), the load decreases slowly to zero after the maximum. The dominant failure for the office and newsprint papers is fibre breakage and pull-out of fibres under the load whereas for the low density papers such as the bathroom tissue, the failure is dominated by fibres being pulled out of the structure, with fewer being broken (Sampson, 2009). The discussion proceeds in section 1.4.

- **Properties of individual fibres and the inter-fibre bonds**

Subjected to load, fibres in the network transfer stress from one to another through the inter-fibre bonds. The load carrying part of a fibre is a fibre segment (between two neighbouring bonds) (Alava and Niskanen, 2006) (section 1.3.4.3).

- **Sheet formation**

It is discussed in section 1.3.4.1.

1.3.4.1 Influence of structural variability

Spatial basis weight variation affects mechanical properties (Norman, 1966; Ramasubramanian, 2001; Alava and Niskanen, 2006). Tendency for all grades of paper is that the tensile strength decreases with a growth of variation of the local mass (Norman, 1966; Nazhad et al., 2000). Due to variation of the mass in paper, stress and strain in the stretched sample is not equally diffused. According to Wong's (Wong et al., 1996) experimental and numerical studies, the local grammage and the local strains are inversely proportional, meaning that high strains occur in regions of relatively low grammage. In a very recent research (Hagman and Nygårds, 2017), the deformation of a paperboard (240 g m^{-2}) during the tensile test was studied. Figure 1-18 presents the transmitted optical image (left) of the sample, the image obtained using thermography (centre) and the image (right) obtained by merging two others. One can observe variation in the mass of the paper: those areas with lower mass / density correspond to the high temperature areas which represent high local strain measured by means of digital image correlation during traction. Also it was found that the energy released during tensile test was caused by the local plastic deformation in the sample.

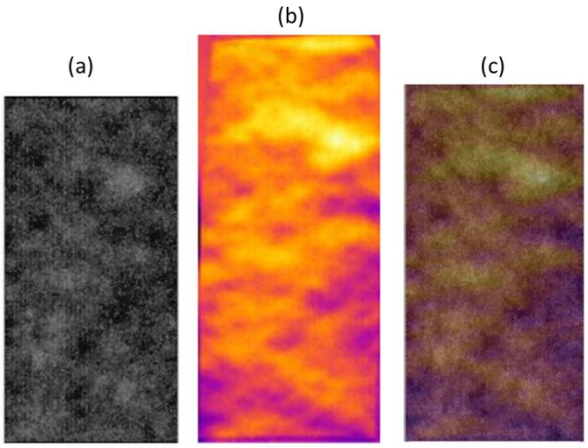

Figure 1-18 : (a) Formation of paper sample, light transmitted image; (b) thermal image of the same sample at 6 % global strain; (c) merged scaled thermal image to the formation image. Flocs correspond to the low temperature areas (Hagman and Nygårds, 2017).

1.3.4.2 Mechanical properties in the thickness direction

Tensile strength

Besides the in-plane mechanical properties, special attention was addressed to the mechanical properties of paper in the thickness direction ZD. The tensile strength in ZD direction is difficult to measure but was proven to be possible using the Z-direction tensile test that estimates the internal bond strength of paper (Fellers, 2009). The uniaxial tensile response of paperboard in ZD (Figure 1-19a) shows that the stress at the rupture is at least ten times lower than those of in-plane directions MD and CD. The elastic modulus in thickness direction E_{ZD} is much smaller than

E_{MD} than E_{CD} due to the layered structure of paper. Figure 1-19b shows that the tensile strength in ZD depends on the apparent density of different chemical pulps. Those results confirm a three-dimensional anisotropy of paper materials.

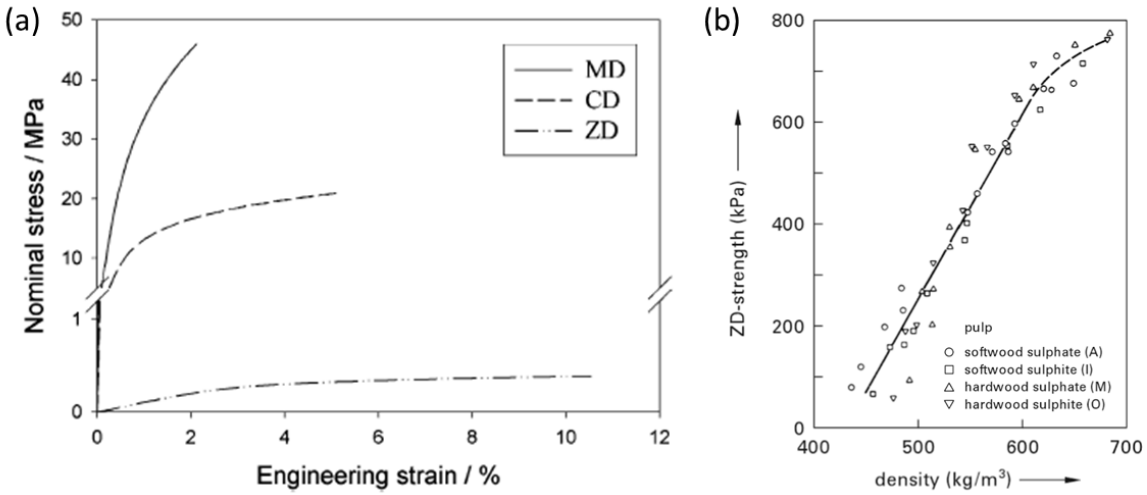

Figure 1-19 : (a) Stress-strain behaviour of the paperboard in the principal material directions (Mäkelä and Östlund, 2003); (b) Z-directional tensile strength vs density of the papers made from different chemical fibres (Fellers, 2009).

Positive and negative Poisson's ratios of paper materials

Generally if a paper web stretches in MD, it contracts in CD exhibiting a *positive Poisson's ratio* (Niskanen and Kärenlampi, 1998). Figure 1-20a shows a graph of evolution of the in-plane lateral strain with MD elongation for different machine – made paper grades. Using equation (1-5) the Poisson's ratio $\nu_{CD,MD}$ is found to be positive for all the values in Figure 1-20a. The Poisson's ratio $\nu_{CD,MD}$ increases with the elongation growth. On the other hand, with the increase of elongation the out-of-plane expands resulting in *negative Poisson's ratio* $\nu_{ZD,MD}$ (Figure 1-20b). It means that the thickness increases for the papers with the elongation growth. This behaviour is called *auxetic* that can also be found among other materials such as foams (McDonald et al., 2011). Poisson's ratios of papers, especially negative ones, have been subjected to several studies (Öhrn, 1965; Baumgarten and Göttsching, 1973; Mann et al., 1979; Stenberg and Fellers, 2002; Verma et al., 2014). Among the studied papers the copy paper is the most auxetic one exhibiting a negative Poisson's ratio $\nu_{ZD,MD}$ = -3 at the axial strain below 0.7 % (Verma et al., 2014). In this case, the thickness of paper was measured using a contact method, i.e. digital micrometer, where during the readout a force was exerted of approximately 7 – 9 N.

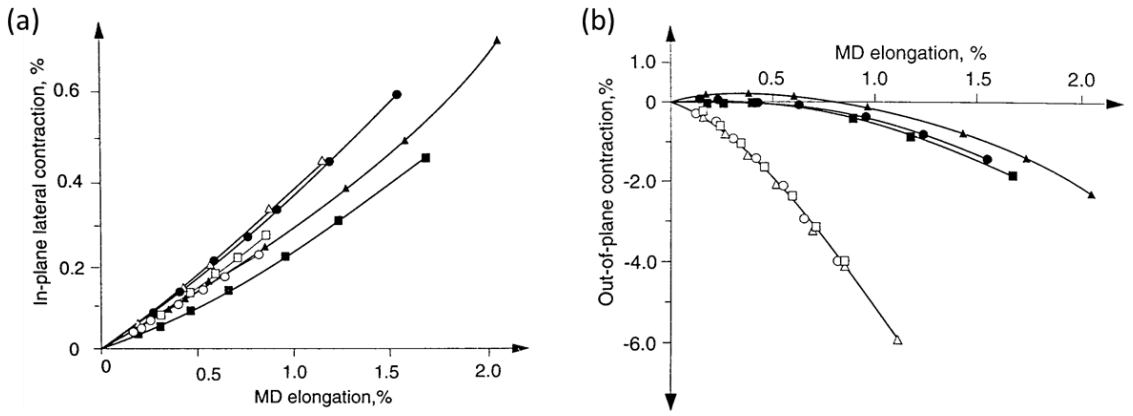

Figure 1-20 : (a) In-plane lateral contraction and (b) out-of-plane contraction (contraction increases upwards) vs MD elongation of different industrial papers: uncoated printing paper (open circles); coated printing paper (open triangles); newsprint (open squares); offset printing paper (closed circles), suck paper (closed triangles), and folding box board (closed squares) (Niskanen and Kärenlampi, 1998)

The phenomenon that causes the auxetic behaviour in papers was related to micromechanical events: due to stretching the fibres that are initially curved, i.e. undulated, pull at the network points, thereby pushing other fibres that lie above and below it in the thickness direction as it is shown in Figure 1-21 (Baum et al., 1984; Stenberg and Fellers, 2002; Verma et al., 2014). The hydrogen bonds were thought to be critical elements in the tensile deformation mechanisms leading to the auxetic response (Verma et al., 2014): the hydrogen bonds linking the fibres do not let them slide past each other during stretching. A developed geometrical model provides a qualitative explanation of the auxetic behaviour of paper (Verma et al., 2014). Moreover, as stated in (Niskanen and Kärenlampi, 1998) the auxetic behaviour may relate to the gradual opening of inter-fibre bonds.

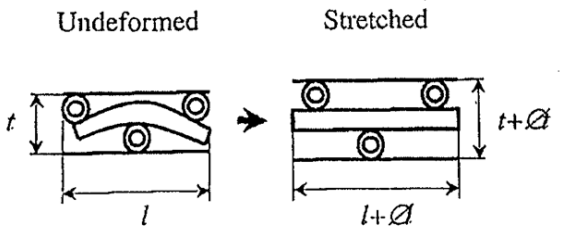

Figure 1-21 : Scheme of the paper cross sections with the connected to each other fibres before and after the stretching. Illustrated in (Stenberg and Fellers, 2002) the author suggested that the transverse fibres separate causing a thickness increase of the paper.

1.3.4.3 Mechanical properties of individual fibres and inter-fibre bonds and its effect on the mechanical properties of paper

Fibres and inter-fibre bonds control together pretty much all the mechanical properties of paper (Alava and Niskanen, 2006). However, only a few measured data is available regarding the fibre and inter-fibre bond properties (K. Niskanen, 2012). The fibres in paper are full of imperfections and present a wide range of variation that affects the fibre properties. Therefore, papers can exhibit a great range of the

mechanical properties. This section contributes to the mechanical properties of the individual fibres and inter-fibre bonds that influence the mechanical behaviour of paper.

Individual fibres

In Section 1.2.2 the morphological characteristics of wood fibres were presented. As it is summarised in Table 1-4, the mechanical properties of various cellulosic fibres depend on their characteristics such as chemical composition, structural organisation and on the orientation of the microfibril angle.

Table 1-4 : Example of structural and mechanical properties of fibre in dry state such as densityρ_{fibre}, cellulose volume V_{cell}, microfibril angle MFA, failure stress σ_f, Young's modulus E ((Wainwright, 1982)).

Species	ρ_{fibre} [g/cm^3]	V_{cell} [%]	MFA [°]	σ_f [MPa]	E [GPa]
Flax	1.45	68	10	840	80 - 110
Softwood	1.55	42	10 - 40	350 - 550	35
Hemp	1.48	73	2.3	920	70
Cotton	1.55	90	28 - 44	300 - 800	13

Moreover, pulping and beating parameters influence the fibre properties and the ability to bond to each other (Retulainen et al., 1998). For example, the chemical pulping causes a fewer fibre damage than mechanical pulp, thus, the fibres of chemical pulp are usually stronger (Gustafsson and Niskanen, 2012).

The load – elongation curve of a single fibre qualitatively resembles the one of the paper when microfibril angle is relatively small: the elastic part is determined by the initial linear section, after there is a non-linear part that is affected by the MFA and the various defects such as crimps, kinks etc. It is stated in (Retulainen et al., 1998) the fibres twists during straining due to spiral S2 layer, however, that cannot happen in a paper sheet due to surrounding network structure. When reaching the maximum stress, the fibre fails immediately. Elastic modulus and failure stress of the fibre depends on the MFA: the smaller the MFA the higher the elastic modulus and the failure stress.

Inter-fibre bonds

In the paper sheet 10 – 40 of inter-fibre bonds are assumed per fibre (Alava and Niskanen, 2006). Strength of the inter-fibre bonds mainly chemically linking the fibres is often related to the shear strength which is the maximum load that the bond can carry when the fibres are displaced relative to each other in parallel to the bonding plane. In Table 1-5 the strength parameters are summarised for two types of fibres coming from springwood and summerwood and their inter-fibre bonds. Summerwood fibres having lower bond diameter exhibit higher bond strength than the springwood. Moreover, the fibre strength is about 20 times higher than the bond strength. Bond strength depends on surface chemical factors: the hemicellulose and

acidic group content of the pulp, the external fibrillation of the fibres, the fines content, and presence of additives (Retulainen et al., 1998). According to Button (Button, 1979), the higher bond strength of summerwood fibres than springwood can be explained by higher elastic modulus, higher fibril angle and higher thickness of summerwood fibres. However, in a recent study, (Jajcinovic et al., 2016) reported that the strength of a single fibre-fibre joint /bond of a hardwood fibre (eucalyptus kraft pulp) is mainly effected by the size of the bonded area.

During drying in the papermaking process the fibres undergo anisotropic shrinkage that creates the shear stresses in the inter-fibre bond area that affect its strength (Salminen et al., 1996). It is suggested that the relevant structural units that control the mechanical properties of a paper are the bonded fibre segments (Retulainen et al., 1998). Extensive literature reviews are available presenting in details the analysis of the inter-fibre bonds (Ebeling, 1976; Salminen et al., 1996; Batchelor et al., 2006; Vainio and Paulapuro, 2007; Schmied et al., 2013; Hirn and Schennach, 2015).

Table 1-5 : Mechanical parameters for cellulose fibres and their inter-fibre bonds (unbleached and unbeaten pine kraft fibres) (Retulainen et al., 1998)

	Fibre parameters		Inter-fibre bond parameters	
	Breaking load [mN]	Breaking stress [MPa]	Breaking load [mN]	Average bond diameter [µm]
Springwood	100	390	4.6	55
Summerwood	190	540	8.5	44

Micromechanical phenomena in papers in the pre-peak region

When a paper sheet is subjected to tensile loading, two phenomena occur at the microscopic level before the failure: (i) the free fibre segments, i.e. the distance between two neighbouring bonded area of a fibre, elongate, partly irreversibly, and (ii) some inter-fibre bonds open gradually.

As it was shown in Figure 1-17a, the elastic modulus, i.e. a measure of elastic energy content, does not change significantly when paper is cyclically stretched in plastic region, thus, the number of fibre segments that carry the load must remain almost constant during the irreversible elongation (Niskanen and Kärenlampi, 1998). Changes of the bonding degree of the paper network induced by beating were observed to have zero effect on the shape of the load – elongation curve, therefore, the opening of bonds cannot explain the nonlinear shape arose after the linear.

So what does actually influence on the shape of the load – elongation curve, and, especially, creation of the plastic region after elastic? As stated in (Alava and Niskanen, 2006), inelastic elongation of paper arises from the plastic elongations of fibres which microfibrils slide relative to each other at the isolated structural imperfections. Therefore, the inelastic behaviour of paper is controlled by the mechanical properties of the fibres. The creep or stress relaxation phenomena of

paper are related to the softening of hemicellulose and lignin in the fibre walls that are in charge of the viscoelasticity of paper (Alava and Niskanen, 2006).

1.3.5 Hygro-mechanical behaviour of paper

Paper materials are extremely sensitive to environmental conditions such as temperature and relative humidity. A fluctuation in the temperature and / or in relative humidity implies morphological changes of fibres such as swelling and shrinking, and, thus, affect the mechanical properties of fibres and inter-fibre bonds and paper network (Haslach Jr, 2000; Alava and Niskanen, 2006; Larsson et al., 2009; Kaarlo Niskanen, 2012).

1.3.5.1 Influence of moisture on the fibres

Hygro-mechanical properties of fibres

Wood fibres that are hygroscopic have a capacity to absorb water either from a liquid or from wet air surrounding it. It is due to the abundance of hydroxyl groups present in wood fibre. Over the range of *RH* from 0 % - 100 % at room temperature (~23°C), the cellulosic fibre expand roughly by 1% in the longitudinal direction and 20 – 30 % in the lateral direction. Generally, the average elastic modulus of wood fibre in dry state is 35 GPa, tensile strength in wet state is 82 MPa, in dry state is 120 MPa (Wainwright, 1982).

Among recent studies, (Toungara et al., 2014) exposed a never-dried softwood fibre to a *RH* cycle in order to quantify the phenomena of a complex deformation such as: expansion and shrinkage of the fibre cross-section area, twisting and bending of the fibre. During the cycle, geometrical variations of the fibre were determined from 3D images obtained by X-ray microtomography (section 1.5). It was shown that for a decrease in *RH* of 80 % to 20 %, the cross-sectional area decreased by 10 %. Such variations were accompanied by a twist of the fibre by almost 250° between its end stages tending to bend with the decrease in the *RH*.

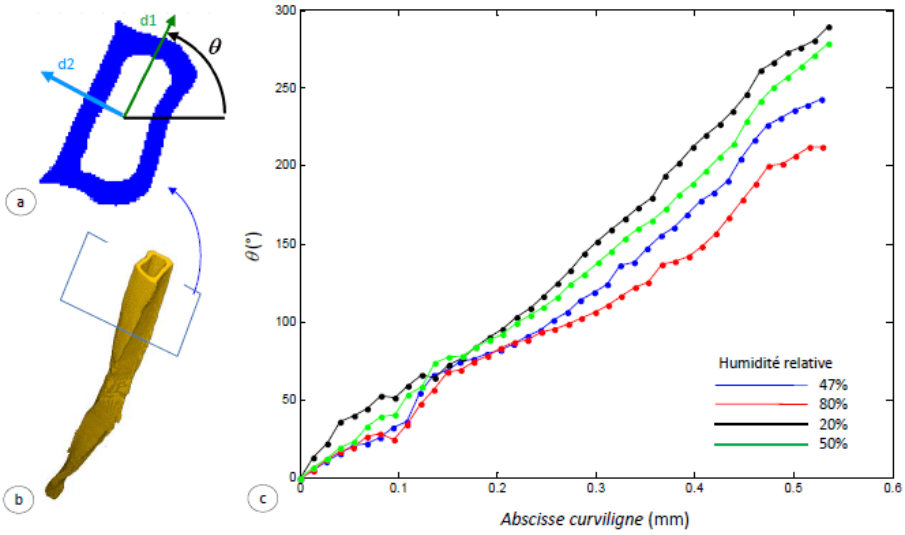

Figure 1-22 : Hygroexpansion of the softwood fibre: (a) cross-section of the fibre; (b) 3D view of the twisted fibre; (c) evolution of the twisting angle of the fibre along the curvilinear abscissa for different RH (Toungara et al., 2014).

A more recent study by (Joffre et al., 2016) presents a mixed numerical-experimental approach where a finite-element updating scheme is used to simulate the swelling of an earlywood spruce fibre going from the experimental fibre geometry at 47 % RH to the predicted geometry of the fiber in the wet state at 80 % RH. The hygroexpansion coefficients are identified by comparing the predicted and the experimental three-dimensional fibre geometry in the wet state. The obtained values are 0.17 of strain per change in relative humidity transverse to the microfibrils in the cell wall, and 0.014 along the microfibrils. In both cases the microfibril angle was found 15°.

1.3.5.2 Hygroscopy of paper materials

Moisture content (MC) of paper is defined as an amount of water relative to the dry weight of the fibres and it depends on the ambient relative humidity and temperature of the surrounding air in equilibrium conditions. The relative humidity (RH) of air is defined as the amount of water vapour in air relative to the amount in saturation.

In paper, water is present in its different forms:

- Free water in the pores between fibres and in the lumen of fibres in the form of liquid;
- Bound water in the micropores of the fibre wall layers;
- Chemically bound water to the hydroxylic and carboxylic acid groups in fibres.

The MC of paper decreases with increase of the temperature or with decrease of RH (Kajanto and Niskanen, 1998). At the saturation conditions (T=23 °C, RH=100 %), the MC of paper is generally 25 – 30 %. When paper is manufactured it contains 6 – 9 % of MC. For a given relative humidity rate at ambient temperature (T), the moisture content in the paper depends on the type of fibres and on the pulping procedure: mechanical pulp contains more moisture than chemical pulp due to differences in the fibre microstructure (section 1.2). Figure 1-23 illustrates the difference of MC for papers made up of mechanical or chemical pulp for a given RH. Once subjected to sorption and desorption cycles, all papers presents a hysteresis similar to the one shown in Figure 1-23, that depends on the constituents of the paper and on the type of papers. After a given number of sorption/desorption cycles, this behaviour tends to linearize.

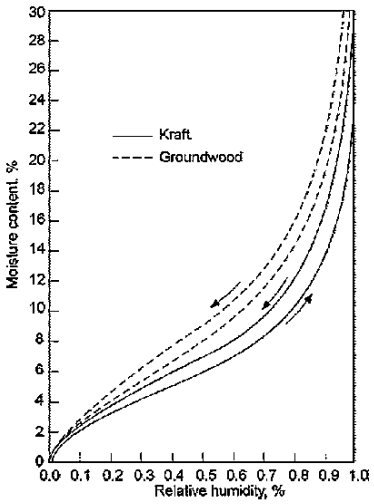

Figure 1-23 : MC vs RH of different papers composed either with (i) chemical pulp or (ii) groundwood at T=50°C. The hysteresis is observed on the graph representing the moisture history in paper network (Niskanen, 2012).

1.3.5.3 Hygroexpansion

Hygroexpansion characterizes the dimensional variations of the material subjected to the variation of moisture. When fibres swell they push the neighbouring fibres further apart which causes local strains over the whole fibre network. The transfer of the local strains determines how much paper expands when the moisture content rise and, inversely, how much it shrinks when moisture is removed.

Figure 1-24 presents hygroexpensive strain that is induced in a freely dried paper sheet during RH variation. The hysteresis in strain originates from the moisture content hysteresis of the fibres.

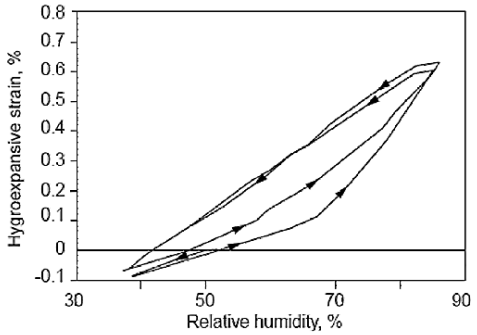

Figure 1-24 : Hygroexpansive strain versus cycling relative humidity in a freely dried laboratory sheet (Kaarlo Niskanen, 2012).

One can observe that the lengths variations (less than 1%) depend on:

- the direction of the paper : they are generally 2 to 5 times larger in CD than in MD

- the history and differ from sorption to desorption. Indeed when the paper is subjected to RH larger than 65%, irreversible dimensional changes occur.

1.3.5.4 Effect of humidity on the mechanical properties of paper

The mechanical behaviour of paper changes with moisture content (Figure 1-25): at low RH paper is stiff and brittle and it fails at low strain; at high RH paper is more soft and ductile and it breaks at high strain value.

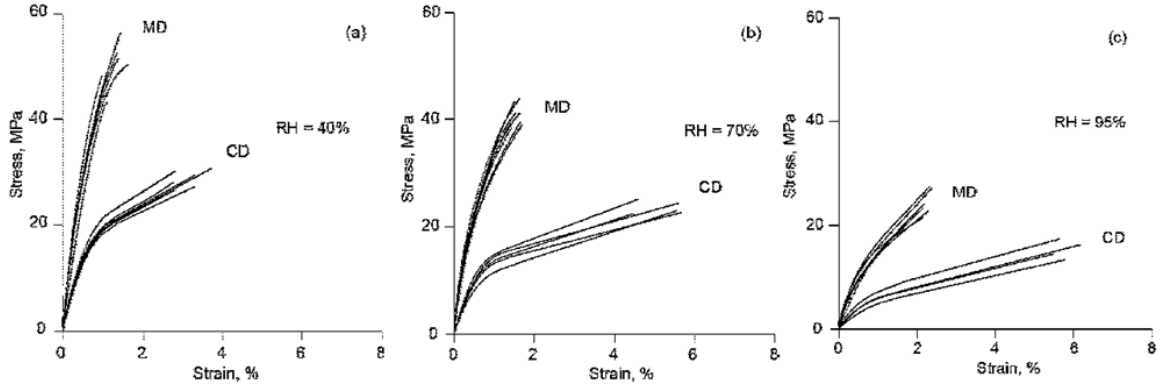

Figure 1-25 : Stress-strain curves of a paperboard presented in MD and CD in different conditions: 40 %, 70 % and 95 % of RH. The corresponding MC are 6.6 %, 9.7 % and 20 % (Yeh et al., 1991)

At high MC, the elastic modulus are lower than at low MC. Figure 1-26 illustrates the influence of moisture content MC on the Young's modulus. The lower the moisture content the higher the Young's modulus. Below approximately 5 % of MC the elastic modulus is independent of MC, above the 5 % of MC the elastic modulus decreases.

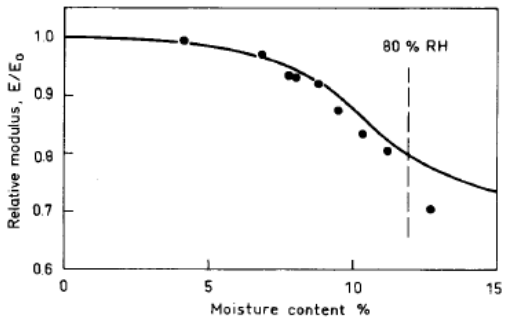

Figure 1-26 : Influence of moisture on the Young's modulus. Measured modulus relative to its value in dry paper (dots) and the corresponding prediction from a laminate model for the fibre wall (solid line) (Salmén et al., 1984).

The ability of the fibres to transfer local stress concentration to neighbouring fibres is the key mechanism related to the paper strength. Moisture softens hemicellulose of the fibres and affects the inter-fibre bonds that cause a decrease of the stress transfer in fibre network of paper resulting in deterioration of the paper strength (Salmen and Back, 1980; Haslach Jr, 2000; Hirn and Schennach, 2015). Figure 1-27 presents evolution of the load at the failure of paper (breaking load) in MD and CD in different RH conditions measured at various loading rate. The

breaking load decreases significantly in MD and slightly in CD with an increase of loading rate in the constant ambient relative humidity (Haslach, 2009). Also it can be assumed that the breaking load decreases approximately linear with increase of RH.

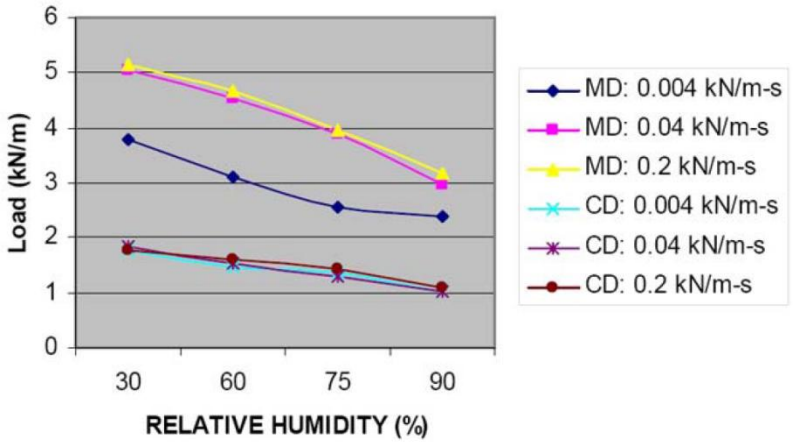

Figure 1-27 : Load at failure versus relative humidity obtained at three different load rates for specimen (150 x 30 mm) loading in MD and CD of a handsheet (75 g/m^2) (Haslach, 2009).

When paper is in the wet state, the fibres are more swollen in the transverse direction than in axial. In the dried state, the internal stresses in the fibre web are created by the anisotropic shrinkage due to resistance of the axial stiffness to the transverse shrinkage (Alava and Niskanen, 2006).

1.3.6 Conclusion

The mechanical properties of the end-use paper and paperboards are extremely affected by the chosen fibres and by the method those fibres were assembled into paper. Subjected to load, fibres in the network transfer stress from one to another through the inter-fibre bonds. Depending on the environmental conditions, the fibres may swell absorbing water from the air or shrink due to drying. Therefore, the mechanical behaviour of paper materials depends on the relative humidity and temperature conditions.

To summarise, paper exhibits an anisotropic mechanical behaviour that mainly depends on:

- The fibre organization inside the paper (volume fraction and formation as well as the process parameters (pulp preparation and paper making process)
- The moisture content of the paper. The elastic modulus and tensile strength decrease with an increase of moisture.

1.4 Fracture mechanics of paper

1.4.1 Introduction

Defects decrease the paper strength under tensile and compressing loadings that may lead to a failure, for example, during paper web manufacturing, transport of paperboards, or converting operations such as creasing and folding. The paper web may fail due to: (i) shives (small bundles of incompletely cooked wood fibres), holes, and cuts (Sears et al., 1965; Gregersen et al., 2000; Uesaka, 2004); (ii) calendaring that cause damage of the fibres when the calender nip passes (Macmillan et al., 1965; Moffat et al., 1973); (iii) variation in the web tension (Parola et al., 2000; Uesaka, 2004). If the paper sheet containing a defect is loaded, the stress concentrations are induced in the vicinity of the defect (Figure 1-28).

At low external stress, the structure containing a defect will not lead to a macroscopic failure. If the external stress is increased, the damage will accumulate near the defect leading to the macroscopic crack propagation. Besides that, as presented in section 1.2.5, the heterogeneities of the paper materials at different length scales and the environmental conditions affect the paper mechanical and fracture behaviour of paper.

In order to understand fundamental reasons of paper failure or to prevent the crack propagation in such material the means of fracture mechanics are usually used. The fracture mechanics is a field of mechanics that examines strength of the structures containing defects and propagation of the cracks in a material. The fracture mechanics aims at relating three factors that influence the strength of a notched material structure: the external loading, the geometry of the structure, and the fracture toughness (Östlund and Märkelä, 2012).

In this section, a brief overview of the existing fracture mechanics' principle and approaches are given in section 1.4.2 and 1.4.3, followed by a short survey of the fracture models application to the paper materials (section 1.4.4.2). Experimental investigations of fracture phenomena in paper materials, effect of the paper microstructure and measurement of the damage zones are described in details in section 1.4.4.

1.4.2 Generalities

Flaws negatively affect strength of the materials. In order to study the impact of the flaws, samples are usually notched. Comparing with a circular hole, a sharp defect (Figure 1-28), i.e. a cut line, rises to the most severe stress concentration, and thus, this is the most critical for the load-carrying capacity of a structure (Östlund and Märkelä, 2012).

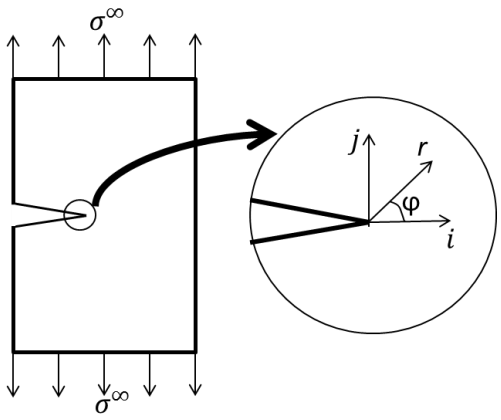

Figure 1-28 : Crack tip coordinates.

Depending on the load application, the crack surfaces have different relative displacement as it is shown in Figure 1-29a. Thus, the three modes can be distinguished as:

- **mode I** – opening mode (tensile stress normal to the crack plane);
- **mode II** – in-plane shear (a shear stress is parallel to the crack plane and perpendicular to the crack front);
- **mode III** – out-of-plane shear (a shear stress is parallel to the crack plane and parallel to the crack front).

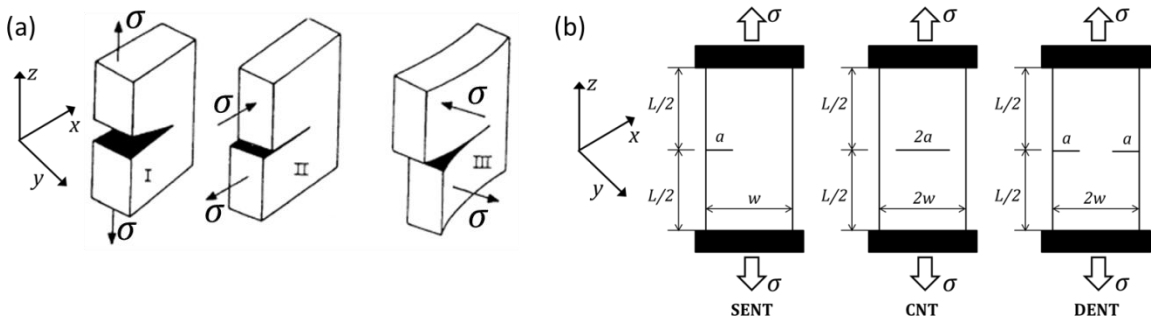

Figure 1-29 : (a) Principal fracture modes I, II, and III regarding the relative displacement of crack surfaces (Mäkelä, 2002); (b) Typical geometries for paper samples for in-plane fracture tests (Coffin et al., 2013).

Three notch configurations presented in Figure 1-29b are commonly used in fracture tests in mode I, which is the only mode investigated during this study. The notch of length a is a slit with sharp tips that is located at L/2 from each clamp. The geometries for in-plane fracture tests are defined such as:

- single edge-notched test (SENT). This is the mode used in this PhD work;
- centre-notched test (CNT);
- double edge-notched test (DENT).

1.4.3 Models of fracture mechanics

Modelling provides a prediction of the behaviour of material structures. In the following section, different fracture models are briefly described in dependence of the type of mechanical and fracture behaviour such as linear elastic, non-linear, elastic-plastic.

1.4.3.1 Linear Elastic Fracture Mechanics (LEFM)

In 1920 Griffith (Griffith, 1920) presented a fracture mechanics theory based on the global energy balance. It says that during incremental crack extension da the total energy of the system does not change:

$$-\frac{dU}{tda} = \frac{dW_s}{tda}, \tag{1-6}$$

where U is potential energy; W_s is the work required to create new crack surfaces; t is the thickness of material with a crack a.

Griffith's model established the basis of LEFM that is the simplest fracture mechanics approach assuming that an overall mechanical behaviour of material is linear elastic (Anderson, 2005). In 1956, Irwin defined the concept of the energy release rate: as the crack increases, the potential energy is released at a rate G that depends on the loading and geometry of the specimen. In a linearly elastic material, the condition for crack growth is:

$$G - \frac{dU}{tda} = \beta(\sigma^{\infty})^2 a/E' \geq G_c, \tag{1-7}$$

where β is a geometric factor; σ^{∞} is the remote stress far away from the crack; E' is an elastic constant, G_c is the fracture energy of the material. Therefore, in order to initiate crack growth, the displacement must be sufficiently high so that elastic energy can be released at the rate of $G = G_c$. Then, an insignificant increase of σ^{∞} will cause the crack growth. The critical value G_c occurring at the onset of crack growth is the *fracture toughness* of the material. Fracture toughness or fracture resistance describes ability of paper to resist a flaw to turn into a growing crack. The fracture toughness depends on specimen size.

A criterion for the crack growth in linearly elastic materials is obtained from the stress field in the vicinity of a crack tip (Irwin, 1957). The stress in the vicinity of a crack tip (Figure 1-28) in mode I is defined as:

$$\sigma_{ij} = \frac{K}{\sqrt{2\pi r}} f_{ij}(\varphi), \tag{1-8}$$

where the coordinates: r is a distance measured from the crack tip and a polar angle φ as defined in Figure 1-28. The i- and j-axes represent the crack orientation. The crack propagates in the direction $\varphi = 0$ where form function f_{ij} is the largest. K is a *stress intensity factor.* It is a characterising parameter of the crack tip that can be determined from the external loading and the geometry of a notched structure.

$$K = \sigma^{\infty}\sqrt{\pi a} f\left(\frac{a}{w}\right), \tag{1-9}$$

where $f\left(\frac{a}{w}\right)$ is a correction factor for the finite width w of specimen. The factor $\sigma^{\infty}\sqrt{\pi a}$ comes from the closed-form solution of a mode I centre crack in an infinite plate.

Once the critical stress state in the vicinity of the crack tip is reached the crack growth initiates. The critical value of stress defines the critical value K_c which is related to the fracture toughness G_c as:

$$G_c = \frac{K_c^2}{E'} \tag{1-10}$$

1.4.3.2 Fracture process zone (FPZ)

Most of the materials exhibit non-linear and irreversible mechanical behaviour at high stresses. Thus, a large amount of the released energy G does not go to the surface energy but rather dissipates as heat when plastic flow occurs around the crack tip. This plastic deformation decreases the stress near notch tip. This area of the plastic deformation has many names: the Plastic Zone, the Process Zone, the Cohesive Zone, and the Fracture Process Zone (FPZ). If the FPZ is a significantly small area near the notch tip in comparison to the in-plane dimensions of material, the LEFM is still applicable and the FPZ is treated as a point in mathematical prospective; otherwise more complex models are necessary.

1.4.3.3 Nonlinear fracture mechanics

Among the years more complex fracture mechanics models were developed and used for the materials which behaviour near the crack tip deviates distinctly from linear elasticity. The examples of those materials are metals (Curry and Knott, 1978), ceramics (Bradt et al., 2012), rocks, concrete (Bazant and Planas, 1997), composites (Whitney and Nuismer, 1974), and paper materials (Östlund and Märkelä, 2012). Below different nonlinear approaches are briefly discussed.

- **J-integral**

For nonlinear elastic materials, for example, metals, a path-independent contour integral known as *J-integral* was proposed in 1968 (Hutchinson, 1968; Rice and Rosengren, 1968). The uniaxial form of the stress-strain expression is:

$$\varepsilon = \frac{\sigma}{E} + \left(\frac{\sigma}{E_0}\right)^n, \tag{1-11}$$

where ε is strain, E is Young's modulus, n is a strain-hardening exponent and E_0 is the strain-hardening modulus.

Accordingly, the stress field in the vicinity of the crack tip:

$$\sigma_{ij} = \alpha \cdot \left(\frac{J}{r}\right)^{\frac{1}{n+1}} \cdot f_{ij}(n, \varphi), \tag{1-12}$$

where α is a scalar multiplier and depends on the material and stress state (plane strain or plane stress), r and φ were defined in Figure 1-28.

According to the theory, the *J*-integral determines the amplitude of the stresses, and the stresses and strains have a uniform distribution within *J*-dominated zone.

In elastic-plastic materials the stress state depends on the strain state and the strain history. Therefore, non-linear and elastic-plastic materials show the same loading behaviour but the behaviour differs under unloading. Since the crack, normally, does not occur during unloading, non-elastic treatment of an elastic-plastic material is capable to describe the fracture processes.

- **Crack Tip Opening Displacement (CTOD)**

In the elastic-plastic materials, initially sharp crack tip blunts due to plastic deformation. In 1961 the elastic-plastic crack tip characterizing parameter was introduced as the crack tip opening displacement (CTOD), δ. The relationship between CTOD and J was revealed (Shih, 1981):

$$\delta = c\frac{J}{E}, \tag{1-13}$$

where c is a dimensionless function of the material parameters and the stress state.

Although it is difficult to measure CTOD directly, a standard test method was developed to determine CTOD at crack growth initiation such as fracture toughness δ_c.

- **Cohesive zone models**

Barentblatt (Barenblatt, 1959) and Dugdale (Dugdale, 1960) proposed a fracture model for the crack tip where plasticity is accounted in the linear elastic materials. According to the cohesive zone modelling, damage occurs in the narrow zone in front of the crack tip. The damage behaviour is described by a cohesive stress-widening curve where, for example for mode I loading, this curve is a function of only the crack widening u_w (Figure 1-30). To mark, the cohesive stress-widening curve describes the stress-strain behaviour of the material after the crack started to propagate, i.e. post-peak behaviour.

At first, model was developed to consider irreversible material behaviour in metal but later on, the model was successfully applied to the non-metal materials such as fibre composites, polymers and quasi-brittle materials including concrete.

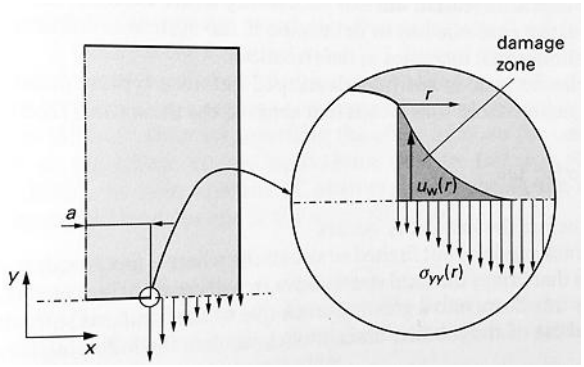

Figure 1-30 : Crack tip modelling using the cohesive zone model. The cohesive stress widening curve is given by $\sigma(u_w)$ (Östlund and Märkelä, 2012).

- **Continuum damage mechanics modelling**

Continuum damage mechanics describe the effect of microscopic fractures at the macroscopic level without making any assumptions about the nature of the microscopic processes (Kachanov, 1958). In this theory, a damage parameter D is included that characterises the average degradation of the material. The simplest version is when a scalar damage parameter D equals either to 0 (undamaged material) and to 1 (completely damaged).

- **Nonlocal and gradient theories**

Nonlocal and gradient theories that have been used to describe deformation of heterogeneous elastic materials were first introduced in the early 1960s (Toupin, 1962; Kröner, 1963). Heterogeneous materials where pores or grains are relatively large compared to the size of, for example, defects, do not obey the classical elasticity theory. In such materials the deformation processes occurring at a smaller scale should be taken into account. Therefore, a nonlocal or gradient theory can be employed providing a framework that enables microstructural effects to be included in a continuum theory by including length parameters in the constitutive equations that limit magnitude of gradients in stress and strain (Maugin and Metrikine, 2010; Askes and Aifantis, 2011; Aifantis, 2011a).

1.4.4 Fracture mechanisms in paper materials

The investigation of the failure mechanisms occurring in paper materials have been subjected to a significant number of studied, sf. (Andersson and Falk, 1966; Goldschmidt and Wahren, 1968; Seth and Page, 1974; Westerlind et al., 1991; Niskanen, 1993; Yuhara and Kortschot, 1993; Tryding, 1996; Niskanen et al., 2001; Salminen et al., 2003; Hägglund and Isaksson, 2006; Alava and Niskanen, 2006; Considine et al., 2011; Östlund and Märkelä, 2012; Mäkelä and Fellers, 2012; Hagman and Nygårds, 2012; Coffin et al., 2013). The above-presented models were tested on paper materials and in this section we will briefly discuss the related studies.

1.4.4.1 Difficulties in measurement of fracture toughness

In paper materials, in comparison with the other mechanical properties, the fracture toughness is one of the hardest to measure because the elastic energy release rate G can easily overshoot the critical value G_c (Niskanen and Kärenlampi, 1998). The value of G_c is measured at the onset of the crack propagation which is rather difficult to determine. Moreover, the complication rises from the size effect (Bažant, 2000). In elastic-plastic materials it is difficult to separate the actual fracture energy from the plastic work as it is uneasy to confine the plastic yielding to a small area on the stress-strain curve. However, in paper materials the fracture toughness is defined as a critical value of the crack tip parameters (K, J, $CTOD$) at the failure instead of at crack growth initiation determined classically (Mäkelä, 2002).

1.4.4.2 Fracture models applied to paper materials

The fracture mechanics models discussed above can be applied to paper materials. A brief description and applicability of different fracture mechanics models are presented in this section such as LEFM and nonlinear fracture mechanics that is summarised in Table 1-6.

Table 1-6 : Summery of the main fracture theories

Fracture theory	Introduced by	Applied to paper materials
LEFM	(Griffith, 1920; Irwin, 1957)	(Andersson and Falk, 1966; Seth and Page, 1974; Seth, 1979; Swinehart and Broek, 1995)
J-integral	(Hutchinson, 1968; Rice and Rosengren, 1968)	(Uesaka et al., 1979); (Yuhara and Kortschot, 1993)
Continuum damage mechanics	(Kachanov, 1958)	(Isaksson et al., 2006; Isaksson and Hägglund, 2007)
Cohesive zone model	(Barenblatt, 1959; Dugdale, 1960)	(Tryding, 1996)
Crack Tip Opening Displacement (CTOD)	(Wells, 1961); (Shih, 1981)	(Steadman and Slone, 1990); (Tanaka et al., 1998)
Nonlocal and gradient theories	(Toupin, 1962; Kröner, 1963; Askes and Aifantis, 2011; Aifantis, 2011b);	(Isaksson and Hägglund, 2013a; Isaksson and Dumont, 2014)

Linear elastic fracture mechanics (LEFM)

As it was discussed in the section 1.2.5, paper exhibits a complex mechanical behaviour defined as viscoelastic and plastic. During a tensile loading of the paper the energy is absorbed in the neighbourhood of the crack tip that hold the paper back from the crack propagation (Donner, 1997). In this area defined earlier as FPZ (Figure 1-31), the microscopic damage occurs where stress concentrations result in extensive, irreversible deformation and damage (Östlund and Märkelä, 2012). The study by (Seth, 1979; Swinehart and Broek, 1995) confirms that the use of classical LEFM is reasonable for paper materials only having sufficiently large structures (w ≥150 mm) with large flaws ($a \geq 50$ mm). Generally the defects are relatively small in paper webs and, thus, the classical LEFM is not applicable.

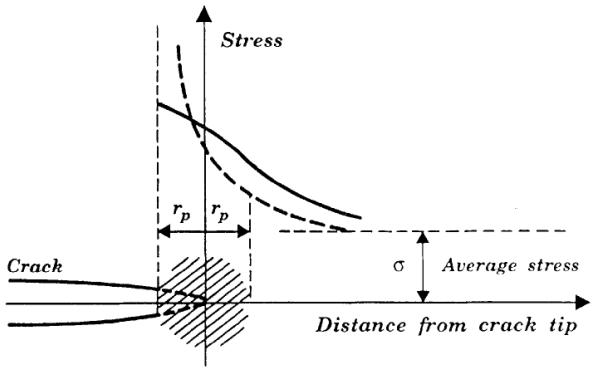

Figure 1-31 : Stress distribution at a crack tip for a linearly elastic material (dashed line) and plastic material such as paper (solid line). Plastic deformation occurs in the hatched region (Niskanen, 1993).

However, it was shown that Griffith's equation can be applied to describe the fracture behaviour of various papers with additional consideration and modification (Donner, 1997; Coffin et al., 2013). Including the nonzero size of FPZ into LEFM model the fracture toughness of paper was successfully characterized (Donner, 1997;

Coffin et al., 2013) for several grades of paper. Moreover, in the recent research by (Coffin et al., 2013) it was shown that using rather narrow sample ($w = 50$ mm) would be sufficient to predict fracture loads for small cracks in large webs.

Nonlinear fracture models

A brief discussion is presented below regarding the main results and conclusions from the applied nonlinear models to the paper materials.

J-integral

Nonlinear fracture mechanics was first applied to the paper materials in 1979 (Uesaka et al., 1979). The J-integral was introduced as a crack tip characterisation parameter for paper and the fracture toughness J_c was experimentally evaluated. It was shown that values of J_c was approximately constant for various crack lengths. However, J_c cannot be used in order to compare the defect-sensitivity of papers because of the material effect n and E_0 in Equation (1-11). Therefore, a numerical simulation is needed in order to determine J and the external loading relationship (Östlund and Märkelä, 2012).

Cohesive zone modelling

The cohesive zone modelling was used for the analysis of damage evolution in papers (Tryding, 1996). This model is not limited to cases of pre-fabricated notches in the tested materials: the localised softening of material can occur in the material and transform into the macroscopic crack under the stress. However, the cohesive zone is not fully developed before a structure with defects becomes unstable, meaning that the theoretical fracture energy is not consumed before the instability occurs.

Figure 1-32 represents a comparison between three fracture mechanics models for the DENT samples in MD and CD loading: LEFM, J-integral and cohesive zone modelling with an incremental elastic – plastic material behaviour. For the tested copy paper LEFM shows worse result for the MD for strain at failure whereas for CD the prediction is pretty accurate. J-integral method exhibits a correct prediction for significantly large cracks. The cohesive zone modelling shows promising results for approximately all crack sizes with a slight deviation for the small cracks.

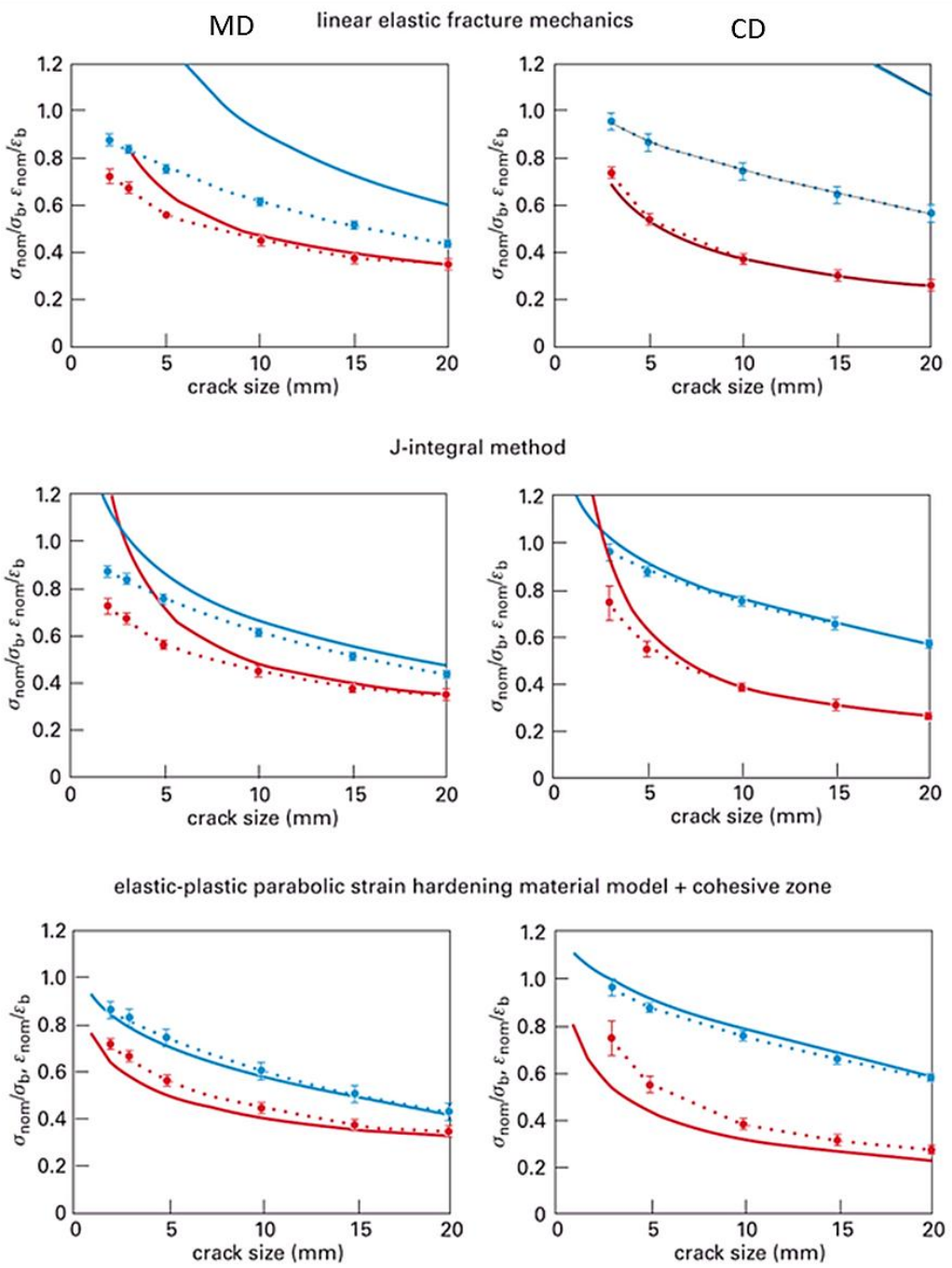

Figure 1-32 : Comparison between results for three different fracture mechanics models. Solid lines depict predicted results and dotted lines – experimental results for stress (in blue) and strain (in red) at failure for DENT samples of copy paper in MD and CD (100 x 50 mm^2). The results are normalised with the values for stress and strain at the failure for unnotched paper (Östlund and Märkelä, 2012).

Nonlocal and gradient theory

Fracture behaviour of dense papers, as discussed above, was significantly studied among years (Mäkelä, 2002). However, the fracture phenomena of low density papers such as tissue papers was relatively less investigated (Isaksson and Hägglund, 2007). Failure of this kind of papers is usually dominated by inter-fibre bonds breakage because of low degree of bonding and weaker bonds in comparison to the fibre

strength (Kettunen et al., 2000). The linear elastic fracture mechanics is not applicable for paper materials because it cannot fully describe stress field around the crack tip. As it was presented before, the nonlocal theory enables to include a microstructural effect into the continuum theory. Usually an internal length scale is introduced into the governing equations that relates to the dimensions of the microstructure and material constituents (Isaksson and Hägglund, 2013b). Therefore, it is essential to find a coupling between the internal length scale and the dimensions of the microstructure. Figure 1-33 shows examples of different papers with dense (a) and sparse (b) networks. A comparison between the models and experimental results for the sparse network is presented in Figure 1-33c where the maximum force is plotted versus the notch length a normalised with the samples width. The difference between LEFM and nonlocal models is obvious, and it is clear that the nonlocal solution is capable of describing the fracture behaviour of a sparse network better than LEFM.

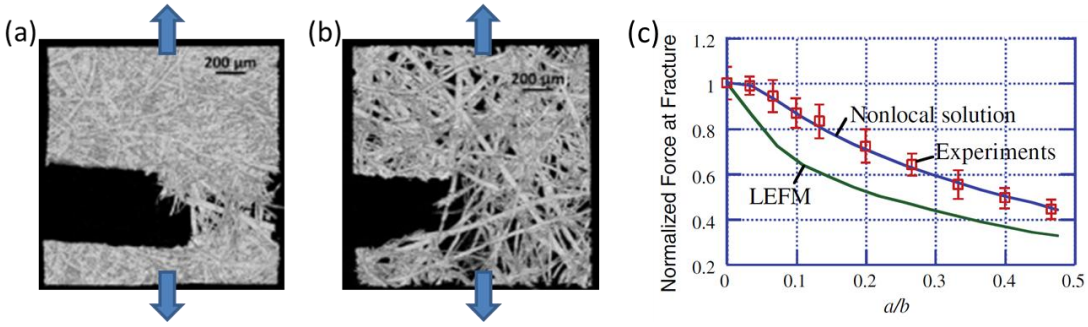

Figure 1-33 : 3D X-ray images of two samples from both high density (a) and low density (b) papers after tensile test (Isaksson et al., 2012); (c) LEFM model predictions and related experiments for the normalized force at fracture in low density paper (Hägglund and Isaksson, 2006).

Microstructural parameters of paper have not been clearly related to the internal length scale; however, fibre length, fibre segments, inter-fibre bond areas were considered as potential candidates (Isaksson et al., 2012).

1.4.4.3 Fracture phenomena in paper materials

As discussed previously, FPZ located in the vicinity of the crack tip causes stress field modification. Microscopic damage in FPZ is accumulated across several millimetres, of fibre length order (Östlund and Märkelä, 2012). In the area near notch tip the material has yielded and/or undergone partial failure (Coffin et al., 2013). FPZ indicates the stress concentration ability of a paper at a notch tip: the larger the FPZ the less the ability of the sheet to concentrate stress around crack tip and the lower the relative sensitivity of the paper to fracture (Coffin et al., 2013). The large size of FPZ results from poor transfer of load.

The size of the FPZ can be introduced in the models but it is rather difficult to experimentally quantify (Coffin et al., 2013). One example of FPZ quantification was proposed by (Niskanen et al., 2001) who used two grades of papers: 1) in the

handsheet of mechanical pulp; 2) in the handsheet of pure softwood kraft (Figure 1-34). The measurement was made on the notched samples impregnated with silicone oil that were subjected to a tensile test. Images were taken using 2D technique in the reflected light where FPZ appeared as white area because the light reflects from broken inter-fibre bonds and fibre ruptures (Figure 1-34).

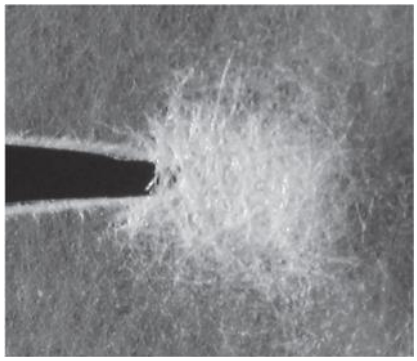

Figure 1-34 : Fracture process zone (FPZ, the white area) near the crack tip in a handsheet of pure softwood kraft impregnated with silicone oil. The crack is just about to start propagating to the right. The FPZ diameter is 3–4 mm (Niskanen et al., 2001).

For the first paper, the FPZ was fairly uniform but extended far out along some long and presumably stiff fibres; for the second paper - damage zone is more homogeneous and wider. In that area in Figure 1-34 the microscopic bond failures occurred just before crack propagation started. FPZ size is 1.2 time the length-weighted fibre length and 2.2 times arithmetic mean fibre length (Niskanen et al., 2001).

Second attempt of FPZ quantification was performed by (Isaksson and Hägglund, 2013a) where using acoustic emission the FPZ width was measured as a standard deviation of the captured fracture sites along the axis perpendicular to the notch. Order of magnitude of FPZ is presented in Table 1-7 summarised from different studies.

Using nonlocal model (Isaksson et al., 2012) suggested that the FPZ in papers depends on the fibre segment length, thus, on density of paper, which was shown to be well in accordance qualitatively with experimental observations. The dense paper exhibits significantly small FPZ size and the straight crack propagation along the main crack plane, whereas the sparse paper had relatively large FPZ size and the crack propagated under the angle.

Table 1-7 : FPZ dimensions of paper materials found in the literature

Literature source	Year	Grade of paper	Fracture process zone (FPZ)		Technique
			MD, [mm]	CD, [mm]	
(Donner, 1997)	1997	Newsprint (43, 49 g/m^2) (cryogenic)	0.5	1.1	Deduced from modified LEFM
		Newsprint (43, 49 g/m^2) (ambient)	1.5	3.7	
(Niskanen et al., 2001)	2001	Handsheet of mechanical pulp 90 % of mechanical pulp, 10 % of chemical pulp)	1 (in width)		Experimental (silicon oil impregnation)

		Handsheet of softwood kraft	Ø 3 - 4		
(Coffin et al., 2013)	2013	Paperboard (200 g/m^2)	2.6	6.5	Deduced from modified LEFM
		Tissue paper (22 g/m^2)	4.2	7.0	
(Isaksson and Hägglund, 2013a)	2013	Handsheet of TMP (60 g/ m^2)	1.74 (in width)		Experimental (acoustic emission)

Influence of paper structure variability on fracture behaviour of paper materials

Crack propagation depends on the structure of paper. The crack propagation direction and the path are influenced by the heterogeneities in the paper structure, for example, the crack rather propagates in the less dense zones of the paper avoiding the flocculated areas (Moffat et al., 1973). The local variabilities are responsible for the variation in strain distribution and affect the fracture process (Castro, 2001).

Micromechanics

In micromechanical models the amount of energy released due to breaks of the fibre segments or the inter-fibre bonds should be considered. The total fracture work is summary of the released energy in all the segments and bond failure. Fibres of the real network are assumed to be 10 times stronger than the bonds so to compensate the energy dissipation in fibre failures a big number of bonds on a fibre have to break for similar geometric effect (Niskanen et al., 1999).

Load transfer in paper sheet increases with beating and wet pressing (Seth and Page, 1983). Beating of the pulp affects sensitivity to fracture. Bither et al. (Bither and Waterhouse, 1992) showed that handsheet of unbeaten pulp was less fracture sensitive than the handsheet of beaten pulp.

1.4.5 Conclusion

Paper is a material with complex structure having disorders which affect crack propagation. Ability of a sheet to concentrate stress is indicated by dimension of the FPZ: the smaller the value of FPZ, the better stress concentration of the sheet. Large FPZ would rather mean that paper material has poor transfer of load which is more characteristic of the sparse networks such as low density papers. Obviously, the different mechanisms of crack propagation occur in low density paper rather than in the dense paper, first of all, due to strength of fibres in comparison to the inter-fibre bonds. Moreover, the low density papers often present higher local grammage variation in the structure than the dense papers. The micromechanical events that occur during the crack propagation in paper materials should be physically explained. It was shown that the LEFM fails in prediction of stresses near the crack tip whereas nonlocal and gradient models are capable of the mechanical behaviour description for papers, even for the sparse networks.

1.5 X-ray microtomography as a tool to study 3D microstructure of natural fibrous materials

1.5.1 Introduction

As mentioned in the previous sections (Section 1.2.4 and 1.2.5), the mechanical and physical properties of paper materials are widely dependent on their microstructures, that is to say, the geometry, content, distribution and orientation of fibres within the porous structure. Improving modelling of physical and mechanical behaviour of paper materials requires the introduction of microstructural descriptors such as the volume fraction or their spatial distribution, the spatial orientation of the pores and fibres. One possibility to quantify the aforementioned microstructural in 3D descriptors in a non-destructive way is to use X-ray microtomography.

Using the penetrating energetic beam the X-ray tomography scanning was successfully performed on different materials, among them: soils (Ando, 2013), rocks (Ketcham, 1997), concrete (Garboczi, 2002), living tissues (Auweter et al., 2014), composites (Le et al., 2008), foams (Maire et al., 2003), snow (Coléou et al., 2001) and wood (Lindgren, 1992; Skog and Oja, 2009; Derome et al., 2011). At its infancy, this imaging technique was used to visualize the inner structure of the analysed sample, and, therefore, to give qualitative analysis of the microstructure. Quantitative image analysis procedures were then developed to perform geometrical and topological analysis to deliver the descriptors of the microstructure (Antoine et al., 2002; Holmstad, 2004; Faessel et al., 2005; Desplentere et al., 2005; Lux et al., 2006; Axelsson, 2007; Rolland du Roscoat et al., 2007; Eberhardt and Clarke, 2002; Viguié et al., 2011; Tsarouchas and Markaki, 2011; Marulier et al., 2015; Joffre et al., 2015; Joffre et al., 2016).

This subchapter is organised as follows: first the principle of X-ray tomography is presented in section 1.5.2, the microstructural characterisation of the paper by this imaging technique as well as the monitoring of the physical and mechanical properties of paper materials in section 1.5.3.

1.5.2 Principles and specificities of different X-ray microtomographs

X-rays is a form of electromagnetic radiation, the wavelength of which is in range between 0.01 to 10 nanometers. When a beam of high energy charged particles, i.e. electrons, is bended or collided with a metal target, the X-rays are generated.

1.5.2.1 X-rays generation and geometries

The X-rays can be generated using two main techniques: (i) anode-cathode type of systems or (ii) synchrotron:

i. In anode-cathode systems, the X-rays are generated by heating a filament with an electric current which emits thermal electrons that are accelerated

to the anode by a voltage potential difference. Every time electrons hit the anode, X-rays are produced. The produced X-ray beam is polychromatic and conic (Figure 1-35a). Due to its dimensions the anode-cathode system can be installed in a laboratory scale X-ray microtomographs.

ii. In synchrotron, a large-scale facility, the electrons emit energy at X-ray wavelength by moving in a large circle and changing their directions. Briefly, the synchrotrons consist of:

- *Booster synchrotron* is a pre-accelerator where the electrons are accelerated to high energy level before being injected into the storage ring.
- *Storage ring* which is a tube of several hundred meters in circumference where the electrons circulate with close to the light speed passing through different types of magnet and in the process producing X-rays.
- The storage ring is surrounded by the *beamlines* towards where the X-ray beams are emitted. Each beamline is designed for a specific type of research.

Beamline that are dedicated to tomography have a beam that can be considered as monochromatic and parallel (Figure 1-35b). Such a beam has a high flux compared to laboratory X-ray source.

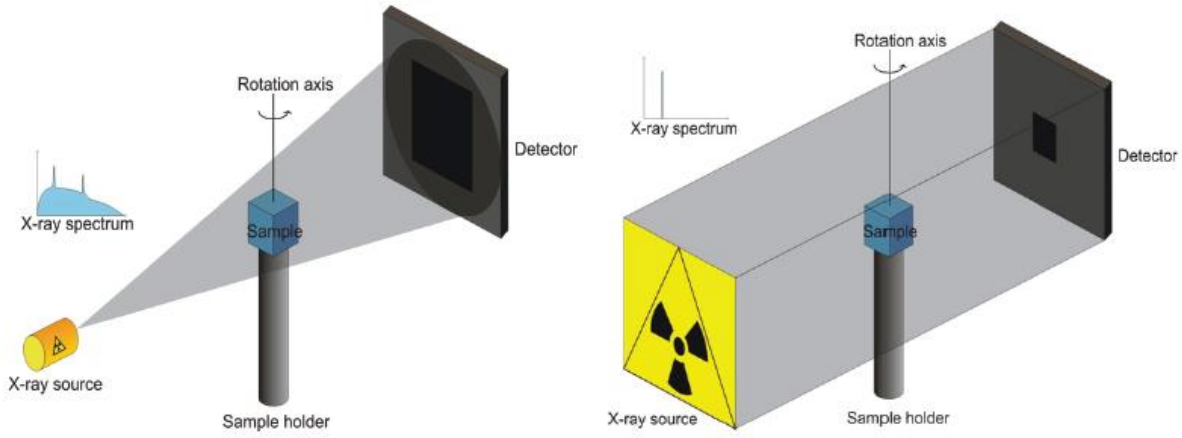

Figure 1-35 : Principle of cone beam geometry (left) and parallel beam geometry (right) (Turpeinen, 2015).

1.5.2.2 X-rays interaction with matter

There are two kinds of X-rays: hard X-rays with high photon energies (>5-10 keV and below 0.2-0.1 nm wavelength) and soft X-rays with lower energy. The hard X-rays can penetrate the matter better than the soft ones. X-rays interact with matter though photoelectrical absorption, Compton scattering and Rayleigh scattering. Since the X-ray photon energy is much higher than the chemical binding energy, the strength of the interactions depends on the energy of the X-rays and the elemental composition of the material. For the soft X-rays and the lower energy hard X-rays

photoelectrical absorption is the dominant interaction mechanisms whereas for the higher energy hard X-rays the Compton scattering dominates (Hsieh, 2003). The main mechanism of interaction of X-rays with the paper materials is photoelectrical absorption.

Going through a media, the X-rays are attenuated. The intensity of X-ray beam decreases exponentially with the distance travelled. This decrease can be modelled using the Beer-Lambert law:

$$I(z) = I_0 e^{-\mu z} \tag{1-14}$$

where I is the intensity (photons per area per unit time) of a monochromatic beam after it travelled through the distance z; I_0 is the initial intensity of the beam; μ is a coefficient of absorption.

Since the beam is monochromatic, the linear attenuation coefficient μ is dependent on the composition and the density ρ of the material for a given X-ray energy E:

$$\mu = \frac{\rho K^* Z^4}{E^3} \tag{1-15}$$

where K^* is a constant, and Z is the atomic number of the absorbing material. The denser the material the more attenuated X-ray beam.

1.5.2.3 X-rays microtomography for material science

In X-ray tomography during scan a number of X-ray projections are obtained from different angles that lead to the whole 3D volume of the inner structure of an object. The projections can be acquired either due to relative rotation of the object or the image acquisition system. The X-ray tomography developed in 1960s for the medical needs has afterwards become a popular tool in material science where depending on the desirable resolution of the images the materials were analysed using the stationary based sources or synchrotron facilities (Baruchel et al., 2000).

The principle of the X-ray 3D image acquisition is following: the X-ray beam passes through an object that attenuates the beam differently depending on the density of the object constituents. Series of radiographs are being recorded for different angular positions for a sample which rotates around an axis perpendicular to the beam. The X-ray projections represent the maps of the density distribution of the object from different angles.

Depending on the beam geometry the magnification is achieved in different ways. In case of the cone beam, emitted from a single point towards the detector, the field of view (FOV) is regulated by moving a specimen closer or further away from the source. For example, if one moves the specimen from the detector towards the source, the FOV decreases, and the specimen is enlarged on the detector due to geometric magnification. Moreover, since the detector has a fixed number of pixels, the effective size of the pixels is also regulated by relative distance of the specimen according to

the detector. In case of the parallel beam, the magnification is achieved using optics coupled with a detector.

1.5.2.4 Modes of acquisition

There are different modes of image acquisition that can be used in X-ray microtomography. One of it is the absorption mode where the densities of the sample are directly imaged using beam absorption. This mechanism of image formation often provides poor contrast when imaging light-element materials such as papers.

For such materials, a need exists to enhance the contrast in the images between the different composite constituents that is to say pores, matrix and fibres. Several strategies were developed. Phase contrast mode allows increasing the edge contrast between objects that attenuate the beam similarly, for example soft solids and fossils (Maire and Withers, 2014). Phase retrieval procedures normally require that images of the same sample are recorded at multiple sample-to-detector distances, as phase contrast increasing with distance. Among different kinds of phase contrast algorithms, the one commonly used is based on Paganin phase retrieval algorithm (Paganin et al., 2002) where instead of taking multiple images, the phase of the object can be reconstructed from a set of projections collected at a single distance. Generally, the X-ray images obtained using phase contrast mode, are easier to process and segment. It is an advantage for paper materials which are often appear in low contrast.

Comparison of laboratory and synchrotron X-ray microtomographs

In the case of paper sample, the advantage of laboratory X-ray microtomography is the availability of the apparatus, the low flux that do not alter the mechanical properties of paper. This apparatus is suitable for analysis around 10 µm of pixel size. However, despite the technical progress of the laboratory apparatus, it is complicated to perform mechanical tests at a resolution of 1 µm in a reasonable time (no more than 2 hours).

In the case of paper sample, the advantage of synchrotron X-ray microtomography is the monochromaticity of the beam adapted for sample that absorbs a few X-ray beam, the high signal-to-noise ratio. The second advantage is the possibility to perform *in situ* and real time acquisition (scan duration below one second) at high resolution. The coherence of the synchrotron beam allows to perform phase retrieval approaches (Paganin et al., 2002, for example) that increase the contrast between the constituents which is the case of paper material.

1.5.3 3D X-ray imaging of fibrous materials such as papers

1.5.3.1 Characterisation of paper structure using X-ray µtomography

Using X-ray microtomography the fibre network as well as the individual fibres and the inter-fibre contacts can be observed and characterized. The quantitative analysis of the 3D paper structure is necessary for predicting, for example, the mechanical properties of paper materials or the liquid transport in it or the paper and liquid interaction.

Volumetric characterisation of microstructure using X-ray microtomography has been successfully performed for different paper types:

- Porosity evaluated on binarised data by the ratio of voxels belonging to the pore phase to the whole number of voxels ((Rolland du Roscoat et al., 2007); (Goel et al., 2001) reported the internal porosity and specific surface area of thick board samples. The determined structural porosity was compared to porosity determined by caliper-basis weight measurements and mercury intrusion porosimetry. The porosity measured in the digital volumes was found to be in fair agreement to the physical measurements. Although the quality of the image is poor.
- Sheet local thickness was measured (i) by (Holmstad, 2004) using the determination of an objective surface, delimiting the paper structure from the surrounding background, it allows an improved thickness measurement by assessing the vertical distance between the two surfaces; (ii) by (Huang, 2010) using local mapping technique where perpendicular to the centre line of paper the thickness was calculated between two surface boundaries.
- Pore structure of paper was studied, among others, (Huang et al., 2002; Sintorn et al., 2005; Axelsson and Svensson, 2010). Pore size distribution in the paper network was investigated by measuring pore chords (Holmstad, 2004), Axelsson et al. (Axelsson and Svensson, 2010) working on 3D paper structure characterisation quantified the individual pores in 3D: surface area, orientation, anisotropy, and size distribution.
- The 3D tracking of individual fibres and morphological characterisation methods were developed by several researchers including (Eberhardt and Clarke, 2002; Lux et al., 2006; Axelsson, 2007; Viguié et al., 2013; Wernersson et al., 2014). In (Axelsson, 2007) the method that allows individualising each fibre is presented that consists in starting in one seed in each fibre and automatically extracting the local fibre orientation and the fibre centre point in each step using 3D information. Wernersson (Wernersson et al., 2014) developed a semi-automatical method whereas Viguie (Viguié et al., 2013) developed an automatic method tested on several fibre networks although it was limited to the rather straight fibres.
- Inter-fibre contacts quantification such as the contact area between fibres in paper have being developed (Wernersson et al., 2014; Viguié et al.,

2013; Marulier et al., 2015; Malmberg et al., 2011). Malmberg et al. (Malmberg et al., 2011) presented a developed method for the inter-fibre contact measurements using the 3D images of the wood-fibre mats with the average diameter of the fibres oriented out-of-plane of 30 µm. First, the fibre lumens were segmented using a watershed based method that resulted in labelling each image voxel as background, fibre or lumen. Then the fibre-fibre contacts were identified as a region between two separated lumens connected by only fibre material using traversing rays along the z-axis of the 3D image. This method works correctly as long as the lumens can be detected which is not always the case since the lumens may be collapsed, especially for the chemical pulp.

- Fibre orientations in the fibrous materials were identified (Altendorf and Jeulin, 2011). Fibre orientation can be analysed using a method by (Axelsson and Svensson, 2010) applied onto the 3D grey scale X-ray image. Using a structure tensor method the orientation estimate was provided for the cellulose fibres in a press felt. The originality of this method is in its out-of-plane fibre orientation measurement that is not possible to obtain using sheet splitting.

1.5.3.2 Monitoring of physical and mechanical behaviour of paper using X-ray microtomograph

Influence of humidity on fibres and paper

The effect of different Relative Humidity (RH) on both an individual fibre and a fibre network structural properties were monitored using *in situ* X-ray microtomography (Viguié et al., 2011; Marulier, 2013; Joffre et al., 2016). For that, the sample was irradiated using a wet air generator installed on the rotation stage of the X-ray microtomograph prior and during the scan. Joffre et al. (Joffre et al., 2016) obtained a geometry of the wood tracheid at two different relative humidity using XµCT in order to identify the hygroelastic deformation of the wood fibre using a mixed numerical-experimental method. This allows monitoring the changes between the different states from ambient to wet state for the wood fibre. The study on the single fibre experiment made on a virgin spruce fibre aims at quantifying the structural changes in the shape of the lumen as well as the twist along the fibres.

The study of (Viguié et al., 2011) aims at following the mesoscopic strains within the paperboard constituted of layers of various grammages. It shows using digital image correlation that mechanism of hygroexpansion for the studied material and of each layer was possible to analyse in the in-plane and out-of-plane directions. Moreover, the microstructural hygroexpansive mechanisms for the pore and fibre phases could also be revealed.

In (Marulier, 2013), the influence of the *RH* on the hygroexpansion was studied for two types of papers: in-plane oriented and in-plane isotropic. The analysis of the reconstructed volumes allowed measuring the out-of-plane hygroexpansion of paper fibrous networks and the hygroexpansion of individual fibres within the fibrous networks. It was found that the hygroscopic strain of tested papers in the thickness is higher in the case of the in-plane isotropic paper compared to the in-plane orientated paper. Moreover, the increase of *RH* deforms the geometry of individual fibres in the fibre network such as fibre centreline in the thickness direction of papers. The results show that the average transversal hygroexpansion of fibres is much more pronounced (one order of magnitude) that the longitudinal one. However these observations set the pace to a local observation of the fibre hygroexpansion mechanisms (centreline elongation, cross section swelling and inclination) that seem to be quite heterogeneous along the fibre centreline. This effect might be due to the presence of the numerous fibre-to-fibre bonds alongside the fibre.

Monitoring of mechanical and fracture behaviour of fibrous materials using X-ray

Mechanical and fracture behaviour of different fibrous materials and composites can be studied using X-ray microtomography when a mini tensile or compression devices that hold a sample is installed on the rotation stage (Hild et al., 2009; Tran et al., 2013; Åslund et al., 2015; Yu et al., 2016; Bouterf et al., 2016). However, the small defects and crack may be challenging to define in fibrous materials due to the low contrast of the components (Yu et al., 2016). Paper materials (tissue paper and a liner) subjected to fracture test were qualitatively analysed using *in situ* X-ray imaging ((Isaksson et al., 2012). This study illustrated in 3D the microstructural evolution of the discrete and continuous microstructures of papers. The advanced image analysis techniques can be applied onto X-ray images in order to quantify the micromechanisms. Among others, the Digital Image Correlation technique was used for different fibrous materials such as stone wool (Hild et al., 2009), and paper materials (Viguié et al., 2010; Åslund et al., 2015). The principle of such technique is in recovering the image feature from first image to the second image from which the displacement or strain (if required) can be deduced.

1.5.4 Conclusion

This section shows that X-ray microtomography is an extremely useful tool for the microstructural characterisation of different fibrous materials, especially paper materials. Since first decent image of the paper (Samuelsen et al., 2001) the X-ray microtomography was highly exploited in order to characterize various paper materials as well as its constituents – fibres and inter-fibre bonds. Moreover, hygro-mechanical behaviour of paper, of the wood fibres and individual fibres in the fibre network was studied using *in situ* X-ray imaging coupled with tensile device.

1.6 Conclusion

The "state of the art" chapter showed that paper, made up of cellulosic fibres linked to each other with hydrogen bonds, is a complex fibrous and porous material that exhibits a 3D multiscale structure such as: the macroscale being the scale of the paper sheet; the mesoscale, the one of the network of fibres; and the microscale, the one of fibres themselves. Moreover, the paper presents structural heterogeneities, and has a layered and an orthotropic structure. The structural properties depend on the nature of the pulp and on the paper making process. The structural organisation implies anisotropic in-plane mechanical properties. Due to the capacity of the constitutive fibres to uptake water, these structural and mechanical characteristics are affected by the relative humidity in the surrounded air. A particular attention was paid on the modelling and experimental analysis of fracture phenomena in papers and it points out the experimental difficulty (i) to relate the structural characteristics to the internal length that are involved in nonlinear fracture models applied to paper, and to (ii) quantify the Fracture Process Zone and (iii) to investigate the influence of humidity on such features, especially in the low density networks. A synthetic overview of the structural characterisation of paper by X-ray microtomography showed the possibility to quantify accurately both porous and fibrous phases in paper at meso and micro scales and described the opportunities brought by the monitoring of the microstructural evolution of the paper when coupled with a tensile device, for example.

Chapter 2. Materials and methods

Content

2.1 Introduction

As mentioned in the first part, the main objectives of the current PhD are to provide a multiscale description of crack propagation mechanisms in papers and to investigate the influence of relative humidity on such mechanisms by taking into account the phenomena that occurs at lower scales (fibres scale or assembly of fibres scales). To fulfil these objectives, an experimental approach was developed. The objective of this chapter is to provide an accurate description of the analysed paper materials and of the developed methods. This chapter is divided in 5 sections:

- Section 2.2 and section 2.3 describe in detail the two studied papers namely a high density and a low density papers, justifies the choice and summarises their main physical and mechanical characterisation using procedure classically used in paper physics.
- Section 2.4 presents the two tensile set-ups developed to investigate the fracture behaviour of the two types of samples under various relative humidities at the three investigation scales: macroscale, mesoscale and microscale.
- Section 2.5 presents the imaging procedures based on classical microscopy and X-ray microtomography to quantify the formation at the mesoscale and microstructural properties.
- Section 2.6 summarised the main steps of the local displacement field measurement procedure in the particular case of paper samples.

2.2 Studied paper material

To study the mechanical and hygro-mechanical behaviour of natural fibrous materials, two paper materials were chosen for their different structural characteristics. The selected papers are:

- *A low density paper* which was specially manufactured for this study. It has started to being investigated in (Hägglund and Isaksson, 2006; Isaksson et al., 2012);
- *A high density paper* such as commercial *tracing paper* ("Tracing paper in roll 40/45 g, 0.750 x 20 m", Clairefontaine®, France)

2.2.1 Low Density Paper

The studied low density paper (LDP) is a tissue paper (Figure 2-1). It was manufactured at very low speed by air-drying (TAD) discussed in Chapter 1, resulting in a sparse fibre network. The LDP was made from bleached unbeaten softwood chemical pulp to a basis weight of 23 gm^{-2} and an apparent thickness of 113 µm ± 7 µm measured according to the standards presented in section 2.3. The

apparent density is about 204 kg/m^3. This paper has therefore a porosity of 86 % leading to a discrete microstructure.

The mean arithmetic fibre length was 1.4 mm, the mean length-weighted fibre length 2.1 mm, and the mean fibre width 31.7 µm. These measurements were obtained using Morfi® (section 2.3.2). The in-plane mechanical anisotropy of the LDP, defined as the ratio between the Young's moduli measured in the MD (E_{MD}) and CD (E_{CD}) directions, was 1.2. On Figure 2-1b, one can observe heterogeneities of the paper structure in dark grey corresponded to the high mass distribution, called flocs (Chapter 1).

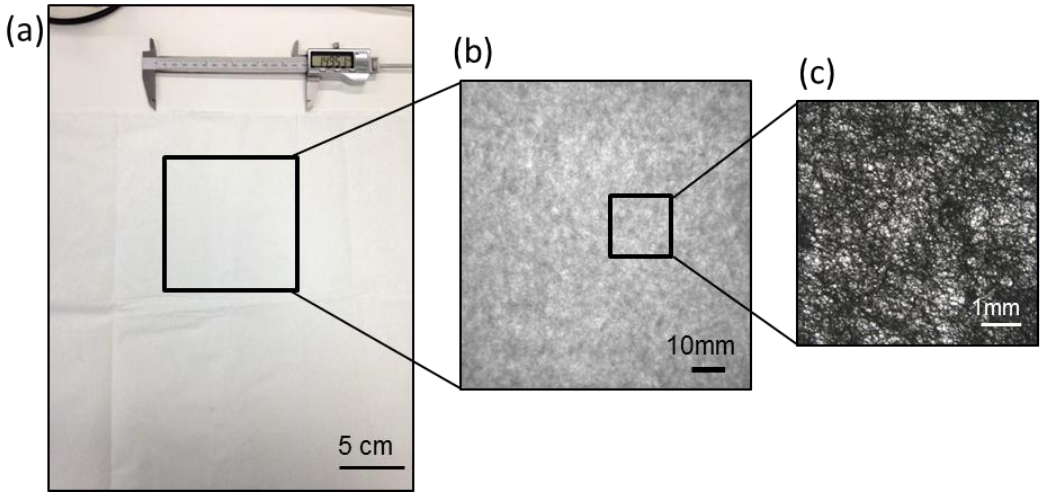

Figure 2-1 : Studied low density paper: (a) image of paper sheet the samples were cut from; (b) transmitted light image taken with Techpap® Paper Formation analyser (Pagora, Grenoble, France); (c) image obtained with optical microscope in transmission.

2.2.2 High Density Paper

The chosen high density paper (HDP), i.e. a tracing paper (Figure 2-2), consists of highly fibrillated fibres from the chemical pulp (Gosh and Chaliha, 1984; Van Der Reyden et al., 1992). This paper has a grammage of 47 g m^{-2} and a thickness of 44 ± 1 µm. The apparent density is about 1068 kg/m^3, leading to a porosity of 0.3. The homogeneous structure of the tracing paper comes from the high refining degree inducing a large amount of fibre-fibre bonds. The dense organisation of the fibre network can be observed in the SEM images in Figure 2-3. Due to the papermaking process, this paper has a bulk porosity that is below 1%, leading to a continuous microstructure. The anisotropy of the tracing paper E_{MD}/E_{CD} was 1.8. Due to its homogeneous structure the tracing paper transmits more light (Figure 2-2b) in comparison with those papers of low opacity, for example, LDP.

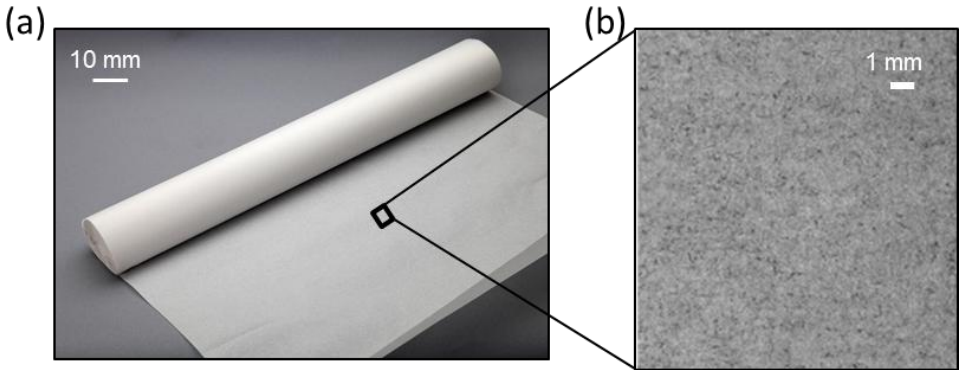

Figure 2-2 : Tracing paper at macroscale (a) and mesoscale (b).

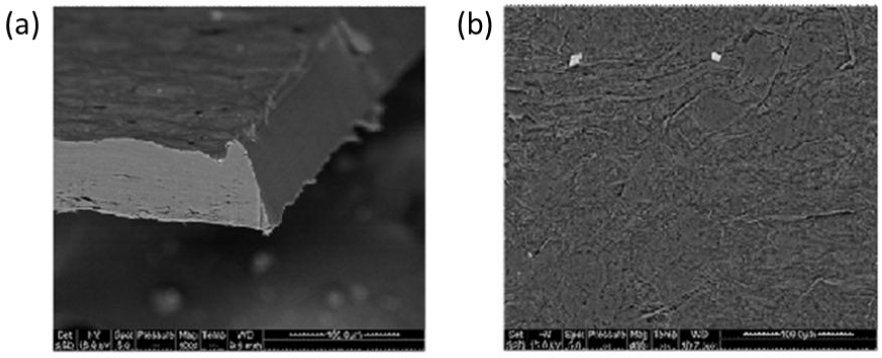

Figure 2-3 : Microstructure of tracing paper obtained with SEM: (a) thickness, (b) top view. The structure shows a network of highly refined fibres (Marulier, 2013).

2.2.3 Sample preparation for mechanical testing

All the samples used for the mechanical tests performed in this study were prepared using a cutting machine (Kongsberg® XL 22, Eskoartwork, Gent, Belgium) located in LGP2, Grenoble (Figure 2-4). The protocol to ensure repeatability of the sample preparation was:

- To avoid any damage of the studied sheet of paper, a sheet of thick paper was placed on the top of studied paper. This assembly was then placed in the machine.
- The samples were then cut automatically according to the chosen geometry. The geometry is manually chosen by the operator (insert of Figure 2-4).

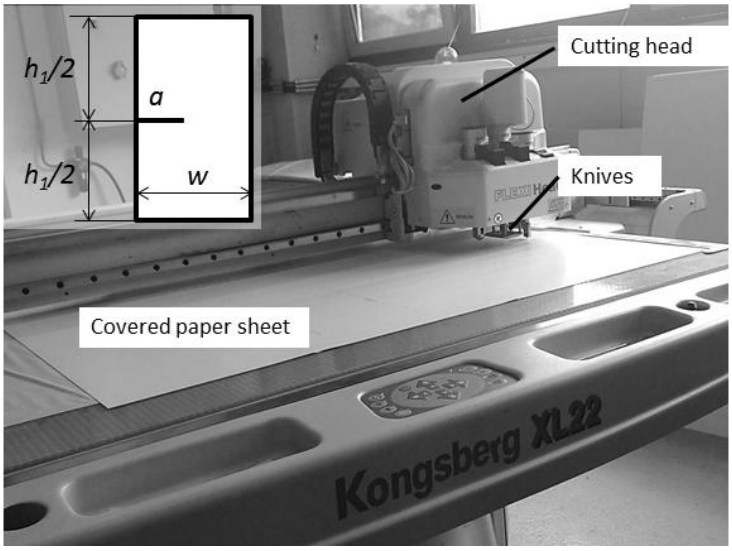

Figure 2-4 : Picture of the cutting machine. In the insert, cutting scheme of paper sample.

Table 2-1 summarises the dimensions of the tested samples: rectangular samples of height (h_1) and width (w) were extracted from the paper roll and a single edge notch of length (a) was made at the mid-height (insert of Figure 2-4). As paper physical and mechanical properties depend on environmental conditions, once prepared, all the studied samples were stored in the conditioning room with a temperature (T) of 24.5°C and a relative humidity (RH) of 50%.

Table 2-1 : Dimensions of the samples for mesoscale and macroscale experiments.

Scale	Width w [mm]	Height h_1 [mm]	notch length a [mm]	a/w [-]
mesoscale	12	12	0	0.00
	12	12	1	0.08
	12	12	2	0.17
	12	12	3	0.25
	12	12	4	0.33
	12	12	5	0.42
macroscale	45	130	0	0.00
	45	130	2	0.04
	45	130	3	0.07
	45	130	4	0.09
	45	130	5	0.11
	45	130	6	0.13
	45	130	7	0.16
	45	130	8	0.18
	45	130	9	0.20
	45	130	10	0.22
	45	130	11	0.24
	45	130	15	0.33
	45	130	20	0.44
	45	130	23	0.51

2.3 Methods used in paper physics for structural characterisation

In this section, we present tools and techniques that are traditionally used in the paper physics in order to measure paper properties and characteristics such as grammage, thickness, density of paper, average fibre length and width, and moisture content of paper. The parameters of the studied papers presented in the previous section were measured using the techniques discussed below.

2.3.1 Grammage and thickness

Before measuring the paper's thickness (t) and grammage (g), the samples were cut into squares of 10-by-10 cm^2 using a scale frame and were stored in a conditioned room at temperature (T) 23 °C and 50 % of relative humidity (RH) during 24 hours. The grammage and the thickness measurements were carried out in this room.

- According to standard (ISO 534:2011), the apparent thickness (single sheet) is measured using a dead-weight micrometer (Figure 2-5) which applies a pressure of 100 kPa on a surface of 2 cm^2 (discussed in section 1.2.4). In HDP 10 different areas were measured and then averaged. Since the LDP is highly compressible paper, the bulking thickness of 10 layers was measured in 10 different areas where the average thickness of the single sheet was calculated from.
- According to standard (ISO 536:2012), 10 different samples were gravimetrically measured. The grammage was simply deduced by dividing the mass by the area. The average value of 10 samples gave a mean grammage of the paper material.

When the paper does not have filler or when neglecting the filler content, the porosity (Φ) of the paper sample can be deduced from these measurements using the following relationship:

$$\Phi = 1 - {}^{g}/_{(t \cdot \rho_{fibre})} \quad (2\text{-}1)$$

where ρ_{fibre} represents the fibre wall density which equals 1550 kg/m^3.

The density of paper (ρ), [kg/m^3] is calculated as:

$$\rho = {}^{g}/_{t} \quad (2\text{-}2)$$

Figure 2-5 : Apparatus to measure thickness of paper installed in LGP2, Grenoble.

2.3.2 Fibre morphology

The fibre characteristics of the produced paper such as their length and the dimensions of their section were evaluated using the fibre analysis apparatus Morfi® (Techpap®, Grenoble, France). The protocol is described below.

2.3.2.1 Preparation

The analysed paper is placed inside a jar with a little amount of distilled water to soak in overnight. This procedure is necessary in order to let fibres separate from each other. In case it is not sufficient for the decent separation, a mixer can be used to improve the separation. The soaked separated fibres are diluted with 4 litres of distilled water and separated into three parts to perform three tests.

2.3.2.2 Test

The suspension prepared according to the protocol above starts moving in front of the camera installed inside of the device. The images of the suspension are automatically taken during a few minutes (Figure 2-6a). An automatic image analysis procedure is applied. The distribution of the length of fibres (Figure 2-6b) can be retrieved from the image analysis. Such a procedure also provides indication on the presence and on the characteristics of fines included in the suspensions.

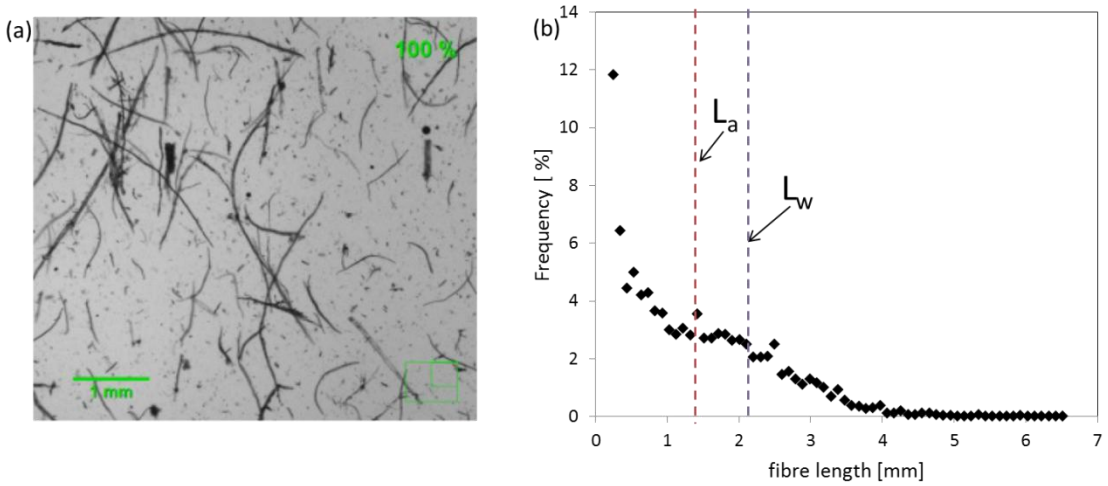

Figure 2-6 : (a) Image of the pulp suspensions inside the Morfi® device (www.techpap.com). (b) Example of fibre length distribution obtained using Morfi® device.

2.3.2.3 Results

A statistical analysis can be performed on the obtained distributions. For example, the mean arithmetic fibre length (L_a) or the mean length-weighted fibre length (L_w) can be evaluated as follow:

$$L_a = \frac{\sum L}{N_T}, \tag{2-1}$$

$$L_w = \frac{\sum L^2}{\sum L} \tag{2-2}$$

where L represents the length of each fibre, and N_T the total number of analysed fibres.

The mean arithmetic fibre length consider equally all the elements of the pulp, whereas the mean length-weighted fibre length gives more importance to the long fibres. In the example of Figure 2-6b which corresponds to LDP, L_a equals to 1,4 µm and L_w 2,1 µm.

2.3.3 Moisture content

The moisture content (MC) of a paper sample is defined as follows:

$$MC = \frac{m_w}{m_d}, \tag{2-3}$$

where m_d and m_w represent the dry mass of sample after drying for 24 h at 105°C and the mass of water present in the paper sample, respectively.

The moisture content of paper sample was measured using the Varimass® device (Techpap®, Grenoble, France) illustrated in Figure 2-7a and b. The samples were subjected to the following Relative Humidity (RH) steps (Figure 2-7c): 10% → 20% → 30%→ 40% →50% → 60% → 70% → 80% → 85% → 80% → 70% → 60% →50% → 40% → 30% → 20% → 10% for 2 hours each at ambient temperature (T=24.5°C). This duration was long enough to make sure that moisture content in the papers was stabilized. During these experiments, the mass of the samples was regularly measured

(Viguié, 2010; Marulier, 2013). The moisture content was deduced from the evolution of the mass as following:

$$\Delta MC = \frac{\Delta m}{m_d}, \tag{2-4}$$

where Δm is the difference between the mass of samples in two consecutive RH steps.

Figure 2-7d illustrates the obtained moisture content of a paper. One can observe that the MC of a paper is different in absorption and in desorption. This classical behaviour is due to the fact that it is easier to uptake water than to remove it (Chapter 1).

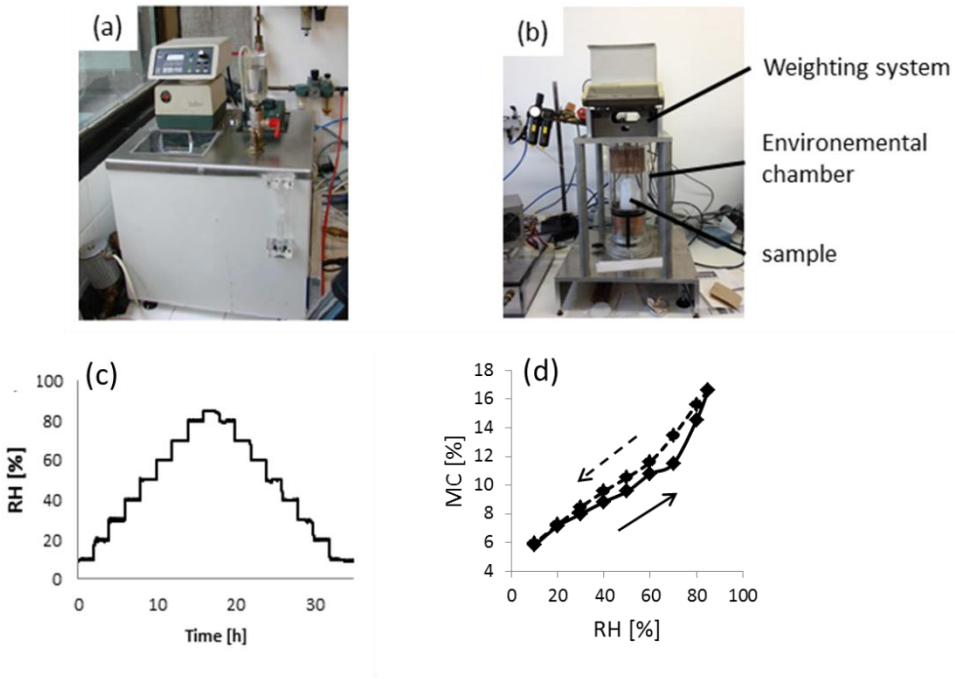

Figure 2-7 : Set-up for moisture content measurement of paper materials: (a) wet air generator that connects to (b) the Varimass® device installed in LGP2, Grenoble. (c) Example of humidity cycle (d) Example of MC vs RH for a paper material at absoption and disoption cycle.

2.4 Developed mechanical set-ups and tools

2.4.1 Macroscopic tensile test under various Relative Humidity

2.4.1.1 Experimental set-up of protocol

The macroscopic tensile tests were performed using a testing machine INSTRON® equipped with a 5 kN load cell (2580-108, Static Load Cell, INSTRON®, Norwood, MA). As mentioned in the Chapter 1, the mechanical response of any paper depends on its moisture content (MC). In order to quantify the influence of MC on the mechanical responses of the studied paper, a setup was developed. In this scope, a climatic chamber was installed around the sample placed in the tensile machine. Figure 2-8 illustrates the developed set-up. The environmental conditions (T and RH)

in this chamber are ensured by air-controlled RH provided by a wet air generator (humidity generator, Techpap® SAS, Grenoble, France). The measurements were conducted in a controlled environment condition at T of 24.5 °C and RH of 10 %, 50 % and 85 %, respectively. All the samples were preliminary stored in the chamber for 2 hours prior to testing. Then the samples were loaded at a speed of 1 mm/min that was chosen in order to be as close as possible to the speed used for the tensile test coupled with a real time *in situ* X-ray imaging (see Section 2.4.2). By testing the other speeds lower than the current, the speed of 1 mm/min was found to be the optimal one that does not significantly alter the mechanical behaviour of the studied paper tested at the standard conditions.

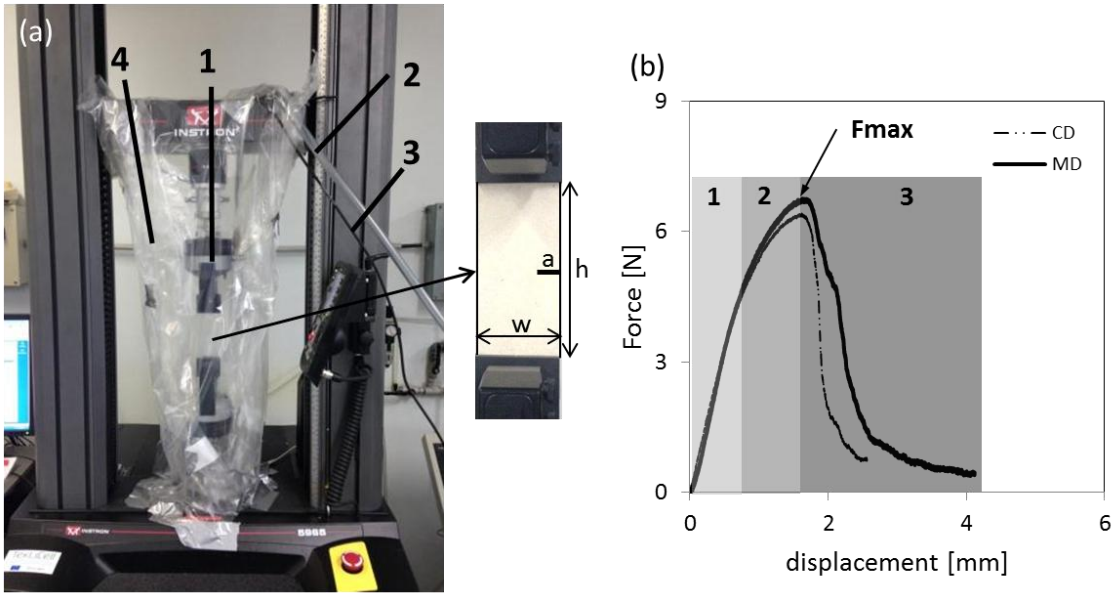

Figure 2-8 : (a) Setup for the tensile test regulated in humidity and temperature: 1 – clamps where the sample was placed, 2 – output from the humidity generator, 3 – cable for the humidity sensor, 4 – humidity chamber; (b) Force as a function of displacement for a tensile test for LDP sample without notch in MD and CD.

2.4.1.2 Preliminary result

Figure 2-8b illustrates the uniaxial tensile behaviour of the considered LDP in machine (MD) and cross (CD) directions in the room conditions. First, the force linearly increased with the applied displacement (zone 1). Then, the force deviated from linearity; this behaviour corresponded to the plastic mechanical response of the paper (zone 2). When the maximum force F_{max} was reached, the crack started propagating (zone 3). In case of LDP, the "non-immediate" rupture is observed when the force decreases slowly from F_{max} toward zero.

Figure 2-9a and b show the mechanical response of the LDP and the HDP, respectively, for the 3 considered RH rates: 10 %, 50 % and 85%. The mechanical properties of both papers decreases with the increase of RH that is coherent with the literature (see the section 1.3.5). One can observe that for both papers, the Young's

moduli decrease, the forces at the peak decrease, displacements corresponding to the force peak increase with the increase of RH as summarised in Table 2-2.

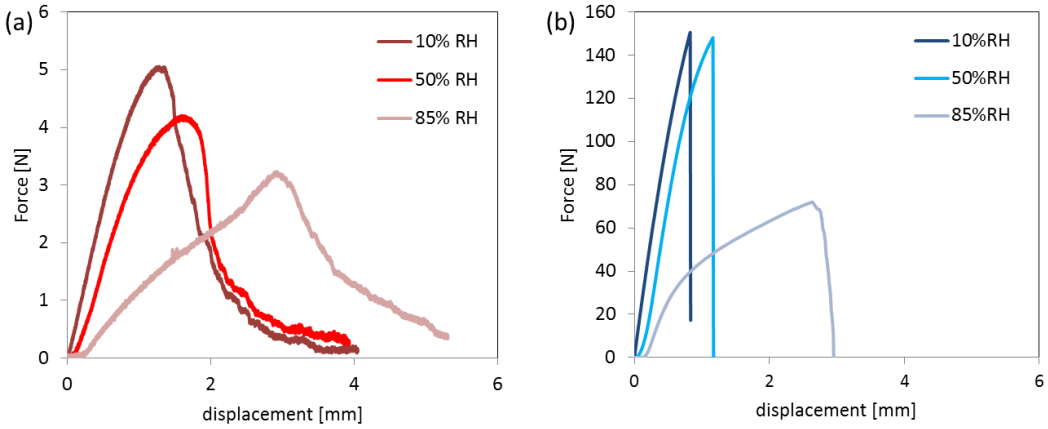

Figure 2-9 : Mechanical behaviour of LDP (a) and HDP (b) at different RH: 10%, 50% and 85%.

Despite of the RH, one can observe a difference in the post-peak behaviour of LDP and HDP in the curves (Figure 2-9). The curves of LDP present a stable decrease of the force, i.e. stable fracture, whereas the curves of HDP show immediate decrease of the force, i.e. immediate fracture. The behaviour of LDP is common for the papers with bond-induced fracture behaviour whereas the HDP exhibits rather fibre-bond-induced fracture.

Table 2-2 : Young's modulus E, force at the peak F_{max}, displacement d_f corresponded to the force peak of the LDP and HDP at 10 %, 50 % and 85 % of RH shown in Figure 2-9.

RH [%]	E [GPa]		F_{max} [N]		d_f [mm]	
	LDP	HDP	LDP	HDP	LDP	HDP
10	0.092	9.5	5.1	151.2	1.2	0.7
50	0.089	9.1	4.2	149.3	1.6	1.1
85	0.029	6.3	3.2	71.6	3.0	2.9

2.4.2 *In situ* tensile test coupled with humidity changes monitored by X-ray tomography

2.4.2.1 Development of a mini tensile device

The mini tensile device used in this PhD work was designed in close cooperation with M. Terrien (LGP2, Grenoble). The development of the device has been evolving through the PhD to be as close as possible to a standard tensile device. Therefore, the following conditions should be fulfilled:

- It has to be as close as possible to standard tensile machine.
- It has to be versatile to be installed on various microscopes such as laboratory (3SR, RX Solutions®, Annecy, France) and synchrotrons (SLS and ESRF) X-ray microtomographs (XμCT) (Section 2.4.2) or such as optical microscope installed in LGP2, Grenoble where the spatial constraints are the following:

- The diameter of the tensile machine should be smaller than 20 mm in order to perform acquisition at a pixel size of 7 µm in 3SR lab XµCT. This small diameter is also required to perform high quality phase retrieval reconstruction in synchrotron;
- The location of the sample in the tensile machine should be compatible with the different distance between the rotation stage;
- The device can be used vertically or horizontally depending on the imaging device.

- It has to be adapted to a rapid change of soft samples due to the limited time available in XµCT

Based on the experience acquired in our group on the development of mini testing machines (Latil et al., 2011; Isaksson et al., 2012; Laurencin et al., 2016), the mini tensile device was developed to fulfil all these requirements. The result is presented in Figure 2-10. The mini tensile device, the height of which is 18 cm, consists of:

- a piezo motor type NanoPZ Ultra-High Resolution Actuator from Newport, installed at the bottom of the mini tensile device. It has a load capacity of 50N, a travel of 12.5 mm and a speed up to 0.2 mm/s.
- a compression/tension load cell of 5 or 50N (type Honeywell Model 34 Miniature), depending on the sample to be analysed, installed on the top of the device. These two elements are protected by aluminium parts.
- dedicated mechanical clamps (Figure 2-10c) and mounting system were developed to allow an easy change of sample.
- a Plexiglas® tube, the thickness of which is 1mm that is transparent to X-ray and that ensures a partial rigidity of the system. The Plexiglas® tube is constituted of two half tubes that are assembled together with four screws. The first half is permanently fixed connecting the upper and bottom parts of the device; the other half can be removed to place the sample between the clamps.

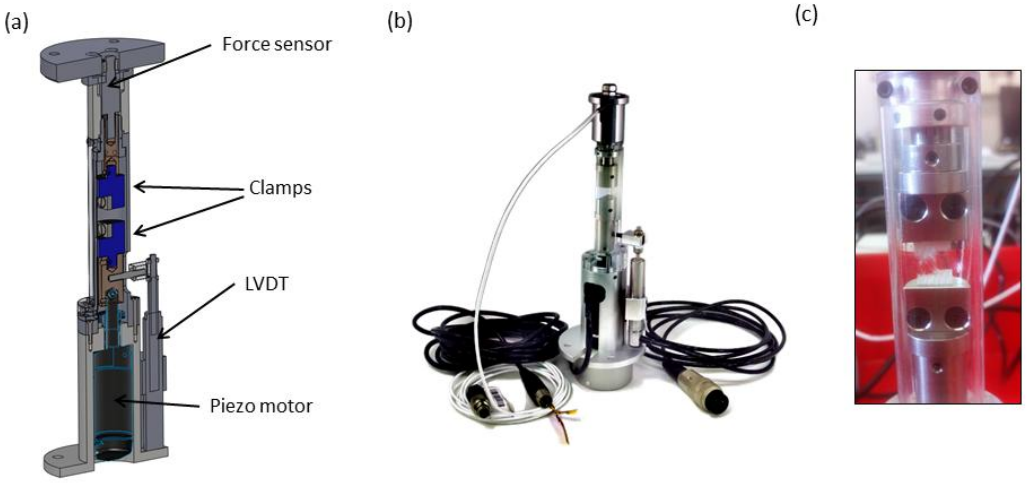

Figure 2-10 : Mini tensile device: (a) 3D synthetic view of the final mechanical design; (b) photograph of the device, (c) zoom on the clamps inside which a broken sample can be observed.

The first tests using this device were carried out on a stationary XµCT installed in 3SR laboratory. The load versus time graph indicated that the rotation of the sample may have affected the measurement of the load due to the cabling. To avoid this, the mini tensile device was improved by:

- adding a slip ring avoiding the rotation of the load cell cable during acquisition which might lead to error in force measurement.
- installing a linear variable differential transformer LVDT (RDP Electronics Ltd D5-D6, UK) to access the displacement especially when high resolution images were acquired.

The mini-tensile device was also equipped with an in-house acquisition software, developed in cooperation with P. Charier (3SR laboratory, Grenoble).

- As in any tensile device, it records force and displacement, allowing deducing strain/stress curve;
- It allows a manual control of the motor's displacement. Therefore, traction tests can be interrupted anytime for the image acquisition.

This acquisition system can be installed in the controlled room of the various XµCT, which avoid entering the XµCT chamber. This is required to perform continuous monitoring of the microstructure while loading.

2.4.2.2 Monitoring a tensile or fracture tests by X-ray

Figure 2-11 illustrates the developed set-ups installed in the two X-ray microtomographs used in this PhD, namely the laboratory one and the synchrotron one.

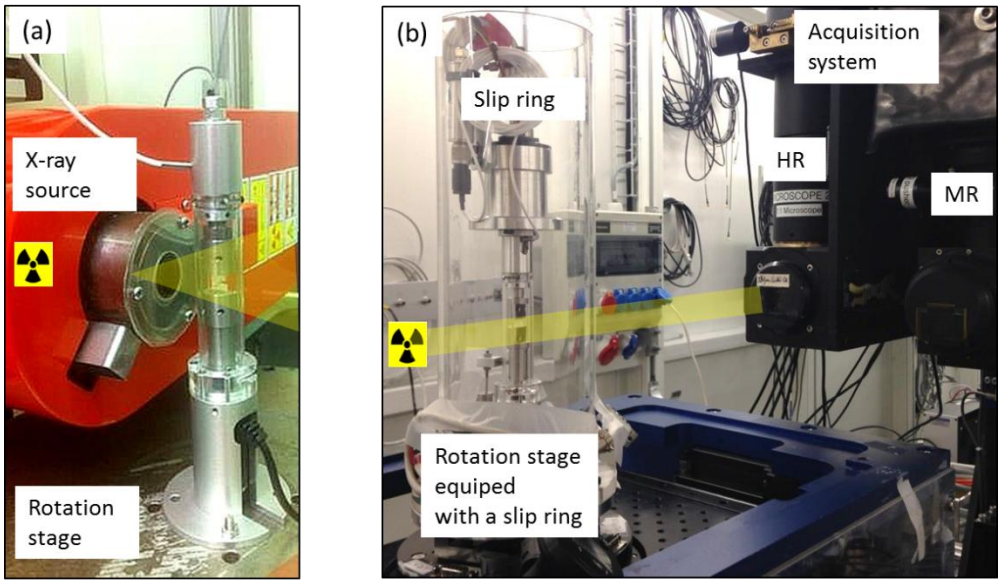

Figure 2-11 : Photograph of the tensile device mounted on the various X-ray tomographs (a) laboratory microtomograph installed at 3SR Laboratory; (b) synchrotron at SLS.

2.4.2.3 Application: fracture tests under various humidity

Experiments carried out at beamline TOMCAT of Swiss Light Source (SLS) were focused on the investigation of crack propagation phenomena at different relative humidity RH conditions. In this scope, few modifications of the set-up were performed to satisfy relative humidity requirements and illustrated in Figure 2-12.

- The output of the wet air generator used for microscopic tests (see section 2.4.1) ends up into a conical part that was placed above the humidity chamber. This is where the regulation takes place. The air flow pressure was adjusted to prevent sample from motion.
- A humidity chamber was designed with a Plexiglas tube in which the mini tensile device was placed. Three holes were made at the bottom of humidity chamber to avoid condensation in the chamber. A control wet air sensor was placed at the bottom of this cell. This sensor generally indicates the chosen RH +/- 2%.

The two parts described above were separated to allow high speed data acquisition. Namely rotating several consecutive times the wet air pipes is generally not compatible with high speed imaging.

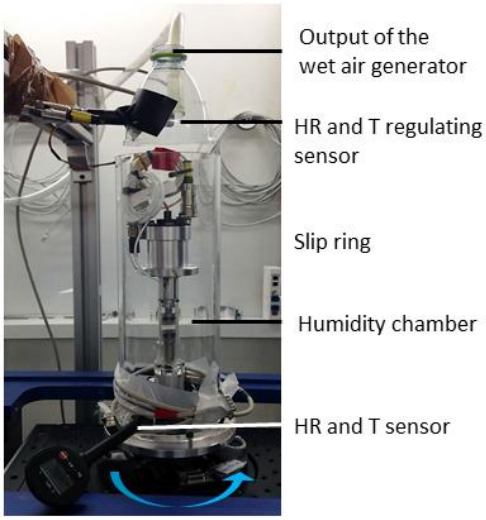

Figure 2-12 : Photograph of the mini tensile device regulated in temperature and humidity installed at SLS.

2.5 Quantification of paper microstructure by image analysis

In order to visualise the structure of paper (section 1.2.4), an optical microscope and an X-ray microtomograph were used. Their main principles were recalled below.

2.5.1 2D image acquisition using optical microscopy

When a cellulosic fibre is illuminated by visible light, part of it is reflected by the surface of the fibre, another part is absorbed by the fibre and the rest is transmitted by the fibre. The amount of transmitted, reflected and absorbed light depends on the incident angle of the light. Considering the fact that paper is a porous assembly of fibres, all the phenomena described above happen to all the fibres. It means that paper under light shows: specular reflexion, scattered reflexion at the surface, scattered absorption, refraction, transmission (Niskanen, 1998).

2.5.1.1 Image acquisition using an optical microscope

2D images were acquired in transmission mode using optical microscope with objective (ZEISS®, Discovery.V20, Plan S1x, Germany), available in LGP2, Grenoble, equipped with a CCD camera (ZEISS®, AxioCam ICc5, Germany). The 2D micrographs were obtained using a transmitted visible light. Figure 2-13 illustrate the microscope and the images obtained for LDP and HDP samples with a chosen pixel size of 7.3 µm. During acquisition the exposure and the white balance were automatically adjusted. The acquired images were 2452 x 2056 pixels size encoded in 24-bit RGB colour coding.

For LDP sample, the dark grey areas (Figure 2-13b) correspond to the fibrous network: darker grey areas correspond to the higher mass distribution in the sample and lighter areas – to the lower mass distribution. The HDP has low opacity, thus, more light was transmitted through the sample (Figure 2-13c). The transmitted light reveals homogeneous structure of paper, however the small dark dots were observed in the image. One can also observe a dark area near the notch tip of the sample corresponding to damage in structure of the tracing paper due to cutting: the air was introduced into the structure creating more reflections of light and, thus less transmission through the thickness of paper. It is hypothesised that the dark dots correspond to the voids between the fibrillated fibres in the tracing paper.

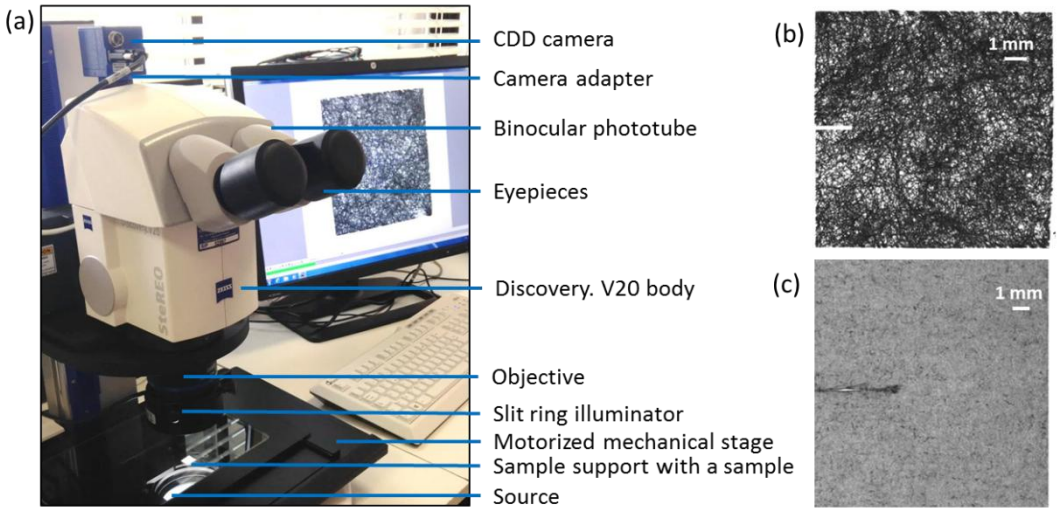

Figure 2-13 : Optical microscope (a) and optical micrographs obtained using the transmitted light mode of LDP (b) and HDP (c) samples.

2.5.1.2 Link between fracture mechanisms and the paper microstructure

For the samples from the chapter 5 subjected to the fracture test, the transmitted light images were obtained following the procedure: first images of the sample were acquired before the test, the sample was placed in the clamps of mini tensile device (Section 2.4), the fracture test were performed, the sample was carefully removed from the clamps of the device and placed back on the microscope to acquire the last image after the test (Figure 2-14).

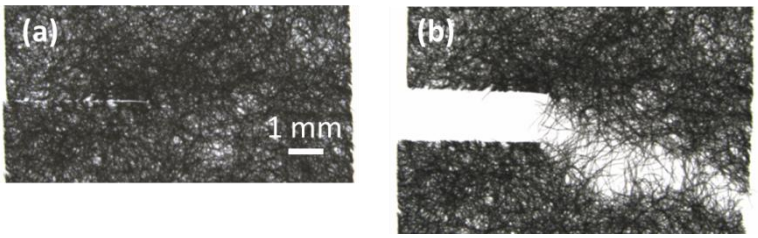

Figure 2-14 : Optical micrographs obtained for a small paper sample using transmitted light before (a) after (b) fracture test at 7.3 µm of pixel width.

2.5.1.3 Image preparation

The original RGB image was converted into 8-bit greyscale images using Fiji image software (https://imagej.net/Fiji).

2.5.2 3D image acquisition and preprocessing

During this PhD, different microtomographs were used: the one located in the 3SR laboratory and the one of the TOMCAT beamline of SLS. The used set-ups are detailed here.

2.5.2.1 Laboratory X-ray microtomography.

The X-ray source of 3SR laboratory is an Hamamatsu Corporation L8121-03 sealed source with a source tension between 40 and 150 kV and a current between 0 and 500 µA. It generates a polychromatic conic X-ray beam. A 1 mm plexiglass was placed at the output of the source to remove the lower energy of the beam. The detector is a flat-panel (Varian PaxSCan® 2520V) that measures the intensity of incident X-ray photons on an array of 1536 x 1920 pixels in either landscape or portrait modes. The scintillator of the detector (Caesium Iodide, CsI) converts X-rays into visible light captured by the array of photodiodes. The distance between the X-ray source, the rotation axis and the detector defines the effective used pixel size, which was chosen to be 6.9 µm. To obtain a high data quality, 900 2D X-ray projection images of the sample were obtained during the 360 ° rotation of the mini tensile device with the sample. One scan lasts about two hours. In this work, the reconstruction software DigiCT version 2.4.2 from Digisens was used which is based on the FDK Algorithm, after Feldkamp, Davis and Kress who describe it as a “convolution-backprojection” algorithm (Feldkamp et al., 1984).

2.5.2.2 Synchrotron X-ray microtomography

The parallel and monochromatic X-ray beam was adjusted at an energy of 20 keV. Two imaging systems were used:

- A high resolution imaging system that consisted in a scintillator of LAG:Ce 20 µm that convert X-ray light into visible light. The magnification was done using Zeiss optics (two consecutives objectives x10 and x2. The effective pixel size was 0. 55 µm using the PCO Dimax (2016 x2016 pixels) detector that has a pixel size of 11 µm. The distance between the detector and the rotation axis was 200 mm allowing phase acquisition. 501 2D X-ray projection images of the sample were obtained during the 180° rotation of the mini tensile device with the sample in about 3s. The reconstructed data were obtained using Paganin phase retrieval mode (Paganin et al., 2002) and filtered back-projection algorithm (Kak and Slaney, 2001);
- A lower resolution imaging system that consisted in a scintillator of LAG:Ce 350 µm that convert X-ray light into visible light. The magnification was done using Zeiss optics (objective x1). The effective pixel size was 6.5 µm using the PCO Edge 4.2 detector (2040 x 610 pixels) that has a pixel size of 6.5 µm. The distance between the detector and the rotation axis was 200 mm, allowing for absorption acquisitions. 2001 projections were recorded over 180° in about 1 minute. The reconstructed data were obtained using absorption mode and regridding reconstruction algorithm (Marone and Stampanoni, 2012).

Regardless the microtomograph, 2D radiograph (Figure 2-15a) exhibits very few information that is visible to the naked eye. The 2D data sets are converted into 3D data sets and a slice of the inner part of the LDP can be observed (Figure 2-15b) at a pixel size of about 7 µm. Such images represent 'mesoscale' images where the network of the fibres can be analysed (Figure 2-15). The higher resolution images with 0.55 µm of effective voxel width shows detailed fibre structure in paper. Those images will be called 'microscale' images.

2.5.2.3 3D X-ray image binarisation

Quantitative image analysis of the paper structure is usually performed on the binarised images where phases were identified that is in our case fibre and pore phases. For that the grey level images (Figure 2-15b) are converted into black and white images by thresholding operation. This is done on the analysis of the histogram of grey levels of the original images. A typical obtained histogram is shown in Figure 2-15c. In this example, one can observe that the number of the dark grey values corresponded to the pore phase prevails over those corresponded to the fibre phase since the material is very porous. However, the range of grey values for the fibre phase is wider than the one for the pore phase. The critical value of thresholding is manually selected based on visual assessment. Thus, the grey values that are below

the critical thresholding value will be turned into black (0) corresponding to pores, and the values above into white (255) corresponding to fibres (Figure 2-15d). Limited by image resolution, the segmentation of every fibre was not perfectly performed as it can be observed comparing Figure 2-15b and d: in order to avoid segmentation of non-constant background the tiny parts of the fibres were denied. The threshold chosen for the 'mesoscale' images (Figure 2-15d) was sufficiently good to "cover" all the voxels in the centre belonging to the fibre phase.

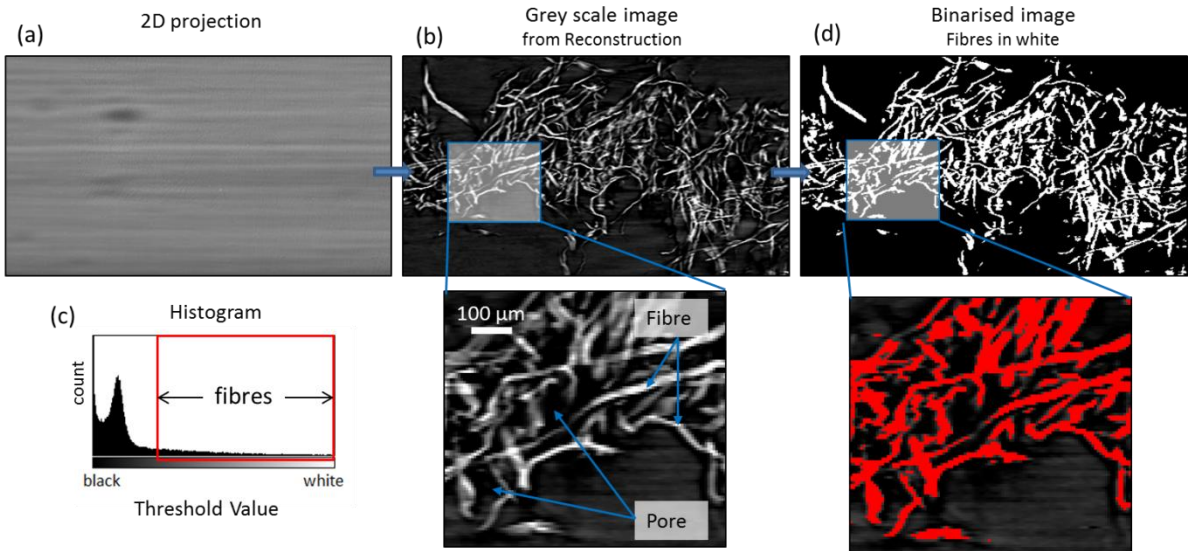

Figure 2-15 : Illustration of the thresholding procedure for the 'mesoscale' images of paper sample (voxel size 6.5 x 6.5 x 6.5 µm^3): a) One of the 2D radiographs obtained using X-ray microtomography before the reconstruction algorithm was applied; (b) A greyscale slice of the 3D image; (c) Histogram of the whole 3D image exhibiting the threshold range chosen for the fibre phase; (d) Binarised slice corresponding to the grey slice.

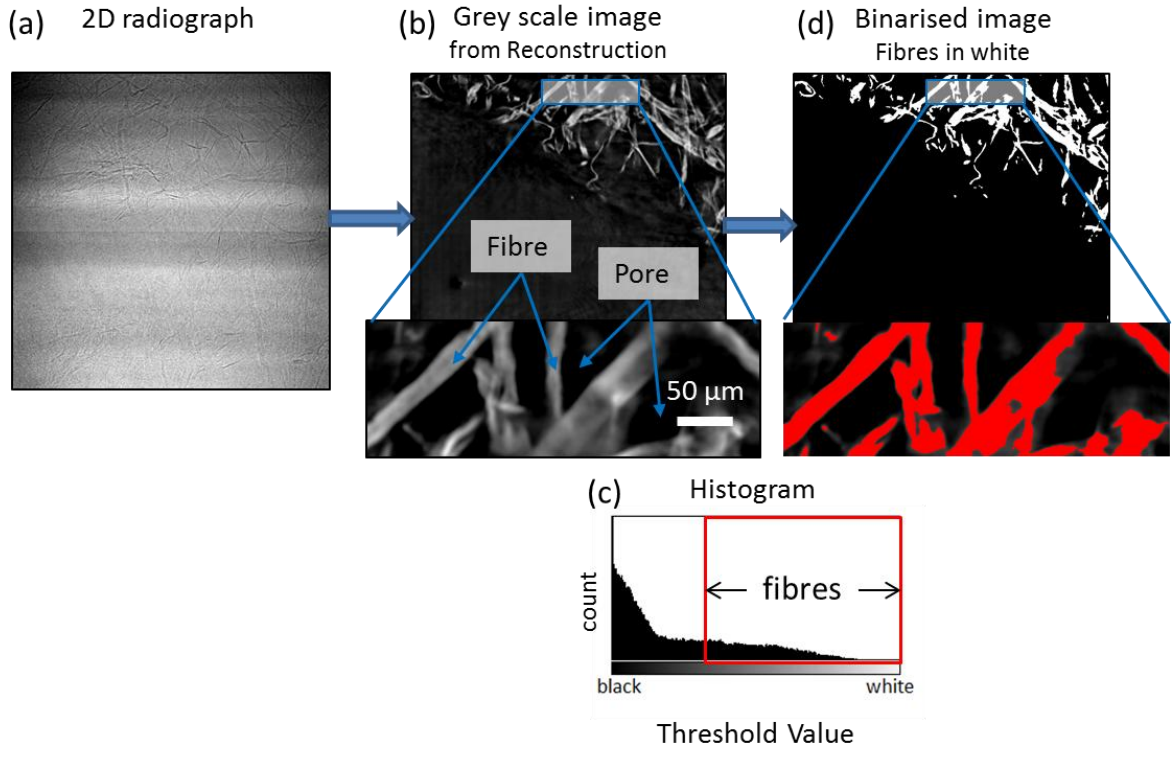

Figure 2-16 : Illustration of the thresholding procedure for the 'mesoscale' images of paper sample (voxel size 0.55 x 0.55 x 0.55 µm^3): a) One of the 2D radiographs obtained using X-ray microtomography before the reconstruction algorithm was applied; (b) A greyscale slice of the 3D image; (c) Histogram of the whole 3D image image exhibiting the threshold range chosen for the fibre phase; (d) Binarised slice corresponding to the grey slice.

2.5.2.4 Ring artefact

Regardless the microtomograph, ring artefacts are systematic intensity distortions that appear in the X-ray images as full or partial rings of a few pixels large in width centred on the rotation axis. The ring artefacts are superimposed on the images as it is shown in example in Figure 2-17 and, thus, may disturb the segmentation of the images. The ring artefacts are caused by pixel errors in the tomographs which appear in the projections as lines along the angular direction. The existing filtering methods allows reducing the ring artefacts before (Tang et al., 2001) as well as after image reconstruction (Axelsson et al., 2006; Lyckegaard et al., 2011). In our work, the high and lower resolution images were treated manually: the ring artefacts and the noise were removed from the binarised images when it was needed.

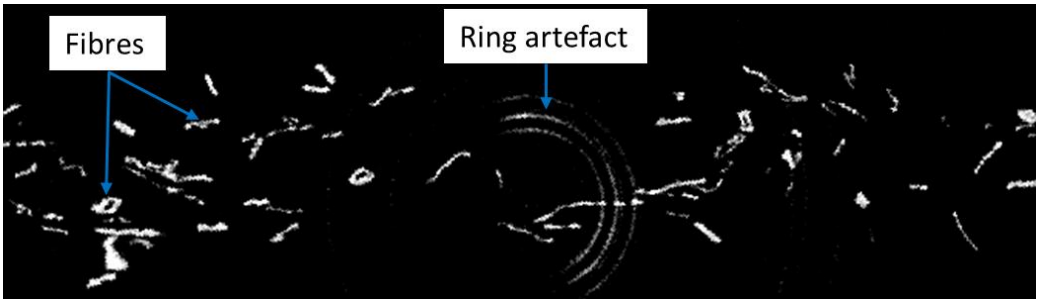

Figure 2-17 : Ring artefact in the greyscale X-ray images of paper network scanned at 1.4 µm of effective voxel size.

2.5.3 Formation characterization

In the particular case of low density papers with a very sparse network, light transmission data can be used to measure mass distribution (Bernie and Douglas, 1996). The areas with variation of light transmission observed in Figure 2-13b correspond to higher mass distribution and lower mass distribution. This section includes the developed original method that allows analysing the effect of local mass distribution on the fracture propagation phenomena in the paper network such as LDP.

2.5.3.1 Image preparation

Images used for this type of analysis were prepared using Fiji® software as following:

- 2D 8-bits greyscale images acquired using transmitted visible light in the optical microscope were adjusted according to the tilt of the samples and to the size of the analysed areas of the samples.
- 3D X-ray images were first binarised and then converted into 2D images called enhanced radiographs using image processing tools such as 'Z project' -> 'Sum slices'. This operation overlays voxels of the fibre phase over each other in thickness direction that allows obtaining 2D greyscale

maps of local mass distribution. The images were converted into 8-bits greyscale images.

2.5.3.2 Two approaches

As work was evolving, two complementary approaches were developed to analyse the local areas such as higher mass distribution areas and lower mass distribution areas in the LDP network. The first approach used in Chapter 4 provides identification of the areas of lower mass distribution named as antiflocs, and the second approach used in Chapters 5 and 6 allows the identification of both types of areas: antiflocs and flocs.

First approach

The image obtained using transmitted visible light in the optical microscope (section 2.5.1) was first binarised using the mean value of grey level of the transmitted image. In this approach we assume that an antifloc is mathematically defined as a connected region of pixels with a lower grey level value than the average grey level value in the entire image. The procedure gave a good visual correspondence between the identified antiflocs and visible low-mass regions in the original image which lends some confidence to the method. The antiflocs areas are shown as ellipses in the transmitted image in Figure 2-18.

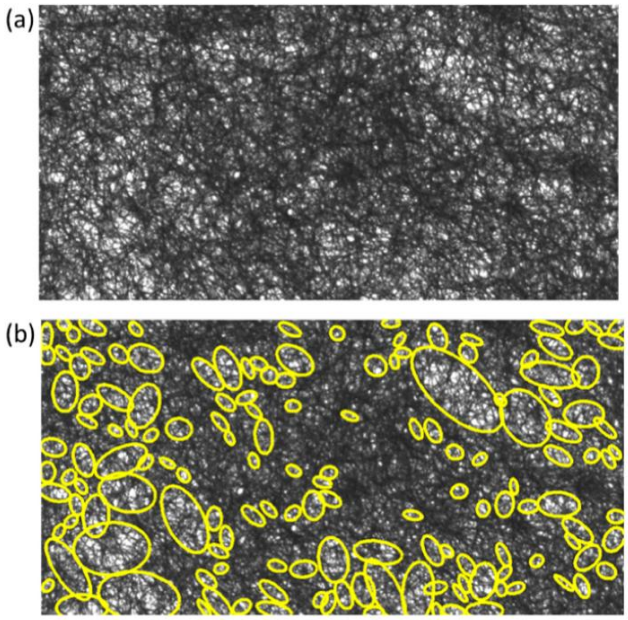

Figure 2-18 : Antifloc detection on a sample of 12 x 6 mm^2: (a) Transmitted light micrograph; (b) Antifloc detection.

Second approach

The second approach was used in order to quantify the positions and the sizes of the flocs and of the antiflocs in two types of 2D images: (i) image acquired using the transmitted light in optical microscope; (ii) enhanced radiograph of X-ray images. An

algorithm was developed using Matlab®. The following procedure was applied to identify flocs (Figure 2-19):

- The considered image is first binarised using a thresholding method.
- This binarised image is then eroded with structural element 'disk' in order to extract the flocs.
- The smaller objects are then removed.

The same procedure was applied on the inverted binarised image to obtain antiflocs (Figure 2-19). In both cases, the obtained areas are identified and are fitted using ellipses. It is obvious that ellipses simplify the shape of the original heterogeneity areas but they provides their centres of mass, locations and their approximate dimensions (major and minor lengths of the ellipse) as well as their orientation. Figure 2-19 illustrates the results obtained with an image taken at a pixel size of 7.3 µm.

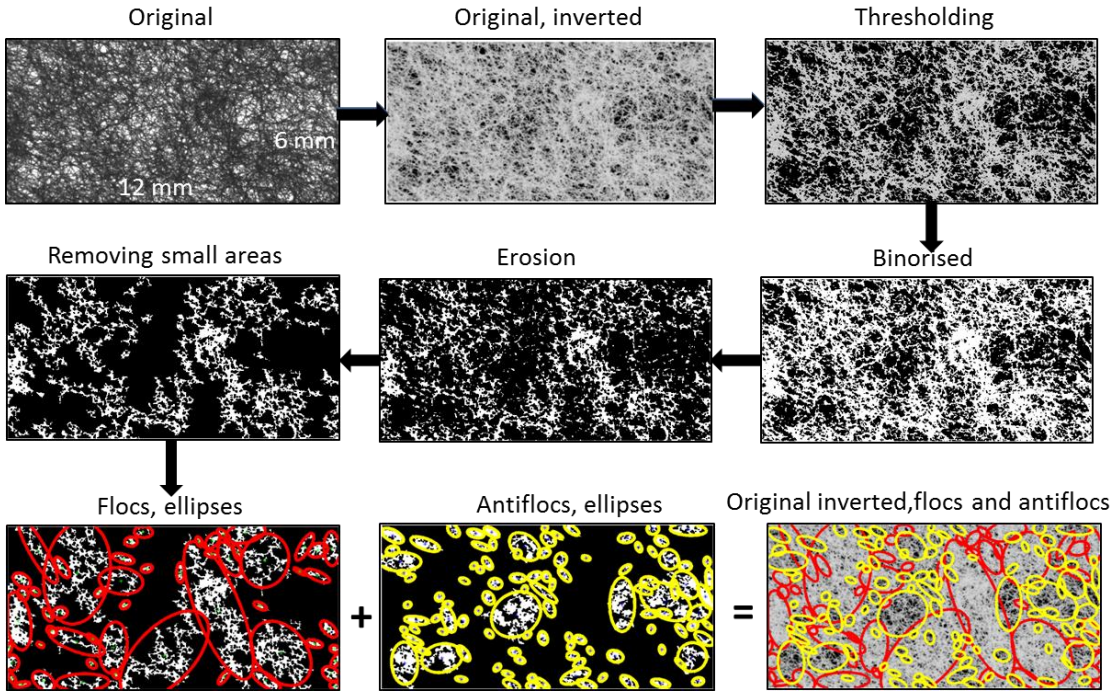

Figure 2-19 : Floc procedure performed using the transmitted image 12 x 6 mm^2. The original image was inverted to show the identified flocs in red and antiflocs in yellow.

The main parameter of the procedure described above is the critical thresholding value. According to a common and simple definition, flocs are the areas with local grammage which is higher than the average one. In our study, the flocs were obtained by thresholding an image with its median grey level value in order to be consistent with the found literature (Jordan, 1986; Laleg and Nguyen, 1995). As it was tested on several images, both median and mean thresholding values give very similar results in flocs and antiflocs identification.

In binarised image (Figure 2-19) the flocs cannot be easily separated. Therefore, we used a common image processing function called erosion that allowed separating

the connected floc areas into individual ones. The binarised images were eroded with structural element 'disk' (radius of 3 pixels) for the transmitted visible light images and 'disk' (radius of 1 pixel) for X-ray enhanced radiographs. Size of the structural element 'disk' was decreased to 1 pixel since the X-ray images contain more detailed information than the images obtained with transmitted light: the zones related the high or low mass distribution in the X-ray image are more distinct.

2.5.3.3 Validation 1: comparison with X-ray radiographs

To validate the procedure described above, we acquired an image of the same paper sample (12 mm x 6 mm) using the microscope in transmitted visible light and the X-ray microtomograph. As the X-ray transmission through a material can be directly related to its local density (see Chapter 1), the enhanced radiograph of the studied sample provides a local map of the mass distribution. Figure 2-20 a and b illustrates the images obtained in visible and in X-ray lights, respectively. Figure 2-20c and d represents the flocs obtained with the procedure described above for both types of images. The images show a good correspondence which ascertained us to use this technique to study the link between the local mass variation and the crack path in both types of images (see Chapter 4, 5 and 6).

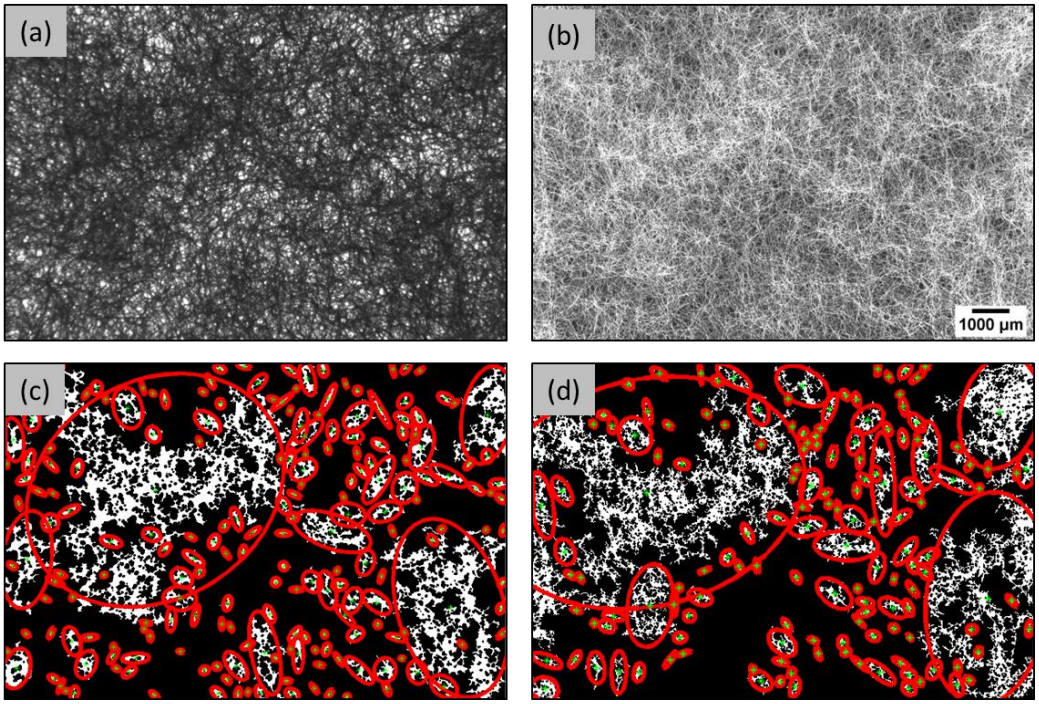

Figure 2-20 : (a) transmitted light micrograph and (b) X-ray radiograph of the same LDP sample; (c) and (d) result of image processing performed on images (a) and (b), respectively. On the row below we are able to distinguish fibre aggregates indicated with ellipses in red, their centroids as well as less dense zones in black.

2.5.3.4 Validation 2: influence of image size on floc identification

The flocs were first identified on a large image acquired at a pixel width of 7.3 µm representing 88 mm x 45 mm. The results are presented in Figure 2-21.

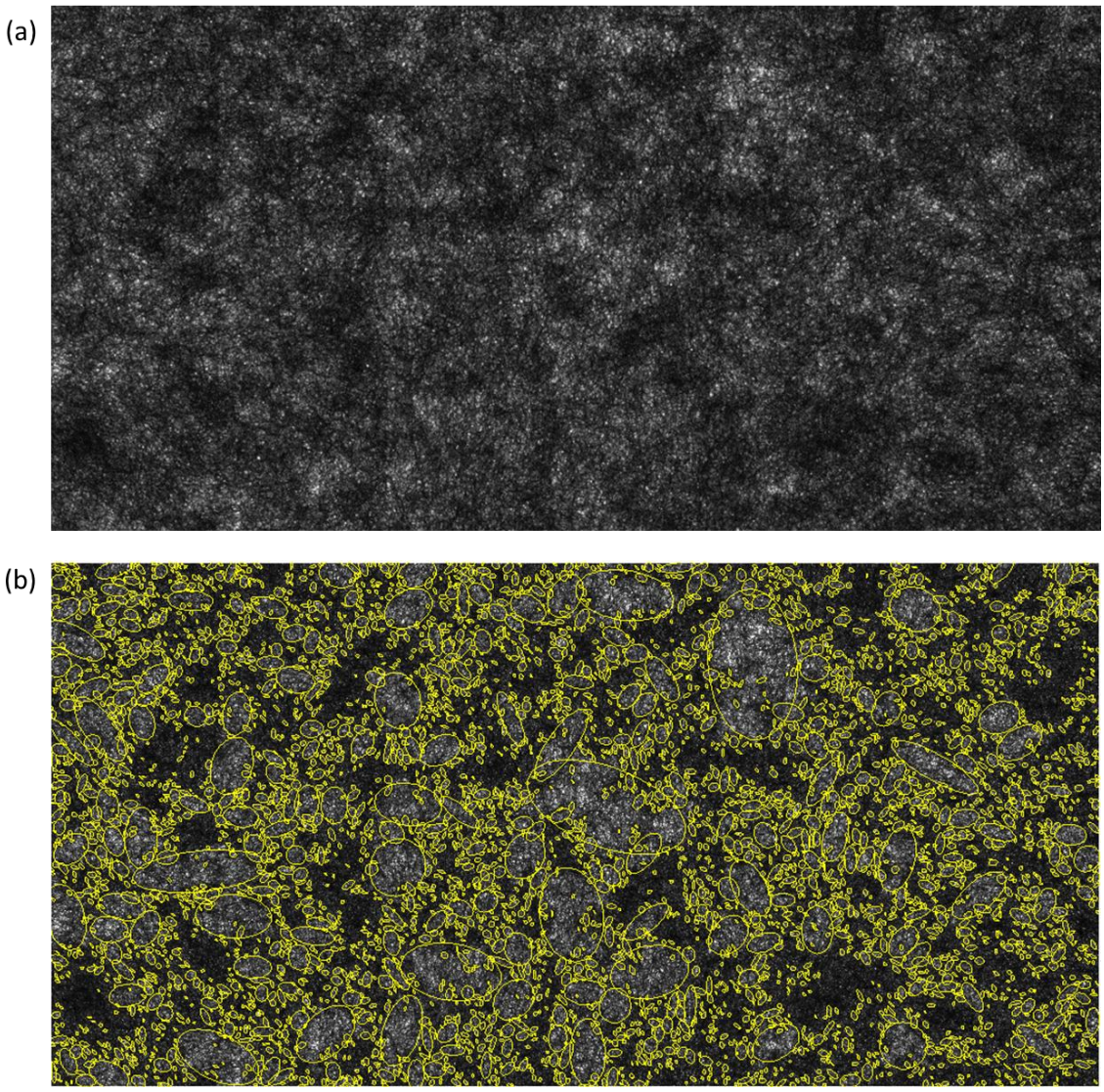

Figure 2-21 : Floc identification using a large image 88 x 45 mm^2.

A part of the original image (Figure 2-22a) representing 12 mm x 6 mm was extracted (Figure 2-22b). The flocs were identified on the large images (Figure 2-22a) and (Figure 2-22c) represents a zoom on the floc identification. The identification of the flocs on the smaller image is presented Figure 2-22d. The visual comparison between both analysis shows that the floc identification is independent on the size of the image. This validates the use of such a procedure on the small image.

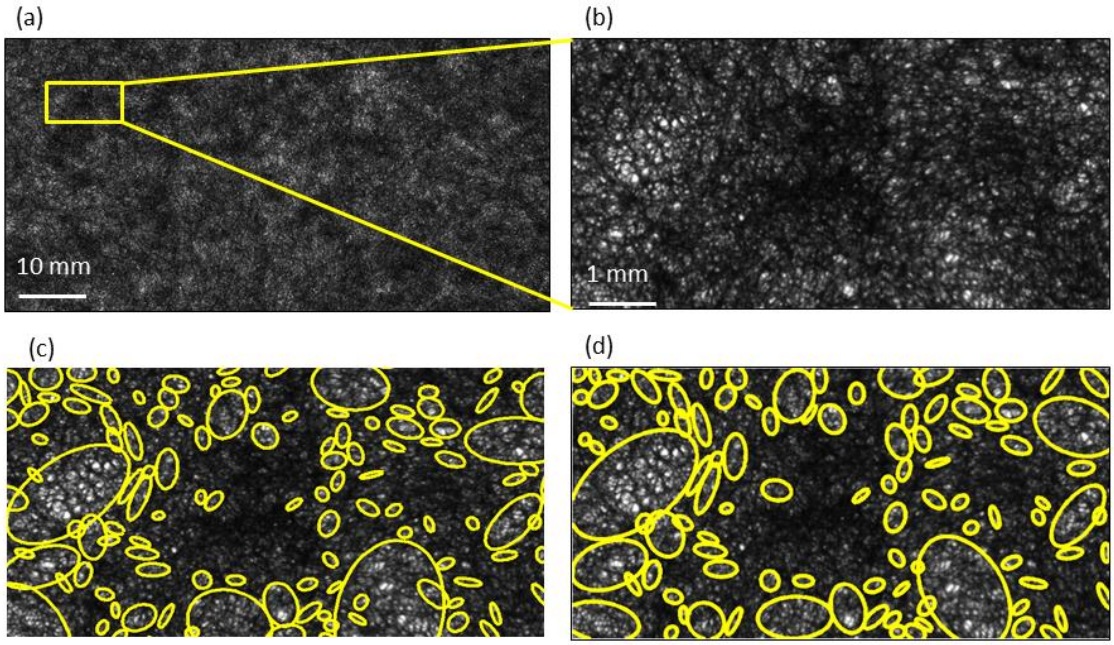

Figure 2-22 : Influence of image size on floc identification (a) original image (b) part extracted (c) zoom on the floc identification obtained on the large image corresponding to the image b (d) floc identification on image (b)

2.5.4 Porosity and thickness measurement based on X-ray images

This method provides a quantitative analysis of the local thickness and porosity variation in thickness direction in paper samples.

2.5.4.1 Preparation of the 3D X-ray datasets

The analysis is performed on the binarised 3D X-ray images (Section 2.5.2). Moreover, the binarised images were cropped in order to remove the clamps from the images. Those images were used to obtain the local thickness and porosity maps using the code developed in Matlab®.

2.5.4.2 Local thickness and porosity procedure

Each 3D dataset is represented as a stack of 2D slices along the thickness (y) direction of the paper sample as it is schematically shown in Figure 2-23(a). A grid with square cells of equal dimensions called Analysis Windows (AW) are applied onto each slice of the stack. This method allows to measure thickness and porosity of the paper samples in thickness direction locally. First, the measurement of local thickness $\tilde{t}$ was performed: in each analysis window AW pixel-by-pixel along y-direction, the two surface boundaries were defined as the first and the last occurrence of the fibre phase (Figure 2-23b). Therefore, the local thickness was calculated as a difference between the two surface boundaries in pixels and in micrometres knowing the pixel size of the image. As a result, we obtained a 2D maps with local thickness variation of the sample. In order to compare the local thickness variation for each loading step

of a sample, every thickness map related to the X-ray image at each loading step was normalized with the mean thickness $< \tilde{t}_1 >$ of all the AW in the first (reference) thickness map of the series: the thickness values in each AW was divided by the value $< \tilde{t}_1 >$.

Afterwards, the porosity maps were created where the local porosity was calculated inside each AW restricted by the obtained surface boundaries identified in the thickness map analysis:

$$\tilde{\Phi} = {}^{N_{pore}}\!/_{(N_{pore} + N_{fibre})}, \tag{2-5}$$

where $\tilde{\Phi}$ is the local porosity of each analysing zone, N_{pore} the total number of pixels in each zone corresponding to the pore phase, N_{fibre} the total number of pixels in each zone corresponding to the fibre phase.

The porosity maps were presented using their absolute values for each AW.

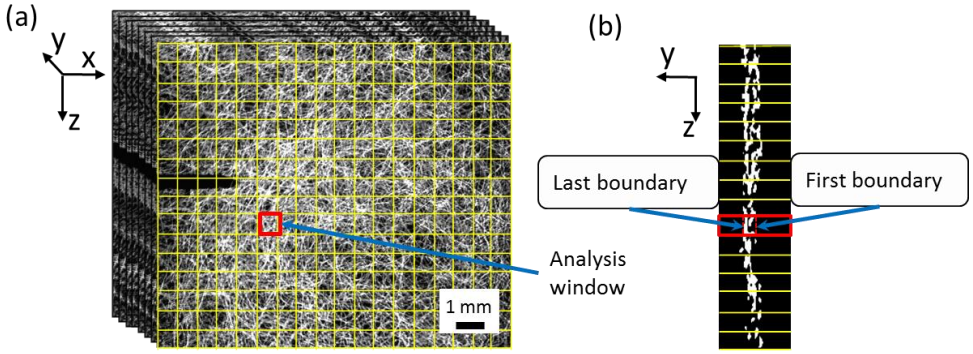

Figure 2-23 : Scheme of local thickness and porosity measurements on a 3D X-ray image using a grid (yellow). Fibres are presented in white and the pores/air in black. (a) The grid (yellow) was applied to each slice XZ of the image in Y direction where the analysis was performed in each analysis window (AW) (example of AW in red); (b) The samples' surfaces (boundaries) were determined in each AW (example in red) in the cross section YZ.

2.5.4.3 Examples of the thickness and porosity maps obtained for paper

Figure 2-24 featuring the local thickness and porosity maps for LDP sample obtained with various sizes of the AW:

a) AW2x2 – size of 2 x 2 pixels, i.e. ~14 x 14 µm^2 (Figure 2-24b and c) illustrates the structural changes in details in both local maps. One can clearly observe the pattern featuring the local thickness increase caused by manufacturing process, i.e. paper sheet transportation on the wire
b) AW10x10 – size of 10 x 10 pixels, i.e. ~70 x 70 µm^2 (Figure 2-24b' and c') give a global quantitative analysis.

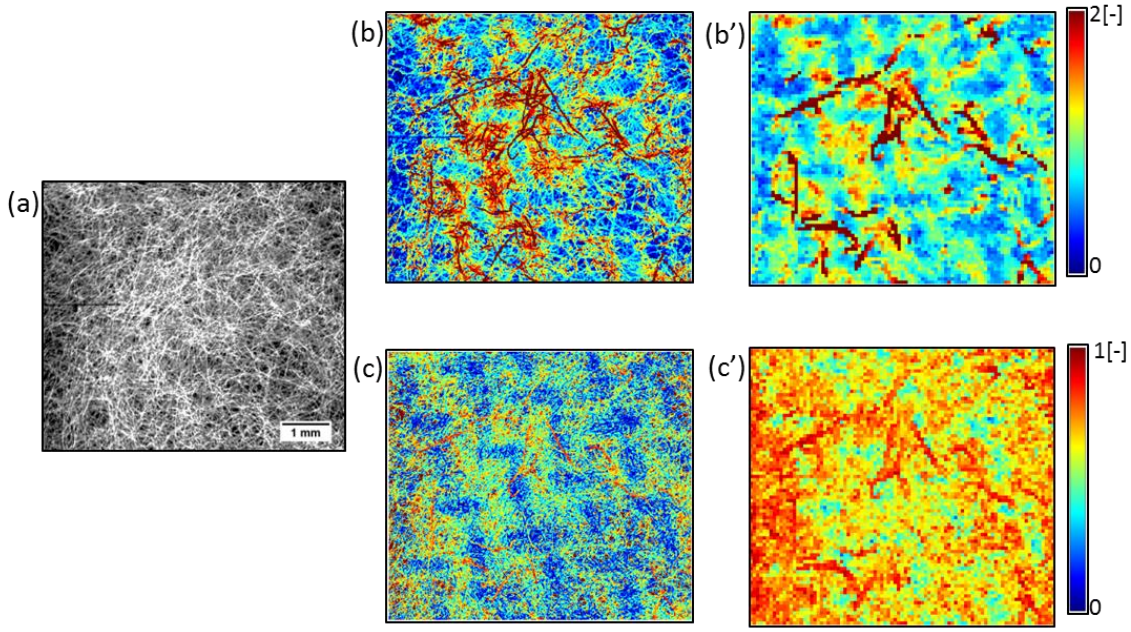

Figure 2-24 : Low density sample analysed with different AW with corresponding: (a) X-ray enhanced radiograph; (b) Local thickness map with AW of 2 x 2 pixels (~14 x 14 µm^2); (b') Local thickness map with AW of 10 x 10 pixels (~70 x 70 µm^2). Both maps were normalised with the mean value of the thickness (140 µm); (c) Local porosity map (AW of 2 x 2 pixels); (c') Local porosity map (AW of 10 x 10 pixels).

2.5.4.4 Choice of the AW dimension

In order to choose the smallest more appropriate size of the AW for quantitative analysis of the porosity, the following approach based on the statistical estimation of Representative Elementary Volume was carried out. Two independent volumes V1 and v2 of size 300 x 300x thickness pixels have been analysed, the pixel size being about 7 µm. In each volume, 15 centre points were defined as the central points of the analysis window. 15 independent subvolumes of size AW x AW x thickness with AW varying from 1 to 19 were extracted. Figure 2-25 represents the evolution of the mean porosity as a function of AW for the two volumes. We can observe that for both volumes, the mean porosity increases and stabilizes whereas the associated standard deviations decrease and stabilize. The transition between both regimes occurs for both samples for AW=9 pixels. Therefore, the AW size of 10 x 10 pixels, that corresponds to ~70 x 70 µm^2, will be chosen for the further local quantitative analysis. This is consistent with the results presented in the literature for images of higher resolution.

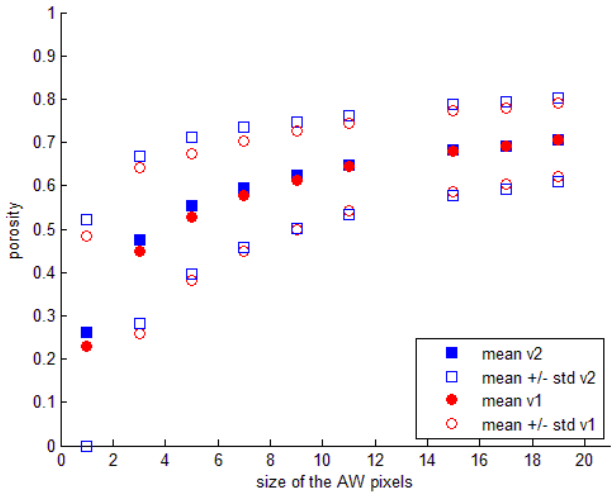

Figure 2-25 : Evolution of mean porosity and the standard deviation vs. different AW for two equal subvolumes v1 and v2.

2.6 Mechanical characterisation using digital image correlation

Digital image correlation is a powerful mathematical tool that can provide full-field measurement of kinematics at the surfaces (2D) as well as within an object (3D) during its deformation (Roux and Hild, 2009; Hall et al., 2010; Viguié et al., 2011). The principle of Digital Image Correlation is to recover the image feature from the first image to the second image from which the displacement can be deduced.

2.6.1 DIC technique used in this study

In this work, Continuum Digital Volume Correlation (DVC) was performed using the python-based code "TomoWarp2" (Tudisco et al., 2015). The TomoWarp2 was successfully used for the geomaterials ((Viggiani et al., 2012), (Tudisco et al., 2015)). It will be the first time the TomoWarp2 code will be used to define the deformation in the paper materials. The principle of the continuum DIC is to define the similarity between two 3D images or parts of images by calculating the normalized correlation coefficient (Hall et al., 2010; Ando, 2013; Khaddour, 2015). The first image is generally referred to as the reference image and the second, acquired after some increment of deformation, as the deformed image.

2.6.2 Input datasets preparation

The result of DVC code is highly affected by the quality of input datasets, i.e. the 3D X-ray images, that should be of sufficient voxel dimension (µm per voxel) and have enough intensity information (grey-levels) contained by each voxels of the image (Hall, 2012). Therefore, in this work, the DVC was performed on the original reconstructed greyscale images that were slightly adjusted according to the following procedure. The original 3D X-ray greyscale images (Table 2-3) were previously

reconstructed and thresholded (Section 2.5.2). Afterwards, the segmented binary images were applied onto the corresponded greyscale images functioning as a mask in order to separate fibre phase from non-constant background value, to decrease noise in the images and to restrict zone of the analysis. Therefore, in the images used for correlation the fibres were represented in greyscale and the rest equalled to zero.

Table 2-3 : X-ray images used as input dataset for DVC and their descriptors

N° chapter	Samples	X-ray µtomography	Voxel size [µm^3]	Dynamic range	Grey-scale levels
5	S1	3SR	6.9 x 6.9 x 6.9	32-bit(float)	2^{32}
6	S5	SLS	6.5 x 6.5 x 6.5	16-bit(integer)	2^{16}

2.6.3 DVC procedure in practice used in this study

The code "TomoWarp2" calculates the displacements in 3D of image points (node) of a regularly spaced grid from reference to the deformed image. The code tracks small "subset" called correlation window, a group of pixels, of the images centred on the grid nodes giving 3D displacement vector mapping for each correlation window. The correlation window is independent of the positions of the fibres. The underlying discrete fibrous structure presented in these images is ignored, that is why this technique is called continuum.

Figure 2-26 schematically presents the DVC methodology that involves the following basis steps:

Parameters:

- Application of a grid of the analysis points (*nodes*) to both of the analysing images as it is shown in 1;
- Definition of a region consisted of a group of pixels centred on each node (*correlation window*). In this work, it is chosen to be roughly the mean width of a fibre of the studied paper in the image.
- Definition of the reduced area of search called *search window* centred on each node in the second image;

Principle:

The Tomowarp2 computes the similarity between two 3D images by calculating the Normalized Cross Correlation (NCC) within each search range. The displacement between two images is measured to the nearest pixel.

$$NCC(u,v,w) = \frac{\sum_{x,y,z} I_1(x,y,z) I_2(x+u,y+v,z+w)}{\sqrt{\sum_{x,y,z} I_1(x,y,z)^2 \sum_{x,y,z} I_2(x+u,y+v,z+w)^2}}, \quad (2\text{-}6)$$

where I_1, I_2 represent the local grey level in the 3D reference and deformed images, respectively; x, y, z are the coordinates in the 3D volume of the images; and u, v, w, denote the integer displacement values along the x, y, z axis of the points of the image I_2 with respect to the corresponding points in the image I_1.

NCC values vary from 0 to 1. The combination of u, v, and w giving the highest NCC value (close to one) are selected as the best match between I_1 and I_2. Since this procedure only allows measuring 3D displacements with an integer precision (to the nearest pixel), the refinements for subpixel was performed by interpolation of NCC (Ando, 2013). The scalar components coming from these measurements (e.g., the displacement, the maximum correlation coefficient, etc) are saved as a 3D matrix. The 3D matrices are turned into 3D images that can be visualized and being measured using the image analysis tools.

Output:

- Definition of the discrete displacement (integer number of pixels) given by the displacement with the best correlation;
- Sub-pixel refinement which allows to obtain more smooth fields (see more in (Hall, 2012) shown in 3;

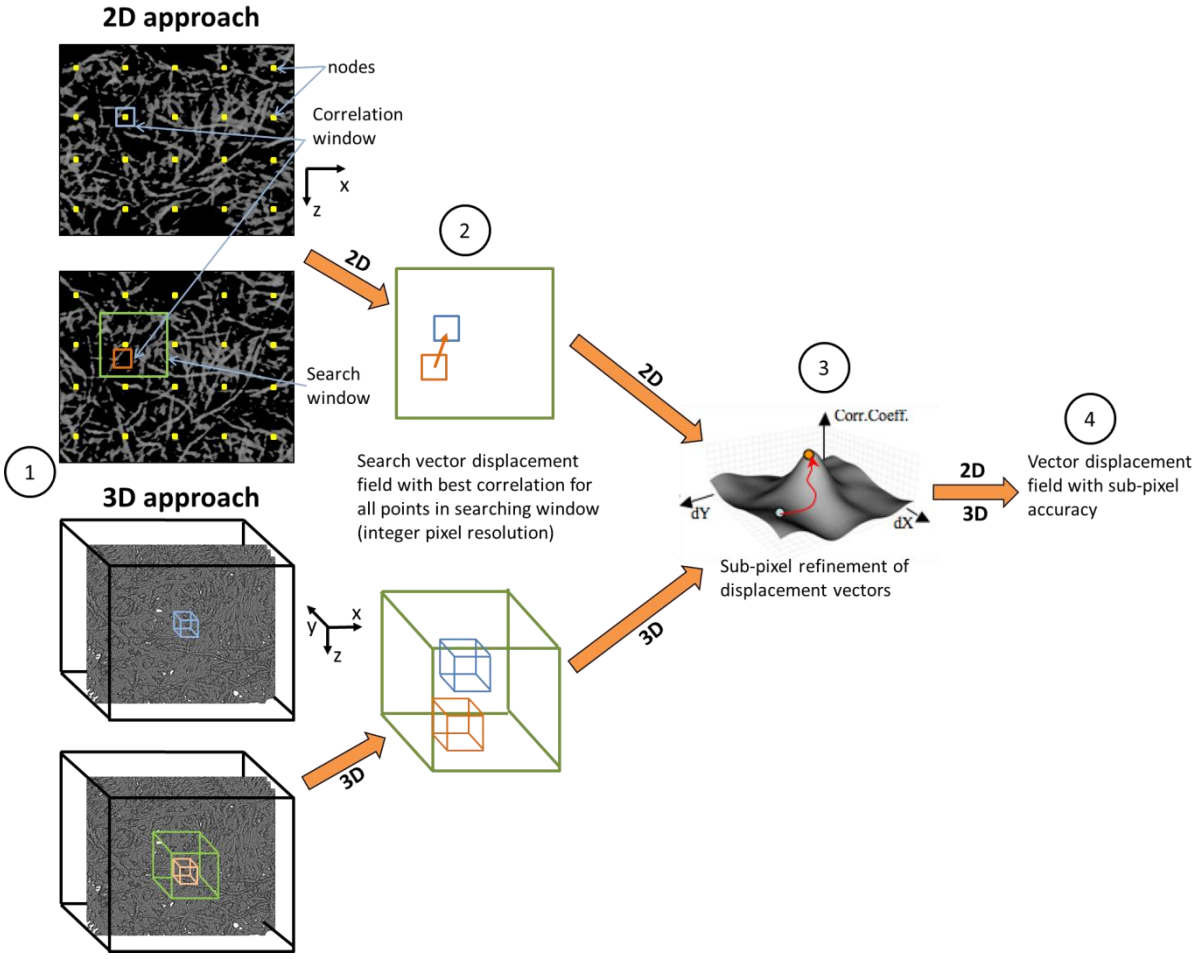

Figure 2-26 : Schematic of 2D (on the one slice of X-ray image of paper) and 3D (on the 3D X-ray image of paper) approach of DIC analysis. The illustration for the third step was taken from (Hall, 2012).

The thickness of the studied paper is small and often the structure is slightly tilted in the images; therefore it was not possible to extract a relevant single slice with required information on deformation. For simpler representation 3D fields are

2D projected through the thickness direction using median values which provide a global overview.

The input and output images are illustrated in Figure 2-27 in the case of paper.

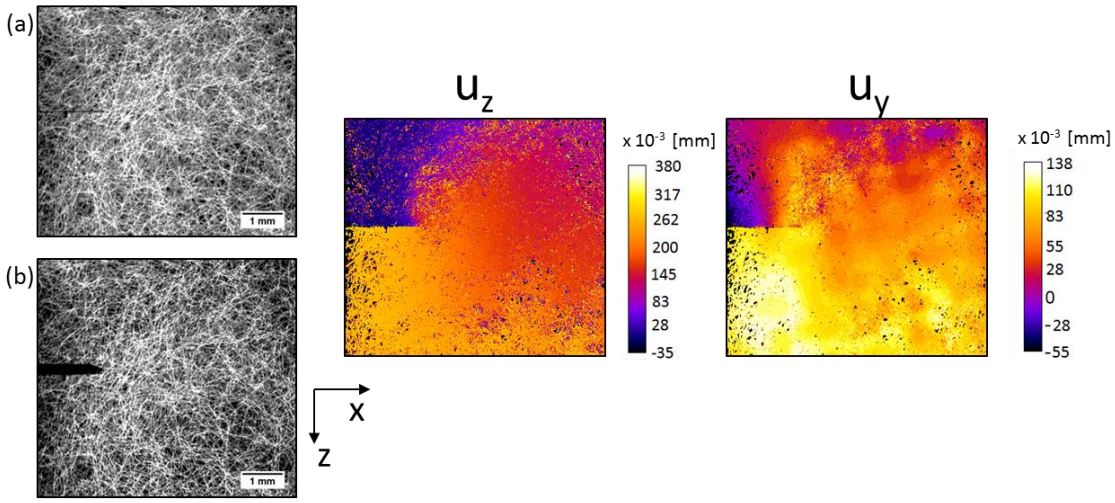

Figure 2-27 : Low density sample loaded in z direction with corresponding: (a) and (b) two X-ray enhanced radiographs and its displacement fields (Uz – in z direction and Uy – in y direction) obtained using Tomowarp2.

2.7 Conclusion

In this chapter, the two types of papers that are investigated within the next chapters are presented and the developed tools were described. The high density paper exhibits a continuous microstructure whereas the low density paper, a discrete one. Mechanical set-ups were designed to investigate the tensile behaviour of both paper under various relative humidities and at microscale, mesoscale and macroscale. To link the macroscopic behaviour of paper with its structure, several imaging procedures have been developed:

- Microscopy was used to quantify the mesoscale structure in a statistical way: localisation of flocs, antiflocs and their structural characteristics
- X-ray microtomography was used to quantify the mesoscale structure, the microstructural parameters such a porosity and thickness, and to visualise the structure at the fibres scales.
- Field measurement can be obtained by digital volume correlation.

All these imaging procedures require the choice of parameters which was discussed.

The following methodology was systematically applied to fulfil experimentally the objectives of the thesis:

i. Macroscopic fracture tests at various relative humidity
ii. Mesostructural analysis by microscopy and image analysis before and after fracture tests

iii. Mesostructural and microstructural monitoring by X-ray imaging during fracture tests under various relative humidity.
iv. Quantification through images analysis procedures and volume correlation of the observed mechanisms.

The two first steps were used in chapter 3 to link the internal length introduced in models to formation. The three last points were used in chapter 4 and 5 to investigate the crack propagation mechanisms for various relative humidity at the mesoscale and microscales.

Chapter 3. Influence of mass distribution in cellulosic fiber materials on the fracture behavior at different moisture conditions

This chapter is based on an article submitted to *International Journal of Solid and Structure*, V. Krasnoshlyk, S. Rolland du Roscoat, P. Dumont, P. Isaksson.

Content

Abstract

The fracture process in two different moisture-sensitive paper materials, a low- and a high-density paper, is studied experimentally and analytically. It is shown that the two papers fracture in a quite different manner. While the high-density paper is smooth and continuous, the low-density paper is substantially discontinuous and has a relative high degree of varying mass distribution. The high-density paper is able to localize fracture to even the smallest defect while a rather large defect is required in the low-density paper to localize fracture. A physical parameter that distinguishes the low-density paper from dense papers is the presence of the clearly observable large variations in the mass distribution, here referred to as antiflocs. It is hypothesized that these antiflocs govern the fracture process. A gradient-enhanced theoretical model is applied to describe and capture this fracture phenomenon and intents to approximate stresses on a subscale. The relatively simple hypothesized fracture theory was remarkably consistent with the experiments and quantitatively captured subscale length-effects in a convenient way. A key observation is that the internal length parameter, used in the hypothesized theory to bridge stresses to a dominant subscale, is linked to the dominant size of large antiflocs present in the material.

3.1 Introduction

The fracture behavior of natural cellulosic fibrous materials such as paper and paper boards has been extensively studied during the past four decades, cf. (Seth and Page, 1974; Niskanen, 1993; Niskanen et al., 2001; Salminen et al., 2003; Isaksson and Hägglund, 2007; Considine et al., 2011; Mäkelä and Fellers, 2012; Hagman and Nygårds, 2012; Coffin et al., 2013). Low-basis-weight paper, commonly referred to as tissue, is widely used on a daily basis for a variety of household needs. Several physical properties distinguish them from printing and packaging papers including tensile response due to a more open network structure offering greater flexibility. Paper essentially consists of a discontinuous stochastic network of cellulose fibers and is usually manufactured by dewatering a fiber-suspension on a wire. The fibers have an inherent capability to form bonds between them without any additives. Since the fibers are much longer than the thickness of the paper sheet, the fiber network is approximately planar. Typically, cellulosic fibers that are used to produce papers are 1-3 mm in length and 20-40 µm in cross-sectional width, depending on their origin (hardwood or softwood fibers) and on the papermaking method (Kaarlo Niskanen, 2012). The porosity of papers ranges from almost 0%, for dense papers, to about 80% for tissue paper materials. Moreover, cellulosic fibers are sensitive to the variations in environmental conditions such as relative humidity and temperature, affecting their dimensions and mechanical properties. As a consequence, the mechanical properties of

papers also depend on their moisture content (Haslach Jr, 2000; Kaarlo Niskanen, 2012).

Several studies have analyzed the defect size sensitivity of different papers, e.g. (Seth and Page, 1974; Hägglund and Isaksson, 2006; Coffin et al., 2013), indicating that classical fracture mechanics theories have severe difficulties capturing the mechanical behavior for low-density paper materials. For high-density papers, a very small defect is sufficient to localize continued crack growth, as foreseen by classical fracture theories. For low-density papers, however, the situation is different because the fracture process seems unaffected by small defects and fracture does not necessary initiate at small defects. Moffatt (Moffat et al., 1973) reported that global fracture passes through regions in the paper having a mass density (or, grammage) below the paper's average. According to experimental and numerical studies, e.g. (Wong et al., 1996; Nazhad et al., 2000), local grammage and local strains are inversely proportional, meaning that high strains occur in regions of relatively low grammage. The mass distribution heterogeneities are often referred to as "flocs" and correspond to fiber aggregates in the network. The measurement of the spatial basis weight variation related to the flocs is hence essential since it may influence the fracture properties. However, estimation of the floc morphology in paper is not an easy task and there is no established standard (Sampson, 2001; Ostoja-Starzewski and Castro, 2003).

Furthermore, when a low-density paper is subject to load on the macroscopic scale, complex deformations arise on the scales below and have to be captured properly, which puts high demands on the spatial resolution of the mechanical model. Linking the stress field on a subscale to a stress field on the scale above is mathematically difficult, especially if the subscale stress is nonhomogeneous and gradients are present, such as in the vicinity of macroscopic singularities at crack tips, randomly positioned defects, pores, or regions of low mass-distributions (and even more so if they are randomly positioned). The wide range of length scales affecting deformation and fracture in low-density papers poses a difficult modeling problem because the relation between the discontinuous microstructure and the prevailing deformation/fracture processes leads to inherent size effects. Hence, if one aims at a material description above the scale of a discrete discontinuous substructure, i.e. within a macroscopic continuum model, it is clear that any fracture model of such materials has to capture length-scale effects occurring at dominating subscales. One way to numerically analyze these fracture phenomena is to use high-resolved numerical models that capture details in the microstructure. Another possibly way is to use e.g. so-called gradient-enhanced continuum models to incorporate length scales analysis (Kröner, 1967; Isaksson and Hägglund, 2009; Askes and Aifantis, 2011; Aifantis, 2011a; Isaksson and Hägglund, 2013b). The later way is exploited in this study. To investigate dominating length scales and connect them to

paper-specific features, the fracture localization behavior of a low-density paper at various moisture conditions is examined. Different crack/defect sizes are evaluated in single edge notch experiments to reveal when a localization transition occur, i.e. at which defect size the global final fracture is localized to the defect rather than nucleated at a remote distance from the defect. This transition length will possibly allow for judging the predominate subscale at fracture.

3.2 Theory

How does a low-density paper's microstructure affect its global fracture behavior? In recent investigations by the authors (Hägglund and Isaksson, 2006; Isaksson and Hägglund, 2009; Isaksson and Hägglund, 2013b), it is concluded that classical continuum mechanical descriptions of low-density papers cannot fully describe deformations near a macroscopic crack mainly because some subscale structural effects alters the local strain and stress fields in the inhomogeneous discontinuous material. Traditionally, deformation and fracture analysis of paper materials were performed using classical continuum theories on the macroscale omitting that these theories were designed to describe deformation phenomena that could be captured by the naked eye, cf. (Seth and Page, 1974; Yuhara and Kortschot, 1993). However, in low-density papers where regions of relatively low mass are relatively large compared to a defect or a crack, global scale deformation fields given by classical continuum mechanics theories are distorted due to the complex deformations taking place at subscales, a phenomenon that is commonly referred to as length effects. Linking the strain/stress fields on a subscale to the strain/stress fields on a scale above is mathematically difficult, especially if the subscale deformation is nonhomogeneous and gradients are present. Several techniques have over the years been suggested to extend traditional continuum formulations to include so-called material-characteristic lengths. A convenient approach is to compute an approximated averaged subscale stress tensor $\bar{\sigma}_{ij}$ in a point (x_1, x_2) as the weighted average of local macroscopic stresses σ_{ij} in a surrounding domain Ω, cf. (Hägglund and Isaksson, 2006; Askes and Aifantis, 2011; Aifantis, 2014)

$$\bar{\sigma}_{ij}(x_1, x_2) = \Upsilon^{-1} \int_{\Omega} f(r)\sigma_{ij}(x_1', x_2')\, d\Omega(x_1', x_2') \;,\; \Upsilon = \int_{\Omega} f(r)\, d\Omega, \tag{3-1}$$

where r is the distance between points (x_1, x_2) and (x_1', x_2'), $f = \exp[-r^2/(4c^2)]/[4\pi c^2]$ is a symmetric interaction kernel and Υ a scaling factor that secure that the two stress tensors are equal for a homogeneous stress state in Ω (i.e. when no gradients in σ_{ij} are present). The range of subscale interactions is given by an internal subscale length c. The formulation (3-1) is based on a physical assumption of mechanical interactions on a subscale via e.g. connected fibers. The

stress $\sigma_{ij}(x_1', x_2')$ can for sufficiently smooth fields be rewritten into a gradient formulation around (x_1, x_2) according to a Taylor expansion,

$$\sigma_{ij}(x_1', x_2') = \sum_{k=0}^{n} \sum_{l=0}^{n} \frac{(x_1' - x_1)^k (x_2' - x_2)^l}{k!\,l!} \frac{\partial^k \partial^l \sigma_{ij}(x_1, x_2)}{\partial x_1^k \partial x_2^l}, \tag{3-2}$$

where n denotes the order of the series expansion. Dropping unsymmetrical terms in (3-2), yields after substitution of (3-2) into (3-1),

$$\bar{\sigma}_{ij}(x_1, x_2) = \sigma_{ij}(x_1, x_2) + \frac{1}{m!} c^{2m} \nabla^{2m} \sigma_{ij}(x_1, x_2) + \ldots, \quad m = 1, 2, \ldots \tag{3-3}$$

Further, taking the Laplacian of (3-3), subtract from the original (3-3), and neglect derivatives of the forth order and higher, an implicit gradient formulation is obtained in a form of a modified Helmholtz equation, cf. (Eringen and Edelen, 1972; Askes and Aifantis, 2011; Aifantis, 2011a):

$$\bar{\sigma}_{ij} - c^2 \nabla^2 \bar{\sigma}_{ij} = \sigma_{ij}, \tag{3-4}$$

where the dependence of the coordinates has been dropped. It would be possible to extend (3-3) to include anisotropic gradient-sensitive lengths, cf. (Aifantis, 2014). However, for simplicity, assume a low-density paper can be considered transversely isotropic on the macroscopic scale, despite the fact that many low-density papers may be strongly anisotropic. As will be discussed later, the studied paper is nearly isotropic and substantially simplifies matters. Assume further that the paper is linearly elastic on the macroscopic scale and a state of plane stress prevails. Then, consider a planar body containing a straight stationary crack, as illustrated in Figure 3-1.

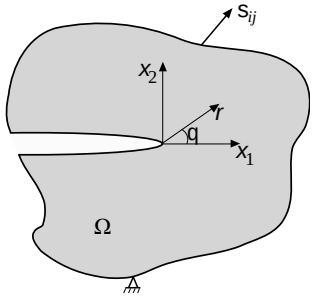

Figure 3-1 : Load and geometry on macroscopic scale.

A Cartesian (x_1, x_2) and a polar coordinate system $(r = [x_1^2 + x_2^2]^{1/2}$, $\theta = \tan^{-1}[x_2 / x_1])$ are introduced with their origins coinciding with the crack-tip. The crack occupies the negative part of the x_1-axis, i.e. $x_1 < 0$ and $x_2 = 0$. Distant from the crack-tip a pure mode I opening field acts and the singular macroscopic stress tensor σ_{ij} is given by:

$$\sigma_{ij} = K_I [2\pi r]^{-1/2} f_{ij}(\theta) \ \text{as} \ r \to \infty, \ i, j = 1, 2, \tag{3-5}$$

where K_{I} is the mode I stress intensity factor (Williams, 1956). The displacement field u_i producing the macroscopic stress field in (3-1) is given by

$$u_i = (1+\nu)K_{\mathrm{I}}[r/(8\pi)]^{1/2} g_i(\theta)/E \ \text{ as } r \to \infty, \tag{3-6}$$

where E is the Young's modulus and ν is the Poisson's ratio. The angular functions $f_{ij}(\theta)$ and $g_i(\theta)$ in (3-5) and (3-6) are found in every book on fracture mechanics. Using (3-4), a mode I gradient-enhanced stress tensor that aim to approximate subscale stresses is computed using the macroscopic stress tensors (3-5) as source terms, i.e.

$$\bar{\sigma}_{ij} - c^2\nabla^2\bar{\sigma}_{ij} = K_{\mathrm{I}}[2\pi r]^{-1/2} f_{ij}(\theta). \tag{3-7}$$

In addition to conditions of traction-free crack surfaces, requirement of finite subscale stresses when $r \to 0$ and $\bar{\sigma}_{ij} \to \sigma_{ij}$ when $r/c \to \infty$ leads to the following expression of the subscale stress component $\bar{\sigma}_{\theta\theta}$ when solving (3-7), cf. (Aifantis, 2011a; Isaksson and Hägglund, 2013b):

$$\bar{\sigma}_{\theta\theta} = \frac{K_{\mathrm{I}}\cos\frac{\theta}{2}}{4\sqrt{2\pi r}}\left[2(1+\cos\theta) + 6c^2/r^2 - \mathrm{e}^{-r/c}[6c^2(1+r/c)/r^2 + 2\cos\theta + 5\right] \tag{3-8}$$

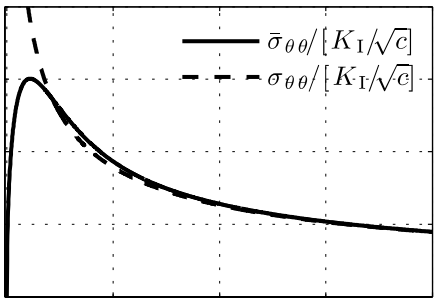

Figure 3-2 : The approximated subscale stress $\bar{\sigma}_{\theta\theta}$, given by (3-8), ahead of the tip contrasted with the macroscopic singular stress $\sigma_{\theta\theta}$ (3-5). The two stresses are similar for about $r/c > 2$.

According to (3-8), the maximum $\bar{\sigma}_{\theta\theta} = K_{\mathrm{I}}[5/2 - 19\mathrm{e}^{-1}/4]/\sqrt{2\pi c} \approx 0.300 K_{\mathrm{I}}/\sqrt{c}$ and is situated on the crack plane at $r/c \approx 1.1$, Figure 3-2. One may notice that the two stresses $\sigma_{\theta\theta}$ and $\bar{\sigma}_{\theta\theta}$ are similar at roughly $r > 2c$ illustrating the important feature that the approximated subscale stress field differs from the macroscopic stress only around mathematical singularities. Hypothesize that cohesive fracture initiates when a subscale hoop-stress $\bar{\sigma}_{\theta\theta}$ reaches a critical level σ_{c}. A natural interpretation of this criterion is to relate it to the macroscopic fracture toughness K_{Ic} through the relation ($\bar{\sigma}_{\theta\theta} = \sigma_{\mathrm{c}}$)

$$K_{\mathrm{Ic}} = \frac{\sigma_{\mathrm{c}}\sqrt{c}}{0.3}, \tag{3-9}$$

which allow for estimations of the length c in standard fracture tests. A deeper discussion of gradient theories and the physical arguments leading to them is found in e.g. (Gitman et al., 2010; Askes and Aifantis, 2011; Hutchinson, 2012; Aifantis, 2014). It is underlined that the approximated subscale stress $\bar{\sigma}_{ij}$ should not be considered as a standard stress field. When one carefully examines the solutions to (3-7) one find that in general the gradient-enhanced stress field is not divergence-free, nor does the work conjugate strain fields satisfy classical compatibility equations in continuum mechanics. For discontinuous materials the classical compatibility equations may, however, not be sufficient to guarantee that subscale strains/stresses can be obtained from single-valued displacement fields. Nevertheless, the physical meaning of divergence in the subscale stress field (and hence not have traditional stress equilibrium) is not entirely understood and has lent some criticism. To some degree we agree with this criticism and the theory may thus be questioned. An interested reader is advised to e.g. (Aifantis, 2014) for a discussion on this matter. The gradient-enhanced stress field should thus be interpreted so that it approximates subscale stresses emerging from displacement jumps at a discontinuous subscale. Even though the meaning of the physical peculiarity $\bar{\sigma}_{ji,j} \neq 0$ is still an open scientific question, the concept has proven powerful and the solutions include lengths that seemingly capture a dominating subscale's heterogenic structure. Although the theory needs further investigations and deeper physical understanding to be convincing it is worth mentioning that a substantial amount of studies during the last decades have identified the need to e.g. include size-dependent strengthening/hardening associated with e.g. nonlinear deformations involving strain gradients and many different theories have been proposed. It is nowadays generally accepted that nonlinear (e.g. plasticity) theories must be higher order, not only by incorporation strain gradients but also in having higher order stresses that are work conjugate to the strain gradients, cf. (Hutchinson, 2012; Aifantis, 2014; Askes and Susmel, 2015).

3.3 Experimental

3.3.1 Materials and sample preparation

Two different kinds of papers were studied: a low-density paper (LDP) and a high-density paper (HDP). Figure 3-3 shows micrographs that were recorded in transmission mode on both papers, using an optical microscope equipped with a camera (pixel size 7.3×7.3 µm^2). For the LDP, the darker areas corresponded to zones that are denser compared to the rest of the sample due to high variation in mass distribution. The HDP had a low opacity, thus, the light was homogeneously transmitted through the sample and the black dots correspond to the paper's roughness (i.e. the HDP have a negligible variation in mass distribution).

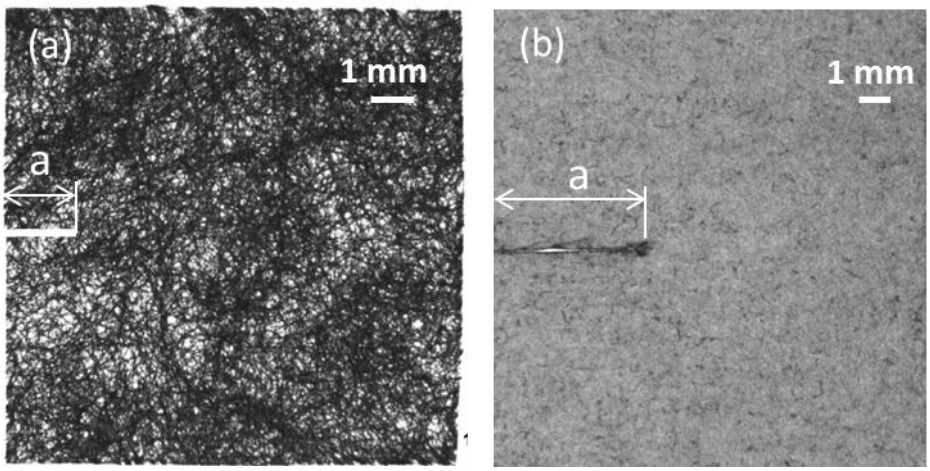

Figure 3-3 : Optical micrographs of the LDP (a) and the HDP (b). A manufactured notch of length a is present in both samples.

The LDP was manufactured at a low speed by "air-drying", resulting in a sparse fiber network. It was made from bleached unbeaten softwood chemical pulp to a basis weight of 23 g/m^2, a thickness of 113±7 µm and a porosity of 86%. The average arithmetic fiber length was 1.4 mm, the average length-weighted fiber length 2.1 mm, while the average fiber width was 31.7 µm, all values measured using a specially designed device for the analysis of pulp morphology (Techpap®, Grenoble).

Papers normally exhibit anisotropic in-plane and out-of-plane structural and mechanical properties which are directly related to the papermaking processs. The main directions of anisotropy are referred to as the machine direction (MD), the cross direction (CD) and the out-of-plane direction (Z). The in-plane mechanical anisotropy of the LDP, here defined as the ratio between the Young's moduli measured in the MD and CD directions, was 1.2 meaning the material is almost transversely isotropic on a global scale. The HDP consisted of highly fibrillated fibers. This paper had a grammage of 47 g/m^2, a thickness of 44±1 µm, and had a bulk porosity that was below 1% leading to a continuous microstructure. The anisotropy of the tracing paper was 1.8. In order to ensure repeatability, all the samples were cut in a rectangular shape (to a width of 45 mm and a height of 130 mm.) in the machine direction using a cutting machine. A notch with length a, which varied from 0 to 23 mm, was cut at one edge at the midheight of the samples.

3.3.2 Moisture content measurements

Using a Varimass device (Techpap, Grenoble), both papers were subject to the following relative humidity in sequential steps: RH= 10% → 20% → 30%→ 40% →50% → 60% → 70% → 80% → 85% → 80% → 70% → 60% →50% → 40% → 30% → 20% → 10%. At each step the samples were hold during 2 hours at a temperature 24.5°C to make sure that the moisture content were stabilized. Additionally, the mass of the samples was regularly measured. Then the moisture content MC were estimated using the relation MC=$\Delta m/m_d$ where Δm is the difference between the

mass of moistened samples in the Varimass device and m_d is a reference mass of the sample after drying in an oven for 24 hours at 105°C.

3.3.3 Tensile tests with controlled environmental conditions

Tensile tests were performed using a standard laboratory tensile machine (2580-108, Static Load Cell, INSTRON®, Norwood, MA) equipped with a 5 kN load cell. The measurements were conducted in a climatic chamber (Figure 3-4a) at a controlled temperature of 24.5°C and a relative humidity of the surrounding air of 10%, 50% and 85%. All the samples were preliminary stored in the chamber for 1 hour prior to testing. The initial distance h between the clamps was 100 mm (Figure 3-4b). Five samples of each paper material were tested at each notch length at a speed of 1 mm/min.

Figure 3-4c shows a typical force-displacement curve obtained for the LDP. Initially, the force increased linearly with the applied displacement (stage 1). Then, the global force deviated from linearity, possibly due to plasticity and microfracture nucleation (stage 2). When the global peak-force $F_{max}$was reached, the crack started to propagate (stage 3).

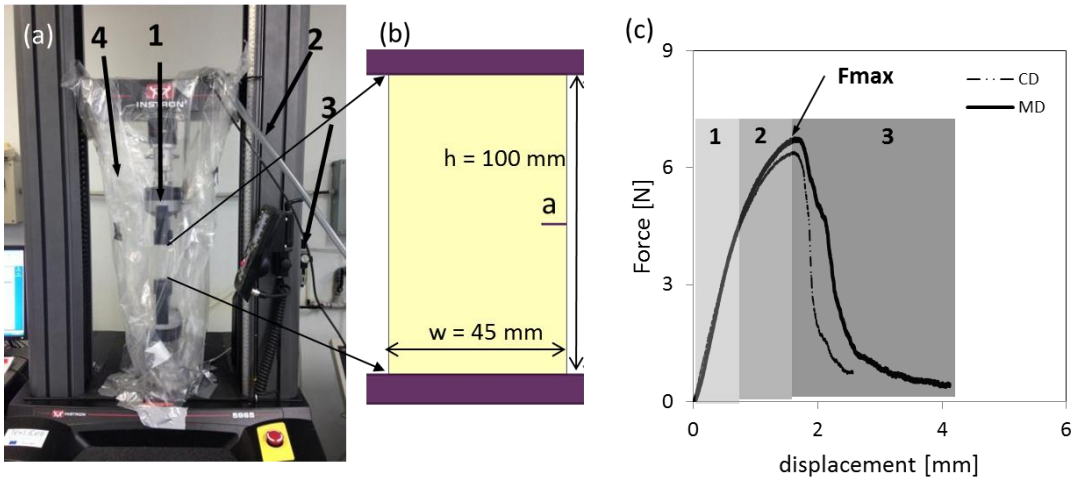

Figure 3-4 : (a) Setup for the tensile test regulated in humidity and temperature: 1 – clamps, 2 – tube from humidity generator, 3 – cable for the humidity sensor, 4 – humidity chamber; (c) Force vs. displacement for a LDP sample without notch in MD and CD.

3.3.4 Mass distribution

A microscope in transmission (ZEISS, Discovery.V20, Germany) equipped with a CCD camera (ZEISS AxioCam ICc5, Germany) was used to measure the mass distribution of the LDP (Komppa, 1988; Sampson, 2001). When a single cellulosic fibre is illuminated by visible light, part of the light is reflected by the surface of the fibre, another part is absorbed by the fibre and the rest is transmitted by the fibre. The amount of transmitted, reflected and absorbed light depends on the incident angle of the light. Considering the fact that paper is a porous assembly of fibres, all the phenomena describe above happen to all the fibres. It means that paper under

light shows: specular reflexion, scattered reflexion at the surface, scattered absorption, refraction, transmission. On images of paper obtained in an optical microscope using visible light, we can observe the light transmitted through the sample. For example, Komppa (Komppa, 1988) showed that the relationship between local light transmission and local grammage is approximately linear for highly scattering papers such as LDP.

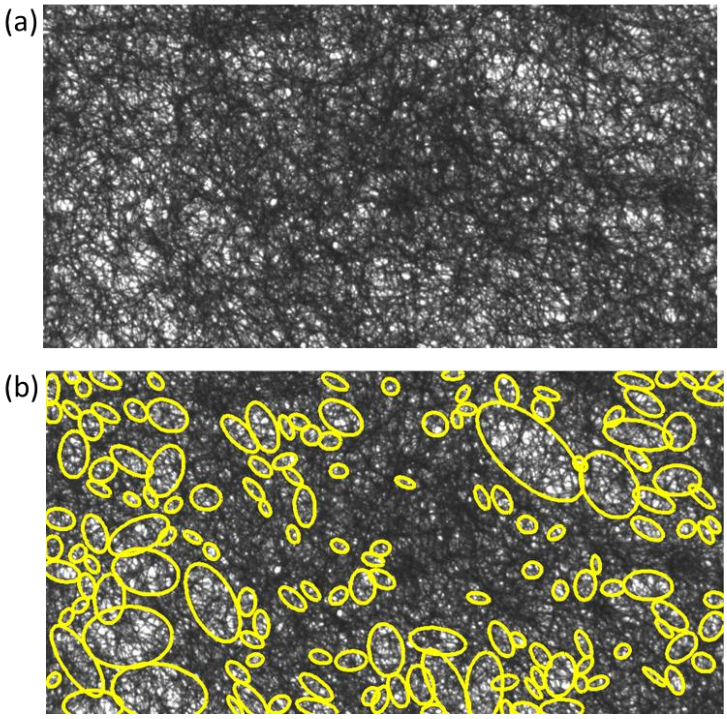

Figure 3-5 : Antifloc identification procedure on a sample of 6 × 12 mm^2: (a) Transmitted light micrograph. (b) Antifloc identification

A LDP sample of 88 × 62 mm^2 was prepared following the preparation procedure described above. Then, an optical image was first binarized using the mean value of the transmitted image, because an antifloc is here mathematically defined as a connected region of pixels with a lower grey level value than the average grey level value in the entire image. To quantify the regions (position, size) of relatively low mass distribution (antiflocs), a Matlab algorithm, detailed in the Appendix, based on the function regionprops, was applied to identify regions of connected pixels. The procedure gave a good visual correspondence between the identified antifloc and the visible low-mass regions in the original image, Figure 3-5, which lends some confidence to the method.

3.4 Experimental results

3.4.1 The moisture content MC vs. RH

Figure 3-6a shows the moisture content MC as a function of relative humidity RH. When RH varied from 10% to 85%, the moisture content increased from 6% to 17%

for the LDP, whereas, when RH varied from 20% to 80%, the moisture content ranged from 3% to 11% for the HDP. In both papers, the moisture sorption and desorption curves exhibited hysteresis. In desorption, the moisture content MC was higher at a given RH than in absorption, showing a classical dependence of the moisture content on both the relative air humidity and the moisture content history (Kaarlo Niskanen, 2012). In addition, the difference in the moisture content of both papers could be related to the difference in the chemical composition of the used raw pulps.

3.4.2 The Young's modulus E vs. the moisture content MC

Figure 3-6b shows the Young's modulus E in the MD for both the LDP and the HDP as a function of the relative humidity RH. Samples without notches were used for these experiments. Both papers exhibited a similar behavior. At low values of relative humidity the Young's modulus were fairly constant in both papers, while at higher relative humidity than about 50%, the modulus decreased. This behavior is well-known for papers. It is reported in (Alava and Niskanen, 2006) that water disrupts hydrogen bonds of cellulose and other polysaccharides of pulp fibers. Besides, not only the interfiber bonds become weaker as the moisture content increases, but also (if present) the matrix made of lignin and hemicelluloses between cellulose crystalline regions softens.

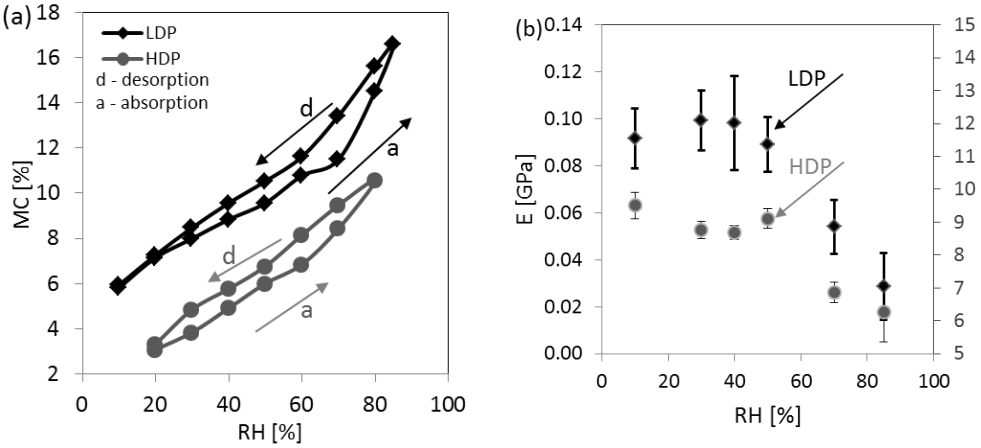

Figure 3-6 : The moisture content (a) and Young's modulus (b) in the LDP and the HDP vs. the relative humidity RH.

3.4.3 Fracture behavior vs. the moisture content MC

Figure 3-7 shows the average global peak-force $\langle F_{\max} \rangle$ estimated at various notch lengths a for the two papers and three different levels of relative humidity.

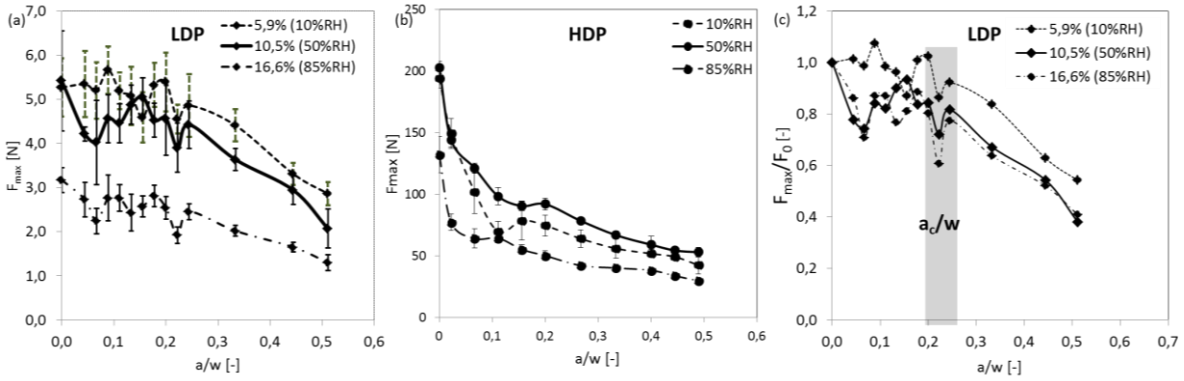

Figure 3-7 : The average global peak-force $\langle F_{max} \rangle$ estimated at various notch lengths a for the LDP (a) and the HDP (b). The notch lengths are normalized with the width of the sample, $w = 45$ mm, and the standard deviation is indicated by the error-bars. (c) The average peak-force $\langle F_{max} \rangle$ normalized with$\langle F_0 \rangle$, the value of $\langle F_{max} \rangle$ at $a = 0$. A critical transition length a_c is indicated, i.e. the notch length $a = a_c$ at which the global fracture load starts to decrease (confidence interval estimated in grey).

The results in Figure 3-7 illustrate that the average global fracture force $\langle F_{max} \rangle$ was quite stable at notch lengths a smaller than roughly 9 mm (i.e. $\frac{a}{w} < 0.2$) for the LDP, even though it slightly fluctuates. For larger notch lengths, however, the global fracture force displayed a clear decrease. The behavior is similar at all investigated relative air humidities (10%, 50% and 85%). Thus, a critical transition length a_c for the LDP is estimated to $a_c \approx 9$ mm. Note also that this length was independent of the relative humidity, showing that it depends on the material structure. For notch lengths lower than this critical length, the fracture initiated at random positions in the paper sample. However, at notch lengths larger than the critical length, the fractures were always localized to the notch tip. This fracture behavior is coherent with previously reported results, cf. (Hägglund and Isaksson, 2006; Coffin et al., 2013). In addition, at both 10% and 50% RH the average global fracture force $\langle F_{max} \rangle$ was about 5 N. However, at higher RH of 85% the fracture force $\langle F_{max} \rangle$ was substantially lower, about 2.5 N. Hence, the global fracture load typically followed the moisture-behavior of the Young's modulus (Figure 3-6).

For the HDP, the results in Figure 3-7 shows that in contradiction to the LDP, the global fracture force $\langle F_{max} \rangle$ decreased with an increase of notch length at all tested humidity levels while the fracture was always localized to the notch tip. This result is similar to the observations by e.g. (Mäkelä and Fellers, 2012; Coffin et al., 2013) and is typical of high-density papers, meaning that the HDP can be considered a continuous material and described by classical theories in fracture mechanics. Also for the HDP one observe that the fracture load typically follows the moisture-behavior of the Young's modulus (Figure 3-6). Importantly, in contrast to the LDP, one cannot identify a critical transition length a_c.

3.5 Analysis and discussion

3.5.1 Distribution of mass

The regions of relatively low mass distribution, i.e. antiflocs, were analyzed with a Matlab code (Appendix). In some way antiflocs may be seen as "semi-pores" in the sense that they have a lower load-carrying capacity than the average of the paper. In the limit when an antifloc's mass distribution tends to zero, the antifloc rather may be regarded as a hole. Hence, the size and the distribution of the antiflocs are useful parameters to characterize the heterogeneity of low-density papers. Figure 3-8 shows the largest antiflocs detected by the algorithm applied on the light transmitted optical image of a LDP of size 88 × 62 mm^2. The antiflocs are mathematically defined as isolated connected regions of pixels with a lower grey level value than the average grey level value in the whole image while the size of an antifloc is defined as the maximum distance between connected pixels in the antifloc. The relatively large antiflocs evenly distributed over the whole domain/image, as one may observe in Figure 3-8b. Figure 3-9a shows a histogram over the sizes of these 150 largest antiflocs.

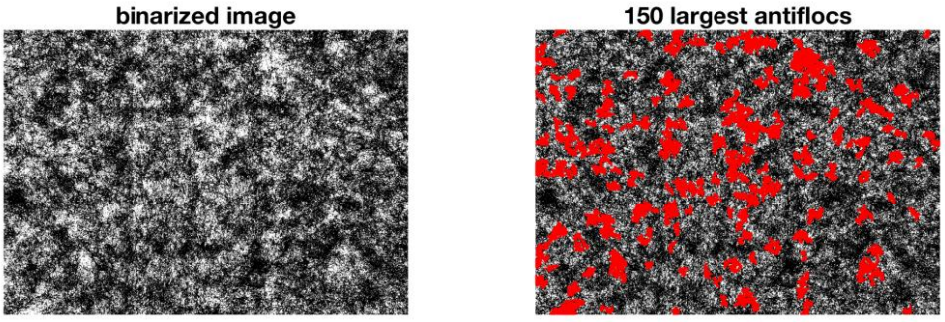

Figure 3-8 : (a) The binarized image of size 88 × 62 mm^2 (pixels with low mass are white). (b) The 150 largest antiflocs (regions of relatively low mass) in the image identified by the Matlab code.

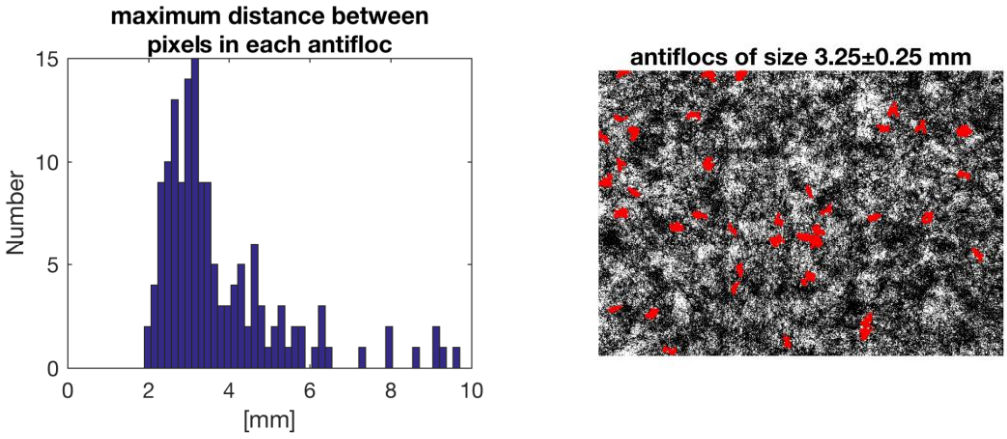

Figure 3-9 : (a) Histogram over the 150 largest antifloc sizes in the image. (b) The population of antiflocs with size 3.25±0.25 mm.

A selection of the 150 largest antiflocs correspond to about one antifloc per 6 × 6 mm^2, a physically reasonable quantity having in mind that the average length-

weighted fiber length is 2.1 mm. The more "large antiflocs" included in the statistical analysis, the peak in the histogram in Figure 3-9a will naturally shift to the left as the antiflocs vanishes while increasing substantially in numbers. It is hence difficult to draw sound statistical conclusions of average size etc. among a population of an arbitrary number of "large antiflocs". Nevertheless, the histogram in Figure 3-9a indicates that antiflocs having a size of about 3-3.5 mm dominate the population of relatively large antiflocs in the LDP. Figure 3-9b shows solely those large antiflocs of size 3.25±0.25 mm and one observe that they are evenly distributed over the whole domain.

3.5.2 The internal length c

The findings in Figure 3-7 shows that the average global fracture force were rather constant at notch lengths a smaller than about 9 mm for the LDP. From this observation one draw the conclusion that a critical defect size to obtain fracture localization in the LDP is $a_c = 9$ mm. Since the global fracture load is constant for $0 \le a \le a_c$, the cohesive stress σ_c is equal to the global fracture stress σ^{∞} when $a \le a_c$, according to the theory. Then, using the hypothesized fracture relation in (3-9), i.e. $K_{Ic} = \frac{\sigma_c \sqrt{c}}{0.3}$, together with the well-known classical macroscopic expression for the fracture toughness of an edge crack, i.e. $K_{Ic} = 1.12\sigma^{\infty}[\pi a_c]^{1/2}$, a relation that links c to a_c for the actual loading situation is

$$c \approx 0.113\pi a_c \qquad (3\text{-}10)$$

Using $a_c = 9$ mm, the internal length c for the LDP is estimated to about 3.2 mm.

3.5.3 Localization

Distant from the dominant macroscopic singularity at the crack-tip, at $r > 2c$ according to (3-8), the subscale stress field $\bar{\sigma}_{ij}$ is approximately equal to the global macroscopic stress σ_{ij}. Providing that the hypothesis that onset of microfractures in the LDP occurs when the subscale stress reaches a certain critical limit σ_c is valid, one realize that a microfracture may nucleate either in the crack-tip region or at random locations at remote distances from the singularity (tip) depending on the magnitude of the defect. For $a \le a_c$ the subscale stress field is approximately homogeneous in the body and equal to the remote macroscopic fracture stress σ^{∞}. Figure 3-10 displays the theoretical stress ratio σ^{∞}/σ_c at various crack lengths for an edge crack using (3-8) under the assumption that microfractures nucleate when the subscale stress $\bar{\sigma}_{qq}$ equals the cohesive stress σ_c. Using (3-8, 3-9) the remote fracture stress σ^{∞} for an edge crack is given by ($K_I = 1.12\sigma^{\infty}[\pi a]^{1/2}$)

$$\sigma^{\infty} \approx \begin{cases} 3.0\sigma_c\sqrt{c/[\pi a]} & \text{if } \sigma^{\infty} < \sigma_c \\ \sigma_c & \text{else} \end{cases} \tag{3-11}$$

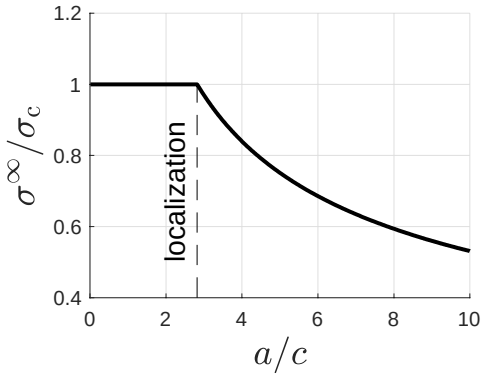

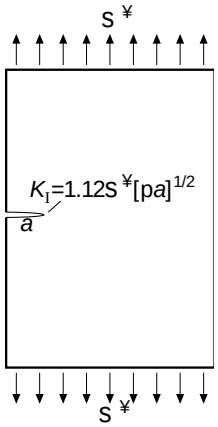

Figure 3-10 : Localization (a) $a = a_c \approx 2.8c$, estimated by (3-11) for an edge crack (b).

One may notice the similarities between the shape of the curves in Figure 3-7, for the LDP, and the theoretical one in Figure 3-10, given by (3-11). The horizontal line in Figure 3-10 represents the situation when the approximated subscale stress field is homogeneous in the whole body. At sufficiently small crack lengths $a \pounds a_c$, the subscale stress field is homogeneous as a result of the averaging, or gradient-enhanced terms, reflected in (3-1). In this region may microfractures nucleate at randomly positioned weak points in the body. At $a > a_c$, indicated by the vertical stretched line, the highest approximated subscale stresses occur at the vicinity of the macroscopic singularity (tip), at $r/c \gg 1.1$ according to (3-8), whereupon the fracture process is localized to the tip region. The critical crack length a_c is roughly $2.8c$ according to (3-10). Thus, a LDP with small variations in mass, i.e. with relatively small antiflocs, is expected to have a smaller internal length c and a smaller critical defect size a_c, which leads to an interesting observation that a substantially more dense paper, such as the HDP or paper boards, is inclined to localize fracture already at very small defects. Hence, the gradient-enhanced fracture theory quantitatively explains why a sparse discontinuous LDP requires a relatively large defect to localize fracture, in contrast to a HDP, which is relatively continuous in this context.

3.5.4 Different scales

A LDP paper is a multiscale material. At least three different structural length-scales may be of interest for the governing fracture process. With reference to Figure 3-11, principally: the paper structure is on the macroscale, the regions of high and low mass distribution (flocs and antiflocs, respectively) as well as the fibers are on a mesoscale (mm), while the interfiber connections (bonds) and the pores between the fibers are on a lower scale, the microscale.

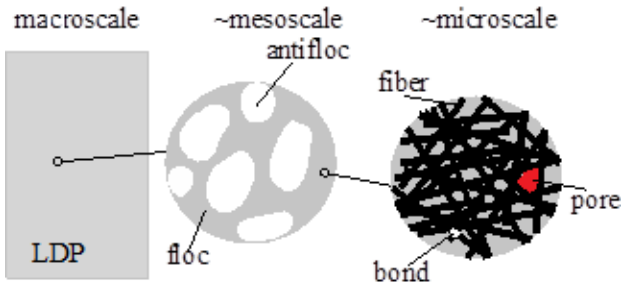

Figure 3-11 : Three possible predominate structural scales at fracture in a LDP.

It is crucial to establish a physically sound connection between the theoretical internal length c and any predominating subscale in the material that influence the fracture process. So, what structural scale is the governing scale at fracture in paper? There are several candidates. From the analysis above it is concluded that since the critical defect size $a_c \approx 9$ mm, the internal length c for the LDP is estimated to about 3.2 mm. The average length-weighted fiber length is about 2.1 mm and could be a candidate. However, the fiber length seems to be of minor importance for the structural fracture phenomena studied here because also very dense papers, such as boards and liners, may have an average fiber length of some millimeters but still behave as traditional continuums (Yuhara and Kortschot, 1993; Mäkelä and Fellers, 2012; Coffin et al., 2013). A physical parameter that distinguishes the LDP from the class of more dense papers is the presence of clearly observable antiflocs, i.e. a large variation in the mass distribution. While e.g. dense papers such as the HDP has a smooth and limited variation in mass, the LDP has a high magnitude of varying mass distribution, i.e. there are several large regions in a LDP of relatively low load-carrying capacity. The regions of low and high mass are clearly visible to the naked eye. Additionally, the sizes of antiflocs are not changing their sizes with the moisture since it is a structural parameter, an observation that further strengthens the hypothesis of the antiflocs importance. As seen in Figure 3-9, the antifloc regions are evenly distributed throughout the LDP and the antiflocs having a size of 3.25±0.25 are the dominating ones. The estimated value of the internal length, 3.2 mm, is surprisingly close to the size of these dominating antiflocs and hence suggests that the most typical size among large antiflocs is a prevailing length scale parameter for fracture of a LDP. This observation seems physically reasonable and may explain why fractures in LDP and HDP are so different. The theoretical hypothesis in Section 3.5.3 supports this observation. If this fracture hypothesis is valid, a consequence is that another low-density paper with smaller mass variations than the studied LDP (i.e. a paper with smaller antiflocs) is likely to have a smaller internal length and critical defect size. Or, put differently, with smaller variations in mass, the critical defect size is anticipated to decrease and the internal length tends to the average interfiber bond distance in the fiber network. In the limit where the variation in mass tends to zero, the material becomes a continuous and (3-8) turns into the classical continuum LEFM stress field solution at a crack tip. Hence, a dense paper is inclined to localize fracture already at very small defects since the internal length is vanishing and the tip stress field tends to singularity. Thus, a key-conclusion is that the hypothesized gradient-enhanced fracture theory quantitatively offers an explanation why a discontinuous LDP requires a large defect to localize fracture in contrast to a

HDP, which always localize fracture to any present defect. However, the applied theory may be questioned from a physical point of view. The strange peculiarity that the approximated subscale stress field is not divergence-free (and hence not in stress equilibrium) need to be thoroughly investigated, explained and clearly understood to support, validate and strengthen the theory. It is crucial that these essential scientific questions are answered.

3.6 Conclusions

The fracture processes in two different moisture sensitive natural cellulosic materials, a low- and a high-density paper, were studied experimentally and analytically. It is shown that the two papers fracture in a different manner. While the high-density paper was smooth and continuous on the macroscopic scale, the low-density paper was substantially discontinuous and has a relative high degree of varying mass distribution, which can clearly be observed with a naked eye. These structural differences influence the materials ability to localize global fracture to present defects. The high-density paper was able to localize fracture to very small defects (<0.5 mm) while a rather large defect (~9 mm) was required in the low-density paper to localize fracture. At defects smaller than that, the global fracture took place at seemingly random positions in the paper. It is hypothesized that different dominating subscales influences the prevailing fracture process in the two materials. Notable is that the fracture behavior is similar at both high and low relative humidity. However, the magnitudes of the global fracture load scales with the moisture-dependent Young's modulus in both papers. A physical parameter that distinguished the low-density paper from dense papers was the presence of the clearly observable large variations in the mass distribution (here referred to as antiflocs). While dense papers has a smooth and very limited variation in mass, the low-density paper has a high magnitude of varying mass distribution, i.e. there were several large regions in the low-density paper that have a relatively low load-carrying capacity. This observation seems to be physical reasonable and may explain why the fracture processes are different. Additionally, the mass distribution is not changing with the moisture level in the paper, which is in accordance with the experiments. A gradient-enhanced theoretical model was applied to describe and capture this fracture phenomenon and intended to approximate stresses on a subscale. The hypothesized fracture theory quantitatively suggests why a discontinuous sparse paper requires a relatively large defect to localize continued fracture in contrast to a dense paper, which is relatively continuous in this context and can be described by classical fracture mechanics theories. The relatively simple fracture theory was remarkably consistent with the experiments and quantitatively captured subscale length-effects in a convenient way. A key observation was that the internal length parameter, used in the hypothesized fracture theory to bridge stresses to a subscale, was linked to an average size of the most common large regions of relatively low mass, or antiflocs, in the low-density paper, which seem to predominantly influence the fracture process. According to the hypothesized theory: if the large regions of relatively low mass would be smaller, the critical defect size to localize fracture would also be smaller, and in the limit of a homogeneous mass distribution the material would become a

classical continuum, which always localize fracture to very small defects. However, even though the hypothesized theory seems promising it may be heavily questioned from a physical point of view. A strange peculiarity that the approximated subscale stress field is not divergence-free needs to be understood in order for the fracture theory to be physically trustworthy. This is a subject for future studies.

Acknowledgements

The work has been partially supported by the LabEx Tec21 (grant no. ANR-11-LABX-0030). Per Isaksson is grateful for the complementary financial support from the Swedish Research Council Formas (grant no. 232-2014-202) and the European Union (H2020 MSCA-RISE project no. 734485 "FRAMED"). The 3SR-Lab is part of Institut Carnot PolyNat (ANR-16-CARN-0025-01) and of the program Glyco@Alps (ANR-15-IDEX-02). M. Party and S. Dufreney at LGP2 Grenoble are acknowledged for their technical support.

Appendix

The Matlab algorithm used to compute the size of the connected regions of low density.

```
V=imread('image.tif');
scalefactor=88/max(size(V));       %size of image (88mm*62mm)
V(V(:)<mean(V(:)))=0; V=logical(V);%threshold with mean value and binarize

subplot(2,2,1); imshow(V); title('binarized image');

CC=bwconncomp(V,8);
numPxs=cellfun(@numel,CC.PixelIdxList); [~,idx]=sort(numPxs);

N=150; idx=idx(end-N+1:end);       %only the N=150 largest antiflocs
subplot(2,2,2), imshow(V); [X,Y]=meshgrid(1:size(V,2),1:size(V,1));
title([num2str(N) ' largest antiflocs']); hold on;
for k=1:N, i=CC.PixelIdxList{idx(k)}; plot(X(i),Y(i),'.','color','r','markersize',.1); end

Le=zeros(N,1); s2= regionprops(V,'Extrema'); %Get properties for the identified antiflocs
subplot(2,2,3), imshow(V); title([antiflocs of size 3.25±0.25 mm]); hold on;
for k=1:N  %Extract N=150 largest antiflocs to compute size
 Extrema=s2(idx(k)).Extrema;
 [~,dist]=knnsearch(Extrema,Extrema,'k',size(Extrema,1));
 Le(k,1)=max(dist(:))*scalefactor; %largest distance beween pixels
 if Le(k,1)>=3 & Le(k,1)<=3.5      %only if 3<size<3.5
   i=CC.PixelIdxList{idx(k)};
   plot(X(i),Y(i),'.','color','r','markersize',.1); drawnow
 end
end

subplot(2,2,4); hist(Le,50); xlim([0 10]); xlabel([mm]'); ylabel('Number');
title({'maximum distance between','pixels in each antifloc'});
```

Chapter 4. 3D visualisation and quantification of the fracture mechanisms in sparse fibre network assessed with multiscale X-ray microtomography

This chapter is based on an article submitted to *Journal of Material Science*, V. Krasnoshlyk, S. Rolland du Roscoat, P. Dumont, E. Ando, P. Isaksson, A. Bonnin, and M. Terrien.

Content

Abstract

The structural changes that are induced by the initiation and the propagation of a crack in a low density paper (LDP) were studied using advanced imaging techniques. Single edge-notched fracture tests (SENT) were performed on LDP samples with different notch lengths using a micro tensile device that was mounted under an optical microscope and in a laboratory or a synchrotron X-ray microtomograph. A multiscale analysis of the initial and deformed structures of samples was performed

using these images. The 2D optical images were used to understand the links between the mesoscale structural variations such as flocs and the so-called "antiflocs" of LDP and the crack path. Medium-resolution X-ray 3D images were used to analyse the spatial variations in the thickness and local porosity of samples as well to plot displacement field maps that are induced by the fracture of LDP. At a finer scale, high-resolution 3D images showed that these mesostructural variations were accompanied by complex fibre and bond deformation mechanisms that were, for the first time, *in situ* imaged. In particular, these mechanisms occurred in the fracture process zone (FPZ) that developed ahead of the crack tip before the crack path became distinct and visible, and were at the origin of the aforementioned thickness variations that developed more particularly along the crack path. They eventually led to fibre-fibre bond detachment phenomena and crack propagation through the fibrous network. These results can be used to enhance the current structural and mechanical models for the prediction of the fracture behaviour of paper.

4.1 Introduction

Ordinary paper is a porous material that consists of natural cellulosic fibres. The cellulosic fibres have an inherent capability to form inter-bonds between them without any additives (Seth, 1979; Salmen and Back, 1980; Nissan and Batten, 1990; Uesaka, 2002; Hirn and Schennach, 2015). Typically, cellulosic fibres are 1-3 mm in length and 20-40 µm in cross-sectional width, depending on their origin (hardwood or softwood fibres) and on the papermaking method (Retulainen et al., 1998; Gustafsson and Niskanen, 2012). Since the fibres are much longer than the thickness of the paper sheet, the fibre network is generally considered to be planar and generally exhibits in-plane structural anisotropy, *e.g.* machine direction (MD) and cross direction (CD), due to papermaking conditions. The porosity of papers ranges from almost zero for dense papers such as tracing papers, to about 85 % for tissues. The layered fibrous structure of papers and the limited conformability of the fibres are at the origin of voids/porosity between them. The porosity of paper plays a significant role, for example, in the paper converting processes such as coating, gluing and printing (Silvy et al., 1995). In addition, the mechanical properties, *i.e.*, tensile strength and fracture behaviour, are fundamental properties for papermaking, converting and printing as they are related to machine runnability. These properties are highly affected by the paper structure, e.g. fibre orientation and spatial distributions, and the structural constituents such as fibres and inter-fibre bonds which in return depend on the pulp preparation and papermaking conditions (Niskanen, 1993; Donner, 1997; Sampson, 2001, Marulier et al., 2012; 2015). As the other papers, low density papers generally exhibit anisotropic mechanical properties as well as a well-pronounced inhomogeneous structure caused by formation where the fibres get entangled in flocs, *i.e.*, regions of relatively high local mass distribution (Dodson, 1996; Isokangas and Leiviskä, 2011).

In particular, the mechanisms of crack propagation in paper materials depend on their density. For instance, high-density papers, *e.g.* packaging or printing papers, exhibit straight crack propagation ahead of a notch, whereas the crack path in low-density papers presents a diffuse behaviour (Isaksson et al., 2012) and other phenomena such as crack tip blunting occur (Isaksson and Dumont, 2014). The tensile behaviour of low-density papers, such as tissues, differs from the printing and packaging papers due to a more open "sparse" network structure, offering greater fibre flexibility (Coffin et al., 2013). When a low-density paper is subjected to a mechanical loading, complex deformations arise on the micrometric and millimetre scales and have to be captured properly (cf. previous chapter). Formation of paper, *i.e.*, local mass variations, causes inhomogeneous deformation in different types of papers: local mass variability affects the variation in the strain distribution and, thus, affects the fracture process in papers (Wong et al., 1996; Considine et al., 2011; Hagman and Nygårds, 2012).

Several techniques have been used to investigate crack initiation and propagation in papers such as for instance acoustic emission (Alava and Niskanen, 2006, Isaksson and Hägglund, 2013), fractography of crack line (Salminen et al., 2003) as well as 2D imaging of silicone-impregnated paper during tensile and fracture tests (Korteoja et al., 1996, Niskanen et al., 2001). Recently, digital image correlation (DIC) and thermography were combined to perform a surface analysis of the strain field and temperature field onto the surface of paper samples during tensile experiments (Hagman and Nygårds, 2017). Acoustic emission enables sound emission of crack-related events to be acquired during crack experiments. However, it is difficult to extract information on the fine scale deformation mechanisms (fibre and/or bond breakage). In Korteoja et al. (1996), 2D image analysis of the silicone-impregnated paper during a tensile test showed that the plastic strain patterns and eventual mesoscopic fractures were affected by the paper formation. Moreover, the fracture initiates and passes through the relatively low mass distribution areas (Moffat et al., 1973). In Hagman and Nygårds (2017), the authors were able to predict where the crack initiates but not where the crack propagates using 2D imaging combined with digital image correlation technique and thermography.

Furthermore, one more open question in fracture mechanics of paper material is the size of the fracture process zone (FPZ) that appears ahead of the notch/crack tip of paper before the crack becomes distinct (Coffin et al., 2013). This zone corresponds to an area around the crack tip where the stresses alter from the global stress in paper (Donner, 1997; Coffin et al., 2013; Niskanen et al., 2001; Östlund and Märkelä, 2012). The size of this zone is seen by many authors as an important parameter for the fracture behaviour of fibre networks such as papers. For instance, it is used as internal length in modified linear elastic fracture mechanics (LEFM) models (Niskanen et al., 2001, Coffin et al., 2013) that are proposed for the prediction of

fracture resistance of paper. There was one attempt to measure the size of the FPZ proposed by Niskanen et al., 2001 which is an invasive procedure as it consists in impregnating the paper sample with a silicone oil and following the crack opening using 2D images acquired under the optical microscope for a medium density paper. However, the authors could not give any detailed description of the deformation and damage mechanisms that occur in the FPZ using this approach. However, information about the nature of the mechanisms that are activated in the vicinity of the crack during crack initiation and propagation would be necessary to validate or not fracture mechanics models for paper. Several questions on the phenomena that govern fracture in paper are still open: How do the fibres deform? Do they show plastic deformation? Do they break? Do fibre-fibre bonds break? What are the mechanisms that lead to their breakage? What is the influence of the structural heterogeneity of paper on these phenomena?

All the aforementioned studies that link microstructural or mesostructural parameters to the crack mechanisms are based on 2D imaging. The main drawback of all these techniques comes from the fact they provide information on the average structural properties in the thickness direction and, therefore, do not take into account the 3D structural effect that arise in the paper structure. X-ray microtomography allows the 3D inner structure of different materials to be visualised in a non-invasive way (Antoine et al., 2002; Salvo et al., 2003; Rolland du Roscoat et al., 2005; Yu et al., 2016), and thus can overcome this drawback and bring complementary information to the ones provided by traditional imaging systems. As mentioned by Yu et al., 2016, this method is suitable to understand the fracture phenomena in fibrous materials.

Therefore to provide a multiscale analysis of the structural evolution of a low density paper during a fracture test, images of paper samples were obtained in this study using either X-ray tomography or optical microscopy. Advanced images analysis tools were developed, first, to investigate the influence of mass variation on the crack propagation and, second, to map the evolution of the local porosity and thickness as well as to visualise at the fibre scale the mechanisms developed during the crack propagation.

4.2 Experimental procedure

4.2.1 Materials and sample preparation

The Low Density Paper (LDP) considered in this study was made from bleached unbeaten softwood chemical pulp and produced at low speed by “air-drying”, resulting in a sparse fibre network that did not show any in-plane preferential fibre orientation. The arithmetic mean fibre length was 1.3 mm and their coarseness was 0.14 mg m^{-1} measured using Morfi apparatus (Techpap®, Grenoble, France). Using

standard techniques (ISO 536: 1995(F) and ISO 534: 2011(F)) of paper science, the basis weight g of paper was measured by dividing the mass of samples by their in-plane areas (100×100 mm^2), and their apparent thickness t was measured using a micrometer which consisted of two parallel plates (diameter of 10 mm) placed in contact with the sample surfaces (static pressure of 100 kPa). The basis weight of LDP was 23 g m^{-2} and the thickness was 113 µm. Its porosity Φ was equal to 86 % and was obtained as follows:

$$\Phi = 1 - \frac{g}{t.\rho_{fibre}}, \tag{4-1}$$

where ρ_{fibre} was the fibre wall density and was equal to 1550 kg m^{-3}.

All the analysed samples were cut in a rectangular shape in machine direction (MD) with width w and initial length h_1 using a cutting machine (Kongsberg® XL 22, Eskoartwork, Gent, Belgium) to ensure the repeatability of the results. Depending on the imaging system, w and h_1 differed (Section 4.2.2). A notch of the length a was cut at the midheight and one edge of the samples, as shown in Figure 4-1a. Since the mechanical properties of papers are highly influenced by the temperature and the relative humidity (Alava and Niskanen, 2006; Haslach, 2000), all the samples were stored at ambient temperature T of 23 °C and a relative humidity RH of 50 % for at least 24 hours before the mechanical experiments. All mechanical experiments were performed in similar ambient conditions.

4.2.2 Single edge-notched fracture tests (SENT) with optical or X-ray imaging techniques

Based on previous experiments (Isaksson et al., 2012), a mini tensile machine was developed and mounted on the X-ray microtomograph rotation stages (Figure 4-1b) as well as under the optical microscope. The samples (Figure 4-1a) that were placed in the clamps (the distance between clamps was denoted h) were subjected to tensile test while the bottom clamp was attached to the piezoelectric motor (NanoPZ Ultra-High Resolution Actuator, Newport, USA) was moving vertically down. The mini tensile device was equipped with a 5-N load cell (MEAS XFTC300, USA) and Linear Variable Differential Transformer (LVDT) (D5/05000U/RA, RDP Electronics Ltd, United Kingdom) displacement sensor. During the experiments, both the normalised force F/w (where F is the measured tensile force, and w the sample width) and the global tensile strain were calculated.

4.2.2.1 SENT with *ex situ* 2D optical imaging

LDP is a type of paper with a relatively high degree of mass distribution variation, which can clearly be observed with a naked eye. The microscopy with a visible transmitted light was used in order to measure the mass distribution in paper (Trepanier et al., 1998; Isokangas and Leiviskä, 2011), as well as to study its influence on the fracture behaviour in paper (Wong et al., 1996). Furthermore, the

choice of this technique for studying the mass variation is supported by the investigation of Komppa (1988) and Dooley and Sampson (2002) where the relationship between local light transmission and local grammage was approximately linear for highly scattering paper which was the case for the LDP analysed in this study.

Two-dimensional optical images of LDP samples of 12×12 mm^2 with 0 and 5 mm single edge notches were taken prior and after the single edge-notched fracture tests at a pixel size of 7.3×7.3 μm^2 (see the example in Figure 4-1a) in transmission mode using a stereomicroscope (ZEISS®, Discovery.V20, Germany) equipped with a CCD camera (ZEISS®,AxioCam ICc5, Germany) and objective (ZEISS®, Plan S 1.0x, FWD 81 mm, Germany). The initial distance h_0 between clamps was set to 6 mm. The black areas in this image correspond to the zones that were denser in the thickness direction compared to the rest of the sample due to high mass distribution variations. One of the SENT typical curves for a sample with $a = 5$ mm obtained using the mini tensile device is shown in Figure 4-2a (dotted line).

4.2.2.2 SENT with 3D *in situ* X-ray imaging

The microstructural changes of LDP during fracture tests were monitored using the X-ray microtomograph installed in the 3SR laboratory and the synchrotron X-ray microtomograph of the TOMCAT beamline of the Swiss Light Source (Paul Scherrer Institut, Villigen, Switzerland). Figure 4-1 shows both experimental setups. The acquisition parameters for each type of X-ray microtomography experiments are given in Table 4-1. For both experiments, 2D X-ray radiographs of the samples were obtained during the full rotation of the mini tensile device with the sample. Then, these radiographs were used to reconstruct the 3D microstructure of the sample, *i.e.*, the spatial distribution of the local X-ray attenuation coefficient. An absorption mode and a filtered back-projection algorithm (Kak and Slaney, 2001) were used for images acquired using the lab microtomograph, whereas the Paganin phase retrieval mode (Paganin et al., 2002) and regridding reconstruction algorithm (Marone and Stampanoni, 2012) were used for the images acquired using the synchrotron microtomograph. Both imaging sources provide complementary information since the 3D images showing the evolution under loading of the paper structure were acquired at a medium resolution using the lab X-ray microtomograph during interrupted SENT, and at a high resolution and during continuous and real-time fracture SENT using the synchrotron X-ray microtomograph. This enabled the evolution of paper to be studied at the network scale and the fibre scale, respectively.

Interrupted SENT - In the lab X-ray microtomograph a scanning time of about 2 hours was necessary to obtain a high quality images of the paper microstructure at a voxel size of 6.9×6.9×6.9 μm^3. Therefore, an interrupted procedure was used: the loading was stopped each time during image acquisition of the sample which was

denoted S1 (Table 1). The load-point displacement rate v was 0.3 mm min^{-1}. The corresponding tensile curve for the sample which was denoted S1 is shown in Figure 4-2a (bold continuous line), whereas several 3D X-ray images illustrate the fibrous network of this sample during loading in Figure 4-2b. As the LVDT sensor could not be used during this test, the tensile curve was adjusted in accordance with the displacement of the clamps measured in the 3D images. Because of the conic beam geometry of the laboratory microtomograph, a slight deformation of the upper clamp and of the image edges is apparent in Figure 4-2b. In the series of images I3 – I5 of sample S1 obtained at different states of deformation, a small distortion of the bottom clamp can be observed due to its shift to the edge of the field of view. These areas were excluded from the analysis of the microstructure or the displacement fields of sample S1.

Continuous SENT - Synchrotron X-ray microtomography enabled real-time X-ray scanning (Mokso et al., 2011; Laurencin et al., 2016) of a sample during continuous SENT, *i.e.*, the acquisition of a sequence of several images of a sample which was denoted S2 (Table 1) without stopping the mechanical loading. Each image of the sequence was obtained using a high-speed detector PCO.Dimax (PCO, Germany) every 200 s with a voxel size of 0.55×0.55×0.55 µm^3. For these experiments, the mini tensile device was placed inside of a special humidity chamber where the environmental conditions were controlled using a humidity generator (Figure 4-1d). The velocity of the motor during the tensile test (0.06 mm min^{-1}) was chosen in order to obtain images of a decent quality. Contrary to the laboratory X-ray microtomograph, the ultra-fast image acquisition (5 ms per projection) and the parallel-like geometry of the synchrotron X-ray beam did not cause any notable image deformation. Figure 4-8 shows the sequence of images (denoted C1 to C10) of the notch tip area (field of view of 1.1×1.1 mm^2) of sample S2 that were acquired. The corresponding force-strain curve is shown in Figure 4-2a (continuous line).

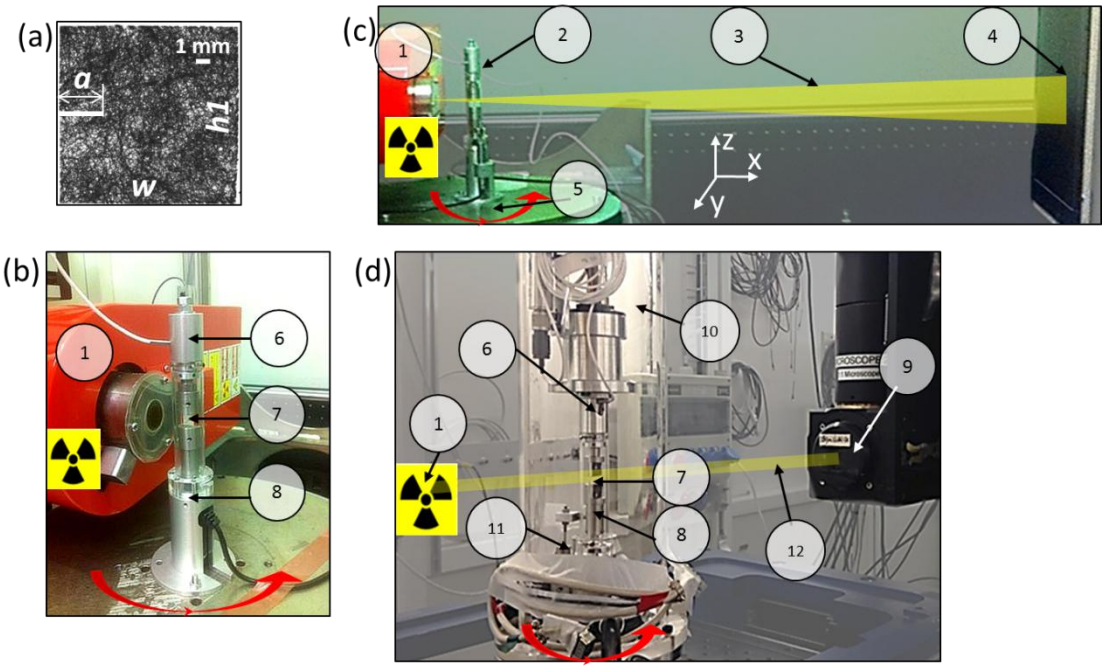

Figure 4-1 : (a) Micrograph obtained using the visible transmitted light of the notched LDP sample. (b) Mini tensile device mounted on the rotation stage in the X-ray microtomograph of laboratory 3SR. Sample was placed between two mechanical clamps. (c) Experimental setup in the X-ray microtomograph of laboratory 3SR. (d) Experimental set-up at the synchrotron X-ray microtomograph of the TOMCAT beamline of SLS. Signs in all the images: 1 – X-ray source; 2 – Mini tensile device; 3 – Schematic conic X-ray beam; 4 – X-ray detector; 5 – Rotating stage; 6 - Force sensor, 7 – Sample; 8 - Piezoelectric motor; 9 – Image acquisition system; 10 – Humidity chamber; 11 – LVDT sensor; 12 – Schematic parallel X-ray beam.

Table 4-1 : Experimental parameters for X-ray microtomography experiments.

X-ray microtomograph		3SR laboratory	TOMCAT
Sample		**S1**	**S2**
1) Voxel size	[µm^3]	6.9×6.9×6.9	0.55×0.55×0.55
2) X-ray characteristics		250 µA, 40 kV	400 mA, 20 keV
3) Number of projections	[-]	900	501
4) Projection size	[pixels]	1536×1920	2016×2016
5) Scan duration	[s]	7200	2.5
6) Scan levels	[-]	5	10
7) Scan type		interrupted	continuous
8) Sample dimensions			
- width w	[mm]	8	12
- height h	[mm]	6	6
- notch a	[mm]	3	4
- a/w	[-]	0.375	0.334

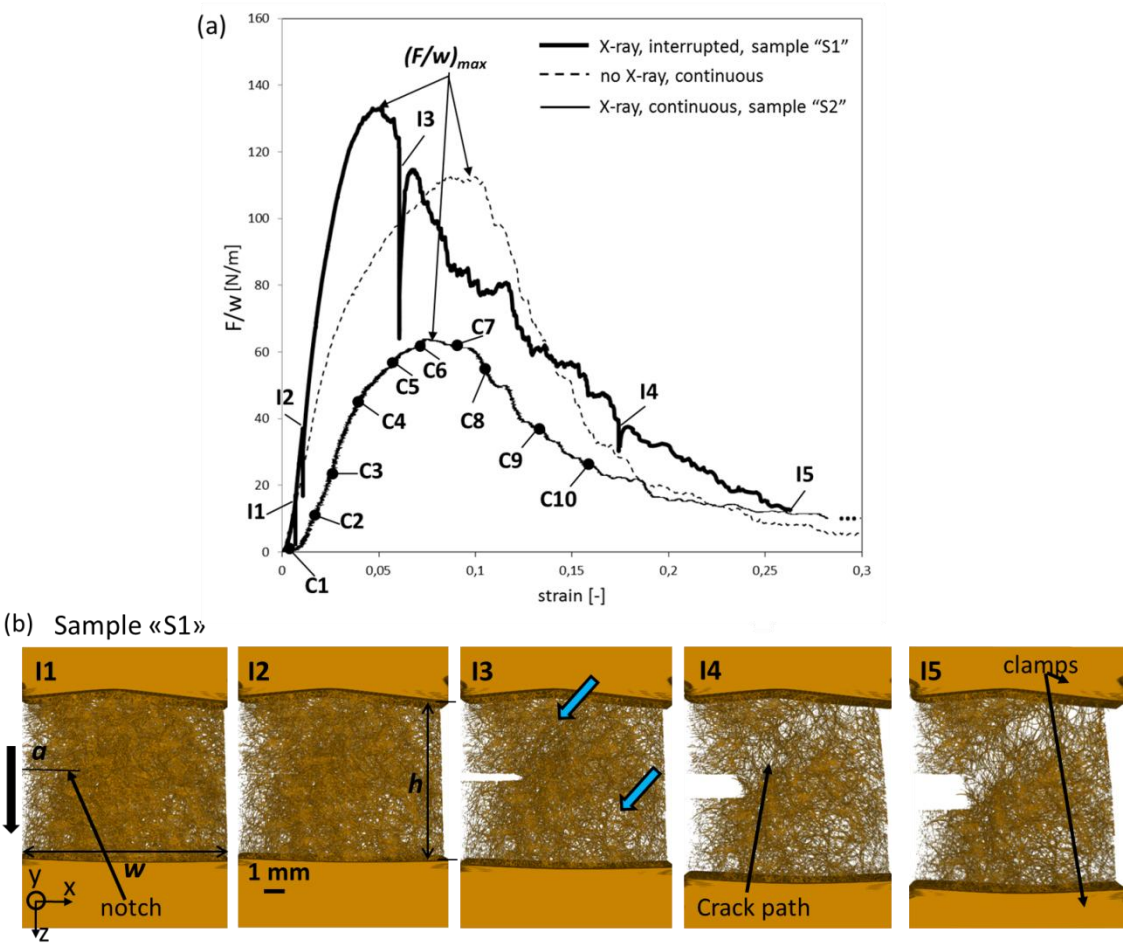

Figure 4-2 : Tensile curves for the LDP samples in (a) were obtained using the mini tensile device. Forces were normalized with the width of the samples. One of the curve (bold continuous line) represents interrupted tensile test with X-ray monitoring (performed at 3SR laboratory) of sample S1 where each X-ray scan (I1-I5) is indicated on the curve and the obtained 3D images (voxel size of 6.9×6.9×6.9 µm^3) are shown in (b). The direction of the moving bottom clamp is shown with a bold black arrow on the image I1. Structural change such as pore size augmentation is indicated with the blue arrows in I3. Continuous tensile test with X-ray monitoring (performed on the TOMCAT beamline of SLS) of sample S2 is represented using a continuous line where X-ray scans (C1-C10) are indicated. Continuous tensile test without X-ray scanning is shown with a dotted line.

4.2.3 Image analysis

The 2D and 3D greyscale images were used to analyse the evolution of the geometry of the samples and extract descriptors of their microstructure. However, for some of the analyses, the reconstructed 3D datasets were converted from greyscale images to binary images using classical image processing tools: a median filter with a radius of 2 pixels (only for images of 0.55×0.55×0.55 µm^3 resolution) followed by thresholding Isodata algorithm (Ridler and Calvard, 1978). When it was needed, the ring artefacts of the 3D images were also manually removed. This segmentation procedure allowed the fibre phase to be separated from the pore phase.

In addition, 2D enhanced radiographs were obtained by projecting the binarised 3D images in the thickness (Y-direction) of the paper samples (Figure 4-7a). The representation of the images aims at better visualizing the quantitative results.

4.2.3.1 Detection of floc and antifloc zones

In order to quantify the positions and sizes of the regions of relatively high mass distribution (flocs) and of relatively low mass distribution (antiflocs), a Matlab® algorithm was developed and applied to 2D binarised images (obtained using optical microscopy images or the aforementioned 2D enhanced radiographs) using the median value of the grey level (Jordan, 1986) in order to minimize effect of the variations in the image contrast. Then, the erosion function with structural element 'disk' (radius of 3 pixels) enabled us to obtain the connected regions of the pixels related to the flocs that were identified using 'regionprops' function. In the case of the antiflocs, the binarised images were inverted and the same procedure was applied to extract the connected regions of pixels. Flocs and antiflocs regions were approximated by ellipses, simplifying the shape of the original heterogeneities but giving an order of magnitude of their approximate dimensions (major and minor ellipse lengths).

4.2.3.2 Local thickness and porosity maps

The thickness and porosity of each sample were measured locally using the 3D binarised images. To that extend, a grid was applied onto each slice of the 3D binarised images, as shown in Figure 4-3. The size of the *Analysis Window (AW)* of the grid was chosen according to the resolution of the images and to the aim of the analysis. For each AW across the thickness, the two surface boundaries were defined as the first and the last occurrence of the fibre phase from which the local thickness $\tilde{t}$ was obtained. Therefore, the thickness map is a 2D image of local thickness variation. Further, to compare local thickness variation of the sample, every thickness map was normalised with the mean thickness $\bar{t}_1$ of the first image of an image sequence.

The porosity maps was obtained from the local porosity that was calculated for each AW restricted by the obtained surface boundaries identified in the thickness map analysis:

$$\widetilde{\Phi} = \frac{N_{pore}}{N_{pore}+N_{fibre}}, \tag{4-2}$$

where $\widetilde{\Phi}$ is the local porosity of each AW, N_{pore} the total number of pixels in each zone corresponding to the pore phase, N_{fibre} the total number of pixels in each zone corresponding to the fibre phase.

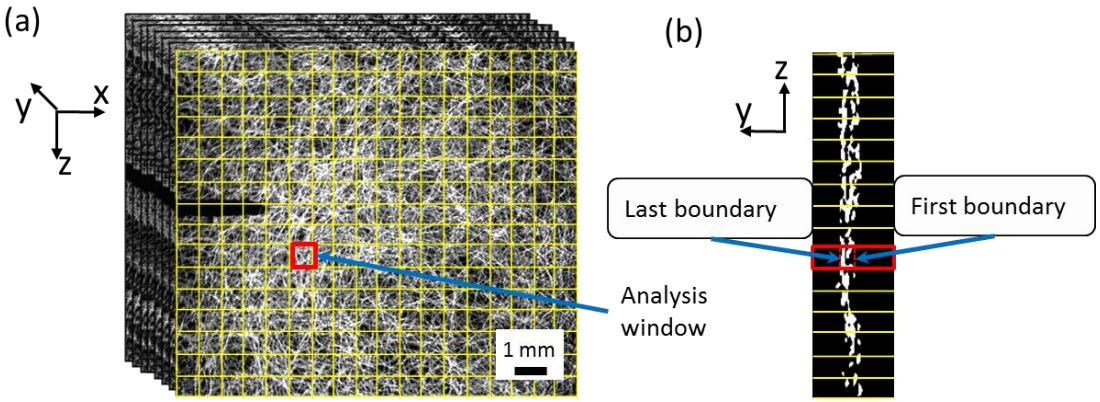

Figure 4-3 : Scheme of local thickness and porosity measurements on a 3D X-ray image using a grid (yellow). Fibres are white and the pores/air black. (a) The grid (yellow) was applied to each slice XZ of the image in the Y direction where the analysis was performed in each analysis window (AW) (example of AW in red); (b) The samples' surfaces (boundaries) were determined in each AW (example in red) in the cross section YZ.

4.2.3.3 Continuum Digital Volume Correlation (DVC)

Digital Image Correlation is a powerful tool that can provide full-field measurement of kinematics at the surfaces (2D) as well as within an object (3D) during its deformation (Roux and Hild, 2009; Hall et al., 2010; Viguié et al., 2011). The principle of Digital Image Correlation is to recover the image feature from a reference image to the deformed image which provides the displacement fields. In this study, Digital Volume Correlation (DVC) was performed using the python-based code TomoWarp2 (Tudisco et al., 2015) which is based on the earlier TomoWarp code (Hall et al., 2009). In this code, (i) a grid of the analysis points (nodes) is first applied over the grey scale 3D images; (ii) a group of pixels surrounding each node of this grid, called correlation window which correspond to the feature, is determined in the reference image. The correlation itself consists in searching for the most similar correlation window in the deformed image based on the statistical measure of correlation, for example, the normalized correlation coefficient (Ando, 2013). The search is usually performed within a reduced area in the deformed image called search window, providing a displacement values such as integer number of pixels. However, to obtain more realistic values, a subpixel refinement is performed.

In this study, this technique was applied to the medium resolution images of sample S1. First, the greyscale images of this sample were masked using its segmented images in order to separate fibre phase from non-constant background value, to decrease noise in the images including ring artefacts and to restrict zone of the analysis. The subpixel refinement was based on the interpolation of the correlation coefficients corresponding to integer displacements (Viggiani et al., 2012). For the 3D images of sample S1 where the mean fibre width was 4 voxels, the correlation window was set to 5 voxels, the node spacing to 2 voxels. In addition, the search window was

set for each image I1 to I5 uniquely as it depended on the clamp opening. The thickness of the studied paper was small and often the structure was slightly tilted in the images; therefore it was not possible to extract a relevant single slice with required information on deformation. Thus, the analysis was only focused on the components of the displacement field. DVC enabled the component of the displacement field to be measured between two successive images, *i.e.*, the displacement components were measured incrementally, for instance between images I1 and I2 and so on, as shown in Figure 4-5b and c. For simpler representation, these 3D fields were projected through the thickness direction using median values which provided a 2D global overview (Figure 4-5).

4.3 Results

4.3.1 Typical mesoscale results

Normalised force *vs.* strain curves – The typical evolution of the normalised tensile force as a function of the global strain of samples are shown in Figure 4-4 for several samples without notch – curves (a) and (b) – and samples with a 5-mm notch –curves (c) and (d). In addition, Figure 4-2a shows several SENT curves obtained under various conditions: a continuous test without X-ray monitoring (dotted line) and an interrupted test (bold continuous line) as well as a continuous test (continuous line) with X-ray scanning. All the samples behaved similarly during these tests and exhibited a typical behaviour for a LDP: the force-strain curves presented a sharp practically linear and smooth increase that was followed by non-linear part that led to the maximum carried force F_{max}. Then, the force slowly decreased until the complete breakage of the sample was reached. During this decrease the curves were irregular. This evolution was certainly related to damage and crack propagation events before the sample breakage. Note that the shape of the curves was similar for the samples with and without notch.

In addition, for sample S1 (bold continuous line), relaxation phenomena are clearly apparent due to the interruption during X-ray acquisition (Figure 4-2a). However, this interruption of the tensile test did not affect the global mechanical behaviour of sample S1, making both types of experiments complementary. Thus, the X-ray beam did not seem to have an effect on the mechanical response of the studied LDP samples, which led confidence in the information that was extracted from the analysis of these images.

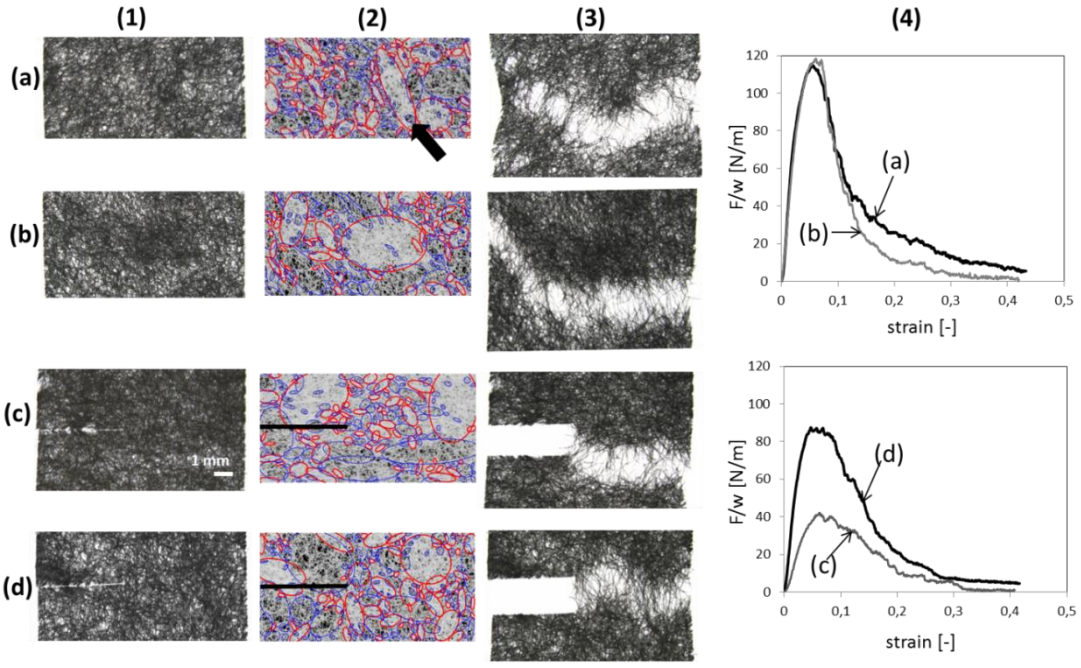

Figure 4-4 : Micrographs of 0 and 5 mm notched samples (12×6 mm^2) before (1) and after crack propagations (3) (fibers – in dark grey); (2): Inversed original images with flocs shown in red (fibers – in light grey), and antiflocs in blue; (4): Tensile curves for the corresponded images of the samples. Forces were normalized using the width of the samples.

Displacement field - The components u_y and u_z of the displacement field in the loading y and the z directions that were obtained for sample S1 are shown in Figure 4-5b and c, respectively. The component u_x is not shown as it did not deliver any complementary information. Images I1 and I2 were taken before the maximum force F_{max} was reached, whereas images I3 to I5 were taken after the maximum force (Figure 4-2). The following comments can be made from the images of the components of the displacement field:

- Prior to the maximum force F_{max}, the components u_y and u_z along the y-axis and z-axis, respectively, exhibited rather smooth variations (Figure 4-5b and c, images I1-I2). However, the component u_z exhibited a transition on both sides of the crack lips. The top part of the sample located above the top crack lip did not seem to move compared to the part of the sample located beneath the bottom crack lip. Further, the variations of the component u_y show that the sample did not exhibit any out-of-plane significant variations.
- The increment of displacement components measured between the images I2 (prior to F_{max}) and I3 (after F_{max}) shows that several heterogeneities appeared during the transition through the force peak. The magnitude of both components increased over the entire sample in terms of absolute value. Above the top crack lip, the displacement u_z remained quite low, whereas the bottom left part moved approximately by 0.22 mm down. The component u_y reveals that the notch lips moved in two out of-plane opposite directions. Ahead of the notch, this

component exhibited heterogeneous patterns. However, it was difficult to ascertain if the locations of these patterns reflected the locations of the flocs or antiflocs that are shown in the images I2 and I3 in Figure 4-5a, whereas such a link was clearly established by Hagman and Nygårds (2017) for paperboards, *i.e.*, a denser material.

- In the maps I3-I4 and I4-I5, *i.e.*, after F_{max}, the heterogeneities of both displacement field components still increased in a remarkable manner. This increase was possibly due to fine scale damage of the fibre network induced for instance by fibre movement or fibre-fibre debonding as fibre patterns can be clearly distinguished. Two distinct zones also appeared in the maps I3-I4 and I4-I5 for the u_z component. The transition zone between these two zones represents the crack path in the maps I3 - I4 and I4 - I5 in Figure 4-5b. The crack path (also apparent in the enhanced radiographs I4 and I5 in Figure 4-5a) is also clearly apparent in the maps I4 - I5 for u_y in Figure 4-5c. Note that the missing part of the paper sample observed in the images I3-I4 was due to large notch lip displacement in the thickness direction that was outside of the search window. It is also interesting to notice that the crack tip exhibited a blunt shape which is typical for LDP (Isaksson and Dumont, 2014).

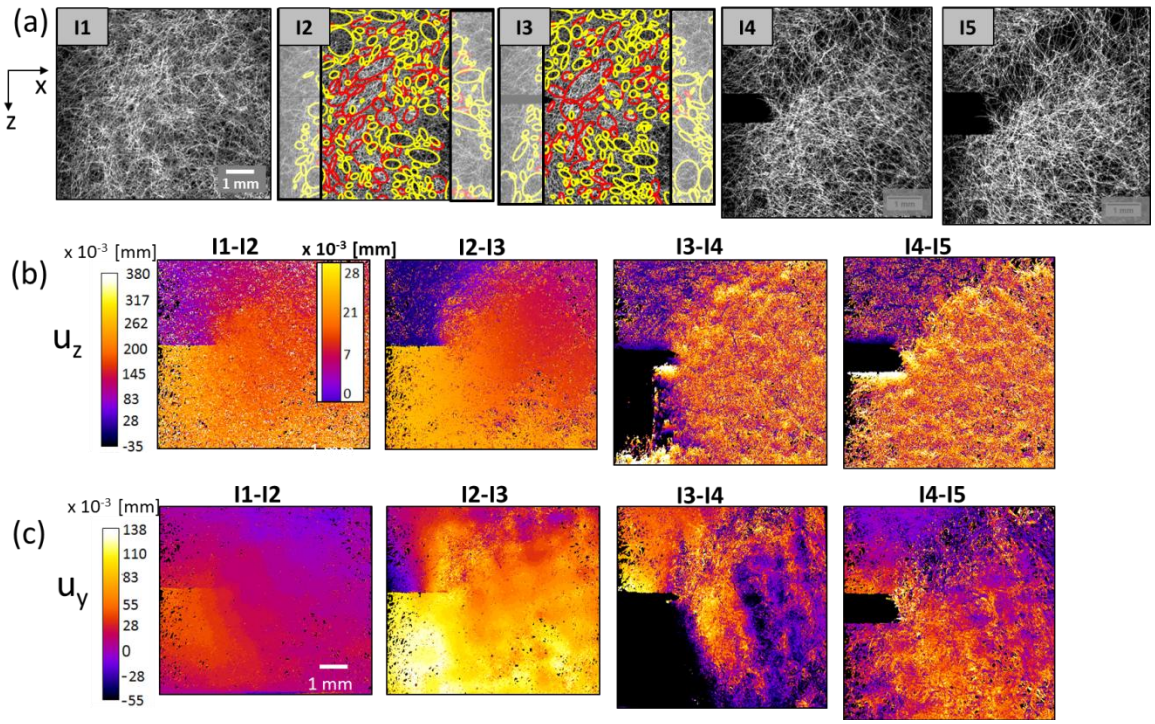

Figure 4-5 : (a) X-ray enhanced radiographs of sample S1 during SENT. Fibres are in grey, and air is in black. On the images I2 and I3 the flocs were detected as red ellipses and antiflocs are yellow ellipses. Due to different intensity the image edges were excluded from the floc identification analysis. (b) Component u_z of the increment of the displacement field in the tensile direction represented using median intensity projections. The colour bar was applied to all the images except I1-I2 with its own bar. (c) Component u_y of the increment of the displacement field in the y-direction represented using median intensity projections.

Influence of the notch length on the normalised force - Figure 4-6 shows the evolution of the maximum normalised force F_{max}/w for various ratios a/w that ranged between 0 and 0.42 for samples with dimensions w=12 mm and h=6 mm. The heterogeneities in the structure related to the paper formation affect its tensile strength (Norman, 1966; Nazhad et al., 2000), therefore, significant error bars can be observed on the graph. The maximum normalised force F_{max}/w for sample S2 indicated in the graph is in the error bar range. The average fracture force $\langle F_{max} \rangle$ was almost stable until a critical ratio $\left(\frac{a}{w}\right)_C$ that ranged between 0.25 and 0.33, thereafter the maximum normalised force decreased. The visual observations of these experiments showed that, if the notch length was less than the critical value, fracture phenomena initiated at a random "weak" area in the paper samples, whereas fracture always localised in the vicinity of the notch tip if the notch length was large enough, *i.e.*, if the ratio was approximately equal to 0.25.

This fracture behaviour is typical for the low density papers, and is coherent with previously reported results, *cf.* previous chapter and Hägglund and Isaksson (2006), Coffin et al. (2013); , where the dimensions of the samples were larger.

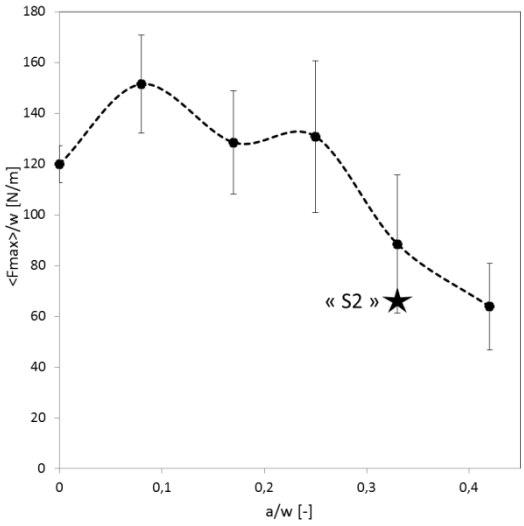

Figure 4-6 : Influence of the notch length a on the normalised maximum force F_{max}. The average peak forces $\langle F_{max} \rangle$ with the error bars were normalized with the widths of the samples (w=12 mm). Sample S2 is indicated on the graph.

4.3.2 Evolution of paper structure at the meso- and microscale during crack initiation and propagation

Both 2D and 3D images allow several comments on the crack initiation and propagation to be made, more particularly on the links the microstructural characteristics of the LDP fibrous network and these phenomena.

Influence of formation on crack path – Besides typical SENT curves, Figure 4-4 shows typical micrographs of the initial and cracked states of notched (a=5 mm) and unnotched samples. The position of flocs and antiflocs in these samples is also shown

in these images. The visual analysis of these images and some other images (not shown here) enabled some principles for the crack initiation and propagation to be proposed:

- Regardless of the presence of notch, cracks tended to propagate in the low mass distribution regions (antiflocs), avoiding the denser regions (flocs). However, in the particular case when the major axis of the ellipse representing a floc was almost parallel to the loading direction (shown for example with the black arrow in Figure 4-4a-2), cracks propagated through the floc connecting the notch tip with the largest antifloc or two largest antiflocs.
- In the samples without notch, e.g. Figure 4-4a,b, the crack always initiated at the largest antifloc in the structure, which was possibly the area showing the weakest mechanical properties in the fibrous network.
- In the samples with a ratio a/w larger than the critical ratio, as shown in Figure 4-4c,d, if the antiflocs were located next to the notch tip, the crack propagated through them (Figure 4-4c). Otherwise, if a floc was ahead of the notch tip the crack was "attracted" to the biggest antifloc in the vicinity of the notch (Figure 4-4d).

In addition, the effect of the flocculated network on the mechanical behaviour could also be noticed on the tensile curves that are shown in Figure 4-4. Crack propagation around flocs seemed to be more energy consuming. For example, the total work of fracture that was estimated from the area under the SENT curves for the notched samples (d) and (c) was 2.1 times larger for sample (d) where the crack had to circumvent several flocs than for sample (c) where the crack could propagate through a "corridor" of antiflocs. Similarly, the unnotched sample (a) with a vertical floc (Figure 4-4a-2) through the crack path presented 1.3 times larger of TWF than the sample (b) that also exhibited a "corridor" of antiflocs.

These observations show the importance of paper formation and how mesoscale structures such as flocs and antiflocs affect the tensile strength and the crack propagation phenomena in LDP as well as their breakage. However, they do not give information on the 3D mechanisms that are involved.

The 3D images of both samples S1 and S2 (Figure 4-2b and Figure 4-8) obtained during SENT illustrate the 3D microstructural changes in a qualitative manner. The 3D images in Figure 4-2b and the enhanced radiographs in Figure 4-7a of sample S1 illustrate stepwise crack nucleation followed by its propagation. The images I1 and I2 obtained in the linear part of the tensile curve (prior to F_{max}) did not exhibit any microstructural differences that could be seen with the naked eye. Changes occurred starting from image I3 (after F_{max}) where the dimensions of some pores increased, for example in the areas shown with the arrows in Figure 4-2b, as well as crack tip blunting. Images I4 and I5 enabled the localisation of the crack to be distinguished as

a zone with large pores along it clearly appeared. The images in Figure 4-2b that were taken at a higher resolution zoomed in the crack tip of sample S2 that exhibited a blunting phenomenon during SENT. In the vicinity of the crack tip, the pore size also showed an increase.

Evolution of the local porosity and local thickness - The quantitative evolution of the local porosity and local thickness of samples S1 during SENT is shown in Figure 4-7b,c. These maps were obtained for a grid with a size of analysis windows (AW) of 10×10 pixels, *i.e.*, approximately 70×70 µm^2.

The maps show large heterogeneities for these mesostructural descriptors of the fibrous network in its initial state (image I1). The thickness map exhibits periodic patterns that are slightly apparent. These patterns could be wire marks and could have been induced during papermaking. Flow and antifloc patterns could also be superimposed to the wire marks and contribute to the overall variations of the LDP thickness. The cross section of the 3D image I1 that is shown on the left-hand side of Figure 4-7d also reveals that local fibre detachment phenomena could contribute to localised thickness variations. The initial mean thickness $\langle \tilde{t} \rangle$ of sample S1 is given in Table 4-2. This thickness was equal to 150 µm and was larger than the apparent thickness obtained using the standard measuring technique (Section 4.2.1) where paper was compressed. The mean porosity of sample S1 in its initial state deduced from the local porosity map was 67 % that is less than the calculated porosity using classical approaches (Section 4.2.1). This difference could arise from the threshold that is complicated on the low resolution images, but could also reflect a local variation in the LDP structure that was present in the S1 sample. As the threshold for the porosity calculation was the same for each image of sample S1, only the porosity variations between images I1 to I5 were considered to be significant.

The porosity and thickness maps of images I1 and I2 did not exhibit significant visual variations of the LDP mesostructure (Figure 4-7). It may be explained by the fact that both 3D images were obtained below the maximum force F_{max}, *i.e.*, in an elastic deformation regime. According to the result given in Table 4-2, the mean thickness in sample S1 slightly decreased between images I1 and I2. This contraction could be related to a Poisson's effect. The out-of-plane Poisson's ratio was estimated as the ratio between $-\langle \varepsilon_{yy} \rangle / \langle \varepsilon_{zz} \rangle$, and was equal to approximately 0.2, which is a possible value for paper (Niskanen and Kärenlampi, 1998). In parallel, the porosity exhibited a slight increase between images I1 and I2.

Close to the notch tip a significant increase in the local thickness and porosity was apparent in the map I3 (after the maximum force F_{max}), as indicated by the zones delimited with two parallel dashed lines. Note that this zone was only visible in these maps and not in the enhanced radiographs (Figure 4-7a). Thereafter, the crack path could be easily recognized in the maps I4 and I5 where the local porosity reached values above 90%, and the local thickness almost doubled. In addition, the average

thickness and porosity given in Table 2 showed an overall increase. This localised increase led to an overall increase in the mean thickness between the initial I1 and the final I5 images that was almost 13.5%, whereas the average porosity $\langle\widetilde{\Phi}\rangle$ exhibited a continuous increase, and the total growth was about 25%. Note that similar fracture mechanisms were observed in other samples of LDP that were also X-ray monitored. Therefore, these observations seem to be typical of crack initiation and propagation phenomena in LDP.

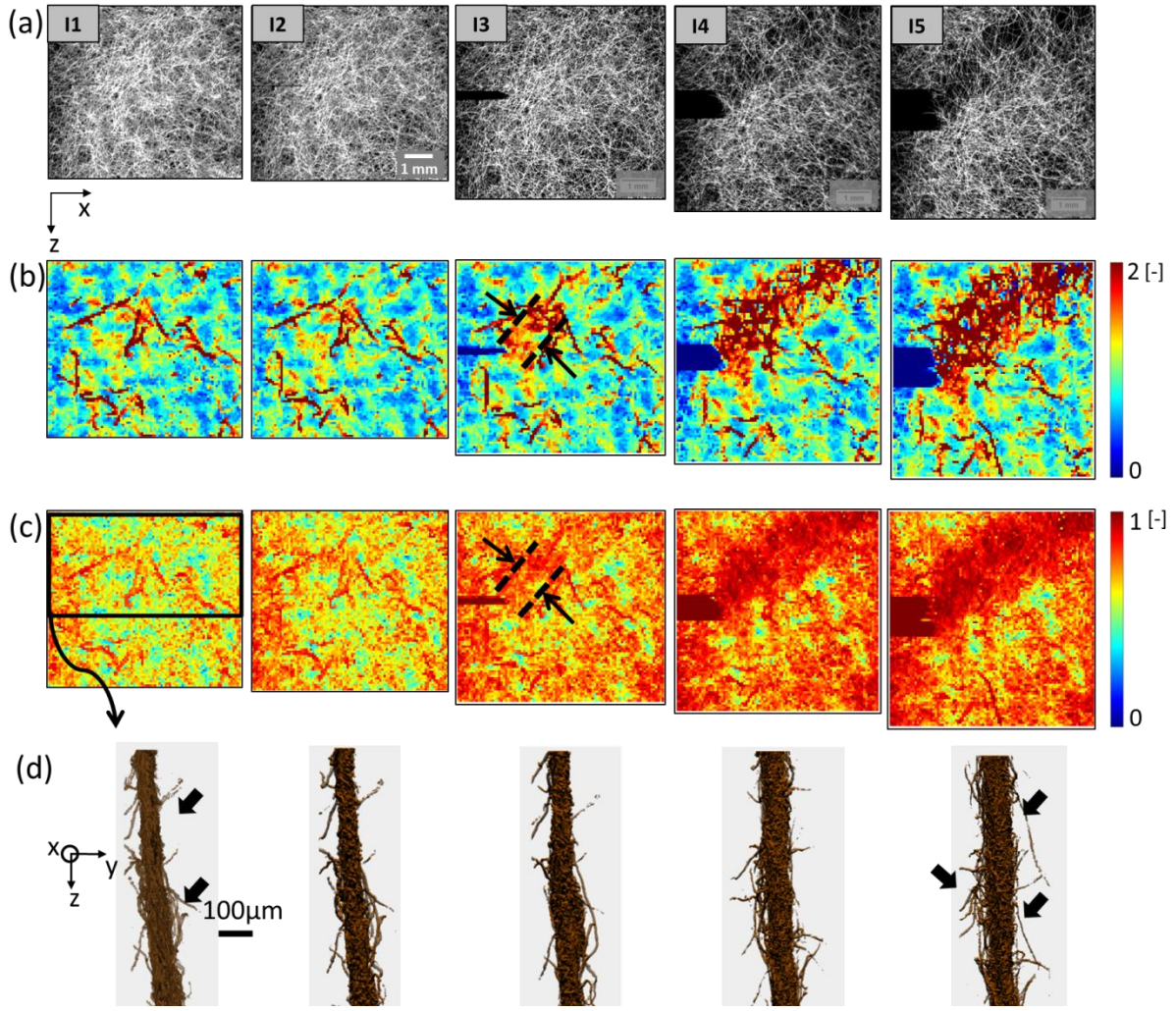

Figure 4-7 : (a) X-ray enhanced radiographs of 3D images of sample S1. (b) Normalised local thickness maps for the corresponding X-ray images, the analysing zone is 10×10 pixels; (c) Local porosity maps for the corresponding X-ray volumes, the analysing zone is 10×10 pixels; (d) Cross-section of the 3D X-ray volumes of upper part of the sample (as it is shown in Figure 4-7c). Fibre detachment is observed and indicated with the arrows. On the images the FPZ is indicated with the dotted lines.

Table 4-2 : Average structural parameters deduced from the local mapping analysed with AW10×10 pixels (70×70 µm^2) with $\langle\tilde{t}\rangle$ the average thickness, $\Delta\langle\tilde{t}\rangle$ the thickness variation considering the thickness in the image I1 as reference, $\langle\widetilde{\Phi}\rangle$ the average porosity, $\Delta\langle\widetilde{\Phi}\rangle$ its variation, $\langle\varepsilon_{yy}\rangle$ and $\langle\varepsilon_{zz}\rangle$ the average out-of-plane and the in-plane strains that were calculated considering the image I1 as the initial configuration of sample S1.

Images	I1	I2	I3	I4	I5
$\langle\tilde{t}\rangle$ [µm]	150.0	139.8	144.4	159.2	179.4
$\Delta\langle\tilde{t}\rangle$ [µm]	-	-10.2	4.6	14.8	20.2
$\langle\widetilde{\Phi}\rangle$ [%]	63.6	66.8	72.7	79.1	79.3
$\Delta\langle\widetilde{\Phi}\rangle$ [%]	-	3.2	5.9	6.4	0.2
$\langle\varepsilon_{yy}\rangle$ [%]	-	-6.8	3.1	9.9	13.5
$\langle\varepsilon_{zz}\rangle$ [%]	-	1.5	6.3	17	26

Fibre-bond detachment mechanisms – Figure 4-7d shows cross-sections of the images I1-I5 of sample S1 during SENT. An increase of fibre detachment phenomena occurred during crack propagation as it is evident for example in the image I5 where fibres that were detached at the end of SENT are shown by black arrows. However, the resolution of these images was not high enough to obtain clear observation of these phenomena at the fibre and bond scale. Therefore, these mechanisms were investigated in detail using the high resolution images of the notch tip of sample S2 (Figure 4-8).

In Figure 4-8, image C3 was taken in the linear part of the force-strain curve prior to F_{max}, images C4-C5 in the non-linear part prior to the force peak F_{max}, image C6 was taken when F_{max} was reached, and images C7 and C10 after F_{max}. The cross sections in Figure 4-8c show the progressive damage of samples and the corresponding thickness growth of the fibre network. In particular, Figure 4-8d and e show two groups of fibres (the group of fibres denoted F1, F2, and F3 and the group of fibres F4 and F5) that were manually extracted from the 3D images. In images C5 (prior to F_{max}), fibre F1 was in full contact with fibre F3, whereas fibre F2 was partially connected to fibre F3. Similarly fibres F4 and F5 were in contact. As evident from these images, during SENT, the imposed stress tended to rotate/twist the fibres (images C5 and C6) and to incrementally modify the geometry of the fibre-fibre bonds (contact area) until they broke (images C7). No preferential location of bond breakage along the fibres could be detected. Finally, once several were broken along a fibre, the detachment of this fibre from the network was observed. Fibre bond detachment was mainly observed just after the force peak, as shown in images C7 for both groups of fibres (Figure 4-8d and e). These phenomena were observed for several fibres in the area near the notch tip. Furthermore, it was also observed that the areas of few fibre-fibre bonds (not presented here) decreased but did not break: the fibres still remained attached, even after the force peak. The fibre rotation and detachment

during tensile test caused the paper thickness increase as it can be noticed in Figure 4-8d and e. Note also that no fibre breakage phenomena were observed during this experiment.

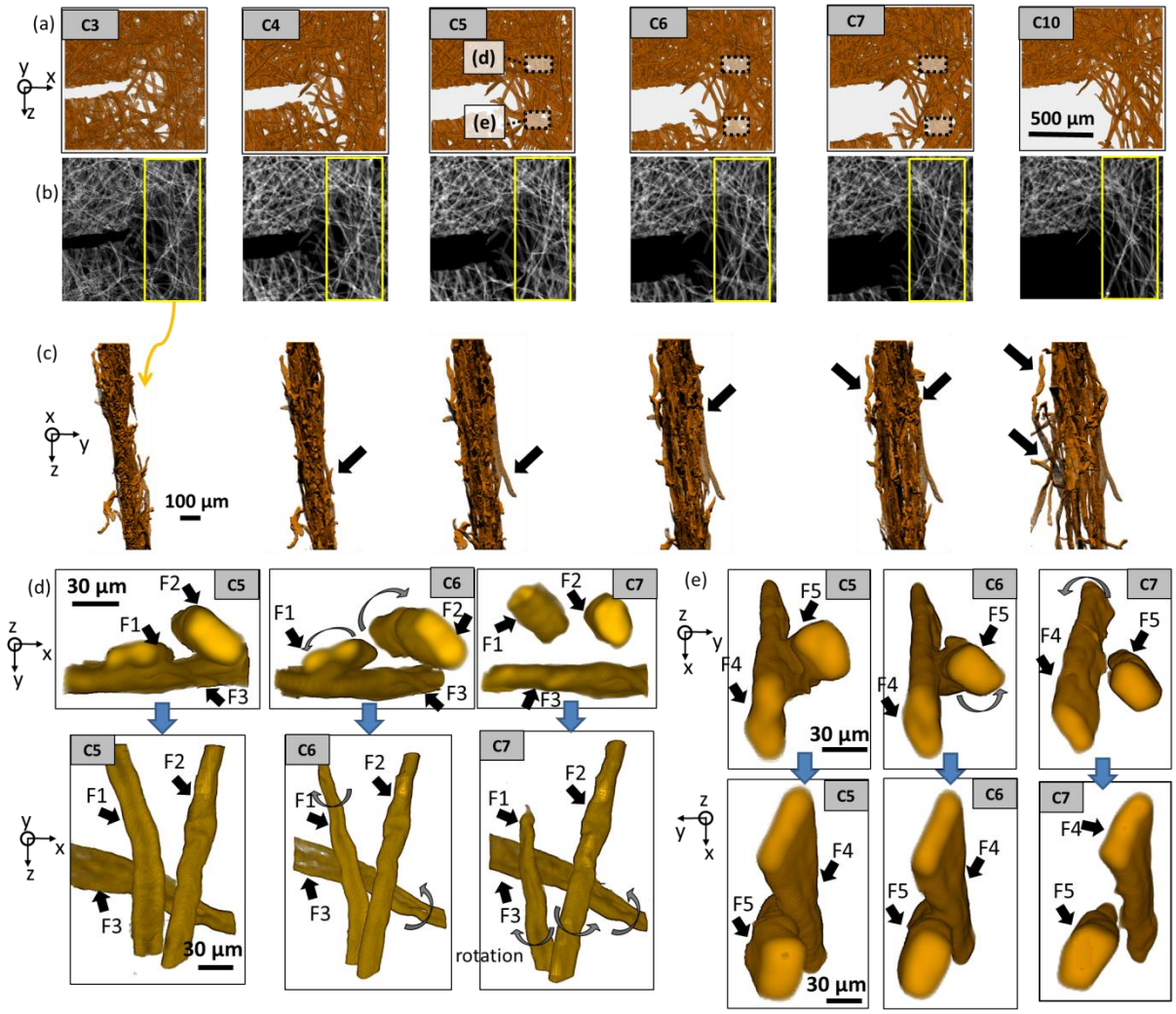

Figure 4-8 : (a) 3D images of sample S2 (voxel size of 0,55×0,55×0,55 µm^3). (b) X-ray enhanced radiographs of sample S2 (fibres are in grey and the air in black). (c) Cross sections of the images ahead of the crack tip. The arrows indicate out-of-plane deformation phenomena that occurred during SENT. (d,e) 3D images of two groups of fibres (F1, F2, F3) and (F4, F5) extracted from the 3D images of sample S2, showing the mechanisms of fibre detachment.

4.4 Discussion

The previous results confirm several previous experimental observations that are related to the fracture of LDP's:

- LDP's exhibit a low sensitivity to the presence of notches (Hägglund and Isaksson, 2006,Isaksson et al., 2012, Coffin et al., 2013), strain localised at the crack tip if the notch length was longer than a critical notch length $a_c \approx 3-4$ m, *i.e.*, for a critical ratio $\left(\frac{a}{w}\right)_c \approx 0.25–0.33$. Note that this length was smaller than the critical length that was determined in the previous chapter, *i.e.*,

approximately 9 mm even if the critical ratios $\left(\frac{a}{w}\right)_c$ were more or less the same. This discrepancy could have several origins. It could result from a variation in the structure of tested LDP samples compared to that of samples that were used in the previous study. However, this would be astonishing as the present samples were cut in the same paper sheet. This difference could also result from an effect of the geometry of samples (Hammond and Fawaz, 2016) since their height h to width w ratios, $h/w = 0.5 - 0.75$, was small. Such a low ratio may induce biaxial effects and result in lower critical notch length. In a previous study (*cf.* chapter 3), a gradient-enhanced model for fracture of low density networks was proposed. This model includes a length scale c. This length was estimated to be 3.2 mm for the studied LDP. In this approach, the critical length a_c is related to the internal length through the following expression (see also Isaksson and Hägglund, 2013):

$$c \approx \chi^2(0.3)^2\pi a_c, \tag{4-3}$$

where χ is a function that appears in the expression for the stress intensity factor which is given by

$$K_I = \chi\sigma^{\infty}\sqrt{\pi a}, \tag{4-4}$$

where σ^{∞} is the remote normal stress field acting far away from the crack. The function χ depends on the geometry of the test specimen, *i.e.*, the ratios a/w and h/w. In the present case, this function was estimated to range between 1.7 and 1.9, whereas for samples with a ratio $h/w \geq 2$, this ratio is equal to 1.12, thereby showing a large increase for the present experiments. However, the effect of the compact geometry of the specimens on the critical notch length should be further investigated, using for instance finite element simulation. In particular, it would be interesting to investigate the effect of out-of-plane displacements of the crack lips that are shown in Figure 4-5.

- The crack tip exhibited a blunt shape, which is characteristic of sparse fibrous networks (Isaksson and Dumont, 2014).
- Cracks did not exhibit a straight path (Salminen et al., 2003, Alava and Niskanen, 2006) and the crack paths were affected by mesoscale heterogeneities such as flocs in the paper structure, as shown by the analysis of crack paths using 2D optical micrographs.

In addition, the 3D images of fracture experiments of the studied LDP gave an original understanding of the mesoscale and microscale phenomena that led to the initiation and propagation of crack within these fibre networks and finally to their breakage. This technique is complementary to fractography which consists in the analysis of the roughness of cracks using 2D images of their profile, digital image correlation to determine the displacement and strain fields, thermography or acoustic

emission. For instance, acoustic emission has been widely used to follow events such as fibre or bond breakage during crack propagation. This technique enables crack events to be detected but it remains difficult to determine the nature of these events. By contrast, the medium-resolution 3D images, *i.e.*, 6.9×6.9×6.9 µm^3 voxel size, and their associated maps of local thickness, porosity and displacement components gave information about the localised deformation phenomena that occurred at the mesoscale in LDP's. Besides, high-resolution images, *i.e.*, 0.55×0.55×0.55 µm^3 voxel size, enabled several observations to be performed *in situ* and in real-time at the fibre or bond scale, *i.e.*, at the microscale, within the fibre network in the vicinity of the crack tip. Several important observations were done using the 3D images:

- The crack tip was preceded by a fracture process zone (FPZ) that exhibited a large thickness increase, *i.e.*, out-of-plane dilatancy phenomena, accompanied by a porosity increase (see for instance the thickness and porosity maps in Figure 4-7) before a distinct crack path or a macroscopic breakage became visible (Niskanen et al., 2001). The size of the FPZ is an important parameter that is taken into account to modify linear elastic fracture mechanics (LEFM) models by including a microstructural length (Niskanen et al., 2001, Coffin et al., 2013). It is seen as a material's parameter which has been shown to depend on the fibre length (Kettunen et al., 2000; Niskanen et al., 2001) for paper. In the studied LDP, the width of this zone was approximately equal to 1.5 mm (images I3 of Figure 4-7 and images of Figure 4-9 for a complementary specimen), *i.e.*, a width close to the aforementioned arithmetic fibre length of LDP. This order of magnitude corresponds to previously estimated sizes of FPZ for papers with quite similar structures such as for instance a tissue paper with a basis weight of 22 g m^{-2} as reported by Coffin et al. (2013). However, such a comparison with literature data is rather difficult as paper density as well as the properties of structural elements, e.g. fibre length or diameter, can largely vary from one paper to another.
- At the microscale, the analysis of high-resolution 3D images (in zones located ahead of the crack tip) showed that fibre-fibre bonds exhibited (large) deformation mechanisms prior to F_{max}. However, no fibre-fibre bond detachments were observed prior to F_{max} in these experiments. These phenomena were observed only after F_{max} in the present experiments. This result confirms previous observations for the accumulation of damage events that have been given by acoustic emission for tensile experiments performed on paper at low strain rates (Alava and Niskanen, 2006).
- In addition, our observations showed that LDP exhibited an increase in its thickness just prior to F_{max} and also after. Besides, the increase in the thickness of the samples was mainly caused by the increase in the thickness of zones where the deformation localised, such as the FPZ. Thus, it could infer from these observations that the microscale bond deformation (prior to F_{max}) and bond

breakage (mainly after F_{max}) and the resulting fibre detachment phenomena that are localised in these peculiar zones were at the origin of the thickness variations of LDP.

- It was also noticed that the slight change from a linear force-strain response of to a non-linear response prior to F_{max} of LDP was related to localised thickness increase (images of Figure 4-10 for a complementary specimen), and thus to localised fibre-fibre bond deformation phenomena. Hence, fibre-fibre bond deformation mechanisms that occurred prior to F_{max} could be at the origin of the apparent plastic mechanical behaviour of this paper. Note that this observation also sheds light on the micromechanisms that occur within the FPZ.
- Finally, the progressive decrease of the SENT curve after F_{max} was related to bond breakage phenomena (Figure 4-2), *i.e.*, damage phenomena. No fibre breakage was observed during these experiments.
- Note also that any clear increase in the thickness was measured for the studied LDP in its elastic regime of deformation, *i.e.*, the first linear part of the force-strain curves. On the contrary, in this deformation regime, the LDP thickness would rather decrease. Thus, contrary to some recent experimental results (Stenberg and Fellers, 2003, Verma et al., 2014) that were obtained for various papers, LDP did not exhibit any auxetic effects. However, as previously mentioned, our observations are also in accordance with the results that have been reported by Niskanen and Kärenlampi (1998).

At the microscale, our observations also showed that fibre bond detachment mechanisms were accompanied by complex deformation mechanisms of the fibres that were in contact (or bonded). It was seen that fibres exhibited complex torsion (and probably bending) movements. The origin of these movements is certainly the complex anisotropic mechanical behaviour of fibres that exhibit torsion-traction coupling effects, due to their peculiar structure (helical arrangement of cellulose microfibrils in the S2 layer of fibres). Of course, dried-in strains due to papermaking operations such as wet-pressing and drying, have also certainly an effect on the magnitude of these deformation mechanisms and would require further investigation.

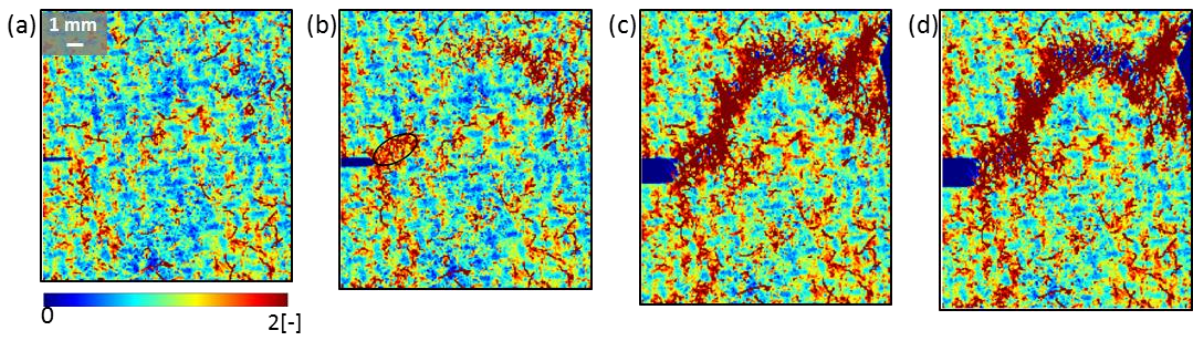

Figure 4-9 : Series of thickness maps of a SENT specimen ($w = 15$ mm, notch length $a = 3$ mm) that shows the FPZ (circled by the black ellipse in the second image of the series) and the development of the crack. Note that the second image was taken prior to F_{max}. Note also a second zone, far from the crack tip, where large thickness variations occurred prior to the complete formation of the crack path.

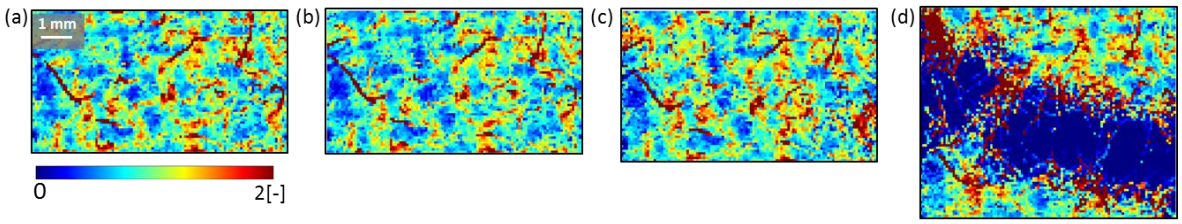

Figure 4-10 : Series of thickness maps of a specimen ($w = 15$ mm, without notch) subjected a tensile experiment. The third image was taken prior to F_{max}, *i.e.*, in the "plastic" deformation regime. The black arrows show two zones that exhibit a marked thickness increase.

4.5 Conclusion

The objective of this study was to experimentally determine the multiscale phenomena that accompany crack initiation and propagation in low density papers (LDP's). Optical and X-ray microtomography imaging techniques during fracture tests combined with advanced image analysis were used to reveal the fracture mechanisms that occurred in LDP. For that purpose, a mini tensile device was designed and enabled the imaging of the sample deformation either under a microscope or during X-ray microtomography *in situ* tensile tests that were performed on single edge-notched samples. The developed image analysis procedures allowed several fracture phenomena in the LDP to be studied: the fracture mostly localised in the antiflocs (the zones of low mass density) of paper, and the crack propagated mainly in the antiflocs, avoiding the flocs (the zones of high mass density). The analysis of 3D images revealed that the crack propagation induced in-plane and out-of-plane deformation phenomena such as the increase in the paper thickness. In particular, these phenomena localised in the Fracture Process Zone (FPZ), *i.e.*, the microscopic fracture localization zone, ahead of the crack tip. The width of FPZ was equal to approximately twice the arithmetic fibre length. In addition, the application of Digital Volume Correlation (DVC) on the 3D X-ray microtomography images allowed us visualise the inhomogeneity of the displacement field observed even before a distinct crack path occurred. These mescoscale changes were accompanied by microscale deformation mechanisms such as, for instance, rotation and twist of the connected fibres during tensile tests, decreasing the contact/bond areas between them and eventually leading to the bond breakage. The rotation and the detachment of fibres were at the origin of an increase of the thickness and porosity in the thickness direction of paper and could also be at the

origin of the apparent plasticity of LDP prior to the maximum tensile force. It would be interesting to complete these results by performing observations of larger specimens using high-resolution X-ray images. This approach would allow us to detect fibre and bond deformation and breakage phenomena all along the crack path at the imaging resolution. Then, these results would be used to test models for the prediction of the evolution of paper structure along a crack path such as for instance the models that give a prediction of the number of fibres that are intercepted by the crack when it develops (Sampson, 2009). It would also help to give a better description of the deformation kinematics of fibres and bonds as local digital image correlation techniques could be used to perform within the fibre network these measurements at a very fine scale.

Acknowledgements

This work has been partially supported by the LabEx Tec 21 (Investissements d'Avenir - grant agreement n°ANR-11-LABX-0030). The authors are grateful for the technical support provided by Mikaël Party, Denis Curtil, from LGP2 laboratory (Grenoble, France), and Pascal Charrier, from 3SR laboratory (Grenoble, France). The authors acknowledge Paul Scherrer Institut (PSI), Villigen, Switzerland, for provision of synchrotron radiation beamtime at the beamline TOMCAT of the Swiss Light Source and Anne Bonnin (PSI) for the help in X-ray image acquisition.

Chapter 5. 3D X-ray real-time and *in situ* characterisation of fracture phenomena of sparse fibre network under different relative humidity conditions

Content

5.1 Introduction

This chapter aims at studying deeply the influence of Relative Humidity (RH) on crack propagation mechanisms in the considered Low Density Paper (LDP). Two series of experiments were conducted. The first one concerns the influence of RH on the crack propagation mechanisms in different samples of the LDP. The second one concerns the influence of a change in RH during the crack propagation.

These two studies were carried out using the experimental tools developed during this PhD and presented in chapter 2: The fracture tests with controlled MC were monitored using the X-ray microtomography set-ups of the 3SR laboratory and of

TOMCAT beamline at SLS at both micro- and mesoscales. The results were obtained using the advanced imaging procedure and digital volume correlation techniques.

This chapter is organised in two sections 5.2 and 5.3, in which the results are presented and discussed. Each section corresponds respectively to the first and the second aforementioned studies.

5.2 Influence of relative humidity on crack propagation mechanisms

5.2.1 Paper samples and tests

The studied paper is a low density paper (LDP) (23 g m^{-2}) described in chapter 2. Its thickness (t) is 113 ± 7 µm measured using standard. The samples of LDP were prepared according to the procedure described in chapter 2. A notch of length a of 4 mm was cut at the mid-height and one edge of the sample. The samples were stored in the ambient conditions: temperature (T°) of 23 °C and a relative humidity (RH) of 52 % for at least 24 hours before the experiment.

5.2.2 Imaging procedures

The experimental multiscale procedure performed at SLS for three RH conditions is recalled:

i. The studied sample was placed in the mini tensile device with an initial distance between clamps of 6 mm and the RH inside of the chamber was regulated to a desired level using the wet air generator.

ii. The initial X-ray 'mesoscale' scan of the paper sample was performed at 6.5 µm of effective voxel width with a time scan of about 45 s. Due to the limited field of view (13.3 x 4.0 mm^2) the image acquisition was performed in two steps: a first 'top' image included a part of the top clamp and the upper half part of the sample and a second 'bottom' image which covers the rest of the sample and a part of the bottom clamp.

iii. The image acquisition system was changed in order to perform a real time X-ray scanning at 0.55 µm of the effective voxel width during a continuous tensile test. This 'microscale' image acquisition was performed at the notch tip area with a field of view of 1.1 x 1.1 mm^2. Each 'microscale' image was obtained in 3 s and a sequence of 10 images were acquired every 200 s to total time of 45 min.

iv. At the end of the tensile test, the image acquisition system was changed back to the lower resolution in order to obtain the final 'mesoscale' according to procedure of step ii.

Due to the difficulty to place the sample in the tensile machine, a pre-stretch of the sample was applied in order to straighten the sample. The velocity of the tensile test of 0.06 mm/min was chosen in order to obtain images of a decent quality during step ii. All the experiments were conducted at room temperature i.e. 25°C. Four samples were submitted to fracture tests for a given RH while imaging as described in next section:

- S1 was scanned at 50 % of RH in an interrupted way in the 3SR laboratory and analysed in detail in chapter 3;
- S2 was scanned at 50 % of RH using a multiscale and continuous approach at SLS which continuous test was presented in chapter 3;
- S3 was scanned at 15 % of RH using a multiscale and continuous approach at SLS in this chapter;
- S4 was scanned at 75 % of RH using a multiscale and continuous approach at SLS in this chapter.

Each obtained data sets was processed as follows:

i. The reconstructed 3D greyscale datasets were converted into binary images where the fibre phase and the pore phase were separated. The noise and ring artefacts were removed when needed.
ii. The binarised 'mesoscale' images, previously concatenated, were used to obtain the local thickness and porosity maps. An analysis window (AW) of 10 x 10 pixels (=65 x 65 µm^2) was chosen.
iii. The binarised concatenated 3D images were projected in the thickness direction of the paper sample to provide 2D enhanced radiographs. Such data were used to analyse the formation of paper.

5.2.3 Preliminary remarks

TOMCAT beamline enabled to perform sophisticated and unique experiment with a complex set-up that lasted 48 hours including the set-up of the X-ray microtomograph by A. Bonnin, the scientist in charge of TOMCAT beamline. Due to the complexity of the whole experiment, our group faced technical problems resulting in the missing data sets. Let's present them in details:

- Due to a misalignment of the rotation stage on which the mini tensile device was mounted and the detector during image acquisition, the 'mesoscale' image of the sample S2 after the traction test was partially acquired and could not be exploited. As mentioned in chapter 3, similar fracture mechanisms are observed when comparing interrupted and continuous tests. Therefore, sample S1 acquire in an interrupted manner was recalled to complete the analysis of the missing data of S2.
- The power glitch caused by the meteorological conditions (storm) resulted in the X-ray beam loss during the real time scanning of the fracture test of

the sample S4. The first two scans of the series were recorded but were unfortunately blurred.

- The fluctuations in the RH ,varying from 70 % to 83 % of RH, during the tests at 75 % RH were due to variation of pressure of the compressed air needed for the wet air generator. We assumed that the test was carried at 75 % RH.
- A small defect appeared in the top 'mesoscale' image: several slices of the bottom of this 3D volume were missing. It comes from the fact that the overlapping zone between top and bottom image was miscalculated, inducing an inaccurate concatenation of top and bottom images. The zone with a small defect is indicated in the images using a rectangle.

Due to the limited amount of time, the partially successful experiment could not have been repeated.

5.2.4 Results

5.2.4.1 Influence of RH on the fracture tests

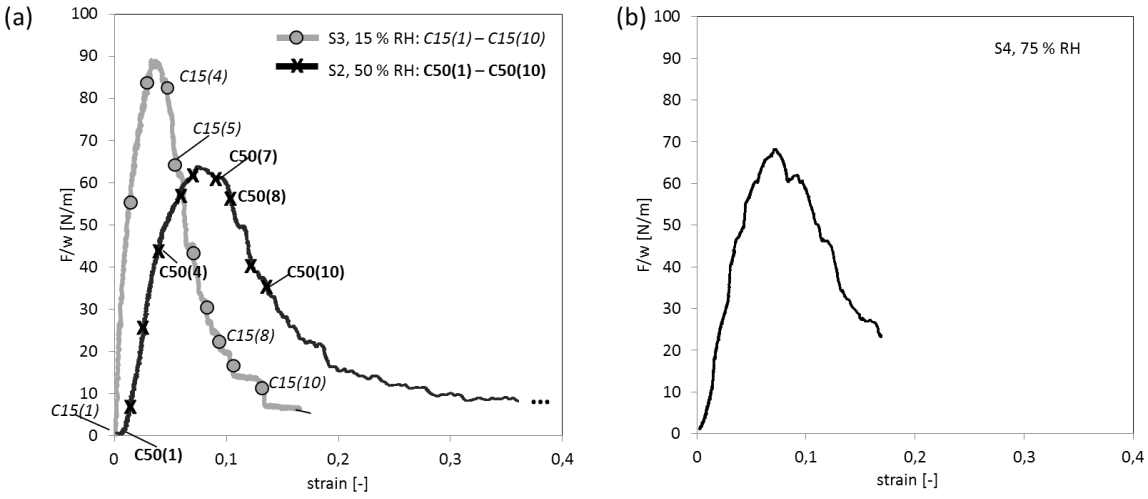

Figure 5-1 : Graphs of the load F/w vs. axial strain: (a) for the samples S2 and S3. Each X-ray scan performed during continuous traction tests is indicated (for S3: C15(1) – C15(10); for S2: C50(1) – C50(10)); (b) for the sample S4.

Figure 5-1a and b represent the strain-stress curves obtained during the three fracture tests at SLS. It should be noticed that force F were normalised according to the width of the sample which is a common way in paper physics (Niskanen, 1998). Regardless the RH, one can observe a similar mechanical behaviour: at small strain a linear region prevails; then the plastic region appears until the peak is reached. The fracture starts to occur at the maximum load and the strength of paper decreases slowly. Those trends of the mechanical responses, typical of low density papers, are coherent with the previous observations documented in the chapters 3 and 4 and the literature review (chapter 1). For sample S2 and S3 we can also observe that the

main characteristics of the curve (Young's modulus, maximum load, size of the plastic regions) are moisture dependant. The difference for the samples S2 and S4 is less pronounced.

5.2.4.2 Influence of formation on crack propagation for various *RH*

Figure 5-2c, Figure 5-3b, Figure 5-4c and Figure 5-5c illustrate the flocs and antiflocs identification on the initial X-ray enhanced radiographs (Figure 5-2a, Figure 5-3a, Figure 5-4a and Figure 5-5a acquired for 50 % *RH* in an interrupted manner, and 15 % *RH*, 50 % *RH* and 75 % *RH* in a continuous manner, respectively. The corresponding final X-ray enhanced radiographs are shown as well. One can observe that regardless the *RH*, the crack propagated in the antiflocs (yellow ellipses in Figure 5-2c, Figure 5-3b, Figure 5-4c, Figure 5-5c avoiding the flocs (red ellipses).

A detail observation of each sample of these figures shows that:

- When the notch tip is surrounded by antiflocs (sample S3 at 15 % *RH*), the crack is attracted by the biggest antifloc and propagated through it.
- When the notch tip is surrounded by flocs (sample S1 at 50 % *RH*), the crack is attracted by the biggest and closest antifloc and propagated around the flocs in the vicinity of the notch.
- When the notch tip is surrounded by two series of antiflocs (sample S4 at 75 % *RH*), the crack is attracted by the longest series of antifloc. Moreover the small floc indicated by an arrow in Figure 5-5b affected the direction of the crack propagation.

This analysis of the link between the location of the notch tip regarding the formation and the location of the crack path is coherent with the observations made in the previous chapter 4 at 50 % *RH*, confirming that the part of the phenomenon are independent of the *RH*.

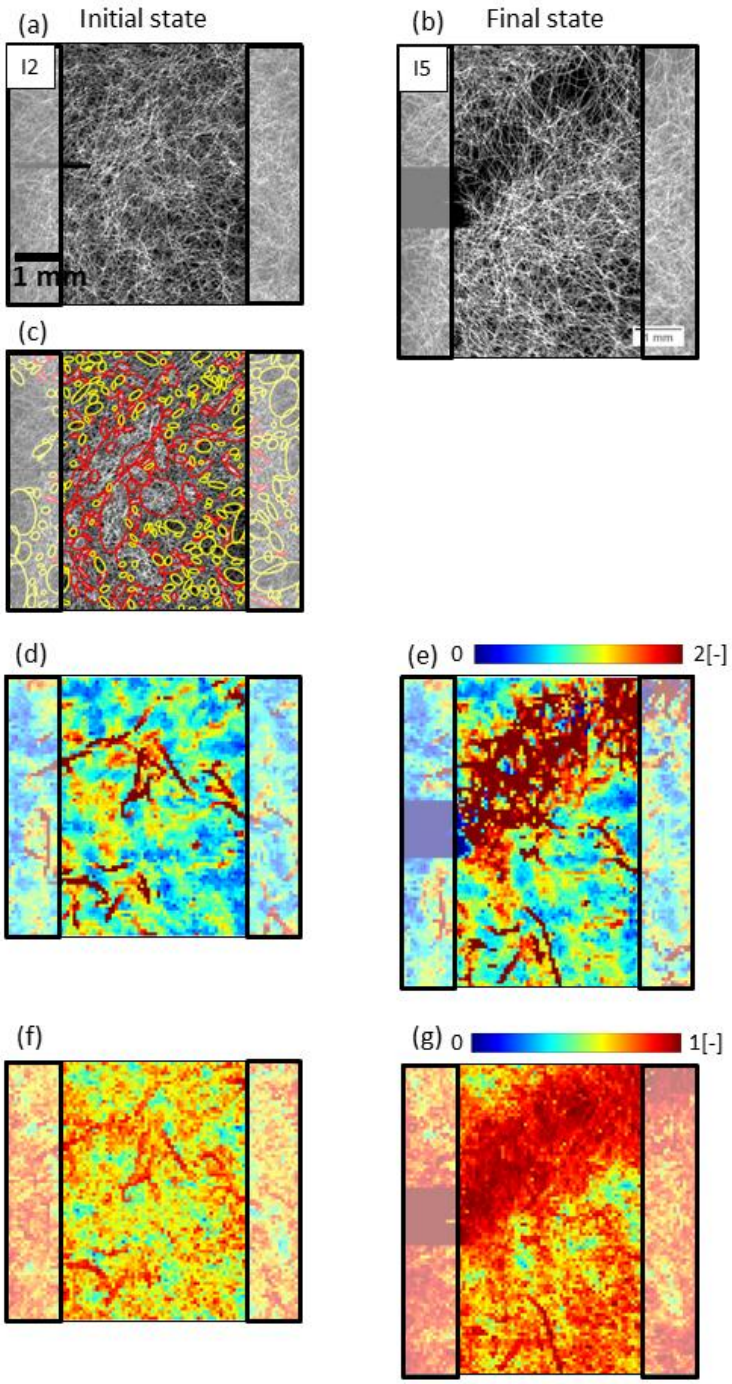

Figure 5-2 : Sample S1: Mesoscale analysis of the interrupted fracture tests carried out at 50% RH (a-b) initial and final enhanced radiographs; (c) floc (in red) and antifloc (in yellow) identification on image (a); (d-e) normalised thickness maps of initial and final states; (f-g) porosity maps of initial and final states. The thickness maps were normalised with the mean thickness of the initial state.

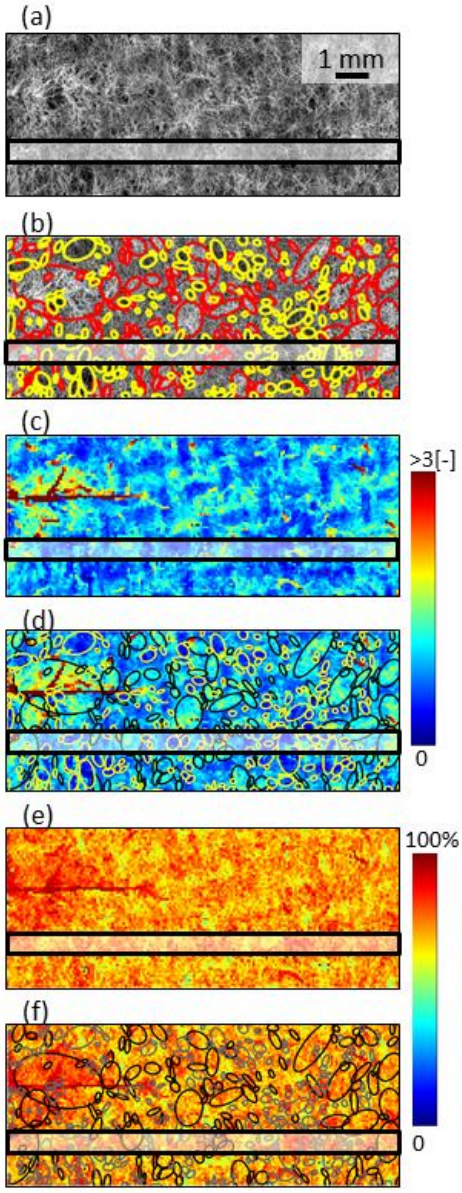

Figure 5-3 : Sample S2: Mesoscale analysis of the continuous fracture tests carried out at 50% *RH* (a) initial enhanced radiograph; (b) floc (in red) and antifloc (in yellow) identification on image (a); (c) normalised thickness map of initial state; (d) floc (in black) and antifloc (in yellow) identification superimposed on the normalised thickness map (e) porosity map of initial and final states, (f) floc (in black) and antifloc (in grey) identification superimposed on the normalised thickness map.

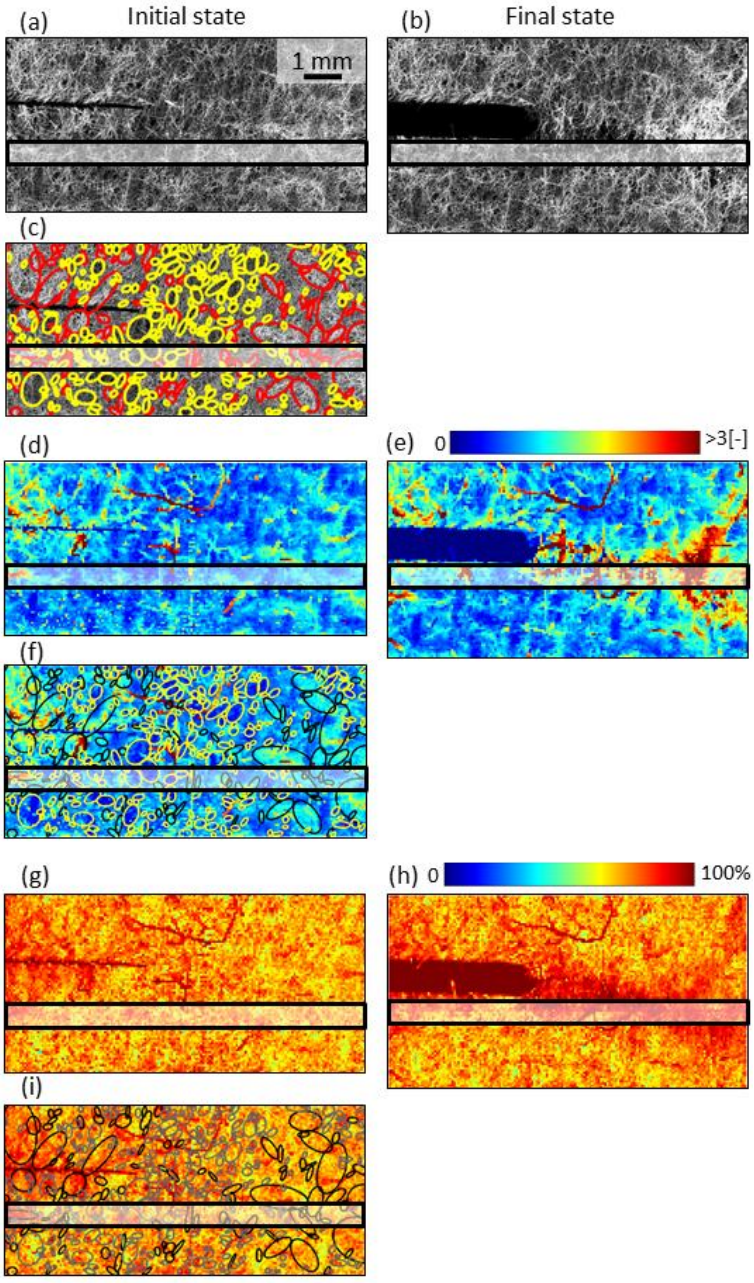

Figure 5-4 : Sample S3: Mesoscale analysis of the continuous fracture tests carried out at 15% *RH* (a-b) initial and final enhanced radiographs; (c) floc (in red) and antifloc (in yellow) identification on image (a); (d-e) normalised thickness maps of initial and final states; (f) floc (in black) and antifloc (in yellow) identification on the image superimposed on the normalised thickness map in the initial state; (g-h) porosity maps of initial and final states; (i) floc (in black) and antifloc (in grey) identification on image superimposed on the normalised thickness map in the initial state.

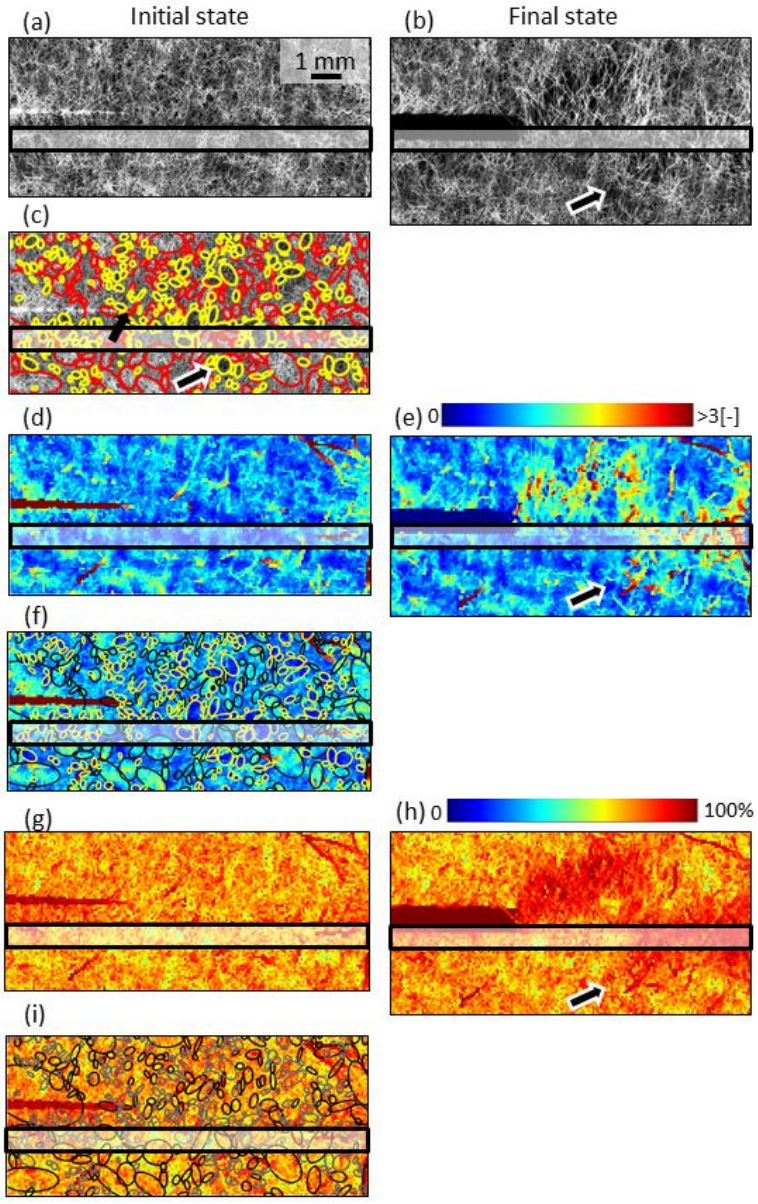

Figure 5-5 : Sample S4: Mesoscale analysis of the continuous fracture tests carried out at 75% *RH* (a-b) initial and final enhanced radiographs; (c) floc (in red) and antifloc (in yellow) identification on image (a); (d-e) normalised thickness maps of initial and final states; (f) floc (in black) and antifloc (in yellow) identification on image superimposed on the normalised thickness map in the initial state; (g-h) porosity maps of initial and final states; (i) floc (in black) and antifloc (in grey) identification on image superimposed on the normalised thickness map in the initial state.

5.2.4.3 Out-of-plane mechanisms

The mechanisms of the crack propagation were analysed in the thickness direction using the local thickness and porosity maps. The obtained results are presented in Figure 5-3b, Figure 5-4c and Figure 5-5c, for 15 %, 50 % and 75 % of *RH*, respectively. All the thickness maps were normalized with their initial mean thickness of 150 µm, 150 µm, and 152 µm, respectively.

For different *RH*, one can observe similar inhomogeneous thickness variation in the initial local maps: the areas with larger thickness correspond to the higher mass distribution, i.e. flocs, in the enhanced radiographs and wise worth. Moreover, higher thickness areas have higher porosity as observed in the porosity maps as illustrated by the images where the floc identification have been superimposed on the corresponding maps (Figure 5-3c, Figure 5-4f, Figure 5-5f).

Regardless the *RH*, crack path can be characterised by a continuous zone of high porosity and high thickness compared to the initial porosity and thickness at similar locations. These area corresponded to the crack paths visualised on the X-ray enhanced radiograph (Figure 5-2b, Figure 5-4b and Figure 5-5b). However in the case of sample S4, the area indicated with an arrow in Figure 5-5b corresponds to an antifloc but could have been visually considered as an existing crack path or a damage zone. As the thickness and the porosity maps of S4 do not exhibit major structural changes in that area, we assume that this area was not significantly affected by the fracture test in the thickness direction. Nevertheless, one can observe the pore size growth, illustrating in-plane mechanisms of deformation.

5.2.4.4 Fracture phenomena observed at the microscale in different RH conditions

Figure 5-6 represents the paper network in 3D for 15 % and 50 % of *RH* obtained at high resolution in the continuous way. Figure 5-7 represents the images of the manually selected fibres from Figure 5-6 acquired along the stress – strain curve: C15(2) and C50(4) were obtained in the elastic region, C15(3), C50(5), and C50(6) were acquired in the plastic region just before the stress peak and C15(4), C50(7) just after the peak. According to Figure 5-6 and Figure 5-7, we can observe that:

- in the elastic domain, the curved fibres become more straight and the inter-fibre bonds remain intact;
- in the plastic region, some fibres start rotating to become straighter which caused a partial bond / contact breakage;
- after the peak, the bonds break and some fibre pull out in the crack path.
- no breakage of the fibres were observed.

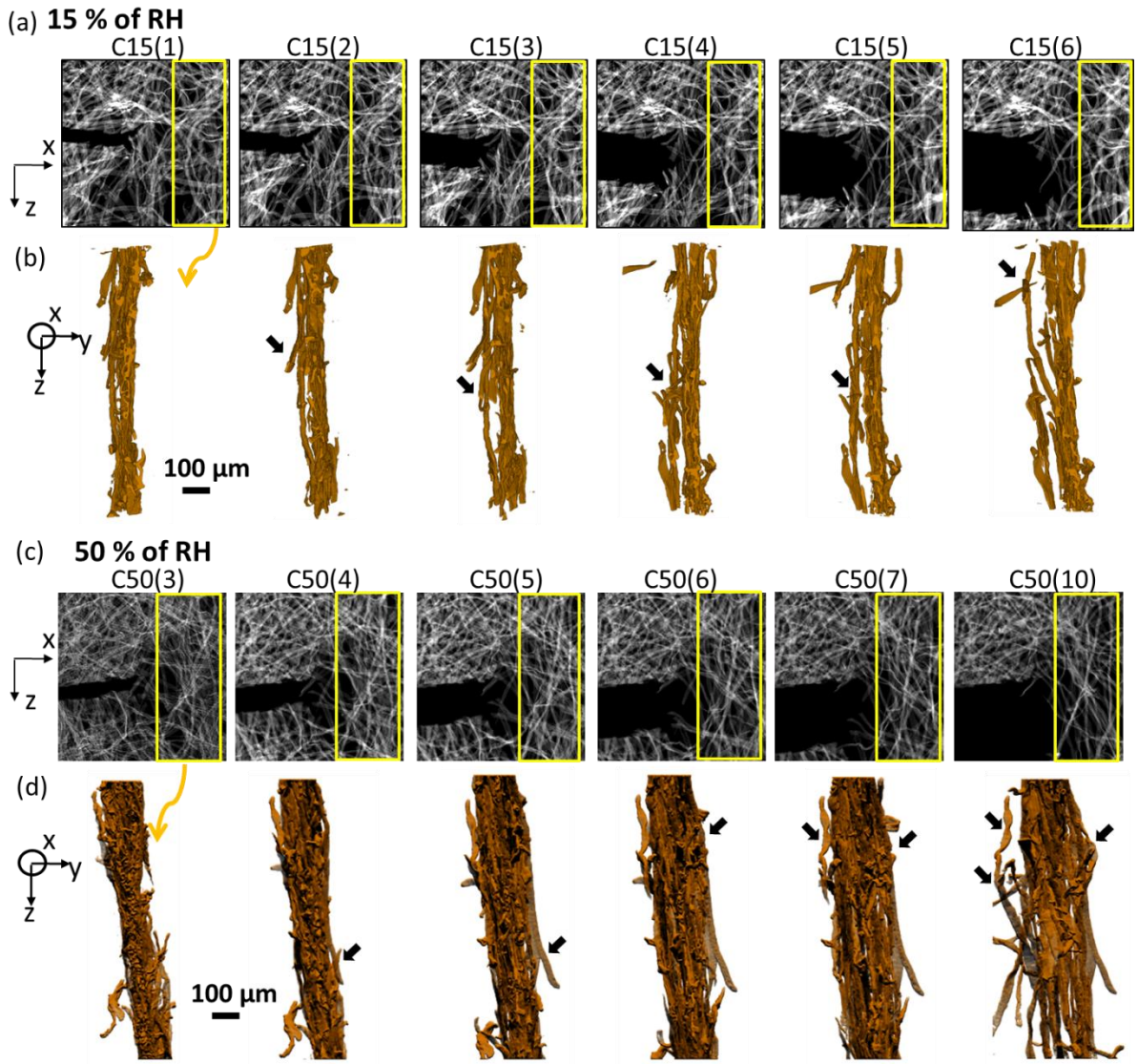

Figure 5-6 : 'Microscale' images of the crack tip area obtained using real-time scanning at 15 % and 50 % of *RH* during tensile test: the X-ray enhanced radiographs obtained at (a) 15 % and (c) 50 % of *RH*; cross section 3D views at (b) 15 % (in greyscale) and (d) 50 % of *RH* (in colour) whereas fibre detachment is indicated with the arrows.

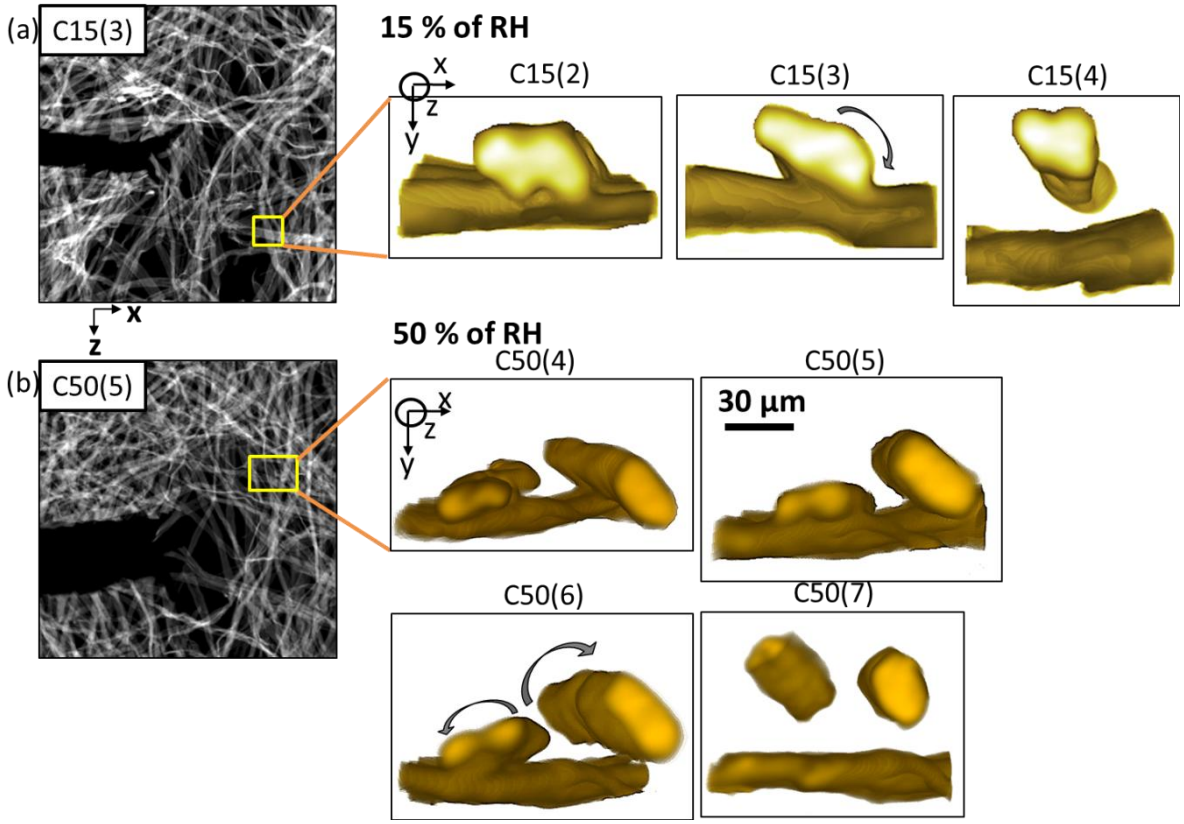

Figure 5-7 : Fibre detachment mechanism in the selected area of the samples (a) S3 and (b) S2. C15(2) and C50(4) were obtained in elastic region, C15(3), C50(5), C50(6) - in the plastic region just before the stress peak and C15(4), C50(7) – just after the peak.

5.2.5 Discussion

5.2.5.1 Influence of *RH* on the mechanical response

According to the experimental results presented above, from a structural point of view there are no major differences in the crack initiation and propagation mechanisms in the studied LDP due to a change in *RH*. The main difference may concern the level of force. Namely, it is well known the mechanical properties of the fibres and of the inter-fibre bonds decrease with an increase of *RH*. The experimental results presented in chapter 3 (Figure 3-7) showed that the evolution of the force versus the notch length independent of *RH*. It first exhibits a plateau and then a linear decrease, however the values of the plateau being moisture dependent. Applying these results to the similar curve for the mesoscale sample (see chapter 4, figure 4-4), we can assume that the proposed fracture tests were performed after the knee. The relatively large error bar (Figure 3-7) for the maximum force is caused by the high structural heterogeneities of the samples and thus, it is difficult to conclude, in a certain way, about the effect of moisture on the mesoscale mechanical behaviour of the samples presented in Figure 5-1.

5.2.5.2 Influence of formation on crack propagation for various *RH*

The results presented in the previous section show that the localization of the crack path is independent on *RH*: it propagates around the floc and in the longest chain of antiflocs. As mentioned in chapter 3, fracture models that aim at describing the crack initiation, are based on an internal length that is independent on *RH*. This internal length was related to the size of antiflocs. Assuming antiflocs can be represented as ellipses, their mean major axis was found to be 223 µm, 220 µm, 221 µm and their minor axis 119 µm, 120 µm and 120 µm for 15 % *RH*, 50 % *RH* and 75 % *RH*, respectively. This shows that the average size of antiflocs or chain of antiflocs is independent on the *RH*, confirming the fact that the size of antiflocs is a good candidate for the internal length for damaging models.

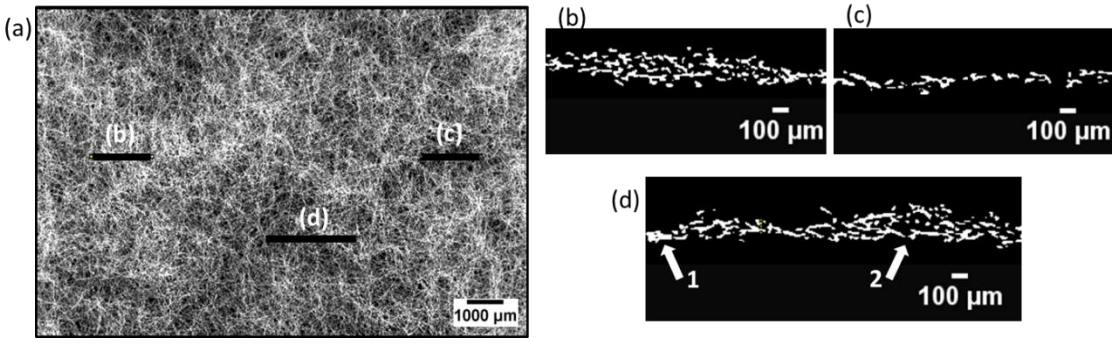

Figure 5-8 : (a) X-ray enhanced radiograph of the LDP. Cross sections from the 3D images were obtained along: (b) floc; (c) antifloc; (d) transition from an antifloc to a floc.

To deepen the understanding of the reason why antiflocs are the areas of fracture localisation and the damage mechanisms, a better analysis of the structure of antiflocs must be perfomed. Figure 5-8 (b-d) illustrates the views of local paper thickness in the floc and the antifloc identified in Figure 5-8a. The visual comparison of these regions shows that the flocs have a larger thickness, a higher porosity and a higher number of fibres than antifloc. This induces fewer inter-fibre bonds in antiflocs than in flocs. As illustrated in Figure 5-6, in LDP the inter-fibre bonds break during loading, and thus, the crack rather propagates in the antiflocs with less number of inter-fibre bonds to break. Moreover, the fact that no fibre breaks can be explained by lower strength of inter-fibre bonds in comparison with the strength of fibres.

5.2.5.3 Out-of-plane mechanisms

- The experimental results on the mesoscale do not show an increase of the thickness with humidity despite the fact that when the cellulosic fibres absorb water from the air their transverse dimension can generally increase up to 30 % (Haslach Jr, 2000; Joffre et al., 2016). This is an effect of the resolution of the 'mesoscale' images. At an effective pixel size of 6.5 µm, the mean fibre width at 50 % of *RH* contains about 4 pixels. If the fibre dries up to 30% of its dimension the fibre width will be about 3 pixels. This difference of 1 pixel is in the error bar of the segmentation of the image.

- The thickness maps in the crack path indicates a high local increase of the local thickness, regardless the *RH*. The 3D views of the initial microstructure in the initial state show that the fibres are not perfectly stretched in the machine direction. The detachment of the fibres in the crack path during the traction is responsible of the thickness increase. On the other hand, no significant out-of-plane fibre detachment was observed outside the crack path. This comes from the fact that above a critical length of the notch, the crack localises at the notch tip (see chapter 3 and 4).

5.2.5.4 Comparison with literature

All the previous observations confirm the results from indirect measurement that aimed at explaining the stress – strain behaviour regarding the micro structural events related to fibres and inter-fibre bonds. For example, using acoustic emission technique (Isaksson et al., 2006) concluded that (i) the main damage mode occurred in rather low density paper was a bond failure (ii) the fibre rearrangement due to tensile tests implies the fibre pull-outs in particular in the fracture path. Using 2D technique (Kettunen and Niskanen, 1998) observed that the damage mechanism occurred due to fibre debonding in the paper sample made of ductile kraft fibres. (Isaksson et al., 2012) stated that the crack growths via bond fractures in the low and in the high density papers qualitatively analysed using X-ray microtomography.

According to (Wong et al., 1996) the local grammage and the local strains are inversely proportional, meaning that high strains occur in regions of relatively low grammage which is coherent with our observations that the crack propagated in the antiflocs.

5.3 Influence of a change in relative humidity during a fracture tests

5.3.1 Paper samples and tests

This investigation was conducted on the sample S4 described in section 5.2.1.

5.3.2 Imaging procedures

The experimental multiscale procedure is summarized below. It consists of two parts: the first part that corresponds to the fracture test carried out at 75 % RH (section 5.2.2) that was stopped before the total failure of the sample. The second part corresponds to the drying of this sample. Here is the protocol:

First part: tensile test at 75% RH

i. 'Mesoscale' image acquisition at 75 % *RH* of the sample before loading;

ii. Fracture test at 75 % of *RH*. The fracture test was stopped when the axial strain reached 17 % after the force peak and the clamps were kept at the same position until the end of the experiment;

iii. 'Mesoscale' image acquisition at 75 % of *RH*.

Second part: drying part

iv. Decrease of the *RH* from 75 % to 22 % inside the humidity chamber that afterwards stabilized at 22 % during 7 min.

v. 'Mesoscale' X-ray image acquisition of the sample at 22 % of *RH* after a stabilization of 70 minutes.

The experiment was conducted at room temperature 25°C.

The obtained images were processed following methods described in section 5.2.2. Moreover, Digital Volume Correlation (DVC) was performed using 3D images of sample S4 obtained at step iii) and v). The input images were previously masked using corresponding binarised images. The top and bottom 'mesoscale' images were correlated separately using the code "TomoWarp2". The obtained results were then concatenated.

5.3.3 Results

5.3.3.1 Mechanical response of the sample to the drying

Figure 5-9 illustrates the temporal evolution of the force and the *RH* during the drying part. One can observe that the humidity can be considered as constant. The variations of *RH* around 10 minutes correspond to interferences between the cabling of the *RH* sensor and the rotation stage during the real time scanning, which is not presented here. One can note an increase of 0.06 N during the drying.

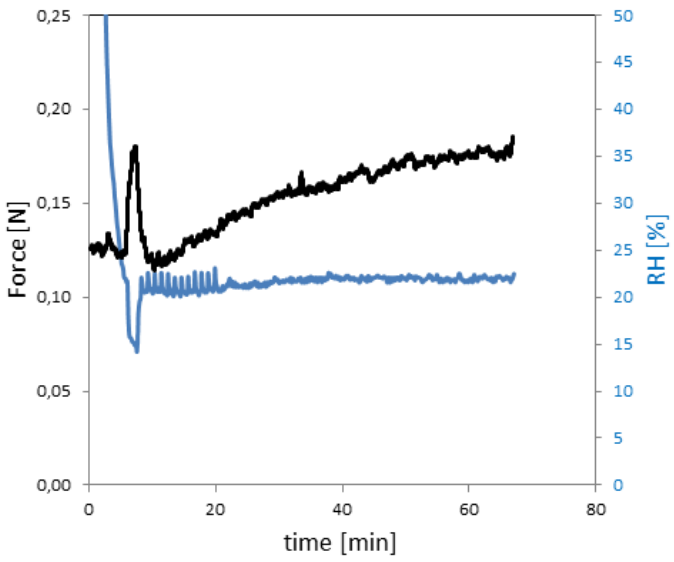

Figure 5-9 : Temporal evolution of force and of the relative humidity during drying.

5.3.3.2 Microstructural changes

Figure 5-10a and b represent the enhanced radiographs in the initial and final state of the drying process, where we cannot visually observe significant changes. The comparison of the local thickness maps presented in Figure 5-10c and d present an average decrease of the thickness of 3.4 µm despite some local increase by 2 – 3 times indicated by arrows up. These microstructural variations occurred mainly in the crack path, damaged including the areas next to the notch lips. The average porosity of the sample remained constant at 76 % and no significant local change of the porosity was observed in Figure 5-10(c).

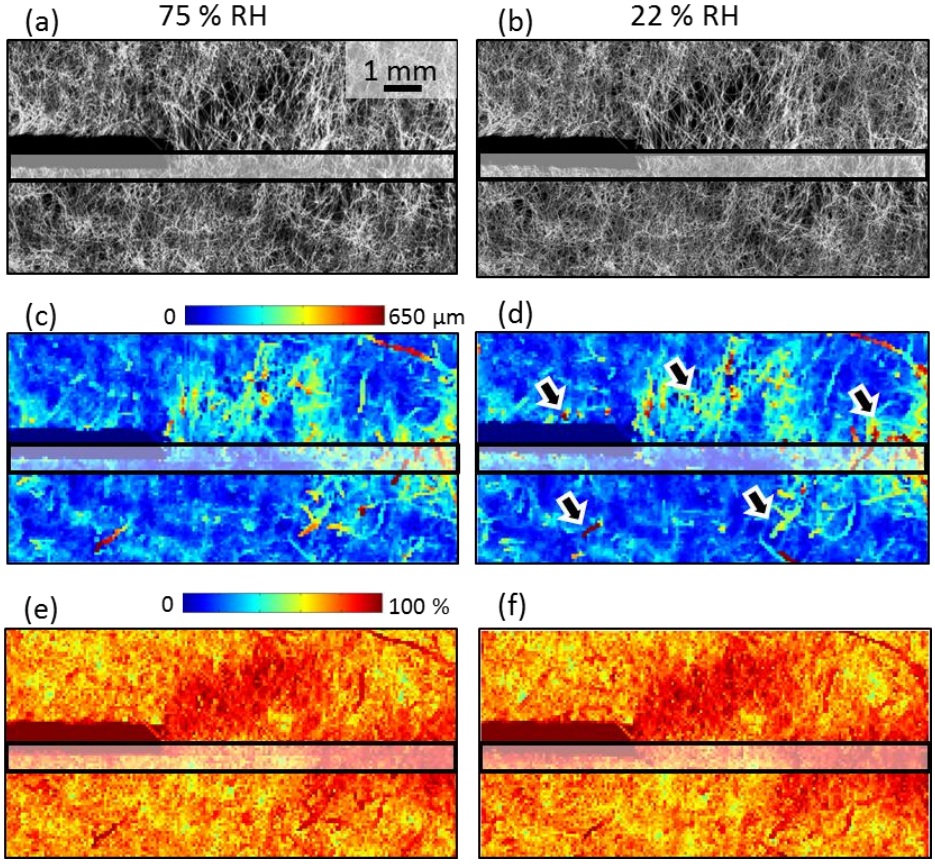

Figure 5-10 : Sample S4: Mesoscale analysis of the drying tests carried out at 75% and 22 % of *RH* (a-b) initial and final enhanced radiograph; (c-d) thickness map of initial and final state; (e-f) porosity map of initial and final state.

5.3.3.3 Displacement fields

The DVC analysis was performed on the 3D X-ray images before and after the drying. In Figure 5-11, the displacement fields in each of three directions: u_x in the in-plane transverse direction (CD), u_y in the thickness, and u_z in the loading direction (MD) are presented according to the procedure described in chapter 2. One can observe an inhomogeneous displacement fields in all three directions:

- In the loading direction (Figure 5-11c), the displacement field u_z indicates a zeros displacement closed to the clamps and a displacement gradient form

each clamp to the centre of the sample. This displacement corresponds to shrinkage of the sample in MD due to the drying. It should be noticed that the increase of the displacement occurred in the area which is slightly below the crack path in Figure 5-11c, on the side of the moving motor;

- In the transverse direction (Figure 5-11d), the displacement field u_x exhibits two smooth gradients: a positive and a negative one from one side towards the centre of the sample. These displacements correspond to shrinkage of the sample in CD due to the drying. However, one can notice a larger variation in the region in front of the notch tip.
- In the thickness direction (Figure 5-11e), the displacement field u_y is heterogeneous. Comparing with Figure 5-11f obtained at 75 % *RH* where the flocs and the antiflocs are indicated, the areas shown with bold black arrows which exhibit negative and positive gradients correspond to the borders between flocs and antiflocs. However, it is not the case for all the heterogeneous areas presented in the u_y field.

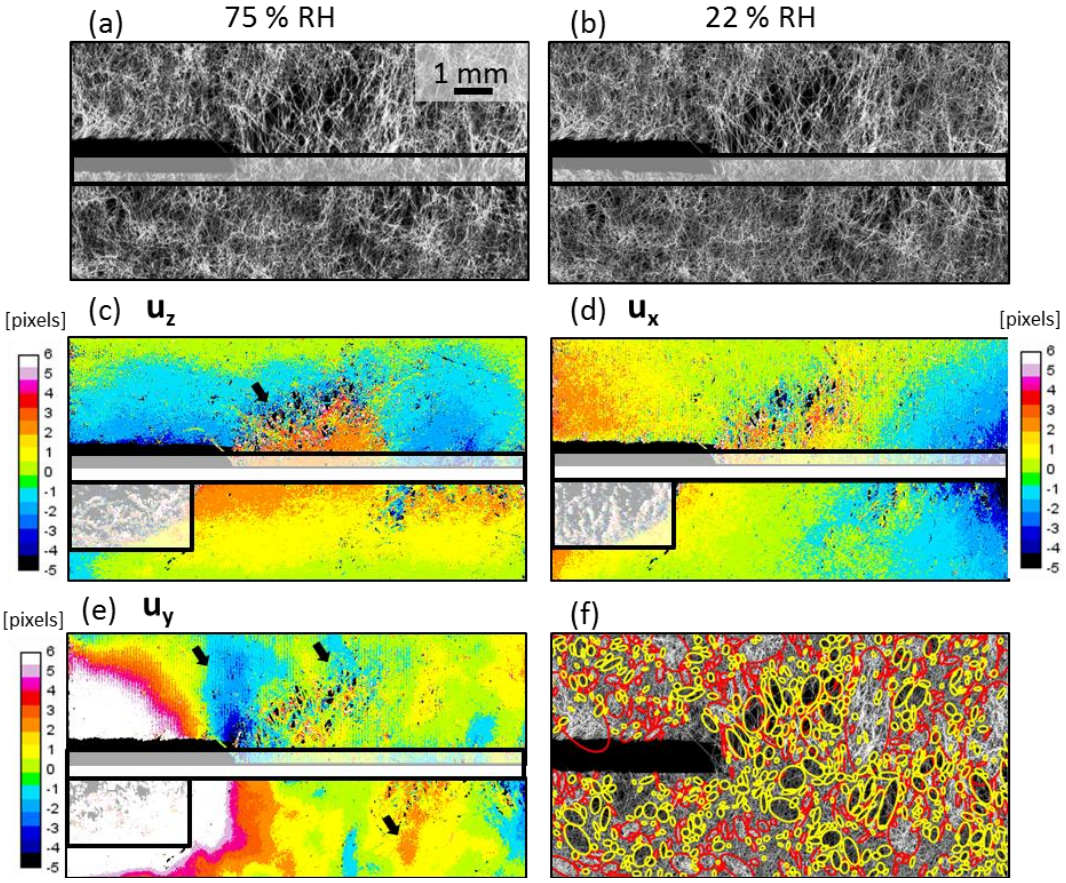

Figure 5-11 : (a-b) The X-ray enhanced radiographs obtained at 75 % and 22 % of *RH*. (c-e) The displacement fields of DVC analysis u_x, u_y, *and* u_z represented in 2D through the median intensity along the thickness direction. Areas of the image concatenation and lower notch lip are covered with rectangular. (f) The X-ray enhanced radiograph at 75 % *RH* with indicated flocs and antiflocs.

5.3.4 Discussion

5.3.4.1 Displacement field

In most papers, fibres tend to align in MD. When the environmental conditions vary, the dimensions of paper change in an anisotropic way: the MD is less affected than the CD because a change of RH affects more the diameter of the fibres than their length. However the displacement fields show similar order of magnitude in both MD and CD. This comes from the fact that the drying is constraint and that the studied LDP exhibits a small mechanical anisotropy as stated in chapter 3.

5.3.4.2 Microscale analysis of phenomena due to change of *RH*

To understand the local increase of the thickness of LDP observed in several areas in Figure 5-10d, these areas were qualitatively analysed. The result is presented in Figure 5-12 showing 3D views of the fibre network in the cross section. The local increase of the thickness mainly corresponds to the detachment of fibre ends from the bulk of LDP (Figure 5-12b). Figure 5-12c captures the mechanisms of the fibre detachment caused by the fibres torsion due to the drying. The fibre torsion mechanism induces a decrease of the inter-fibre bond area and its breakage in some cases. This is coherent with the properties of cellulosic fibres: when a fibre goes from the wet state to a drier one, the fibre rotates following its natural micro fibril angle (see chapter 1). The torsion of the individual fibres is limited due to the fact that the fibres are linked together by chemical bonds. However if strength of the inter-fibre bonds is lower than the effort (force/moment) that are induced by the torsion of the fibres caused by drying, the bonds fail allowing the fibres to follow their natural angle (Figure 5-12c). The fibre torsion due to drying can be noticed in the Figure 5-12d that was only partially attached to the other fibres.

5.3.4.3 Towards the link between mechanical response of paper and its microstructural evolution

On the curve presented in Figure 5-9, a clear increase of the force is linked to the drying process. Moreover, fluctuations of the force can be observed which are not caused by the resolution of the sensor: a local increase of the force curve is always followed by a decrease. This local variation may be due to the competition between the fibre torsion due to drying and the fibre detachment. It might come from the fact that when the fibre torsion becomes higher than the bond energy, the inter-fibre bond breaks. A more time resolved acquisition could help to interpret the observed phenomenon. Moreover the spatial resolution of the images reduced the opportunity to answer the following questions regarding the local areas where significant increase of the thickness was observed: was the inter-fibre bond area partially decreased due to the previous traction test? If yes, did the drying induce enough torsion mechanism to break the bonds?

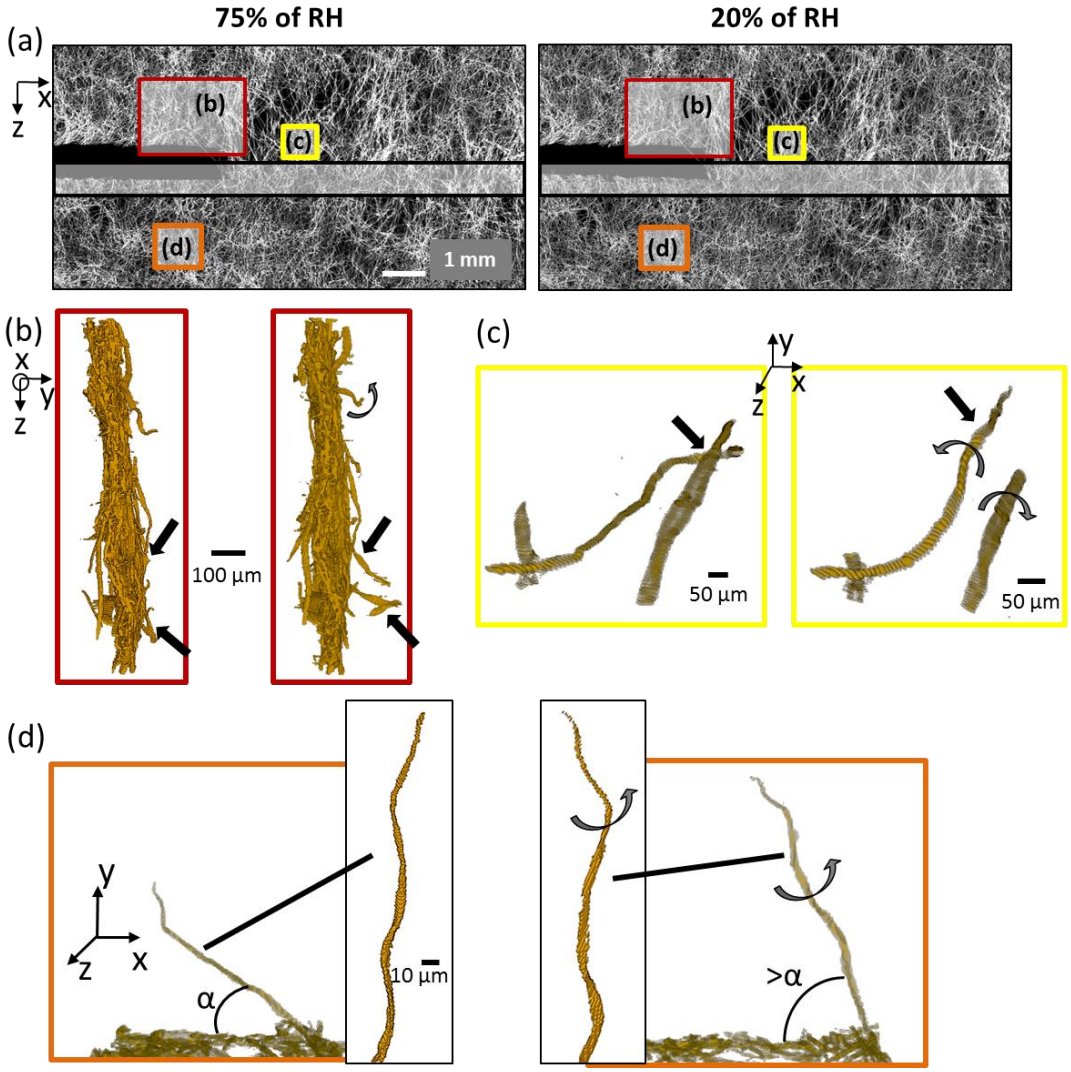

Figure 5-12 : Sample S5 at 75% of *RH* and 20 % of *RH*. (a) The X-ray enhanced radiographs. Modification of the microstructure of paper sample presented in parts: (b) out-of-plane fibre detachement; (c) fibre rotation causes its detachement; (d) Fibre torsion causes its displacement.

5.4 Conclusions

In this chapter, first, the influence of relative humidity *RH* on the fracture mechanisms of low density paper LDP was studied. Second, the influence of a change in *RH* on the crack propagation in paper was investigated. This analysis was made using the 3D imaging tools developed in this study (3D X-ray monitoring of the fracture tests followed by the advanced image analysis procedures). It enabled to show that:

- The mechanisms of crack initiation and propagation of the sample, are independent of the *RH*: they propagate around the flocs in the longest chain of antiflocs, and are due to bond breakage, fibre detachment and fibre pull out.

- The constraint drying of the pre-damaged sample implies a shrinkage of the sample and bond breakage in the vicinity of the visible crack path but also in damaged zone elsewhere (far away from the crack path).

Although the methodology proposed in this chapter need to be improved to increase the spatial and temporal analysis of the evolution, these results are quite encouraging as they bring the preliminary results to validate the models dedicated to the forecast of such phenomenon.

General conclusions and perspectives

Conclusions

The main objective of this work was to investigate the fundamental mechanisms leading to crack initiation and propagation in papers. In the papers, the spatial organization of the fibre networks induces long range effects when crack propagates in such media which are hard to capture. This study deals with the experimental multiscale characterization of fracture mechanisms in low density papers (LDP), i.e., sparse fibrous networks, which exhibit a very specific behaviour in regard to crack propagation such as, for instance, a low sensitivity to defects unless these defects reach a critical length.

In the "state of the art", presented in **chapter 1**, a particular attention was paid on the modelling and experimental analysis of fracture phenomena in papers and pointed out the experimental difficulty (i) to relate the structural characteristics to the internal length that are involved in nonlinear damage models applied to paper and to (ii) quantify the Fracture Process Zone (FPZ) and to (iii) investigate the influence of humidity on such features. In order to bring the necessary experimental data, an experimental approach, detailed in **chapter 2**, was developed based on multiscale and Multiphysics mechanical tests. Several various original experiments were performed to investigate these mechanisms. First, a series of macroscopic single edge-notched fracture tests were performed to investigate the structural changes and deformation mechanisms of tested fibrous networks under various relative humidity conditions. Second, a series of mesoscopic and microscopic images were obtained by *in situ* micromechanical tests coupled with advanced imaging techniques (optical microscopy and more particularly X-ray microtomography). For that purpose, a mini tensile device was designed that enabled the imaging of the sample deformation either under a microscope or during X-ray microtomography. Imaging quantification procedures were developed to investigate the structural changes and the deformation mechanisms during fracture tests at the meso- and microscales of tested fibrous networks under various relative humidity conditions.

Chapter 3 was dedicated to the link between the macroscopic behaviour and the mesoscale structural features. The fracture processes in two different moisture sensitive natural cellulosic materials, a low and a high density paper, were studied experimentally and analytically. It was shown that (i) the two papers fracture in a different manner, (ii) their fracture behaviour was independent of the moisture content and (iii) the magnitudes of the global fracture load scales are moisture-dependent. The different behaviour between both papers for any moisture content can be linked to the high spatial mass distribution in the low density paper compared to the high density paper. The applied fracture theory was remarkably consistent

with the experiments and quantitatively captured subscale length-effects in a convenient way. A key observation was that the internal length parameter, used in the hypothesized fracture theory to bridge stresses to a subscale, was linked to an average size of the most common size of large regions of relatively low mass, so-called antiflocs.

Chapter 4 was dedicated to the experimental study of the multiscale phenomena that accompany crack initiation and propagation in low density paper at ambient conditions. Optical and X-ray microtomography imaging techniques during fracture tests combined with the advanced image analysis were used to reveal the fracture mechanisms that occurred in LDP. It was shown that the fracture mostly localised in the antiflocs of the paper, and the crack propagated mainly in the antiflocs, avoiding the flocs confirming the crucial role of the antiflocs already mentioned in chapter 2. The analysis of 3D images revealed that the crack propagation induced in-plane and out-of-plane deformation phenomena such as the increase in the paper thickness. In particular, these phenomena localised in the FPZ ahead of the crack tip. The width of FPZ was equal to approximately twice the arithmetic fibre length. In addition, the application of Digital Volume Correlation (DVC) on the 3D X-ray microtomography images allowed us to visualise the inhomogeneity of the displacement field observed even before a distinct crack path occurred. These mesoscale changes were accompanied by microscale deformation mechanisms such as, for instance, rotation and twist of the connected fibres during tensile tests, decreasing the contact/bond areas between them and eventually leading to the bond breakage. The rotation and the detachment of fibres were at the origin of an increase of the thickness and porosity in the thickness direction of paper and could also be at the origin of the apparent plasticity of LDP prior to the maximum tensile force.

In **chapter 5**, first, the influence of relative humidity RH on the fracture mechanisms of LDP was studied. Second, the influence of a change in RH on the crack propagation in paper was investigated. This analysis was made using the 3D imaging tools developed in this study (3D X-ray monitoring of the fracture tests followed by the advanced image analysis procedures). It enabled to show that the mechanisms of crack initiation and propagation of the sample at the microscale are independent of the RH: they propagate around the flocs in the longest chain of antiflocs, and are due to bond breakage, fibre detachment and fibre pull out. Then we showed that the constraint drying of the pre-damaged sample implies a shrinkage of the sample and bond breakage in the vicinity of the visible crack path but also in damaged zone elsewhere (far away from the crack path).

Perspectives

The experimental tools based on X-ray microtomography brought the first visualisations of the mechanisms of fracture propagation in low density paper at a high resolution. Moreover, a quantitative analysis was performed at the scale of the assembly of fibres. In order to be even more accurate, a quantitative analysis should be carried out at the fibre scale by (i) identifying each fibre and each fibre-fibre contact in each loading stage and by (ii) following all the identified objects from one loading state to another. It was partially done manually in this work. An automatic procedure must be developed to gather enough information on the microstructural changes. This experimental advance would allow quantifying the fibre rearrangement (elongation, rotation or displacement) and the evolution of fibre-fibre contact area. Such information will allow answering some remaining questions experimentally in 3D raised in the various studies:

- What are the predominant mechanisms depending on the strain applied to the sample? Is it fibre reorientation? Elongation? Modification of the fibre-fibre bond? What is the percentage of fibres or fibre-fibre contact affected by each of this mechanism in each part of the mechanical curve?
- What is the average energy necessary to break bonds? The forecast tools coupled with the mechanical response of the sample would be able to measure the average energy necessary to break bonds in various situations: fracture tests at various moisture content or influence of a change in moisture content on a damaged paper. This information is missing to carry out realistic 3D simulations in the case of LDP crack initiation and to improve the current models.
- Does the internal length involved in models that aim at capturing the initiation of the crack path evolve during the failure process i.e. during propagation, which modifies the microstructure and the shape of the stress field?

All those experimental results are necessary to improve and / or validate the current models regarding both fracture mechanisms and moisture diffusion. In order to complete these results, the observations of larger specimens using high-resolution X-ray images and larger field of views should be performed. This approach would allow us to detect fibre and bond deformation and failure phenomena all along the crack path. Then, these results would be used to test models for the prediction of the evolution of paper structure along the crack path such as, for instance, the models that give a prediction of the number of fibres that are intercepted by the crack when it develops. The damage mechanisms far away from the crack path could also be quantified.

References

Aifantis, E.C., 2011a. A note on gradient elasticity and nonsingular crack fields. J. Mech. Behav. Mater., 20, pp.103–105.

Aifantis, E.C., 2014. Gradient material mechanics: perspectives and prospects. Acta Mech., 225(4–5), pp.999–1012.

Aifantis, E.C., 2011b. On the gradient approach–relation to Eringen's nonlocal theory. Int. J. Eng. Sci., 49(12), pp.1367–1377.

Alava, M. and Niskanen, K., 2006. The physics of paper. Rep. Prog. Phys., 69(3), pp.669–723.

Altendorf, H. and Jeulin, D., 2011. 3D directional mathematical morphology for analysis of fiber orientations. Image Anal. Stereol., 28(3), pp.143–153.

Anderson, T.L., 2005. Fracture mechanics: fundamentals and applications, CRC press.

Andersson, O. and Falk, O., 1966. Spontaneous crack formation in paper. Sven. Papperstidning, 69(4), p.91.

Ando, E., 2013. Experimental investigation of microstructural changes in deforming granular media using x-ray tomography. Doctoral thesis. Université de Grenoble, France.

Antoine, C. et al., 2002. 3D images of paper obtained by phase-contrast X-ray microtomography: image quality and binarisation. Nucl. Instrum. Methods Phys. Res. Sect. Accel. Spectrometers Detect. Assoc. Equip., 490(1), pp.392–402.

Askes, H. and Aifantis, E.C., 2011. Gradient elasticity in statics and dynamics: an overview of formulations, length scale identification procedures, finite element implementations and new results. Int. J. Solids Struct., 48(13), pp.1962–1990.

Askes, H. and Susmel, L., 2015. Understanding cracked materials: is Linear Elastic Fracture Mechanics obsolete? Fatigue Fract. Eng. Mater. Struct., 38(2), pp.154–160.

Åslund, P.E., Hägglund, R., Carlsson, L.A. and Isaksson, P., 2015. An analysis of strain localization and formation of face wrinkles in edge-wise loaded

corrugated sandwich panels using a continuum damage model. Int. J. Solids Struct., 56, pp.248–257.

Auweter, S. et al., 2014. X-ray phase-contrast imaging of the breast—advances towards clinical implementation. Br. J. Radiol., 87(1034), p.20130606.

Axelsson, M., 2007. 3D tracking of cellulose fibres in volume images. 2007 IEEE International Conference on Image Processing. IEEE, p. IV-309.

Axelsson, M. and Svensson, S., 2010. 3D pore structure characterisation of paper. Pattern Anal. Appl., 13(2), pp.159–172.

Axelsson, M., Svensson, S. and Borgefors, G., 2006. Reduction of ring artifacts in high resolution X-ray microtomography images. Joint Pattern Recognition Symposium. Springer, pp. 61–70.

Barenblatt, G.I., 1959. The formation of equilibrium cracks during brittle fracture. General ideas and hypotheses. Axially-symmetric cracks. J. Appl. Math. Mech., 23(3), pp.622–636.

Barnett, J. and Bonham, V.A., 2004. Cellulose microfibril angle in the cell wall of wood fibres. Biol. Rev., 79(2), pp.461–472.

Baruchel, J., Buffiere, J.Y. and Maire, E., 2000. X-ray Tomography in Material Science, Hermes Science.

Batchelor, W., He, J. and Sampson, W., 2006. Inter-fibre contacts in random fibrous materials: experimental verification of theoretical dependence on porosity and fibre width. J. Mater. Sci., 41(24), pp.8377–8381.

Baum, G., Pers, K., Shepard, D. and Ave'Lallemant, T., 1984. Wet straining of paper. Tappi J., 67(5), pp.100–104.

Baumgarten, H. and Göttsching, L., 1973. Triaxial deformation of paper under tensile load. Proc. 1973 Fundam. Prop. Pap. Relat. Its Uses.

Bažant, Z.P., 2000. Size effect. Int. J. Solids Struct., 37(1), pp.69–80.

Bazant, Z.P. and Planas, J., 1997. Fracture and size effect in concrete and other quasibrittle materials, CRC press, USA.

Berg, J.-E. and Gradin, P.A., 1999. A micromechanical model of the deterioration of a wood fibre. J. Pulp Pap. Sci., 25(2), pp.66–71.

Bernie, J.-P. and Douglas, W.M., 1996. Local grammage distribution and formation of paper by light transmission image analysis. Tappi J., 79(1), pp.193–202.

Bither, T. and Waterhouse, J., 1992. Strength development through refining and wet pressing. Tappi J., 75(11), pp.201–208.

Boadway, J., Murray, F., Cote, L. and Gray, J., 1963. The influence of flaws on tensile strength of newsprint webs. Pulp Pap. Mag Can 64 2C, pp.T84–T88, T118.

Bouterf, A. et al., 2016. Failure mechanisms of plasterboard in nail pull test determined by X-ray microtomography and digital volume correlation. Exp. Mech., 56(8), pp.1427–1437.

Bradt, R.C. et al., 2012. Fracture Mechanics of Ceramics: Composites, R-Curve Behavior, and Fatigue, Springer Science & Business Media.

Brännvall, E., 2009. Overview of pulp and paper processes. In: Pulp chemistry and technology. Ek M., Gellerstedt G., Henriksson G., Germany, pp. 1–12.

Button, A.F., 1979. Fiber-fiber bond strength: A study of a linear elastic model structure.

Campbell, W.B., 1959. The mechanism of bonding. Tappi, 42(12), pp.999–1001.

Castro, J., 2001. Influence of random formation on paper mechanics: experiments and theory. Dissertation. Doctoral thesis. Georgia Tech, Atlanta, Georgia.

Coffin, D.W., Li, K. and Li, J., 2013. Utilization of modified linear elastic fracture mechanics to characterize the fracture resistance of paper. In: 15th Fundamental Research Symposium. Cambridge, UK, pp. 637–672.

Coléou, C. et al., 2001. Three-dimensional snow images by X-ray microtomography. Ann. Glaciol., 32(1), pp.75–81.

Considine, J.M. et al., 2011. Evaluation of strength-controlling defects in paper by stress concentration analyses. J. Compos. Mater., 46(11), pp.1323–1334.

Corte, H. and Kallmes, O., 1962. Statistical geometry of a fibrous network. In: The Formation and Structure of Paper. pp. 13–46.

Cresson, T. and Luner, P., 1990. The characterization of paper formation. II: The texture analysis of paper formation. Tappi J., 73(12), pp.175–185.

Cresson, T.M., Tomimasu, H. and Luner, P., 1990. Characterization of paper formation. I, Sensing paper formation. Tappi J., 73(7), pp.153–159.

Curry, D. and Knott, J., 1978. Effects of microstructure on cleavage fracture stress in steel. Met. Sci., 12(11), pp.511–514.

Deng, M. and Dodson, C., 1994. Paper: An Engineered Stochastic structure. TAPPI PRESS Atlanta.

Derome, D., Griffa, M., Koebel, M. and Carmeliet, J., 2011. Hysteretic swelling of wood at cellular scale probed by phase-contrast X-ray tomography. J. Struct. Biol., 173(1), pp.180–190.

Desplentere, F. et al., 2005. Micro-CT characterization of variability in 3D textile architecture. Compos. Sci. Technol., 65(13), pp.1920–1930.

Dodson, C., 1996. Fibre crowding, fibre contacts and fibre flocculation. Tappi J, 79(9), pp.211–216.

Dodson, C.T., Oba, Y. and Sampson, W.W., 2001. On the distribution of mass, thickness and density in paper. Appita J., 54(4), pp.385–389.

Donner, B., 1997. An heuristic model of paper rupture. In: Proceedings of fundamentals of papermaking materials-11th fundamental research symposium. pp. 1215–1247.

Dooley, N. and Sampson, W., 2002. Opportunities for improved light transmission formation analysis. Dep. Pap. Sci. UMIST Manch.

Dugdale, D.S., 1960. Yielding of steel sheets containing slits. J. Mech. Phys. Solids, 8(2), pp.100–104.

Ebeling, K., 1980. A critical review of current theories for the refining of chemical pulps. International Symposium on Fundamental Concepts of Refining. pp. 1–36.

Ebeling, K., 1976. The Fundamental Properties of Paper Related to Its Uses. F Bolam Tech Div BPBIF Lond., p.304.

Eberhardt, C. and Clarke, A., 2002. Automated reconstruction of curvilinear fibres from 3D datasets acquired by X-ray microtomography. J. Microsc., 206(1), pp.41–53.

Ek, M., Gellerstedt, G. and Henriksson, G., 2009. Paper Chemistry and Technology, Walter de Gruyter.

Ek, M., Gellerstedt, G. and Henriksson, G., 2009a. Paper products, physics and technology, Walter de Gruyter.

Ek, M., Gellerstedt, G. and Henriksson, G., 2009b. Pulping chemistry and technology, Walter de Gruyter.

Emerton, H., Page, D. and Hale, W., 1961. Structure of papers as seen in their surfaces. The formation and structure of paper. 2nd Fundamental Research Symposium: Tech. Sect. Brit. Paper & Board Makers' Assn. pp. 53–99.

Enomae, T., Han, Y.-H. and Isogai, A., 2008. Z-Directional distribution of fiber orientation of Japanese and western papers determined by confocal laser scanning microscopy. J. Wood Sci., 54(4), pp.300–307.

Eringen, A.C. and Edelen, D., 1972. On nonlocal elasticity. Int. J. Eng. Sci., 10(3), pp.233–248.

Faessel, M., Delisée, C., Bos, F. and Castéra, P., 2005. 3D Modelling of random cellulosic fibrous networks based on X-ray tomography and image analysis. Compos. Sci. Technol., 65(13), pp.1931–1940.

Farnood, R.R., 1995. Sensing and modelling of forming and formation of paper. Doctoral thesis. University of Toronto, Canada.

Feldkamp, L., Davis, L. and Kress, J., 1984. Practical cone-beam algorithm. JOSA A, 1(6), pp.612–619.

Fellers, C., 2009. Paper physics. In: Paper products, physics and technology. Ek M., Gellerstedt G., Henriksson G., Germany, pp. 25–68.

Feng, C., 2012. Soft X-ray formation measurement of low density materials and compressive response characterization. Master Thesis, Miami university, Oxford, Ohio, USA.

Garboczi, E.J., 2002. Three-dimensional mathematical analysis of particle shape using X-ray tomography and spherical harmonics: Application to aggregates used in concrete. Cem. Concr. Res., 32(10), pp.1621–1638.

Gitman, I.M., Askes, H., Kuhl, E. and Aifantis, E.C., 2010. Stress concentrations in fractured compact bone simulated with a special class of anisotropic gradient elasticity. Int. J. Solids Struct., 47(9), pp.1099–1107.

Goel, A. et al., 2001. Characterization of three-dimensional structure of paper using X-ray microtomography. Tappi J., 84(5), pp.72–72.

Goldschmidt, J. and Wahren, D., 1968. On the rupture mechanism of paper, DTIC Document.

Gosh, S.K. and Chaliha, B.P., 1984. Tracing paper. IPPTA, 21(4), pp.57–69.

Graeffe, J. and Nuyan, S., 2005. An online laser caliper measurement for the paper industry. Optical Metrology. International Society for Optics and Photonics, pp. 318–326.

Gregersen, O., Hansen, A., Tufa, L. and Helle, T., 2000. The influence of fibre shives on calender cuts in newsprint. J. Pulp Pap. Sci., 26(5), pp.176–179.

Griffith, A., 1920. The phenomena of flow and rupture in solids: Phil. Trans Roy Soc Lond Ser A, 221, pp.163–98.

Guerrero Serrato, A., 2008. Investigation of wet paper cohesive properties. Master Thesis, Georgia Institute of Technology, USA.

Gustafsson, P.-J. and Niskanen, K., 2012. Paper as an engineering material. In: Mechanics of paper products. Niskanen K., Germany, pp. 5–26.

Hägglund, R. and Isaksson, P., 2006. Analysis of localized failure in low-basis-weight paper. Int. J. Solids Struct., 43(18), pp.5581–5592.

Hagman, A. and Nygårds, M., 2012. Investigation of sample-size effects on in-plane tensile testing of paperboard. Nord. Pulp Pap. Res. J., 27(2), p.295.

Hagman, A. and Nygårds, M., 2017. Thermographical analysis of paper during tensile testing and comparison to digital image correlation. Exp. Mech., 57, pp.325–339.

Hall, S. et al., 2010. Discrete and continuum analysis of localised deformation in sand using X-ray μCT and volumetric digital image correlation. Geotechnique, 60(5), pp.315–322.

Hall, S. et al., 2009. Strain localisation in sand under triaxial loading: characterisation by X-ray micro tomography and 3D digital image correlation. Proc 1st Int Symp On Compu Geomech (ComGeo 1). pp. 239–247.

Hall, S.A., 2012. Digital image correlation in experimental geomechanics. ALERT Dr. Sch., pp.69–102.

Hämäläinen, J. et al., 2014. Mathematics in paper-from fiber suspension fluid dynamics to solid state paper mechanics. J. Math. Ind., 4(1), p.1.

Hämäläinen, T., 2008. Modelling of fibre orientation and fibre flocculation phenomena in paper sheet forming. Doctoral thesis. Tampere University of Technology, Finland.

Haslach, H.W., 2009. Time-dependent mechanisms in fracture of paper. Mech. Time-Depend. Mater., 13(1), pp.11–35.

Haslach Jr, H.W., 2000. The moisture and rate-dependent mechanical properties of paper: a review. Mech. Time-Depend. Mater., 4(3), pp.169–210.

Hild, F., Maire, E., Roux, S. and Witz, J.-F., 2009. Three-dimensional analysis of a compression test on stone wool. Acta Mater., 57(11), pp.3310–3320.

Hirn, U. and Schennach, R., 2015. Comprehensive analysis of individual pulp fiber bonds quantifies the mechanisms of fiber bonding in paper. Sci. Rep., 5.

Hollmark, H., Andersson, H. and Perkins, R., 1978. Mechanical properties of low-density sheets. Tappi, 61(9), pp.69–72.

Holmstad, R., 2004. Methods for paper structure characterisation by means of image analysis. Doctoral thesis. NTNU, Norway.

Hsieh, J., 2003. Computed Tomography: Principles, Design, Artifacts, and Recent Advances, SPIE Press.

Huang, S. et al., 2002. Transverse and in-plane pore structure characterisation of paper. Appita J., 55(3), pp.230–234.

Huang, Y., 2010. Structural Mapping of Paper Towels: Comparison of Twin Laser Profilometry and Synchrotron X-ray Micro-computed Tomography.

Hutchinson, J., 1968. Singular behaviour at the end of a tensile crack in a hardening material. J. Mech. Phys. Solids, 16(1), pp.13–31.

Hutchinson, J.W., 2012. Generalizing J2 flow theory: Fundamental issues in strain gradient plasticity. Acta Mech. Sin., 28(4), pp.1078–1086.

Irwin, G.R., 1957. Analysis of stresses and strains near the end of a crack traversing a plate. J. Appl. Mech., 24, pp.361–364.

Isaksson, P. and Dumont, P., 2014. Approximation of mode I crack-tip displacement fields by a gradient enhanced elasticity theory. Eng. Fract. Mech., 117, pp.1–11.

Isaksson, P., Dumont, P. and Rolland du Roscoat, S., 2012. Crack growth in planar elastic fiber materials. Int. J. Solids Struct., 49(13), pp.1900–1907.

Isaksson, P., Gradin, P. and Kulachenko, A., 2006. The onset and progression of damage in isotropic paper sheets. Int. J. Solids Struct., 43(3), pp.713–726.

Isaksson, P. and Hägglund, R., 2013a. Acoustic emission assisted fracture zone analysis of cellulose fibre materials. J. Compos. Mater., 47(22), pp.2865–2874.

Isaksson, P. and Hägglund, R., 2007. Analysis of the strain field in the vicinity of a crack-tip in an in-plane isotropic paper material. Int. J. Solids Struct., 44(2), pp.659–671.

Isaksson, P. and Hägglund, R., 2013b. Crack-tip fields in gradient enhanced elasticity. Eng. Fract. Mech., 97, pp.186–192.

Isaksson, P. and Hägglund, R., 2009. Structural effects on deformation and fracture of random fiber networks and consequences on continuum models. Int. J. Solids Struct., 46(11), pp.2320–2329.

Isokangas, A. and Leiviskä, K., 2011. Analysis of formation and floc size on the basis of optical transmittance, University of Oulu, Control Engineering Laboratory, Finland.

Izumi, H. and Yoshida, Y., 2001. Development and application of a system for determining paper nonuniformity. Jpn. TAPPI J., 55(5), pp.109–118.

Jajcinovic, M., Fischer, W.J., Hirn, U. and Bauer, W., 2016. Strength of individual hardwood fibres and fibre to fibre joints. Cellulose, 23(3), pp.2049–2060.

Joffre, T. et al., 2015. A 3D in-situ investigation of the deformation in compressive loading in the thickness direction of cellulose fiber mats. Cellulose, 22(5), pp.2993–3001.

Joffre, T. et al., 2016. A Method to Measure Moisture Induced Swelling Properties of a Single Wood Cell. Exp. Mech., 56(5), pp.723–733.

Jordan, B., 1986. Specific perimeter-a graininess parameter for formation and print-mottle textures. Pap. Ja Puu, 6(7), pp.476–482.

Kachanov, L., 1958. Time of the rupture process under creep conditions. Isv Akad Nauk SSR Otd Tekh Nauk, 8, pp.26–31.

Kajanto, I., Laamanen, J. and Kainulainen, M., 1998. Paper bulk and surface. In: Paper Physics. Niskanen K., pp. 89–115.

Kajanto, I. and Niskanen, K., 1998. Dimensional stability. In: Paper Physics. Papermaking science and technology. Niskanen K., Helsinki, Finland, pp. 222–259.

Kak, A.C. and Slaney, M., 2001. Principles of computerized tomographic imaging, SIAM.

Kallmes, O. and Ayer, J., 1987. Light scanning system provides qualitative formation measurement. Pulp Pap., 61(4), p.99.

Kappel, L., Hirn, U., Bauer, W. and Schennach, R., 2009. A novel method for the determination of bonded area of individual fiber-fiber bonds. Nord Pulp Pap Res J, 24(2), pp.199–205.

Keller, D.S., Branca, D.L. and Kwon, O., 2012. Characterization of nonwoven structures by spatial partitioning of local thickness and mass density. J. Mater. Sci., 47(1), pp.208–226.

Keller, D.S., Lewalle, J. and Luner, P., 1999. Wavelet analysis of simulated paper formation. Pap. Ja Puu, 81(7), pp.499–505.

Ketcham, R., 1997. Three-dimensional quantitative textural analysis of metamorphic rocks using high-resolution computed X-ray tomography: Part I. Methods and techniques. J. Metamorph. Geol., 15(1), pp.29–44.

Kettunen, H. and Niskanen, K., 1998. Fiber debonding along a crack front in paper. MRS Proceedings. Cambridge Univ Press, p. 153.

Kettunen, H., Yu, Y. and Niskanen, K., 2000. Microscopic damage in paper. Part II: Effect of fibre properties. J. Pulp Pap. Sci., 26(7), pp.260–265.

Khaddour, G., 2015. Multi-scale characterisation of the hydro-mechanical behaviour of unsaturated sand : water retention and triaxial response. Doctoral thesis. Université Grenoble Alpes, Grenoble, France.

Kimura, M., Iwasaki, Y., Kadoya, T. and Oda, M., 1979. Study on determination of paper thickness by mercury buoyancy method. J. Jpn. Wood Res. Soc. Jpn.

Komppa, A., 1988. Measurement of formation. Pap. Ja Puu, 70(3), pp.243–250.

Korteoja, M. et al., 1996. Local strain fields in paper. Tappi J., 79(4), pp.217–223.

Kröner, E., 1967. Elasticity theory of materials with long range cohesive forces. Int. J. Solids Struct., 3(5), pp.731–742.

Kröner, E., 1963. On the physical reality of torque stresses in continuum mechanics. Int. J. Eng. Sci., 1(2), pp.261–278.

Laleg, M. and Nguyen, N., 1995. The specific perimeter of fibre flocs: a criterion of paper formation. J. Pulp Pap. Sci., 21(10), pp.J356–J361.

Larsson, P.A., Hoc, M. and Wågberg, L., 2009. The influence of grammage, moisture content, fibre furnish and chemical modifications on the hygro-and hydro-expansion of paper. 14th Fundamental Research Symposium on Advances in Pulp and Paper Research Location: St Annes Coll, Oxford, England. pp. 355–388.

Latil, P. et al., 2011. Towards the 3D in situ characterisation of deformation micro-mechanisms within a compressed bundle of fibres. Compos. Sci. Technol., 71(4), pp.480–488.

Laurencin, T. et al., 2016. 3D real-time and in situ characterisation of fibre kinematics in dilute non-Newtonian fibre suspensions during confined and lubricated compression flow. Compos. Sci. Technol., 134, pp.258–266.

Le, T.-H. et al., 2008. X-ray phase contrast microtomography for the analysis of the fibrous microstructure of SMC composites. Compos. Part Appl. Sci. Manuf., 39(1), pp.91–103.

Lindgren, O., 1992. Medical CT-scanners for non-destructive wood density and moisture content measurements. Doctoral thesis. Luleå University of Technology, Skellefteå, Sweden.

Lindström, S., 2008. Modelling and simulation of paper structure development. Doctoral thesis. Mid Sweden University, Sundsvall, Sweden.

Lindström, T., Wågberg, L. and Larsson, T., 2005. On the nature of joint strength in paper-A review of dry and wet strength resins used in paper manufacturing. 13th fundamental research symposium. The Pulp and Paper Fundamental Research Society Cambridge, UK, pp. 457–562.

Luner, P., Kärnä, A. and Donforio, C., 1961. Studies in Interfiber Bonding of Paper. Tappi, 44(6), pp.409–414.

Lux, J., Delisée, C. and Thibault, X., 2006. 3D characterization of wood based fibrous materials: an application. Image Anal Ster., 25(1), pp.25–35.

Lyckegaard, A., Johnson, G. and Tafforeau, P., 2011. Correction of ring artifacts in X-ray tomographic images. Int J Tomo Stat, 18, pp.1–9.

Macmillan, F., Farrel, W. and Booth, K., 1965. Shives in newsprint: Their detection, measurement and effects on paper quality. Pulp Pap. Mag. Can., 66(7), pp.T361–T369.

Maire, E. et al., 2003. X-ray tomography applied to the characterization of cellular materials. Related finite element modeling problems. Compos. Sci. Technol., 63(16), pp.2431–2443.

Maire, E. and Withers, P., 2014. Quantitative X-ray tomography. Int. Mater. Rev., 59(1), pp.1–43.

Mäkelä, P., 2002. On the fracture mechanics of paper. Nord. Pulp Pap. Res. J., 17(3), pp.254–274.

Mäkelä, P. and Fellers, C., 2012. An analytic procedure for determination of fracture toughness of paper materials. Nord. Pulp Pap. Res. J., 27(2), p.352.

Mäkelä, P. and Östlund, S., 2003. Orthotropic elastic–plastic material model for paper materials. Int. J. Solids Struct., 40(21), pp.5599–5620.

Malmberg, F. et al., 2011. Measurement of fibre–fibre contact in three-dimensional images of fibrous materials obtained from X-ray synchrotron microtomography. Nucl. Instrum. Methods Phys. Res. Sect. Accel. Spectrometers Detect. Assoc. Equip., 637(1), pp.143–148.

Mann, R.W., Baum, G.A. and Habeger Jr, C.C., 1979. Determination of all nine orthotropic elastic constants for machine-made paper. IPC Tenchical Pap. Ser., (84).

Marone, F. and Stampanoni, M., 2012. Regridding reconstruction algorithm for real-time tomographic imaging. J. Synchrotron Radiat., 19(6), pp.1029–1037.

Marulier, C. et al., 2015. 3D analysis of paper microstructures at the scale of fibres and bonds. Cellulose, 22(3), pp.1517–1539.

Marulier, C., 2013. Etudes multi-échelles des couplages entre les propriétés hygroélastiques des papiers et leur microstructure. Doctoral thesis. L'université de Grenoble, Grenoble, France.

Maugin, G.A. and Metrikine, A.V., 2010. Mechanics of generalized continua. Adv. Mech. Math., 21.

McDonald, S.A. et al., 2011. In situ 3D X-ray microtomography study comparing auxetic and non-auxetic polymeric foams under tension. Phys. Status Solidi B, 248(1), pp.45–51.

Moffat, J., Beath, L. and Mihelich, W., 1973. Major factors governing newsprint strength. The Fundamental Properties of Paper Related to its Uses, Transactions of the 5th Fundamental Research Symposium. pp. 118–150.

Mokso, R. et al., 2011. Following dynamic processes by X-ray tomographic microscopy with sub-second temporal resolution. 10th international conference on X-ray microscopy. AIP Publishing, pp. 38–41.

Nazhad, M.M., Harris, E.J., Dodson, C.T. and Kerekes, R.J., 2000. The influence of formation on tensile strength of papers made from mechanical pulps. Tappi J., 83(12).

Niskanen, K., 2012. Mechanics of paper products, Walter de Gruyter.

Niskanen, K., 2012. Micromechanics. In: Mechanics of paper products. Niskanen K., Germany, pp. 197–230.

Niskanen, K., 1998. Paper physics. Finnish paper engineers' association and TAPPI., Gullichsen J., Paulapuro H., Finland.

Niskanen, K., 1993. Strength and fracture of paper. Products of Papermaking: Transactions of the Tenth Fundamental Research Symposium. 10th Fundamental Research Symposium, Oxford, UK, pp. 641–725.

Niskanen, K., Alava, M., Seppälä, E. and Aström, J., 1999. Fracture energy in fibre and bond failure. J. Pulp Pap. Sci., 25(5), pp.167–169.

Niskanen, K., Kajanto, I. and Pakarinen, P., 1998. Paper structure. In: Paper Physics. 19. Niskanen K., Finland, pp. 14–53.

Niskanen, K. and Kärenlampi, P., 1998. In-plane tensile properties. In: Paper physics. Niskanen K., pp. 138–191.

Niskanen, K., Kettunen, H. and Yu, Y., 2001. Damage width: a measure of the size of fracture process zone. In: 12th Fundamental Research Symposium, Oxford, UK.

Nissan, A.H. and Batten Jr, G.L., 1990. On the primacy of the hydrogen bond in paper mechanics. Tappi J., 73(2), pp.159–164.

Norman, R., 1966. Dependence of sheet properties on formation and forming variables. In: Consolidation of the Paper Web. pp. 269–309.

Nuyan, S., Graeffe, J. and Moisio, H., 2006. Recent advances in online caliper measurement. Annual meeting, Pulp and Paper technical association of Canada. p. 39.

Öhrn, O., 1965. Thickness variations of paper on stretching. Sven. Papperstidning, 68(5), pp.141–149.

Östlund, S. and Märkelä, P., 2012. Fracture properties. In: Mechanics of paper products. Niskanen K., Berlin, Germany, pp. 53–65.

Ostoja-Starzewski, M. and Castro, J., 2003. Random formation, inelastic response and scale effects in paper. Philos. Trans. R. Soc. Lond. Math. Phys. Eng. Sci., 361(1806), pp.965–985.

Paganin, D. et al., 2002. Simultaneous phase and amplitude extraction from a single defocused image of a homogeneous object. J. Microsc., 206(1), pp.33–40.

Page, D., 1960. Fibre-to-fibre bonds part 1: a method for their direct observation. Pap. Technol., 1(4), pp.407–411.

Page, D., 1989. The beating of chemical pulps–the action and the effects. Transactions of 9th Fundamental Research Symposium, Fundamentals of papermaking. MEP, London. p. 1.

Parola, M., Kaljunen, T. and Vuorinen, S., 2000. New methods for the analysis of the paper web performance on the press. 27th IARIGAI Research Conference. pp. 203–218.

Perkins, R.W., 2002. Mechanical behaviour of paper and boards. In: Handbook of physical testing of paper. Mark R.E., USA, pp. 1–76.

Ramasubramanian, M., 2001. Physical and mechanical properties of towel and tissue. Mark Al, pp.661–696.

Raunio, J.-P. and Ritala, R., 2013. Method for detecting free fiber ends in tissue paper. Meas. Sci. Technol., 24(12), p.125206.

Raunio, J.-P. and Ritala, R., 2012. Simulation of creping pattern in tissue paper. Nord. Pulp Pap. Res. J., 27(2), p.375.

Retulainen, E., Niskanen, K. and Nilsen, N., 1998. Fibres and bonds. In: Paper Physics. Niskanen K., Finland, pp. 54–87.

Rice, Jr. and Rosengren, G.F., 1968. Plane strain deformation near a crack tip in a power-law hardening material. J. Mech. Phys. Solids, 16(1), pp.1–12.

Ridler, T. and Calvard, S., 1978. Picture thresholding using an iterative selection method. IEEE Trans Syst Man Cybern, 8(8), pp.630–632.

Rolland du Roscoat, S., 2007. Contribution à la quantification 3D de réseaux fibreux par microtomographie au rayonnement synchrotron: applications aux papiers. Doctoral thesis. Grenoble INP, Grenoble, France.

Rolland du Roscoat, S. et al., 2007. Estimation of microstructural properties from synchrotron X-ray microtomography and determination of the REV in paper materials. Acta Mater., 55(8), pp.2841–2850.

Rolland du Roscoat, S., Bloch, J. and Thibault, X., 2005. Synchrotron radiation microtomography applied to investigation of paper. J. Phys. Appl. Phys., 38(10A), p.A78.

Roux, S. and Hild, F., 2009. Digital image correlation and fracture: an advanced technique for estimating stress intensity factors of 2D and 3D cracks. J. Phys. Appl. Phys., 42(21), p.214004.

Salmén, L. et al., 1984. A treatise on the elastic and hygroexpansional properties of paper by a composite laminate approach. Fibre Sci. Technol., 20(4), pp.283–296.

Salmen, N.L. and Back, E.L., 1980. Moisture-dependent thermal softening of paper, evaluated by its elastic modulus. Tappi, 63(6), pp.117–120.

Salminen, L., Alava, M. and Niskanen, K., 2003. Analysis of long crack lines in paper webs. Eur. Phys. J. B-Condens. Matter Complex Syst., 32(3), pp.369–374.

Salminen, L., Räisänen, V., Alava, M. and Niskanen, K., 1996. Drying-induced stress state of inter-fibre bonds. J. Pulp Pap. Sci., 22(10), pp.J402–J407.

Salvo, L. et al., 2003. X-ray micro-tomography an attractive characterisation technique in materials science. Nucl. Instrum. Methods Phys. Res. Sect. B Beam Interact. Mater. At., 200, pp.273–286.

Sampson, W., 2004. A model for fibre contact in planar random fibre networks. J. Mater. Sci., 39(8), pp.2775–2781.

Sampson, W., 2009. Materials properties of paper as influenced by its fibrous architecture. Int. Mater. Rev., 54(3), pp.134–156.

Sampson, W., 2006. Structure and tensile theory of paper (6 Lectures), Structural natural fibres.

Sampson, W., 2001. The structural characterisation of fibre networks in papermaking processes - a review. The Science of Papermaking, Transactions of the XIIth Fundamental Research Symposium Baker CF. pp. 1205–1288.

Sampson, W.W., 2008. Modelling Stochastic Fibrous Materials with Mathematica®, Springer Science & Business Media.

Samuelsen, E.J. et al., 2001. Three-dimensional imaging of paper by use of synchrotron x-ray microtomography. J. Pulp Pap. Sci., 27(2), pp.50–53.

Sara, H., 1978. The Characterization and Measurement of Paper Formation with Standard Deviation and Power Spectrum. Doctoral thesis. University of Helsinki, Helsinki, Finland.

Schmied, F.J. et al., 2013. What holds paper together: Nanometre scale exploration of bonding between paper fibres. Sci. Rep., 3.

Scott, W.E., Abbott, J.C. and Trosset, S., 1995. Properties of paper: an introduction, Tappi Press.

Sears, G., Tyler, R. and Denzer, C., 1965. Shives in newsprint: The role of shives in paper web breaks. Pulp Pap. Mag. Can., 66(7), pp.T351–T360.

Seth, R., 1979. Measurement of fracture resistance of paper. Tappi, 62(7), pp.92–95.

Seth, R. and Page, D., 1974. Fracture resistance of paper. J. Mater. Sci., 9(11), pp.1745–1753.

Seth, R. and Page, D., 1983. The stress-strain curve of paper. In: The Role of Fundamental Research in Paper Making. Brander J., London, pp. 421–454.

Shih, C., 1981. Relationships between the J-integral and the crack opening displacement for stationary and extending cracks. J. Mech. Phys. Solids, 29(4), pp.305–326.

Silvy, J., Caret, C., Belamaalem, B. and Mahrous, M., 1995. The Three-dimensional structure of paper: methods of analysis and implications on his physical properties. International Paper Physics Conference, September. pp. 11–14.

Sintorn, I.-M., Svensson, S., Axelsson, M. and Borgefors, G., 2005. Segmentation of individual pores in 3D paper images. Nord. Pulp Pap. Res. J., 20(3), pp.316–319.

Skog, J. and Oja, J., 2009. Heartwood diameter measurements in Pinus sylvestris sawlogs combining X-ray and three-dimensional scanning. Scand. J. For. Res., 24(2), pp.182–188.

Södemark, C. and Tryding, J., 2009. Packaging. In: Paper products, physics and technology. Pulp and paper, chemistry and technology. Ek M., Gellerstedt G., Henriksson G., Berlin, Germany, pp. 257–286.

Stenberg, N. and Fellers, C., 2002. Out-of-plane Poisson's ratios of paper and paperboard. Nord. Pulp Pap. Res. J., 17(4), pp.387–394.

Ström, G., 2009. Paper and printing. In: Paper products, physics and technology. Pulp and paper, chemistry and technology. Ek M., Gellerstedt G., Henriksson G., Berlin, Germany, pp. 234–256.

Sung, Y. et al., 2005. Applications of thickness and apparent density mapping by laser profilometry. 13th Fundamental Research Symposium, Cambridge. pp. 961–1007.

Sung, Y., Farnood, R. and others, 2007. Characterizing anisotropy of the deterministic features in paper structure with wavelet transforms. J. Ind. Eng. Chem. Seul, 13(2), p.225.

Swinehart, D. and Broek, D., 1995. Tenacity and fracture toughness of paper and board. J. Pulp Pap. Sci., 21(11), pp.J389–J397.

Tanaka, T. et al., 1998. Changes in Mechanical Properties Induced by Humidity and Fatigue Properties of Paper. Bull.-Jpn. Soc. Print. Sci. Technol., 35, pp.10–18.

Tang, X., Ning, R., Yu, R. and Conover, D., 2001. Cone beam volume CT image artifacts caused by defective cells in x-ray flat panel imagers and the artifact

removal using a wavelet-analysis-based algorithm. Med. Phys., 28(5), pp.812–825.

Toungara, M. et al., 2014. Observation 3D et modélisation de l'hygroexpansion de fibres lignocellulosiques. Colloq. MécaMat.

Toupin, R.A., 1962. Elastic materials with couple-stresses. Arch. Ration. Mech. Anal., 11(1), pp.385–414.

Tran, H. et al., 2013. 3D mechanical analysis of low-density wood-based fiberboards by X-ray microcomputed tomography and digital volume correlation. J. Mater. Sci., 48(8), pp.3198–3212.

Trepanier, R., Jordan, B. and Nguyen, N., 1998. Specific perimeter: a statistic for assessing formation and print quality by image analysis. Tappi J., 81(10), pp.191–196.

Tryding, J., 1996. In-plane fracture of paper. Dissertation. Doctoral thesis. Lund University, Lund, Sweden.

Tsarouchas, D. and Markaki, A., 2011. Extraction of fibre network architecture by X-ray tomography and prediction of elastic properties using an affine analytical model. Acta Mater., 59(18), pp.6989–7002.

Tudisco, E. et al., 2015. Full-field measurements of strain localisation in sandstone by neutron tomography and 3D-volumetric digital image correlation. Phys. Procedia, 69, pp.509–515.

Turpeinen, T., 2015. Analysis of microtomographic images of porous heterogeneous materials. Doctoral thesis. University of Jyväskylä, Jyväskylä, Finland.

Uesaka, T., 2002. Dimensional stability and environmental effects on paper properties. Handb. Phys. Test. Pap., 1, pp.115–171.

Uesaka, T., 2004. Web breaks in pressroom: a review, Report, Fibre Science and Communication Network, Sundsvall, Sweden.

Uesaka, T., Okaniwa, H., Murakami, K. and Imamura, R., 1979. Tearing resistance of paper and its characterization. Jpn. TAPPI J., 33(6), pp.403–409.

Vainio, A. and Paulapuro, H., 2007. Interfiber bonding and fiber segment activation in paper. BioResources, 2(3), pp.442–458.

Van Der Reyden, D., Hofmann, C., Baker, M. and Mecklenburg, M., 1992. Modern transparent papers: materials, degradation, and the effects of some conservation treatments. MRS Proceedings. Cambridge Univ Press, p. 379.

Verma, P., Shofner, M.L. and Griffin, A.C., 2014. Deconstructing the auxetic behavior of paper. Phys. Status Solidi B, 251(2), pp.289–296.

Viggiani, G. et al., 2012. ALERT Doctoral School 2012: advanced experimental techniques in geomechanics, ALERT Geomaterials.

Viguié, J. et al., 2011. Analysis of the hygroexpansion of a lignocellulosic fibrous material by digital correlation of images obtained by X-ray synchrotron microtomography: application to a folding box board. J. Mater. Sci., 46(14), pp.4756–4769.

Viguié, J. et al., 2010. Analysis of the strain and stress fields of cardboard box during compression by 3D Digital Image Correlation. Applied Mechanics and Materials. Trans Tech Publ, pp. 103–108.

Viguié, J., 2010. Comportements mécanique et hygroexpansif des matériaux lignocellulosiques pour l'emballage rigide. Doctoral thesis. Grenoble INP, Grenoble, France.

Viguié, J. et al., 2013. Finding fibres and their contacts within 3D images of disordered fibrous media. Compos. Sci. Technol., 89, pp.202–210.

Wainwright, S.A., 1982. Mechanical design in organisms, Princeton University Press.

Walker, J. and Butterfield, B., 1996. The importance of microfibril angle for the processing industries. N. Z. For., 40, pp.34–40.

Wernersson, E., Borodulina, S., Kulachenko, A. and Borgefors, G., 2014. Characterisations of fibre networks in paper using micro computed tomography images. Nord Pulp Pap Res J, 29(3), pp.468–475.

Wernersson, E.L., 2014. Characterisation of wood-fibre—based materials using image analysis. Doctoral thesis. Uppsala University, Uppsala, Sweden.

Westerlind, B., Carlsson, L. and Andersson, Y., 1991. Fracture toughness of liner board evaluated by the J-integral. J. Mater. Sci., 26(10), pp.2630–2636.

Whitney, J.M. and Nuismer, R., 1974. Stress fracture criteria for laminated composites containing stress concentrations. J. Compos. Mater., 8(3), pp.253–265.

Williams, M., 1956. On the stress distribution at the base of a stationary crack. J. Appl. Mech., 24, pp.109–114.

Wong, L., Kortschot, M. and Dodson, C., 1996. Effect of formation on local strain fields and fracture of paper. J. Pulp Pap. Sci., 22(6), pp.J213–J219.

Yeh, K., Considine, J. and Suhling, J., 1991. The influence of moisture content on the nonlinear constitutive behavior of cellulosic materials. Proceedings of the 1991 International Paper Physics Conference, TAPPI. pp. 695–711.

Yu, B., Bradley, R., Soutis, C. and Withers, P., 2016. A comparison of different approaches for imaging cracks in composites by X-ray microtomography. Phil Trans R Soc A, 374(2071), p.20160037.

Yuhara, T. and Kortschot, M., 1993. The J-integral as a parameter for characterizing the fracture toughness of paper. Prod. Papermak. Proc. 10th Fundam. Res. Syposium Oxf. Ed CF Bak. Pira Int. Leatherhead 1993.